UNIVERSITY OF SOUTHAMPTON

FACULTY OF ENGINEERING AND PHYSICAL SCIENCES
School of Physics and Astronomy

Investigating Excitonic States in Transition Metal Dichalcogenide Monolayers and Heterobilayers Using Resonance Raman Spectroscopy

by

Liam P. McDonnell

A thesis submitted in partial fulfillment for the
degree of Doctor of Philosophy

February 2020

UNIVERSITY OF SOUTHAMPTON

ABSTRACT

FACULTY OF ENGINEERING AND PHYSICAL SCIENCES
School of Physics and Astronomy

Doctor of Philosophy

INVESTIGATING EXCITONIC STATES IN TRANSITION METAL DICHALCOGENIDE MONOLAYERS AND HETEROBILAYERS USING RESONANCE RAMAN SPECTROSCOPY

by Liam P. McDonnell

This thesis investigates the excitonic states in transition metal dichalcogenide monolayers (TMDC) and heterobilayers using resonance Raman spectroscopy. The resonance Raman behaviour of monolayers of $MoSe_2$ and WSe_2 are probed at 4 K for both the A and B excitons and reveals the involvement of both neutral excitons and trions. For $MoSe_2$ when resonant with the B exciton several Raman peaks at 481.1, 531.2 and 581.1 cm^{-1} exhibit an anomalous resonance behaviour. This is due to a double resonance with the neutral B exciton and a lower energy state at 1.802 eV, which is likely the 2s excited state of the A exciton. In monolayer WSe_2 resonance Raman behaviour is observed at the A and B excitons along with an additional resonance at 1.866 eV, which is attributed to the 2s excited state of the A exciton. A unique Raman peak at 494 cm^{-1} is also discovered when resonant with the WSe_2 2s state and has an asymmetric resonance profile. This asymmetry is the result of a double resonance process involving the 2s state at 1.866 eV and a higher energy state at 1.904 eV, which is attributed to either an excited state (3s/4s) or a dark excitonic state. Heterobilayer samples of $MoSe_2/WSe_2$ were investigated with twist angles of 57° (HS1) and 6° (HS2). For HS1 new low frequency Raman peaks are identified, which have a different characteristic spectra when exciting the $MoSe_2$ or WSe_2 excitons. These peaks are the result of zone folding with both the moiré and crystallographic superlattices. The resonance profiles of the low frequency peaks demonstrate an unexpected coupling of these peaks only to trions which is not yet understood. For HS1 when resonant with the WSe_2 B exciton new Raman peaks at 290.7, 309.1 and 353.8 cm^{-1} are observed. The peaks at 309.1 and 353.8 cm^{-1} are assigned to the $A_2''(\Gamma)$ phonons associated with WSe_2 and $MoSe_2$ respectively. The presence of Raman peaks associated with the $MoSe_2$ layer at the WSe_2 B exciton suggests hybridisation of WSe_2 and $MoSe_2$ excitonic states. The symmetry associated with the $A_2''(\Gamma)$ phonons indicates that this hybridisation may involves the WSe_2 B exciton and an interlayer exciton.

Contents

List of Figures

List of Tables

Declaration of Authorship

I, Liam P. McDonnell , declare that the thesis entitled *Investigating Excitonic States in Transition Metal Dichalcogenide Monolayers and Heterobilayers Using Resonance Raman Spectroscopy* and the work presented in the thesis are both my own, and have been generated by me as the result of my own original research. I confirm that:

- this work was done wholly or mainly while in candidature for a research degree at this University;
- where any part of this thesis has previously been submitted for a degree or any other qualification at this University or any other institution, this has been clearly stated;
- where I have consulted the published work of others, this is always clearly attributed;
- where I have quoted from the work of others, the source is always given. With the exception of such quotations, this thesis is entirely my own work;
- I have acknowledged all main sources of help;
- where the thesis is based on work done by myself jointly with others, I have made clear exactly what was done by others and what I have contributed myself;
- none of this work has been published before submission

Signed:...

Date:..

Acknowledgements

Firstly the completion of this thesis would not have been possible without the invaluable guidance provided by my supervisor Prof. David C. Smith, who has supported me throughout this research project. I am grateful for both his patience and encouragement over the past few years. Likewise this research could not have been completed without the support of the technical staff who keep the department running. In particular I would like to thank Kathleeen Leblanc for helping me navigate the perils of the cleanroom. Special thanks also go to Justin Harris who has kept our group supplied with precious liquid helium.

I would like to thank Dr Joe Spencer for both his friendship and previous stewardship of the resonance Raman system. A special thanks also goes to Jacob Viner who has been a boost to the group and has assisted with collection of the data contained in this thesis. I wish him the best of luck with his own research and completion of his PhD. I would also like to acknowledge the support of other students in the QLM group who have helped me navigate the world of experimental physics.

Of course I would like to thank my family Andrew, Denise, Kieran, Callum and Matthew McDonnell for their support throughout my time at University. If they can glean one thing from this thesis I hope it is the difference betweeen Ramen and Raman. Finally Fiona Walsh deserves a special mention for supporting me through the highs and lows of PhD life and I am exceedingly lucky to have her in my life.

Chapter 1

Introduction

The exciton, a quasi-particle formed from a bound electron and hole, was first proposed in 1931 by Frenkel [1, 2], and extended to semiconducting crystals by Wannier and Mott [3]. The binding energy of these excitons is of the order of 0.01 eV in bulk semiconductors, for example in silicon the exciton binding energy is 14.7 meV [4]. A consequence of their small binding energy is that the excitonic states are only observed at low temperatures in bulk semiconductors. However, in 2D systems the confinement of the electron and holes results in increased exciton binding energies. This was first demonstrated in 1984 for GaAs quantum wells [5]. Recently the discovery of Graphene by Novoselov et al. in 2004 [6] has redefined the field of 2D materials allowing monolayers of crystals to be produced with thickness's below 0.7 nm. The truly 2D nature of Graphene has revealed remarkable properties including excellent mechanical strength, massless Dirac fermions and observation of the quantum hall effect [6, 7, 8].

The ability to produce monolayers from layered bulk crystals, which are weakly bound together by Van der Waals forces, has led to the development of a wide range of new 2D materials. These include the transition metal dichalcogenide family of materials (TMDC) [9], black phosphorous [10], hexagonal Boron-Nitride (hBN) [11] and there are over 1000 possible 2D materials predicted [12]. The availability of a broad range of 2D materials results in a range of electrical properties including semiconductors [9], insulators [13] and superconductors [14] along with ferromagnetic [15], piezoelectric and ferroelectric materials [16]. In addition these materials provide potential platforms for the observation of exotic excitations, such as Weyl fermions and Majorana bound states [17, 18]. The large excitonic binding energies, of the order of $\sim$ 500 meV, are also ideal for exploring the properties of many body excitonic states including excitons, trions and biexcitons [19], and allow these states to be observed at room temperatures [20]. TMDC's as a subset of these 2D materials are particularly promising due to their electrical and optical properties. In the monolayer limit several TMDCs become direct band gap semiconductors in the visible range and have been demonstrated in photovoltaics, photodiodes, transistors, photodetectors and chemical sensing applications [21, 9, 22].

The symmetry of monolayers TMDCs results in valley dependent optical selection rule and so are a promising platform for Valleytronics [23]. The mechanical properties of these 2D materials also makes them a promising candidate for applications in flexible electronics [24, 25].

Recent advances have enabled the fabrication of novel homobilayers and heterostructures from 2D materials [26, 27]. The weak nature of the Van der Waals forces between these 2D materials allows for the formation of structures composed of several layers with arbitrary twist angles. A consequence of this alignment is the emergence of moiré patterns in these structures with a periodicity determined by the twist angle. Moiré interferences is able to modify the electronic and optical properties resulting in surprising physical properties such as the appearance of superconductivity and Mott insulator states in twisted bilayer graphene [28, 29]. This degree of freedom allows for tuning the properties of Van der Waals structures and allows for the observation of novel effects such as Hoftstader's Butterfly [30]. Furthermore, control over the stacking orientation, availability of a broad range of 2D materials and potential compatibility with planar fabrication techniques offers the potential for the practical realisation of novel optical and electronic devices using TMDCs in the future.

1.1 Motivation

I commenced my PhD in September 2015 at the University of Southampton in the Nanomaterials group. During my undergraduate course I worked in the same group to develop a resonance Raman protocol for conducting these measurements on extreme nanowires at cryogenic temperatures [31]. Following this I was keen to apply this technique to other nanomaterials in order to probe the underlying physics of optical transitions. At this time the field of research on 2D materials was gaining significant momentum following the discovery that MoS_2, a material previously used as a solid state lubricant [32], transitions to a direct band gap semiconductor at the monolayer limit [9]. Monolayer TMDCs presented an exciting class of materials with novel electronic and optical properties to explore using resonance Raman spectroscopy (RRS). In particular the large binding energy of excitons in these materials allows for the possibility of exploring the many body physics of these excitonic states [33, 34]. Several papers had also been published investigating the resonance Raman behaviour of TMDC materials [35, 36] but were limited in their scope by only being carried out at room temperature. As a result these experiments were unable to investigate the interactions between more complex many body excitations such as trions. The application of low temperature RRS presented an exciting opportunity to contribute to the understanding of optical transitions and scattering via phonons in these materials.

1.2 Resonance Raman Spectroscopy of monolayer WS_2

The experimental chapters in this thesis present the results of RRS on encapsulated monolayers and heterobilayers composed of $MoSe_2$ and WSe_2. Prior to this work I also explored the resonance Raman behaviour of monolayer WS_2 as a function of temperature from 4 to 295 K. The outcome of this investigation was a first author publication in Nano Letters, which was published in January 2018 [37]. This work allowed me to develop both the experimental methodology and theoretical basis for interpreting the resonance Raman spectra of TMDCs materials. Nevertheless, for brevity I have elected to avoid a rigorous discussion of this work in my thesis due to the abundance of experimental results obtained on encapsulated TMDC monolayers and heterobilayers samples. Instead a brief summary of the key results from this investigation are provided below. Of course if the reader desires a more complete discussion of these results then please refer to ref [37].

The resonance Raman results reported in ref [37] were performed on a WS_2 monolayer grown via chemical vapour deposition (CVD) on a silicon oxide coated substrate. Resonance Raman spectra were attained at excitation energies between 1.95 to 2.15 eV probing the WS_2 A exciton. Resonance Raman profiles were obtained for the A_1', E', 2ZA, LA and 2LA phonons and an unassigned peak at 485 cm^{-1}. The intensity profiles for the different phonons revealed a consistent asymmetry present only a low temperatures. To explain this asymmetry required a single scattering event Raman model involving two excitonic states with interstate scattering allowed. The excitonic states involved were identified as the WS_2 neutral exciton and trion. These results revealed three separate Raman scattering channels corresponding to scattering between exciton-exciton, trion-trion and exciton-trion states. The amplitudes associated with these scattering channels were extracted and allowed the relative scattering strength of the A_1' and E' phonons to be determined as a function of temperature. The scattering model used to explain the resonance Raman profiles for the single phonon Raman peaks was also applied to fit the profiles associated with higher frequency multiphonon Raman peaks. These multiphonon Raman peaks involve the scattering to large wavevector excitonic dark states and analysis of their profiles indicates the coupling of bright excitons to to bright trions via large wavevector states. Overall these results establish the presence of excitons, trions and dark excitonic states participating in the Raman scattering process and provides a powerful tool for investigating the different scattering channels available in TMDC materials.

1.3 Organisation

This section provides a brief description of the chapters contained within this thesis.

Chapter 2 provides a discussion of the theoretical concepts required for understanding the work in this thesis. The properties of monolayer TMDCs are presented including their crystal symmetries, electronic band structure, properties of exciton and their role in optical transitions. This is followed by a discussion of the properties of heterobilayers, such as the formation of interlayer excitons, and moiré effects. Finally phonons in TMDCs are discussed followed by a detailed description of Raman scattering and resonance Raman spectroscopy.

Chapter 3 presents the experimental methodology used for the experiments presented in this thesis. The fabrication methods required to produced the samples used in this thesis are discussed, followed by a description of the experimental setup for the resonance Raman measurements and a discussion of experimental considerations such as laser heating, spot size and repeatability. Lastly the techniques used for data analysis including background subtraction, fitting of the Raman spectra and analysis of the resonance Raman profiles are presented.

Chapter 4 presents the results of RRS on an encapsulated monolayer of $MoSe_2$, including a discussion of the potential assignments for the different Raman peak and an analysis of the resonance behaviour at the $MoSe_2$ B exciton.

Chapter 5 presents the results of RRS of an encapsulated WSe_2 monolayer. Again the assignment of the single phonon and multiphonon Raman peaks are discussed followed by analysis of the resonance Raman data. For WSe_2 resonance Raman behaviour is reported for three different excitonic states associated with the WSe_2 1s A and B excitons and resonance with an excited 2s state of the A exciton.

Chapter 6 presents the RRS of heterobilayers of $MoSe_2/WSe_2$ with different twist angles. The Raman spectra for the monolayers and heterobilayers are compared and assignments of new Raman peaks are proposed. The resonance Raman profiles for the heterostructures when resonant with both the $MoSe_2$ and WSe_2 A and B excitons are analysed, followed by a section presenting the resonance Raman behaviour of new low frequency Raman peaks. An analysis and discussion of the resonance Raman results follows and details the potential hybridisation of intra and inter-layer excitonic states and the effects of moiré and crystallographic superlattices on the vibrational and excitonic properties.

Chapter 7 then summarises the conclusions of the experimental results presented and the potential for RRS as a tool for studying 2D materials, followed by an outlook considering further work that may result from this thesis and the future direction of 2D materials.

Chapter 2

Theoretical Background

Transition metal dichalcogenides have generated huge interest in the field of 2D materials, due to their remarkable electronic and optical properties. In particular monolayer TMDCs have allowed the realisation of valley polarisation advancing the emerging field of valleytronics [23]. This chapter aims to provide an overview of the theory required to understand and interpret the experimental results in subsequent chapters. As such, we discuss the electronic and optical properties of monolayer TMDCs and provide a discussion of the effects of combining different TMDC monolayers to form novel heterostructures. Following this the general theory of Raman scattering and resonance Raman spectroscopy is presented, along with an overview of the current progress in using Raman spectroscopy to study TMDCs. Whilst the detail provided in this chapter is sufficient for our discussion of the resonance Raman experiments, we also recommend ref [38] if the reader desires a more thorough discussion of the theory of Raman scattering.

2.1 Transitions Metal Dichalcogenides Crystal Structure

Transition metal dichalcogenides are a family of materials consisting of a layer of transition metal atoms sandwiched between two layers of chalcogen atoms. These materials have the general chemical formula AB_2 where A denotes the transition metal atoms e.g Mo, W, Re, Hf, and B refers to the chalogen atoms e.g S, Se, Te. In bulk form these materials are composed of stacked layers and are weakly bound together by Van der Waals forces, similar to Graphite, this structure allows TMDCs to be thinned to the monolayer limit using the mechanical exfoliation technique developed for graphene [39]. A top down view of the crystal structure for a single TMDC layer is presented in Figure 2.1 and clearly shows the hexagonal symmetry of the crystal lattice. Each transition metal atom in the lattice is bonded to six chalcogen atoms and has trigonal prismatic co-ordination [40] as shown in Figure 2.1 panel b). In addition, TMDC layers with octahedral co-ordination where the two planes of chalcogen atoms are rotated relative

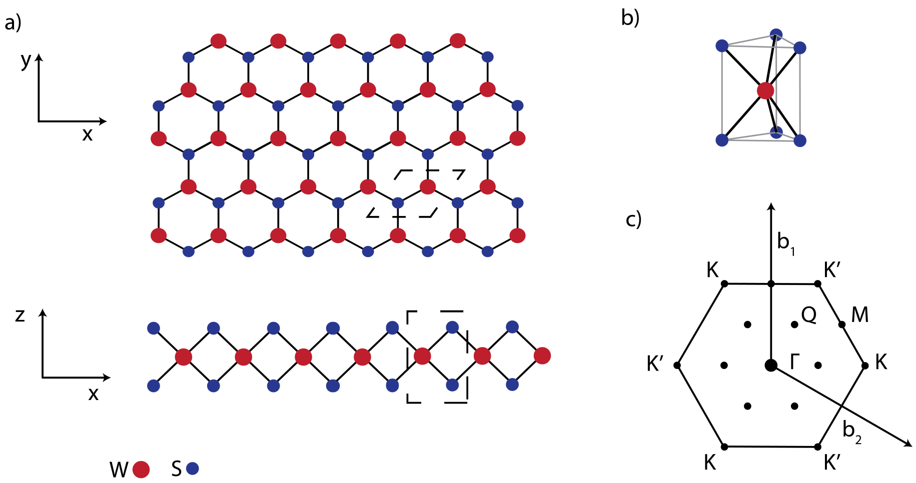

Figure 2.1: Panel a) shows both a top down and side view of a TMDC monolayer with the red and blue circles representing the Transition metal and chalcogen atoms respectively. The unit cell of the lattice is indicated in both the top down and side view by the dashed outlines. Panel b) then shows the trigonal prismatic co-ordination of the atoms as indicated by the grey lines with the chemical bonds between atoms indicated by the black lines. Panel c) then shows the first Brillouin zone of the TMDC layer with the high symmetry points at Γ, M, Q and K/K′ labelled and the arrows showing the reciprocal lattice vectors b_1 and b_2.

to each other by 180 degrees can also exist. These two co-ordinations possess different electronic properties, for example MoS_2 with trigonal-prismatic co-ordination is semiconducting [41], whereas with MoS_2 with octahedral co-ordination is metallic[42]. The octahedral co-ordination does not occur naturally and so in this thesis we confine our discussion to the trigonal prismatic TMDC structures [43].

The stacking of layered TMDC structures with trigonal prismatic co-ordination can be described using the notation set out in ref [44]. Where AA describes two layers exactly aligned, AA′ indicates aligned layers with one layer rotated by 180 ° so that the chalcogen atoms are aligned with the transition metal atoms in the other layer, and AB stacking indicates a transition metal atom is aligned with a chalcogen atom resulting in a staggered pattern with the remaining atoms appearing over the centre of the hexagonal lattices. In literature AA′ and AB stacking are also referred to using a bulk TMDC notation as 2H and 3R phases respectively [45]. From this notation there are five possible high symmetry stacking orders given by AA, AA′, AB, A′B and AB′ [46]. The number of layers in TMDC materials and their stacking order naturally result in different crystal symmetries. For bulk TMDC materials the point group describing the crystal symmetries is the D_{6h} group, whereas a monolayer has D_{3h} point group. However, in the few layer regime the stacking orders of the layers and relative twist angles can result in a broad range of different crystal symmetries. The stacking order and resulting crystal symmetries of structures produced from TMDC layers are of particular importance in

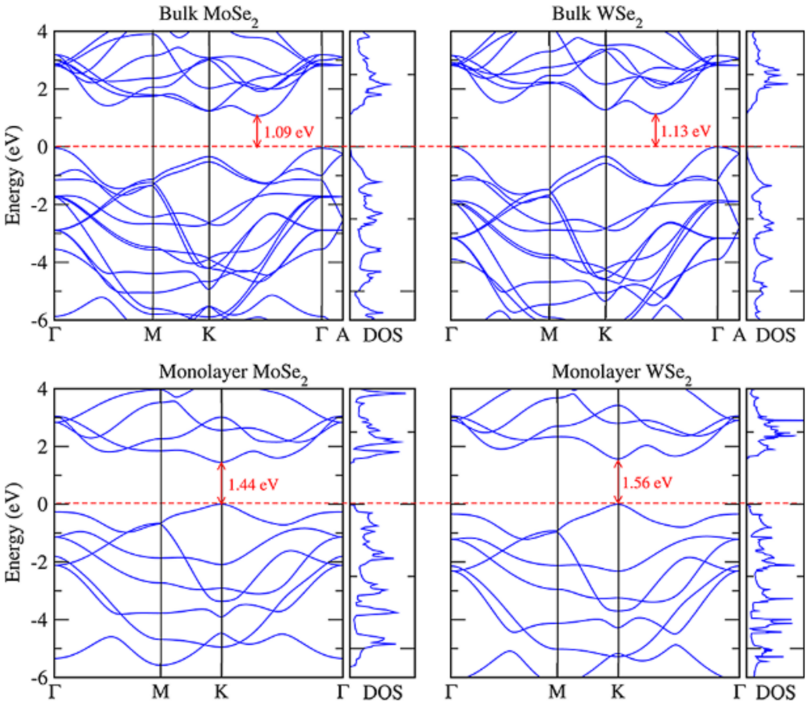

Figure 2.2: Electronic band structures calculated using DFT by Kumar et al. for monolayer and bulk MoSe$_2$ and WSe$_2$. Reprinted with permission from [62]. Copyright American Chemical Society.

determining the electronic bandstructure, optical selection rules and Raman selection rules [47, 48, 49].

2.2 Electronic Structure and Properties of TMDCs

The diversity of the TMDC family of materials results in a variety of different electronic properties dependent on the composition of the layers. For example, Nb, Pd, and Pt disulphides and diselenides are semimetals at room temperature but show superconducting transitions at lower temperatures [50, 14, 51]. This is complemented by a broad range of both indirect and direct band gap semiconductors including Hf, Re, Mo and W disulphides and diselenides [9, 52, 53, 54, 55] with at least 38 stable semiconducting TMDCs predicted [56]. Of particular interest in this thesis are MoS$_2$, MoSe$_2$, WS$_2$ and WSe$_2$ TMDCs which are all indirect band gap semiconductors in bulk and transition to direct gap semiconductors in the monolayer limit [9, 57, 58]. The band structures of bulk and monolayer TMDCs have been studied extensively both theoretically using Density Functional Theory (DFT) [59, 60, 61, 62] and experimentally through Angle Resolved Photo-emission Spectroscopy (ARPES) measurements [63, 64].

The first Brillouin zone for a TMDC monolayer is shown in Figure 2.1 panel b) with the high symmetry points denoted by Γ , M, Q (or Λ point), K and K′ are shown where K and K$'$ are inequivalent in momentum space. For bulk MoS_2, $MoSe_2$, WS_2 and WSe_2 the electronic structure gives rise to an indirect band gap between the valence band maxima at the Γ point and the conduction band minima at the Q point [65]. Whereas, in the monolayer limit these materials demonstrate a direct band gap between the valence band maxima and conduction band minima at the K/K$'$ points [9, 57, 58]. The transition from direct to indirect band gap as a function of the sample thickness can be understood by considering the resulting contribution of the electron orbitals in the crystal to the electron wave functions at the high symmetry points, which are reported by Zhu et al. and Liu et al. [66, 67]. These reveal that at the K/K$'$ point the states are dominated by the Mo-$d_{x^2-y^2}, d_{xy}, d_{z^2}$ orbitals and the states at the Γ and Q points are predominantly the result of the Sp_z orbitals. When the number of layers in a TMDC sample is decreased the quantum confinement of the electron orbitals in the z direction causes a significant increase in the energy of the states at the Γ and Q points in the band structure, while the energy of the states at the K/K$'$ points remain relatively unchanged. This results in a transition from indirect to direct band gap at the monolayer limit[9]. The electronic band structure for both monolayer and bulk of $MoSe_2$ and WSe_2 is shown in Figure 2.2. Comparison of the bulk and monolayer bandstructure shown in Figure 2.2 for each material clearly shows a transition from indirect to direct band gap.

In monolayer TMDCs the breaking of inversion symmetry of the crystal lattice has importance consequences for the electronic properties and leads to a spin valley coupling [68, 69]. At the K/K$'$ points for a monolayer the two valleys are symmetric with rotational symmetry C_3 (three fold rotation) and results in the K and K$'$ Bloch states having opposite phases[70]. As a result the K/K$'$ points have opposite sign for their orbital magnetic moments and Berry curvatures [71]. The difference in these electronic properties due to the inequivalent nature of the K and K$'$ valleys is known as pesudospin and is commonly referred to by the valley index where $\tau_v = \pm 1$. The difference in the Berry curvatures allows for the observation of the valley hall effect when an electric field is applied in plane and is similar to the spin Hall effect [72]. Whereas, the dependence of the orbital magnetic moment on the valley index allows for the pseudospin to be addressed by magnetic fields allowing for valley Zeeman splitting [73]. This also results in a valley-dependent optical selection rule where the K and K$'$ valleys couple to different circular polarisations σ_+ or σ_-. The appearance of these valley dependent properties is a general consequence of the breaking of spatial inversion symmetry [68]. For a bilayer system the inversion symmetry can be recovered for the AA$'$ stacking orientation, however, for AB stacking and other arbitrary orientations of the crystal lattice inversion symmetry can remain broken [49].

A significant contribution to the TMDC electronic band structure is the effect of spin orbit coupling at the K points. This arises from the coupling of the orbital angular momentum of the electrons to the spin state via the spin orbit interaction [74] and results in eigenstates of the total angular momentum given by $j = l + s$. In the bandstructure

Table 2.1: Values of the electronic properties of monolayer TMDCs. These were obtained from Kosmider et al. 2013 [75] and Berkelbach et al 2013 [76] as indicated by ^{a} and ^{b} respectively. The conduction and valence band spin splitting are given by CB and VB respectively, and EB$_X$ is the exciton binding energy.The spin splitting of the conduction and valence bands is given by $\Delta E_{CB,VB} = E_\uparrow - E_\downarrow$ and so values can be positive or negative.

Material	Band gap	CB (meV)	VB (meV)	EB$_X$ (meV)
MoS$_2$	x	-3 ^{a}	147 ^{a}	540 ^{b}
MoSe$_2$	y	-21 ^{a}	186 ^{a}	470 ^{b}
WS$_2$	z	27 ^{a}	433 ^{a}	500 ^{b}
WSe$_2$	v	38 ^{a}	463 ^{a}	450 ^{b}

of TMDCs this leads to a spin splitting of both the valence and conduction bands at the K (K$'$) points [66]. For comparison the spin orbit splitting of the valence and conduction band for MoS$_2$, MoSe$_2$, WS$_2$ and WSe$_2$ are provided in Table 2.1. From Table 2.1 it is clear that the valence band splitting (Δ_{VB}) is much larger then the conduction band splitting (Δ_{CB}) with values between 147 and 463 meV, whereas the CB splitting ranges from 3 to 38 meV. The CB splitting also demonstrates a sign change when comparing Mo and W TMDCs, and results in the lowest energy conduction band having a different spin to the highest energy valence band in the W materials.

2.2.1 Excitons in Monolayer TMDCs

An exciton is a quasiparticle consisting of a bound pair of an electron and a hole in a semiconductor or insulator. These form when an incident photon excites an electron from the valence band to the conduction band and then becomes bound to a hole in the valence band forming an exciton with an energy below the electronic band gap. In quantum wells the binding energies of excitons are relatively low, for example in an GaInAs/InP the binding energy is $\sim$ 17 meV [77]. However, in monolayer TMDCs the exciton binding energies are significantly higher due to reduced dielectric screening and confinement to two dimensions resulting in enhanced Coulomb interactions [78, 79]. The predicted binding energies of excitons in TMDCs range from 0.3 to 1.1 eV [78, 76, 33], with experimental measurements demonstrating binding energies between $\sim$ 0.3 to 0.8 eV [80, 81, 82]. The large binding energies also enables the observation of excited excitonic states analogous to those of the hydrogen atom [80]. The energies of these excited states in semiconductors can be predicted by the Rydberg series as described by Equation 2.1. Where E$_n$ is the energy of the nth state, E$_g$ is the energy of the band gap, R is the Rydberg constant, K is the wavevector and M is the reduced mass of the exciton. In monolayer TMDCs the energies of the excited states follow a non-hydrogenic Rydberg series due to the dielectric screening in the material [80].

$$E_n = E_g + \frac{\hbar^2 K^2}{2M} - \frac{R}{n^2} \tag{2.1}$$

The electronic band structure for monolayer TMDCs is dominated by the valence band splitting arising from the spin orbit coupling. This produces two different excitons which are referred to in literature as the A and B excitons [83, 84]. There are also higher energy excitonic states with a broad contribution between 2.3 and 2.8 eV typically labelled as the C exciton and has been attributed to a high density of states near the Γ point due to band nesting[85, 79]. In bilayer and few layer materials it is also possible for additional excitonic states to be observed, which are labelled the A′ and B′ states. These arise from the formation of interlayer A and B excitons and are observed at higher energies due to the spatial separation of the electron and hole resulting in a reduced exciton binding energy [86].

The large binding energies of excitons in TMDC monolayers also allows for the formation of other many body quasi-particles. Frequently observed in TMDCs is the charged exciton (trion) which can be composed of either two electrons and a hole (eeh) or an electron and two holes (ehh) producing both negatively or positively charged quasi-particles [19, 20, 87]. These trions are observed to have binding energies of between 21 and 43 meV in the different TMDC materials and are an order of magnitude larger than in quantum well systems [88, 89]. It is also possible for higher order many body quasiparticles to occur in monolayer TMDC materials with both neutral and charged biexcitons reported [87, 90, 91, 92, 93]. In addition, photoluminescence spectra of TMDC monolayers have revealed multiple peaks associated with trions in monolayer WSe_2 [94, 95]. The three body nature of the trion allows for bright states involving both intra-valley trions with all three particles localised in momentum space and inter-valley trions with either an electron or hole located in the opposite K valley [88]. Overall there are a broad array of different excitonic states which can be investigated in monolayer TMDCs and allows the probing of many body effects.

2.3 Electronic Structure and properties of TMDC heterobilayers

So far the discussion of the electronic properties has focused on monolayer TMDCs and homobilayers. However, the fabrication of structures composed of two different TMDC layers and the encapsulation of monolayers between other 2D materials such as hBN can modify the electronic and optical properties. The following sections provide details of moiré interference effects, and the properties of interlayer excitons formed in these heterostructures.

2.3.1 Interlayer Excitons

Recent advances in the fabrication of 2D materials, using methods such as stamp transfer and CVD growth [96, 97], has allowed the realisation of Van der Waals stacked heterostructures. The choice of any of the 2D semiconducting layers results in a type II band alignment with the energy minima for the electrons and holes occurring in the different layers [98]. This allows for the formation of interlayer excitons where the electrons and holes are spatially separated in different layers. To date these interlayer excitons have been observed in a variety of different heterobilayer structures [26, 99, 100, 101] and have many desirable properties such as long lifetimes, ultrafast charge transfer and are potential platforms for high temperature Bose-Einstein condensates [102, 103, 104, 105, 106].

The energy of interlayer excitons is dependent on the band alignment of the two constituent monolayers, twist angle, and the interlayer exciton binding energy [98, 107]. The binding energy of the interlayer exciton is dependent on the screening of the coulomb interaction and the spatial separation of the layers. The out of plane separation of the electrons and holes results in a dipole moment, which can be used to tune the energy of the interlayer exciton by applying an external electric field [108]. The separation of the electron and hole also reduces the overlap of their wave functions resulting in exciton lifetimes a order of magnitude larger than the intralayer excitons in TMDCs [26]. The twist angle between the layers in these heterobilayers can results in moiré effects and a momentum space mismatch between the $K(K')$ points in the Brillouin zone [109]. This can produce both direct and indirect interlayer excitons and can be used to tune their properties by changing the sample twist angle [104, 110]. The charge transfer between the layers in heterobilayer systems is fast occurring within 50 fs of excitation, and is insensitive to the sample twist angle [103]. For charge transfer at the K point the interlayer coupling is predicted to be weak due to the in plane nature of the electrons. This ultrafast charge transfer is proposed to occur via phonon mediated processes with states at the Γ and Q points, which are de-localised across the two layers [111, 105, 112]. Optically interlayer excitons have demonstrated a robust valley polarisation with long depolarisation times [113, 114] and preservation of the spin valley polarisation of optically excited electrons and holes when transferred across the layers [115].

2.3.2 Moiré Interference

A moiré pattern occurs when two periodic arrays are superimposed on top of each other resulting in a new periodic pattern, an example of this can be seen in Figure 2.3 for two hexagonal lattices with twist angles of 0 and 10 °. This moiré pattern has been extensively studied and has applications ranging from to the measurement stress and strain in materials, increasing the resolution of microscopy set-ups and is frequently encountered in display technologies[116, 117, 118]. The availability of a range of two dimensional materials and the development of deterministic stacking techniques such as viscoelastic stamp transfer has resulted in the fabrication of Van der Waals stacked structures [96, 119]. A consequence of these stacked structures is a moiré pattern resulting from the two overlapped crystal lattices [120, 121]. The resulting moiré pattern introduces an additional periodicity to the crystal structures and alters the electronic band structure and optical properties of the material. The most prominent example of these effects is the so called "magic angle" of 1.1 ° for twisted bilayer Graphene, which

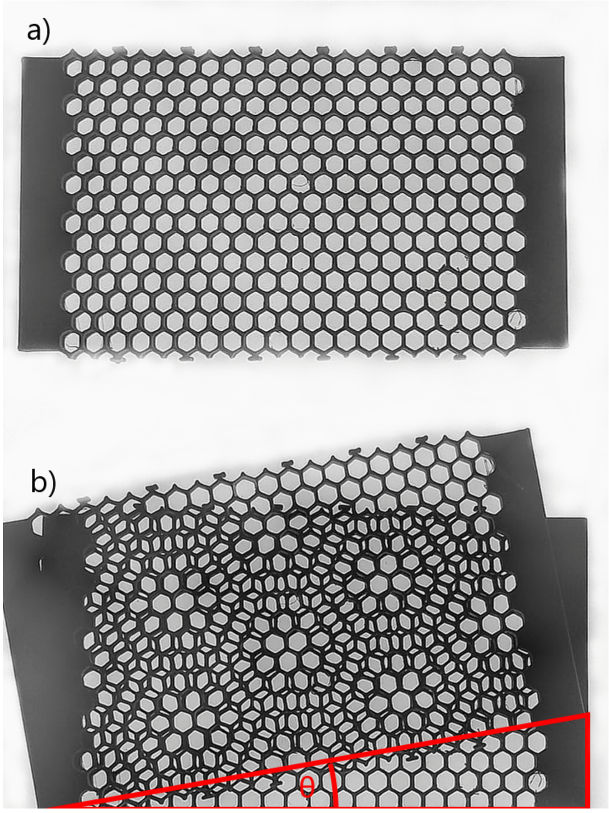

Figure 2.3: Example of moiré interference for a 2D hexagonal lattice panel a) shows the two lattices aligned with a twist angle of 0° and panel b) show the two lattices with a twist angle of $\sim$ 10°.

results in a superconducting transition [28]. The ability to vary the twist angle in these materials provides an additional degree of freedom in device fabrication not possible in other solid state systems.

When considering the effects of stacked Van der Waals structures it is necessary to consider both the crystallographic and the moiré super lattices resulting from the alignment of the two constituent monolayers. The moiré and crystallographic superlattices both describe the periodicity of the moire interference pattern, however the reciprocal lattice vectors describing the crystallographic superlattice are additionally constrained as they must describe translation between indistinguishable points in the crystal lattice. As a result the unit cells associated with the moire and crystallographic superlattices are only equivalent for certain twist angles. For a crystallographic superlattice a pair of indices are defined (m,n) where (m≠n) and related to the superlattice vectors $V_1=mb_1+nb'_1$ and $V_2=mb_2+nb'_2$, where $b/b'_{1,2}$ are the reciprocal lattice vectors for the different monolayer TMDCs. From this formulation the wave vector of the crystallographic superlattice is given by Eq 2.2.

$$K_c \propto \frac{2sin(\frac{\theta}{2})}{|m-n|} \tag{2.2}$$

Whereas, the moiré wave vector can be given by the relation shown in Eq 2.3.

$$|k_m| = 2bsin(\frac{\theta}{2}) \tag{2.3}$$

Where θ is the relative twist angle between the constituent layers in the heterostructure. A consequence of this is that the moiré and crystallographic reciprocal lattice vectors can have different magnitudes and are only equivalent when m-n=1. It is also apparent that K_m and K_c are both smaller than the monolayer reciprocal lattice vector, which allows for zone folding of the Brillouin zone of the constituent monolayers leading to the formation of moiré sub-bands and the observation of large wavevector zone folded phonons [122, 123].

The relative rotation between the two layers also results in momentum mismatch of the K points in the electronic band structure dependent on the twist angle [124]. This can be seen in Figure 2.4, which shows the first Brillouin zones for the two constituent monolayers and are also rotated relative to each other by θ. The interlayer excitons formed in TMDC heterostructures can be either direct or indirect dependent on the alignment of the layers [125]. The moiré potential also allows for trapping of excitons producing quantum dot like states whilst preserving the selection rules for circularly polarised light [126, 109]. This has been proposed as a method for producing uniform nanodot arrays and may allow for investigation of topological excitons, and entangled photon sources [127].

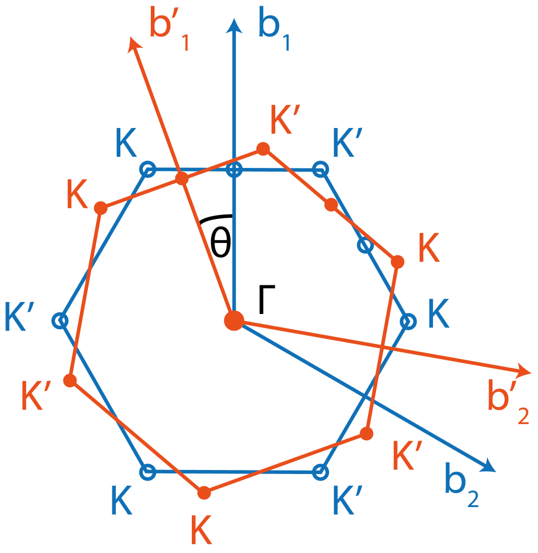

Figure 2.4: The Brillouin zone for two stacked layers are shown with the bottom layer (blue) and top layer (orange) with the high symmetry K points shown for each layer along with the reciprocal lattice vectors given by $b_{1,2}$ and $B'_{1,2}$. The twist angle between the two Brillouin zones is given by θ and can

2.3.3 Hybridisation of Excitons

Comparing the excitons in our TMDC layers to hydrogen atoms an obvious possibility is the hybridisation of states similar to the formation of molecular bonding orbitals. In particular the hybridisation of intralayer and interlayer excitons has been recently reported in heterobilayers [122, 128], and the theoretical behaviour of these hybridised excitons has been recently addressed by Ruiz-Tijerina and Falko in ref [129]. The theoretical approach presented in ref [129] considers the effect of the moiré interference in a resonant and non-resonant regime, where resonance occurs for small band offsets in the heterostructure and is dominated by the moiré effects. The twist angle or gating dependence of the interlayer exciton energy allows for hybridisation of the inter and intralayer excitons retaining the optically bright nature of the intralayer excitons and polar nature of interlayer excitons. Therefore, the application of a electric field perpendicular to the plane of the sample should allow for modulation of the hybridised states. This hybridisation of intra and interlayer excitons is demonstrated to occur for both the A and B intra-layer excitons in heterostructures and is dependent on the energies of the excitonic states and so hybridisation and so its not expected to occur simultaneously for all intralayer excitons.

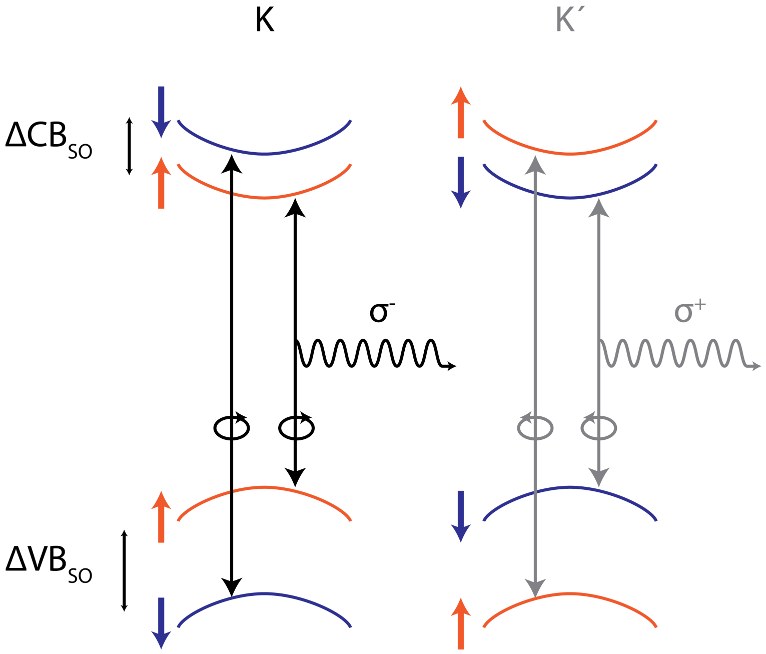

Figure 2.5: Schematic of the optical valley selection rule in monolayer TMDCs for the spin split conduction band and valence band extrema. The colours of the bands indicate if the associated states are spin up (orange)or spin down ()blue). The colours of the arrows and emitted photons then represent the valley index and polarisation of light with σ^+ (grey) and σ^- (black).

2.4 Optical Properties

As discussed in relation to the electronic band structure the energy of the indirect band gap between the Γ point and Q point increases significantly, such that in the monolayer limit there is a transition to direct band gap between the K/K′ valence band maxima and conduction band minima. For indirect band gap semiconductors the excitation (recombination) of an electron from the valence band maxima (conduction band minima) to the conduction band minima (valence band maxima) requires interaction with a phonon in the crystal lattice to provide a change in momentum. As a result monolayer TMDCs demonstrate relatively intense photoluminescence emission due to the direct band gap in these materials [130, 131]. Furthermore the presence of excitons in TMDCs is significantly enhanced due to their large binding energies. Consequently, the optical spectra of TMDCs are dominated by the presence of excitonic transitions. These excitons are apparent in absorption or reflectance contrast measurements with three states typically observed, which are labelled as the A,B and C excitons [132, 133, 82, 134]. Similarly the large binding energy of the TMDCs also allows for other many body quasiparticles including trions, biexcitons and charge biexcitons to be observed.

In addition for monolayer TMDCs the breaking of inversion symmetry results is an optical selection rule coupling different circular polarisations of light to the K/K′ valley. This can be understood from time reversal symmetry which gives $E_\uparrow(k)=E_\downarrow(-k)$. When combined with inversion symmetry given by $E_{\uparrow}(k)=E_{\uparrow}(-k)$ we find that the two expressions result in $E_{\uparrow}(k)=E_{\downarrow}(k)$. So for TMDCs with inversion symmetry the conduction and valence band states at the K/K′ valleys are indistinguishable. Whereas, in monolayers the breaking of inversion symmetry produces states at the conduction and valence bands which have locked spins and valley indexes [69]. This results in a valley dependent optical selection rule where circularly polarised light (σ^+ or σ^-) allows the excitation of states at a particular K(K′)valley [70]. This circular dichroism is not limited to monolayer TMDCs but can appear in other TMDC structures where the inversion symmetry is broken such as AB stacked bilayers [135]. It is also possible to break the inversion symmetry in AA′ bilayers by applying an electric field perpendicular to the plane of the material [136]. The ability for valley polarisation to occur dependent on the stacking geometry in few layer systems is particularly important when considering the properties of Van der Waals heterostructures.

2.4.1 Dark Excitonic states

Thus far the optical properties of bright excitonic states observed in optical spectroscopy experiments have been discussed. However, in TMDC layers intra and inter-valley scattering can allow for dark excitons to be formed. A dark excitonic state is one which cannot radiatively recombine due to a mismatch in either momentum or spin between the conduction and valence band states. Both spin and momentum dark excitons have been reported in TMDCs for neutral excitons and trions [48, 137, 138]. Practically dark states in TMDCs have significantly longer lifetimes than their bright counterparts and are desirable for valleytronics[139, 140]. In W based TMDC dark excitons play a significant role in the optical properties due to the lowest energy conduction states and the K(K′) valleys being spin forbidden. In our experiments dark excitons are of interest as they can couple to bright states via scattering with large wavevector phonons [141] and so can be observed in Raman scattering experiments.

2.5 Phonons

Phonons are the quantum of vibrations propagating in a crystalline lattice and are important when considering the thermal and electronic properties of materials [142]. There are two types of phonons known as acoustic and optical phonons. For a crystalline lattice with a single atom in the unit cell only acoustic phonons are possible. Physically these vibrations arise from the in-phase displacements of the atoms from their equilibrium positions. In TMDCs there are three possible acoustic phonon branches corresponding to a longitudinal acoustic mode (LA),transverse acoustic (TA) and out of plane acoustic mode (ZA). For a crystalline material which contains more than one atom in the unit cell the different atoms movements can also be out of phase resulting in the optical

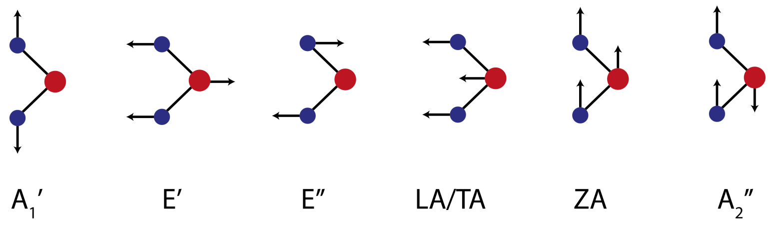

Figure 2.6: The atomic displacements of the vibration modes possible in a monolayer TMDC and are labelled according to their irreducible representations.

phonons [142]. The unit cell of a TMDC monolayer contains a transition metal and two chalcogen atoms and so there are 9 degrees of freedom associated with displacements of the atoms. The point symmetry group for a TMDC monolayer is the D_{3h} and has the irreducible representation given by: $\Gamma = 2A_2'' + A_1' + 2E' + 2E''$ [143]. Where A denotes out of plane motions and E represents doubly degenerate motions in the xy plane. As a result there are nine vibrational modes expected in monolayer TMDCs. Three of these modes are acoustic phonons corresponding to an A_2'' mode which represents the out of plane acoustic phonon and is referred to as the ZA mode, and a E' mode corresponding to the longitudinal and transverse acoustic modes which are denoted as TA and LA respectively. For clarity the acoustic phonons throughout this thesis will be identified as the LA, TA and ZA phonons. There are six optical phonons the A_2'' and A_1' correspond to the out of plane modes and the E' and E'' modes which are in plane vibrations and each consist of two branches corresponding to their longitudinal and transverse (LO or TO) modes. For each of the vibrational modes the atomic displacements are illustrated in Figure 2.6. As previously discussed monolayer and bulk TMDCs have different crystal symmetries and so have distinct irreducible representation. As a result the vibrational mode labelled as A_1' in monolayer is equivalent to the A_{1g} mode using bulk notation. To simplify the discussion of vibrational modes in this thesis the monolayer notation has been used throughout to label the different phonons.

The energy of the different phonons can be calculated using DFT to obtain the phonon dispersion relations. The phonon dispersion relation calculated by Bilgin et al. [144] for monolayer $MoSe_2$ is shown in Figure 4.3 with the different phonon branches labelled accordingly. From Figure 4.3 it is clear that the acoustic phonons tend to zero for small wavevectors, and is due to long wavelength acoustic phonons corresponding to a macroscopic translation of the crystal. Approaching the K and M high symmetry points in the phonon dispersion relation the acoustic phonons frequencies transition from an approximately linear dependence on wavevector to a non-linear regime with relatively constant phonon frequencies [40, 62]. In contrast the optical phonons have a non-zero frequency for all wavevectors and are relatively constant as a function of wavevector and are found to have frequencies between 150 to 500 cm^{-1}. For Raman scattering experiments the phonon dispersion relations are a useful tool in evaluating the different underlying processes which contribute to the Raman spectra.

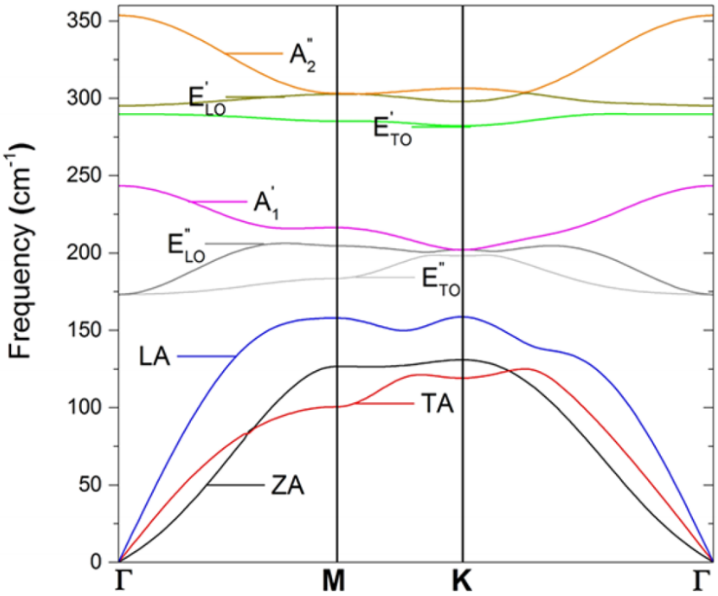

Figure 2.7: The phonon dispersion relation for monolayer $MoSe_2$ calculated using DFT by Bilgin et al. Reprinted with permission from [144]. Copyright 2019 American Chemical Society.

2.6 Raman Spectroscopy

Raman spectroscopy is a well established and powerful technique for probing the vibrational properties of both molecular and solid state systems and is in widespread use across numerous scientific disciplines. In the emerging field of 2D materials Raman spectroscopy has found frequent use in the investigation of Graphene as a non destructive probe that can provide information on electron-phonon coupling, doping, strain and disorder [145, 146, 147]. For those studying 2D TMDCs, Raman spectroscopy has become commonplace due to the ability to rapidly determine the number of layers in these materials [148, 52]. This section will provide an overview of the theory of Raman scattering for both single and two phonon processes; resonance Raman spectroscopy and an overview of the results of Raman spectroscopy in monolayer TMDCs. A general overview of the theory of Raman scattering can be found in references [38, 74]. For a more complete review of the Raman spectroscopy of TMDCs we also recommend references [143, 149].

2.6.1 Raman Scattering

Raman scattering is the inelastic scattering of light with low energy excitations, such as phonons, polarons, plasmons or magnons [38]. In contrast to Rayleigh (elastic) scattering of light where the energy of the photon is unchanged Raman scattering is inelastic resulting in the emission of a photon with a different energy to the initial photon.

Overall Raman scattering is a weak optical process with only 1 in $\sim 10^7$ photons being Raman scattered [74] Whilst it is possible for photons to directly scatter with phonons this interaction is weak unless the photon and phonon have comparable energies [74]. For Raman scattering using light in the visible range of the spectrum the process must involve the coupling of the photon to electrons in the material producing intermediate states which are scattered by phonons in the material. As a result, the interaction of interest in Raman scattering processes is the electron-phonon interaction with Hamiltonian ($\hat{H}_{ep}$). This matrix element can be calculated using different perturbations, such as, deformation potentials and the Frölich interaction [74]. In both cases the matrix elements involve the phonon creation and annihilation operators and so allow for both emission or absorption of phonons. Therefore, the resultant photon from Raman scattering can have a higher energy, due to absorption of a phonon and known as Anti-Stokes scattering or can have a lower energy due to emission of a phonon and is known as Stokes scattering. The probability of either process is determined from the phonon occupation number, which is given by the Bose-Einstein distribution in Eq 2.4. For Anti-Stokes and Stokes processes the scattering rate is then proportional to N_{ph} and $N_{ph}+1$ respectively [74]. As a result at low temperatures the probability of Anti-Stokes Raman scattering tends to zero. In this thesis the experiments presented are at low temperature and as a result we deal exclusively with Stokes Raman scattering processes.

$$N_{ph}(\hbar\omega_{ph}) = (e^{\frac{\hbar\omega_{ph}}{k_b T}} - 1)^{-1} \tag{2.4}$$

For a single phonon Stokes Raman scattering process an incident photon with energy E_1 excites an electron from the valence band of the material via the electric dipole interaction($\hat{H}_{ed}$). This created an intermediate state (i) involving either an unbound electron hole pair or a bound exciton. The intermediate state i is then scattered via the electron-phonon interaction ($\hat{H}_{ep}$) resulting in a new intermediate state j and the emission of a phonon with energy E_{p1}. The intermediate state j then recombines radiatively via the dipole interaction emitting a photon with energy E_2. A convenient tool for considering these Raman scattering processes is the use of Feynman diagrams. The diagram for a single phonon Stokes process is shown in Figure 2.8. The vertices in the diagram represent the different interaction matrix elements for the dipole and phonon interactions. The propagators then represent the different particles/quasiparticles involved in the process i.e photons, phonons and excitons.

For a single phonon process the wavevector of the incident phonon is typically negligible and so to conserve wavevector the emitted phonon must have a wavevector **k**=0. Therefore, only zone centre phonons at the Γ point in the phonon dispersion relation can be observed (see Figure 4.3). In addition, to single phonon processes higher order scattering processes are also possible involving multiple phonons. These processes can also allow for the participation of large wavevector phonons. In the case of a two phonon

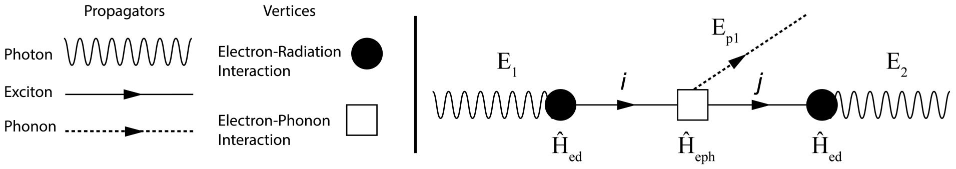

Figure 2.8: Feynman diagram of the scattering process for a single phonon Stokes Raman process.

process the overall wavevector has the form $\mathbf{k}_{p1}+\mathbf{k}_{p2}=0$ and so the total wavevector is conserved. These peaks are referred to as overtones when the energy of the involved phonons is identical or as combination modes when the two phonons have different frequencies. It is also possible to observed Raman processes involving both emission (Stokes) and absorption (Anti-Stokes) and are known as difference modes. As a result, Raman spectra particularly when resonant can contain numerous peaks associated with different scattering processes. In addition to the required conservation of wavevector the visibility of Raman peaks in a given spectra is also dependent on the Raman selection rules, which arise due to the crystal symmetry and the scattering geometry, and for resonance Raman the nature of the underlying electronic states [74].

2.6.2 Resonance Raman Scattering

The intensity of the Raman scattering is dependent on the geometry of the scattering process and the underlying electronic states in the material. When the energy of the incident photon is resonant with a real electronic state the intensity of the Raman scattering can be enhanced by several orders of magnitude. This enhancement of the Raman intensity is known as resonance Raman scattering. As a result it is possible to obtain additional information on the underlying electronic states, and electron-phonon interactions involved in the Raman process by measuring the spectrum as a function of incident photon energy. The intensity of the Raman scattered light as a function of excitation energy can be derived from third order perturbation theory [150]. However, it is easier to derive these expressions by using the Feynman diagrams for the Raman scattering processes and Fermis golden rule [74]. The expression for the Raman scattering cross-section for a single phonon process is shown in Eq 2.5. It is possible to derive this expression by considering the vertices in the Feynman diagram sequentially. The first vertex represents introduces a electric-dipole interaction to the numerator $\hat{H}_{ed}$ and a term in the denominator E_1-E_i-iΓ_i. Where Γ_i is known as the broadening factor and is introduced due to the finite lifetime of the intermediate state τ_i and are related by Eq 2.6 [38]. The next vertex involves the electron-phonon interaction so introduces the $\hat{H}_{ep}$ into the numerator and the term E_1-E_{p1}-E_j-iΓ_j into the denominator. The final vertex for the recombination of the intermediate state adds an additional $\hat{H}_{ed}$ matrix element and introduces a term into the denominator of E_1-E_{p1}-E_2 and represents the overall conservation of energy in the process and is instead given by a delta function.

$$I(E) \propto |\sum_{i,j} \frac{\langle 0,n| \hat{H}_{ed} |i,n\rangle \langle i,n| \hat{H}_{ep} |j,n+1\rangle \langle j,n+1| \hat{H}_{ed} |0,n+1\rangle}{(E_1 - E_i - i\Gamma_i)(E_1 - E_{p1} - E_i - i\Gamma_i)}|^2. \tag{2.5}$$

$$\Gamma = \frac{\hbar}{\tau} \tag{2.6}$$

Using the Feynman diagram approach, it is necessary to consider all possible permutations of the different vertices in the scattering process. For each matrix element the interaction can result in either the emission or absorption of a photon or phonon, and so there are a total of six different scattering processes which can contribute to the Raman intensity for a single phonon process. However, of these six terms only the contribution associated with the process depicted in Figure 2.8 is considered in Equation 2.5. This is valid as the other scattering processes are only resonant with one of the two intermediate states (i or j), whereas the process in Figure 2.8 can be doubly resonant due to the small difference in the energy of the intermediate states, and so is the dominant term in the Raman intensity expression [74]. From Eq 2.5 it is clear that there will be an enhancement of the Raman intensity when either of the two denominators tend to zero. This results in two resonance conditions for a single phonon process known as the incoming and outgoing resonances and are satisfied when the conditions given in Eq 2.7 & 2.8 are met, where E_L is the excitation energy of the laser.

$$E_L = E_i \, (incident \, resonance) \tag{2.7}$$

$$E_L = E_i + E_{p1} \, (outgoing \, resonance) \tag{2.8}$$

2.6.2.1 Resonance Raman scattering with multiple electronic states

A possibility when considering the resonance Raman behaviour of a material is the involvement of multiple underlying electronic states. In TMDCs there are a variety of different excitonic states which can be observed in optical measurements including neutral excitons, trions, biexcitons and localised states. The separations between these states are $\sim$ 20 to 60 meV, and so are similar to the energies of the phonons observed in TMDCs. Therefore, it is not possible to consider these states as separate discrete resonances due to the overlap of their resonance conditions. When resonant with a single electronic state the Raman intensity (see Eq 2.5) results in a characteristic profile with two peaks of equal intensity corresponding to the incoming and outgoing resonance conditions. As a result, a key characteristic of resonance with multiple excitonic states is an asymmetry to the observed resonance profile. There are two additional considerations to make for multiple excitonic states these are interference between the different resonance terms and the possibility of interstate scattering.

$$A(E) \propto \sum_{i,j} \frac{\langle 0,n| \hat{H}_{ed} |i,n\rangle \langle i,n| \hat{H}_{ep} |j,n+1\rangle \langle j,n+1| \hat{H}_{ed} |0,n+1\rangle}{(E_1 - E_i - i\Gamma_i)(E_1 - E_{p1} - E_i - i\Gamma_i)} \tag{2.9}$$

For a single phonon Raman resonance with multiple excitonic states it is necessary to introduce a summation over the different possible scattering processes. For this discussion it is useful to consider the amplitude associated with the scattering process and not the intensity. Where the Raman scattering amplitude is given in Eq 2.9. The amplitude of the Raman scattering process is complex and so allows for interference effects between the different Raman processes. If the scattering process involves different initial and final states for each channel then the summation of $\Sigma|A^2|$ and so no interference occurs [38]. On the other hand if there are multiple intermediate states that can scatter between the initial and final state then the Raman intensity is by the summation $|\Sigma A|^2$, and so does allow for interference between the different processes.

It is also necessary to consider the possibility for interstate scattering between the excitonic states involved in the scattering process. In this case the Raman process can be simultaneously resonant with multiple real electronic states. In the single phonon process described so far this is known as double resonance Raman scattering. For higher order processes involving multiple intermediate states, such as multi-phonon Raman scattering, this can lead to multiple resonance conditions being simultaneously satisfied allowing for triple and even higher order resonant Raman. The simplest case involves two real electronic states and so results in four terms in the Raman scattering equation corresponding to two terms describing scattering with states i, j, independently and two terms allowing for interstate scattering from i to $_j$ and vice versa. For the scattering between states i and j it is assumed that the matrix element for this process is symmetric and so M$_{ij}$=M$_{ji}$. Therefore, the amplitudes of these processes are related by A$_{ji}$=A$_{ij}$$*$ [38]. As a result when resonant with multiple excitonic states it is necessary to ensure a summation over all possible Raman scattering processes including those terms allowing for interstate scattering. This analysis can provide additional information regarding the relative scattering strength of these different Raman processes [37].

2.6.2.2 Higher order resonance Raman scattering processes

So far the discussion of resonance Raman scattering has been confined to the single phonon process shown in Figure 2.8, however higher order Raman processes are also allowed. For second order Raman scattering it is possible to have two phonon or single phonon scattering via defects, and for two phonon Raman scattering this process can

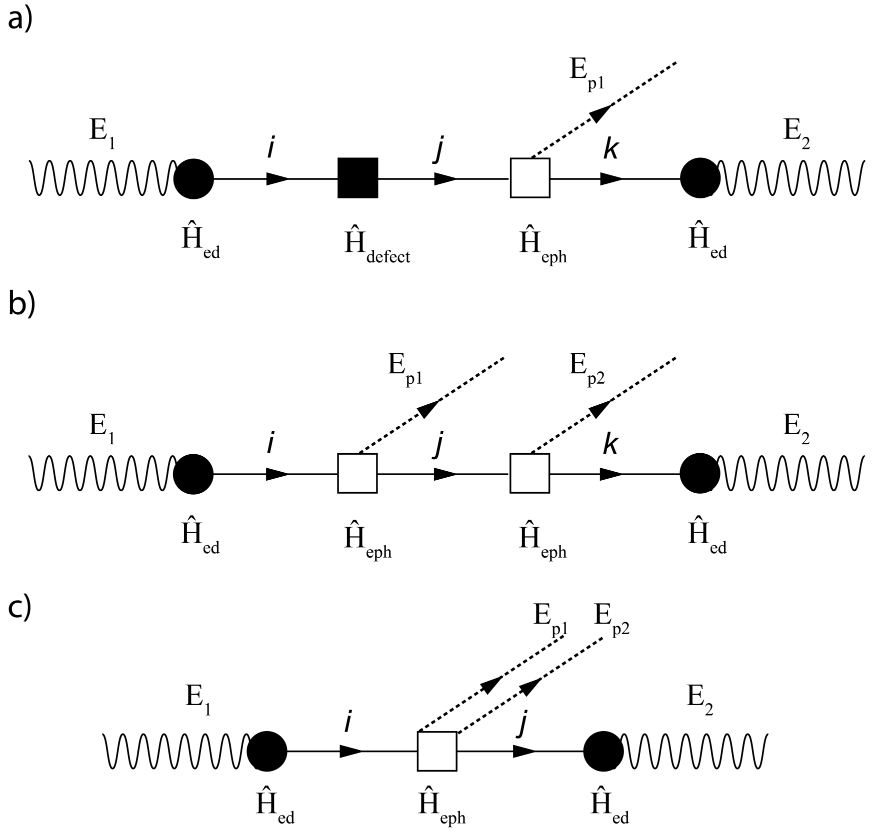

Figure 2.9: Feynman diagrams for the three possible higher order scattering processes. a) single phonon mediated defects scattering b) two phonon sequential scattering and c) two phonon simultaneous scattering.

occur either simultaneously or sequentially [38]. The Feynman diagram for these Raman scattering processes are then shown in Figure 2.9 panels b) & c). Following the same principles as used in the single phonon process we can then derive the expressions in Eq 2.10 & 2.11 for simultaneous and sequential Raman scattering respectively. For the sequential case there is an additional vertex in the scattering process due to the emission of a second phonon and another intermediate state k. This introduces an additional H_{ep} matrix element into the numerator and another resonance term in the denominator given by E_1-E_{p1}-E_{p2}-E_i-iΓ_i. Whereas, the simultaneous case is analogous to a single phonon process except the electron-phonon interaction is replaced by the matrix element for a two phonon process H_{epp}. As a result it should be possible to distinguish between these two scattering processes by comparing the resonance profiles of single phonon and two phonon Raman peaks. However, it is possible for these processes to involve intermediate states which are not strongly resonant in which case simultaneous and sequential two phonon or higher order processes can have identical resonance behaviour [38].

$$I(E) \propto |\sum_{i,j} \frac{\langle 0,n| \hat{H}_{ed} |i,n\rangle \langle i,n| \hat{H}_{epp} |j,n+1\rangle \langle j,n+1| \hat{H}_{ed} |0,n+1\rangle}{(E_1 - E_i - i\Gamma_i)\,(E_1 - E_{p1} - E_i - i\Gamma_i)}|^2. \tag{2.10}$$

$$I(E) \propto |\sum_{i,j} \frac{\langle 0,n| \hat{H}_{ed} |i,n\rangle \langle i,n| \hat{H}_{ep} |j,n+1\rangle \langle j,n+1| \hat{H}_{ep} |k,n+2\rangle \langle j,n+2| \hat{H}_{ed} |0,n+2\rangle}{(E_1 - E_i - i\Gamma_i)\,(E_1 - E_{p1} - E_j - i\Gamma_j)\,(E_1 - E_{p1} - E_{p2} - E_k - i\Gamma_k)}|^2. \tag{2.11}$$

The other process illustrated in Figure 2.9 panel a) is a defect mediated single phonon scattering process. Similar to the two phonon sequential process there are two scattering events with the excited electronic excitation in this process. One of which is the typical electron-phonon interaction and results in the emission of a phonon and the other is a elastic scattering event, which can occur via a defect. This process introduces an additional vertex corresponding to scattering with a defect and the appropriate Hamiltonian $\hat{H}_{defect}$. The defect scattering process is elastic in nature and allows for scattering to a large wavevector intermediate state (j) with wavevector K_j=q and is then followed by a second scattering event involving the emission of a phonon with energy E_{p1} with wavevector K_{p1}=-q satisfying conservation of momentum. As a result it is also possible to observe Raman peaks associated with large wavevector single phonons. The availability of electronic states at large wavevectors may also allow for the observation of dispersive Raman peaks where the frequency of the peak varies as a function of excitation energy. This can also be observed for the case of two phonon sequential Raman scattering which also involves large wavevector intermediate states. Analysis of these processes is more complex and requires a summation over the phonon dispersion [141]. The involvement of large wavevector states should be expected to produce a different resonance Raman behaviour for these processes. However, as seen in Figure 4.3 the dispersion of phonons near the K and M point in TMDCs can be relatively flat. Therefore, it is possible that although a Raman peak maybe dispersive the change in frequency of this peak as a function of excitation can be too small to discern in experimental measurements. Whilst, these Raman scattering processes involving large wavevector phonons are more complex they can provide information regarding the nature of large wavevector dark states.

2.6.3 Raman Spectroscopy of TMDs

The Raman spectra of TMDCs has been investigated first in the 1970s and 80s for bulk crystals of MoS_2 and WS_2 [151, 83]. An exemplar Raman spectra for a monolayer of $MoSe_2$ near resonance with the $MoSe_2$ B exciton is presented in Figure 2.10. Near resonance there are at least 14 Raman peaks visible in the spectrum associated with both single phonon and multiphonon processes. In non-resonant Raman scattering on TMDCs the Raman peaks typically observed are the zone centre optical phonons. Of these peaks the crystal symmetry and resulting Raman selections rules result in only the A_1' and E' being Raman active in monolayer TMDCs when exciting in a back scattering geometry [48]. These peaks are located between $\sim$ 240 and 290 cm^{-1} in both $MoSe_2$ and WSe_2 TMDCs.

The A_1' and E' Raman peaks are particularly useful due to the shift in their frequencies as a function of layer number, which was first observed for MoS_2 and WS_2, and occurs due to the change in interlayer coupling as a function of layer number [152, 76, 52]. The number of layers also determines the number of observed Raman peaks due to the change in interlayer coupling and crystal symmetry resulting in additional peaks and Davydov splitting [153, 154, 155, 156]. The sensitivity of these Raman peaks allows for the measurement of strain, thermal conductivity, and interlayer forces [157, 158, 159, 160]. The change in frequency of the Raman peaks has been utilised as a probe during functionalisation or alloying of TMDC layers as an in situ measurement of the stoichiometry [161, 162]. Polarisation resolved measurements of the Raman spectrum

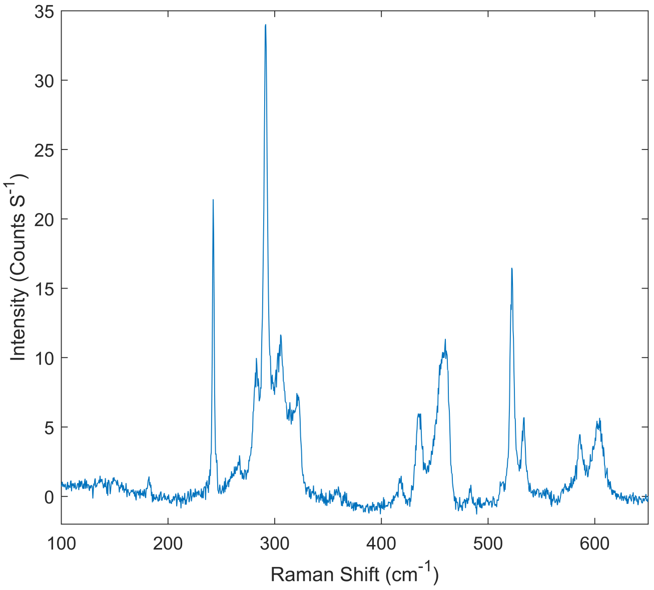

Figure 2.10: Exemplar Raman spectra obtained on a monolayer of $MoSe_2$ near resonance with the B exciton using an excitation energy of 1.845 eV and at a temperature of 4 K.

can also be used to determine the symmetry of the Raman peaks, orientation of the crystal lattice [163, 164]. The phonons in TMDC have also allowed for the observation of chiral phonons with non-zero angular momentum [165, 166]. These chiral phonons are important to the inter-valley scattering in monolayer TMDCs and allow for conservation of angular momenta associated with the different valley polarisations [167].

The remaining Raman peaks in Figure 2.10 are associated with higher order multiphonon Raman processes and also provide additional information on the TMDC layer. A particular example is the use of the intensity of the LA Raman peak as a measure of defect density in TMDCs [168, 169, 170]. Higher order Raman scattering processes can involve large wavevector states and so these peaks can provides information on inter-valley scattering, phonon dispersion and dark excitonic states [171, 172, 141, 173]. Furthermore, when considering bilayer and few layer TMDCs the number of Raman peaks that arise increases due to changes in crystal symmetry and the potential for collective motions of the layers leading to layer and shear breathing modes, which appear between 10 to 50 cm^{-1} [44]. These Raman peaks are absent in monolayers of MoS_2, $MoSe_2$ and WSe_2 and are used to identify the number of layers in a sample and differentiate between the different bulk stacking orientations [174, 175, 176]. However, in monolayer WS_2 there are several reports of an anomalous Raman peak appearing in this low frequency range [177, 178, 179]. More recently the intensity of the shear mode has been investigated as a method for probing the defect density in MoS_2 [180]. In twisted homobilayers and heterostructures with arbitrary stacking orientations the shear and layer breathing modes have been suggest as a useful metric for determining the quality of the interlayer coupling [27] . The effect of twist angle in these materials on the Raman spectra is also apparent with new peaks appearing as the result of zone folding due to moiré interference, and was first observed in measurements of Graphene [181, 123].

2.6.3.1 Resonance Raman Spectroscopy TMDCs

Resonance Raman spectroscopy is a well-established tool for studying low dimensional systems, including nanotubes, nanowires, and Graphene and allows information on the electronic structure, coherence lifetime, electron-phonon coupling and dark states [182, 183, 184]. In general it is possible to separate resonant Raman studies into two subtly different categories namely resonance and resonant Raman scattering. The distinction between these two cases is that resonant Raman scattering investigates the Raman spectra near a resonance in the material, whereas resonance Raman scattering probes the Raman response as a function of excitations energy and so provides additional information regarding the underlying electronic states. The former technique is frequently employed in TMDCs due to the availability of excitation energies in commercial Raman systems (1.96, 2.33, 2.41 eV), which are near resonance with an excitonic state. This near resonant enhancement of the Raman intensity allows for weaker Raman peaks associated with second order processes to be investigated [185, 186, 162].

Reported resonant Raman studies have probed the tuning of the resonance conditions as a function of temperature and pressure [187], gate dependence on [188], and effect of layer number [171, 189, 190, 162]. These measurements indirectly observe the effect of tuning the excitonic states involved in the Raman process, whereas resonance Raman measurements are used to directly determine the resonance conditions and nature of the involved excitonic states.

Resonance Raman spectroscopy measurements of mono and few layer TMDCs have been reported for MoS_2, $MoSe_2$, WS_2 and WSe_2 [191, 36, 192, 193, 194]. For MoS_2, $MoSe_2$ and WS_2 these results have demonstrated resonance enhancement of the Raman scattering with the A, B and C excitons [36, 193, 194]. Whereas, for WSe_2 only resonance enhancement with the B and C excitons has been reported [35, 193, 156]. For monolayer MoS_2 the resonance Raman behaviour of 2nd order Raman processes has been investigated revealing several peaks with dispersive behaviour, which has been attributed to inter-valley scattering with phonons near the M and K points [141]. The Raman enhancement at the C exciton in monolayer TMDCs has also been reported to be significantly stronger than at the A and B excitons, and may be attributed to differences in the strength of the electron-phonon interaction. Resonance Raman measurements of monolayer TMDCs also enable the observation of several weaker forbidden Raman peaks, such as the E'' and A_2'' phonons [194, 195, 153]. This is possible because of the breakdown of the Raman selection rules during resonance measurements [196]. Combining resonance Raman measurements with low temperatures also allows investigation of the difference in electron-phonon coupling of neutral excitons and trions [197, 37].

For encapsulated samples of monolayer WSe_2 there are several observations of phonon associated with the hBN layer when resonant with excitonic states in the TMDC layer [198, 199, 190]. The resonance behaviour of these peaks has been reported [198] and reveals that the hBN phonons are doubly resonant with the WSe_2 A exciton and a higher energy state that has yet to be identified. The hBN phonons have been attributed to the out of plane optical phonons in hBN (ZO), and the coupling of these phonons to electronic states in the WSe_2 layer is attributed to interfacial Raman scattering [199]. The resonance Raman response of encapsulated TMDC monolayers and heterostructures has yet to be fully investigated and may allow provide further information on electron phonon interactions between different 2D materials.

Overall Raman spectroscopy of TMDCs and 2D materials can yield useful information on a range of different material properties. Resonance Raman spectroscopy in particular provides information on the electron-phonon interaction and electronic states in these materials. Indirectly the effects of electron-phonon interactions and scattering processes are apparent in photoluminescence measurements contributing to scattering between exciton and trion states [200, 201], relaxation processes [202], valley depolarisation [203], lifetime of excitonic states and as a mechanism for ultrafast charge transfer [111]. As a result understanding of these processes through Raman measurements has applications in the realisation of TMDCs in optoelectronic applications.

Chapter 3

Experimental Apparatus and Methods

This chapter presents details of the experimental equipment and methods used in the investigations of monolayer TMDCs and heterostructures using resonance Raman spectroscopy. There are three main sections contained within this chapter describing: the sample structure and fabrication techniques; optical spectroscopy setup and resonance Raman protocol; and the fitting procedures used during data analysis.

3.1 Summary of Experimental Conditions

The following gives a brief summary of the samples and experimental conditions used when carrying out the measurements in Chapters 4 to 6.

The experiments presented in this thesis were carried out using the encapsulated sample shown in Figure 3.1. The sample is fabricated from mechanically exfoliated layers of $MoSe_2$, WSe_2, hBN and graphite crystals which are deposited onto a silicon substrate with a 300 nm thick oxide layer. The layers were stacked using a dry transfer technique to allow the encapsulation of monolayers of $MoSe_2$ and WSe_2 between layers of hBN, with the top and bottom layer having thickness of 32 nm and 30 nm respectively. The hBN layers act as a atomically smooth substrate and protective barrier preventing the contamination of the sample surface by adsorbents. The graphite layers act as transparent gate electrodes, but are not used in the experiments discussed in this thesis. The fabricated sample has four distinct sample regions; these are monolayer regions of both $MoSe_2$ and WSe_2 and two heterobilayers formed from the $MoSe_2$ layer being placed on top of a WSe_2 layer. These different samples areas are shown in Figure 3.1.For the heterobilayers the resulting regions labelled HS1 and HS2 have twist angles of 57 and 6° respectively. This sample was fabricated and provided by the Nanoscale Optoelectronics

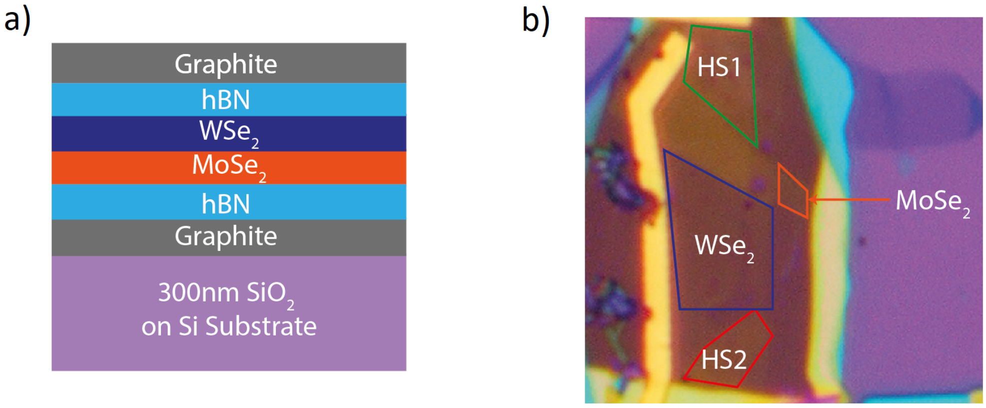

Figure 3.1: a) Cross sectional diagram of heterostructure sample. b) Optical microscope image of the heterostructure sample with different regions indicated the outlined areas with monolayer MoSe$_2$ and WSe$_2$ shown by the orange and blue respectively and the two heterostructure regions labelled as HS1 (θ=57) and HS2 (θ=6) outlined in green and red respectively.

laboratory based at the University of Washington and led by Prof Xiaodong Xu. The high quality of the samples produced by this group is clearly evident from their published works on both TMDC monolayers and heterostructures [204, 205, 206, 26, 113, 109].

For all measurements presented in this thesis the samples have been mounted inside a liquid helium flow cryostat and kept at a temperature of 4 K. Photo-luminescence measurements have been carried our using 1.97 eV and 2.33 eV excitation energies. Resonance Raman measurements have then been carried out using excitation energies from 1.59 eV to 2.25 eV with a step size in the range of 2.5-5 meV. Polarisation resolved measurements have been used with linearly polarised light incident on the sample and spectra obtained using an analyser in both the perpendicular and parallel orientations. This allows unpolarised luminescence and polarised Raman to be easily distinguished allowing the removal of unwanted luminescence by subtraction of the parallel and perpendicular spectra. All optical measurements were carried out in a backscattering geometry. The power used for these measurements was kept below 110 μW to avoid non-linear optical and thermal effects.

3.1.1 Mechanical Exfoliation

To produce the the encapsulated monolayers and heterobilayer structures probed in this thesis requires high quality monolayers of WSe_2 and $MoSe_2$. These were fabricated using mechanical exfoliation, which was first used by Novoselov et al. in 2004 when rediscovering Graphene [39]. There are also several alternative techniques to mechanical exfoliation including chemical vapour deposition, atomic layer deposition and molecular beam epitaxy [207, 208, 209], which aim to provide wafer scale monolayers of 2D materials. However, at present the highest quality crystals are those produced via mechanical exfoliation [210].

Mechanical exfoliation is a low cost technique and can be used to generate a range of 2D materials such as MoS_2, $MoSe_2$, WS_2, WSe_2, hBN and Graphene [211]. The main requirement for this process is that the bulk crystal of the material is composed of stacked layers which are weakly bound together by Van der Waals forces [39]. High quality bulk crystals are now readily available for a wide range of 2D materials and are produced using the chemical vapour transport process [212]. The exfoliation process involves the bulk crystal being placed onto an adhesive tape which is folded over and peeled back repeatedly to thin the bulk crystal. The loaded tape is brought into contact with the target substrate and peeled off to deposit a range of different size crystals with varying thickness. This process is low cost and is compatible with a range of different substrates [213, 214]. The most commonly used substrate is silicon wafer with an oxide coating. As a substrate this is particularly useful as the thickness of the oxide can be controlled to enhance the contrast of monolayer flakes [215] allowing for rapid identification of monolayers. The monolayer flakes can be identified using either optical contrast microscopy, Raman spectroscopy or AFM [215, 52, 216]. The choice of substrate when depositing flakes via mechanical exfoliation is also important as this can modify the optical and electronic properties of the monolayers due to dielectric screening, doping from the substrate and surface roughness [217, 218, 219].

Overall mechanical exfoliation has several advantages when compared to alternative methods due to the availability of a broad range of 2D materials, high quality of materials, low cost and ability to rapidly prototype with different materials. There are several disadvantages to mechanical exfoliation when compared to other techniques deposition, such as the limited size of the exfoliated flakes, lack of control over sample position and low yield of monolayers [211, 220]. In particular the small size of the exfoliated flakes is a limiting factor in the scalability of devices fabricated using TMDCs.

3.1.2 Encapsulation of Stacked Van der Waals Structures

The fabrication of monolayer TMDCs onto bare silicon oxide coated substrates was initially used for investigation of these materials electrical and optical properties [9, 221, 19, 222, 26]. The quality of the TMDC monolayers is determined by both intrinsic and extrinsic factors. The intrinsic quality of a sample is determined by the size of the crystal domains, presence of grain boundaries and the resulting defect density in the material [223, 224]. Whereas extrinsic factors include the roughness of the substrate, doping, adsorption and chemical modification [225, 226, 227]. Whilst the semiconducting TMDCs (MoS_2, $MoSe_2$, WS_2 and WSe_2) are relatively stable in air, over time oxidation and adsorption onto the surface can occur modifying the materials properties [228].

Several processes have been explored attempting to passivate or clean the sample surfaces and improve the material quality using annealing, superacid treatment and mechanical cleaning [229, 131, 230]. However, the most effective method involves the sandwiching of the monolayer in between layers of hexagonal Boron Nitride (hBN). As a material hBN is a polymorph of Boron Nitride composed of a single layer of atoms with each Boron atom bonded to three Nitrogen atoms forming a hexagonal lattice [13]. The hBN layer is atomically smooth with all atoms in a single plane, chemically inert and is an insulator with a bandgap of ~ 5.955 eV [231] and so is ideal for use as a substrate and protective layer. The encapsulation of monolayer TMDCs between layers of hBN has been shown to prevent the degradation of the material properties resulting from exposure to atmosphere or photo-doping [232, 225]. Encapsulated samples have demonstrated improved electrical performance [233] and optical properties with line widths approaching the intrinsic limit [234, 235] and allowing for the fine structure of the excitons to be explored [95].

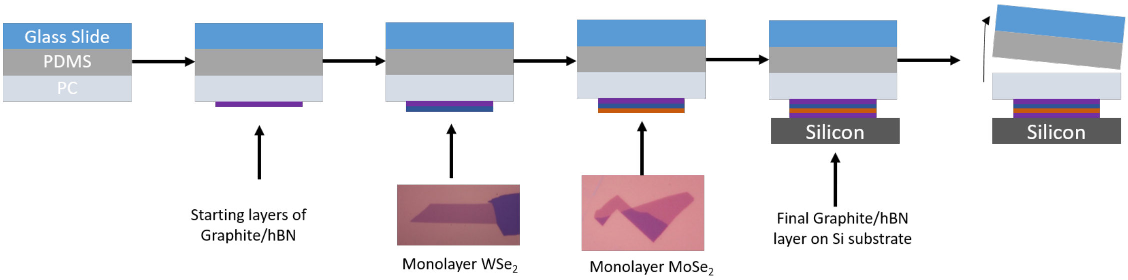

Figure 3.2: Illustration showing the stamp transfer process used to fabricated encapsulated monolayers and heterostructures.

The fabrication of encapsulated and stacked heterostructures requires the ability to deterministically position the different 2D materials. There are two methods to achieve this known as dry and wet transfer respectively [119, 236]. The encapsulated monolayers and heterostructures produced in this thesis were fabricated using a dry transfer technique with a polycarbonate (PC) and polydimethylsiloxane (PDMS) stamp [119]. The fabrication process involves a glass slide being prepared with a layer of PDMS followed by a layer of polycarbonate. The starting material either graphite or hBN is exfoliated directly onto the PC layer and a suitable flake identified using an optical microscope. The other constituent flakes are produced by mechanical exfoliation onto several oxide coated silicon substrates and the required flakes identified optically. For the fabrication of heterostructures with different twist angles the orientation of the crystal axes for each of the TMDC layers can be determined at this stage using linear polarisation-resolved second harmonic generation. For each layer the stamp is brought into contact with the desired flake using a micro-manipulator with the stamp heated to maximise the adhesion between the stack and target flake. The stamp is then peeled off adding a new layer to the stack. Once the desired stack has been produced the final substrate with the bottom layer is aligned and heated to 150 C allowing the PDMS stamp to be removed leaving the PC layer and stack on the silicon substrate. The polycarbonate layer is removed with a solvent wash in chloroform and IPA and is dried using nitrogen gas before being annealed in a mixture of 95% Argon 5% Hydrogen at 400 C for 2 hours.

Overall mechanically exfoliated TMDC flakes offer a high quality platform for probing the fundamental physics of these novel 2D materials. Encapsulated samples allow for the intrinsic optical and electronic properties to be probed. The application of the stamp transfer technique allows the fabrication of a variety of Van der Waals heterostructures and control of the sample the twist. The transfer technique also allows for the use of other 2D materials such as Graphene to form electrical contacts with the TMDC material and act as gate electrodes [237], and the positioning of TMDCs onto novel substrates such as nano-pillar arrays or optical waveguides [238, 239].

3.2 Resonance Raman Spectroscopy Setup

The following section details the experimental apparatus used for optical measurements of both TMDC monolayers and heterobilayers, including photoluminescence and resonance Raman spectroscopy. All of the measurements presented in this thesis have been performed at 4 K requiring the use of cryogenic equipment. The main spectroscopic technique used to study TMDC monolayers and heterobilayers in this thesis is resonance Raman spectroscopy. The main requirement for these measurements is a continuously tunable laser system, and a system for removing unwanted Rayleigh scattered light that is able to operate over a broad spectral range. This is acheived by using several different laser sources to excite the sample and a Trivista triple spectrometer to measure the Raman spectra. A schematic of the experimental setup is shown in Figure 3.3.

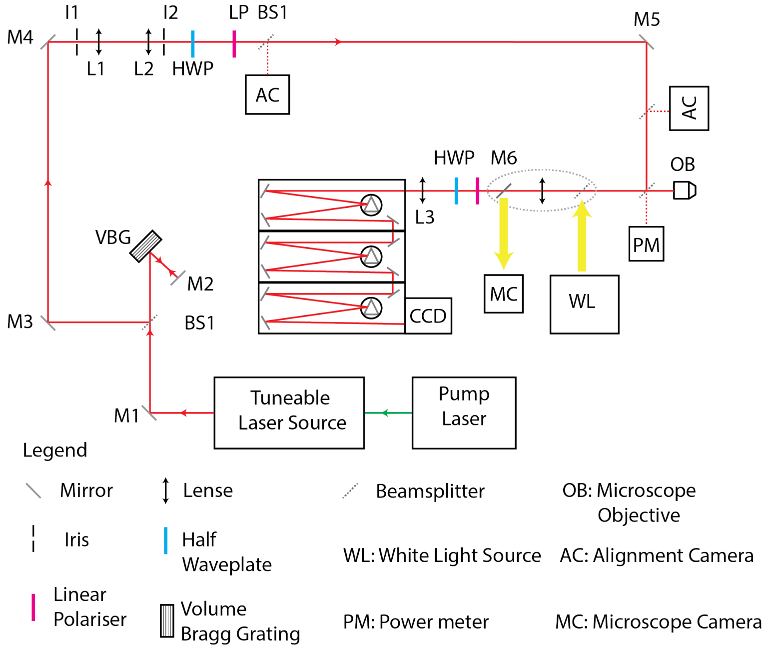

Figure 3.3: Schematic showing setup used for resonance Raman and photoluminescence spectroscopy measurements.

3.2.1 Laser Sources

The primary requirement for high resolution resonance Raman measurements is a continuously tunable laser source. The experiments in this thesis probe the A and B excitons for monolayer $MoSe_2$ and WSe_2, which requires excitation energies from 1.6 to 2.25 eV. To access this spectral range we used two laser systems, a Coherent Mira 900 Titanium Sapphire laser and a Coherent Cr-599 dye laser. The Mira 900 can operate in both CW and pulsed modes and can continuously tune from 1.24 to 1.77 eV. The Cr-599 dye laser is a CW laser and can operate continuously from 1.74 to 2.25 eV by using three different laser dyes. The three laser dyes used in these experiments are DCM, Rhodamine 6G and

Table 3.1: Table showing wavelength ranges of laser sources used in resonance Raman experiments.

Laser Source	Medium	Wavelength Range (nm)
Mira 900	Titanium Sapphire	700-1000
Cr 599 Dye Laser	DCM	610-700
	Rhodamine 6G	570-630
	Rhodamine 110	545-590

Rhodamine 110. The tuning range for both the dye laser and Mira 900 are provided in Table 3.1. In both cases the laser systems are pumped using either a Coherent Verdi or Laser Quantum Finesse 532nm laser, which can be used to obtain measurements with an excitation energy of 2.33 eV. When tuning the laser systems an Ocean Optics HR 4000 high resolution USB spectrometer is used to determine the desired output wavelength. It is necessary to filter the output from the lasers to ensure any unwanted fluorescence is removed and doesn't appear in the experimental measurements. This is of particular importance for Raman spectroscopy due to the relatively weak nature of the Raman signal. There are two different systems used for filtering the different laser systems. For the CR-599 dye laser the filtering is achieved using multiple Optigrate volume Bragg gratings and for the Mira 900 a Photon etc tuneable filter is used. These two setups allow for filtering of the laser sources over the complete tunable range. In Figure 3.3 the tunable Photon etc filter is not shown, but replaces the VBG setup indicated in the schematic when using the Mira 900 laser system.

When performing both resonance Raman and photoluminescence measurements the incident power needs to be controlled to avoid damaging the sample. To achieve this the output power from the laser sources is controlled using a broadband half wave-plate and linear polariser. The power incident on the sample is then determined by measuring the transmitted power of the laser at the beam splitter positioned before the microscope objective. The transmitted power is measured using a Newport 2832-C power meter and 818 IR low power attenuator and is calibrated for use over the full spectral range of our laser systems. This setup allows for precise control over the incident power of the laser sources during spectroscopy measurements.

3.2.2 Sample Mounting and Positioning

For all of the experiments presented in this thesis the sample has been mounted inside a Oxford Instruments Microstat Hires liquid helium flow cryostat. This allows the sample temperature to be controlled from 4 K to 500 K and is designed to minimize vibration and drift in the sample position. Optical access for spectroscopy measurements is achieved through a sapphire window and is suitable for optical measurements from UV to near IR wavelengths. Inside the cryostat the sample is mounted onto a copper heat sink and is secured by conductive silver paint providing good mechanical and thermal contact.

For low temperature measurements the cryostat is pumped to vacuum using a Pffeifer HiCube vacuum system consisting of a diaphragm and turbomolecular pump and allows the sample to be held at high vacuum ($\sim 10^{-6}$ mbar). The temperature of the sample mount is determined using a calibrated RhFe sensor. Once the sample has cooled and the system has reached thermal equilibrium the temperature stability is <0.1 K over the course of the experiment.

To accurately position the sample the cryostat is mounted onto three linear translation stages allowing three axis XYZ control. Each translation stage is equipped with a computer controlled micrometer and can be positioned with sub micron accuracy. This is necessary to ensure that measurements are obtained on the same sample area and allows for precise positioning onto the different sample regions. To locate the sample area of interest when mounted in the cryotat a custom made in situ microscope is utilised and the layout of this system is shown in Figure 3.4. This system uses a power stabilized tungsten halogen lamp as a broad band white light source for illuminating the sample and can also be used for reflectivity measurements. The white light from the lamp is collimated and passed through two apertures, which act as a field stop and aperture stop. The light is then directed onto the back of the microscope objective using beam splitter BS2 as seen in Figure 3.4. For all of the measurements presented in this thesis the microscope objective used is a Olympus x50 LMplan with a numerical aperture of 0.55 NA and a working distance of $\sim$ 6 mm. The reflected light from the sample is directed back through the objective and beam splitters BS1 and BS2 and then passes through a tube lens to form an image of the sample and can directed onto either a camera for imaging or onto a optical fibre coupled for reflectivity measurements. When imaging a Chameleon CMLN-1352M CCD USB camera has been used and allows both the sample and position of the incident laser spot to be observed simultaneously. The position of the sample is then adjusted to align the incident laser spot with the region of interest on the sample for spectroscopic measurements. When performing photoluminescence or Raman measurements BS2, M1 and the tube lens which are used for imaging are removed to allow the light from the sample to be coupled into the spectrometer.

3.2.3 Raman Detection

Raman scattering is a difficult process to observe as it is a weak optical process and required filtering of the Rayleigh scattered light to be observed. In addition, for resonance Raman spectroscopy the system must also be capable of filtering the laser light across a broad wavelength range. To achieve this a Princeton Instruments TriVistas Triple Spectrometer equipped with a Roper Scientific PyLoN LN/400 BR liquid Nitrogen cooled CCD has been used for both resonance Raman and photoluminescence measurements.

The spectrometer consists of three Czery-Turner design spectrometers that are linked together. The first two stages of the spectrometer act as a bandpass filter, and are used to

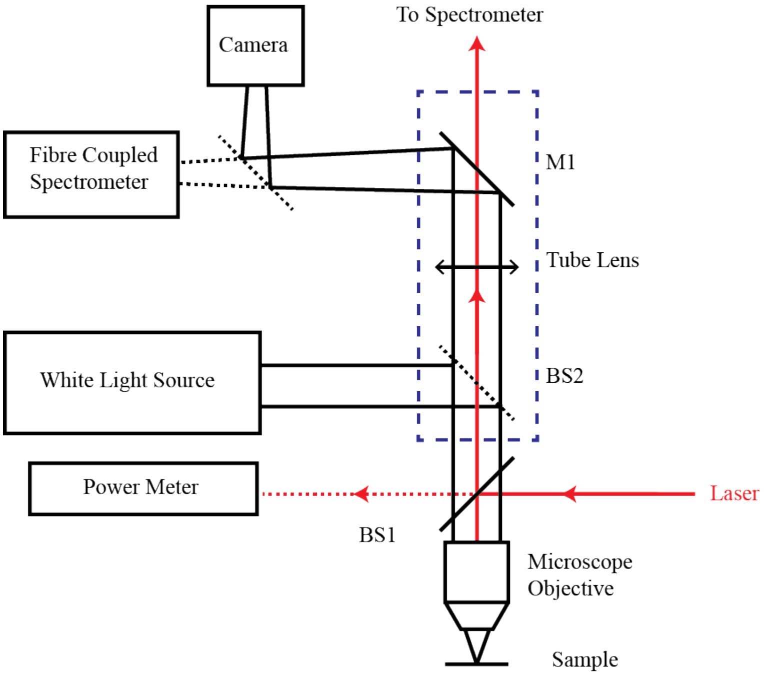

Figure 3.4: Schematic for microscopy setup and reflectivity measurements, components shown inside the dashed blue box are removable.

remove the Rayleigh scattered laser light. For resonance Raman spectroscopy this allows the spectrometer to be calibrated to ensure rejection of the Rayleigh scattered light at each excitation wavelength. In comparison commercial Raman systems rely on notch filters to remove the laser light and so require a different filter for each wavelength. The first two stages can be operated in either additive mode or subtractive mode. Additive mode allows for higher resolution measurements, whereas subtractive mode allows for the best stray light rejection. For all the measurements presented in this thesis the spectrometer was operated in subtractive mode to provide the best stray light rejection with the first and second stages both using gratings with 900 g/mm. The scattered light once filtered by the first two states is coupled into the third stage of the spectrometer where the light is dispersed onto the liquid nitrogen cooled CCD for detection. For the measurements presented in this thesis with a 1500 or 1800 g/mm grating has been used in the third stage. The 1500g/mm grating is used for the majority of spectra as the greater dispersion allows a larger frequency range to be measured with a single spectra. Whereas, the 1800 g/mm grating is used when higher resolution measurements are required and is capable of measuring the low frequency range of the spectrum allowing the Raman spectra to be measured to within 10 cm^{-1} of the laser line. When referring to the different grating configurations the labels indicate which grating is used in each stage. For example 9-9-15 indicates the first two stage are both 900 g/mm and the final stage is using the 1500 g/mm.

Both the spectrometer and CCD used in this system are sensitive to both the wavelength and the polarisation state of the scattered light. As a result during experiments it is necessary to ensure that the polarisation of light into the spectrometer is kept fixed. To achieve this a linear polariser followed by a half waveplate is positioned in the beam path before the spectrometer as shown in Figure 3.3. The polariser can be used as an analyser is orientated either horizontal or vertically relative to the optical bench. The input polarisation into the spectrometer is kept constant by rotating the half wave plate to ensure the input polarisation into the spectrometer is vertical. To correct for the wavelength dependence of the spectrometer and detector the spectral response of the system was calibrated using a blackbody source. The light source used for this calibration was an Ocean optics LS-1 -Cal-Int-220 tungsten halogen lamp, which produces a well defined blackbody spectrum. The light from the lamp was coupled into the spectrometer using a linear polariser to control the polarisation and spectra were measured over the operational range of the spectrometer. The calibrated data for the tungsten halogen lamp was compared to the measured spectral data and used to determine a efficiency correction for the spectrometer. When measuring Raman spectra the efficiency of the detector is accounted for during data analysis by use of a custom Matlab function.

3.2.4 Experimental Considerations

The following sections provide details of several experimental considerations, such as the characterisation of the laser spot size, sample power dependence and repeatability of the Raman intensity.

3.2.4.1 Spot Size Measurements

The Raman intensity obtained with each laser system is dependent upon both the alignment and coupling into the spectrometer, and the spot size of the laser sources. The size of the laser spot when focused on to the sample also defines the spatial resolution for the Raman and photoluminescence measurements. For both the Ti:Saph and Dye laser the spot size of the laser at the sample has been determined using a "knife edge" measurement. In this case a clean Si substrate was mounted in the cryostat and the laser was focused onto the sample surface. Raman spectra were then measured whilst translating across the sample edge with a step size of 1 μm. The intensity of the silicon peak at 520 cm^{-1} was obtained as a function of position and is shown in Figure 3.5. The intensity data shows a clear drop in intensity near $\sim$ 30 μm corresponding to the translation over the edge of the substrate. The data was fitted to a Gaussian error function as shown by the red line in Figure 3.5. The first derivative of the Gaussian error function is a Gaussian line shape as shown in Figure 3.5 panel b) where the width of the line shape corresponds to the diameter of the laser spot. In each case the width of the laser has been determined by finding the point at which the intensity of the profile is 10% of its peak value. The resulting diameters of the laser spot are 2.8 and 3.1 μm for the dye and Ti:Saph lasers respectively.

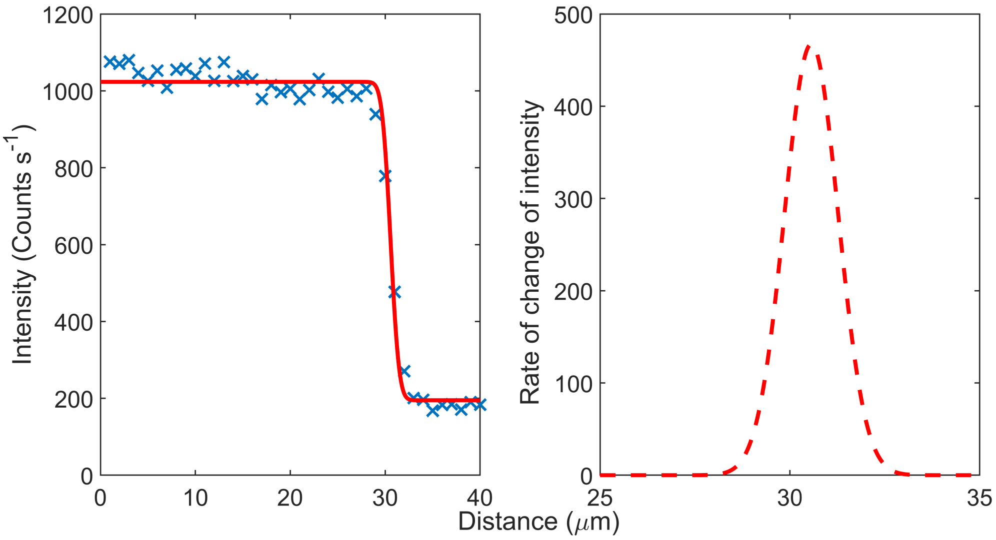

Figure 3.5: Panel a) shows the Silicon Raman peak intensity as a function of distance translating across the sample and shows a significant decrease at the sample edge. Panel b) then shows the first derivative of the data in panel a) and has been fitted to a Gaussian line shape.

3.2.5 Repeatability of Raman measurements

During resonance Raman measurements when tuning between each excitation energy the wavelength dependence of the optical components requires adjustment of the beam path to ensure the same alignment. Slight variations in the beam alignment can alter the coupling into the spectrometer introducing a random variation in the measured Raman intensity. To ensure the alignment of the beam path is identical for each wavelength the Raman setup includes several irises (Figure 3.3) which are used for coarse alignment. For more precise alignment two Thorlabs DCC 1645C USB CMOS cameras are positioned along the beam path in the experimental setup as shown in Figure 3.3. When realigning the setup these cameras are used to walk the beam and ensure the same optical path is the same for each measurement. In addition, when performing the resonance Raman measurements a rigorous procedure is followed to ensure repeatability. A complete description of this procedure can be found in ref [31]. This allows for the resonance Raman intensity profiles to be measured with a repeatability of $\sim 10\%$ as demonstrated in ref [31].

The repeatability of Raman intensity is determined by measuring the Raman spectra at a fixed wavelength several times during the resonance Raman experiments. Figure 3.6 shows the repeat Raman spectra obtained on HS1 at 1.766 eV during a resonance Raman experiment. The intensity of the Raman peak at 250 cm^{-1} has been determined from fitting and the resulting mean intensity and standard deviation were found to be 323.9 ± 15.2 counts per second. The repeatability is defined as the ratio of the standard deviation and the mean, and for the Raman spectra in Figure 3.6 is found to be 4.7%.

As a result the repeatability of our measurements is within the 10% variation expected for our resonance Raman setup and experimental procedure [31].

3.2.6 Power Dependence of Raman measurements

When performing resonance Raman measurements optimisation of the incident power is important as higher powers can minimise the measurement time allowing these experiments to be completed within a reasonable time frame. On the other hand, the use of too high an incident power can permanently damage the sample or result in localised heating. At cryogenic temperatures laser heating is a particular concern and can occur more easily due to the lower heat capacity of the sample as predicted using the Debye model [142]. This effect may also vary as a function of excitation energy due to the change in absorption of the material. Therefore, laser induced heating could be particularly significant when resonant with the excitonic states. For TMDCs several other power dependent effects have been reported, such as quenching of the neutral exciton PL peak as a function of increasing power [225, 226]. This effect is attributed to either doping of the sample from the substrate or adsorption of molecules onto the sample surface modifying the dielectric response. However,for encapsulated TMDC samples the photoluminescence emission has been demonstrated to show no significant power dependence [225, 226]. If there is no significant laser heating or modification of the sample properties due to doping we expect the Raman intensity to depend linearly on the incident power. Whereas, modification or heating of the sample would result in a non-linear power dependence.

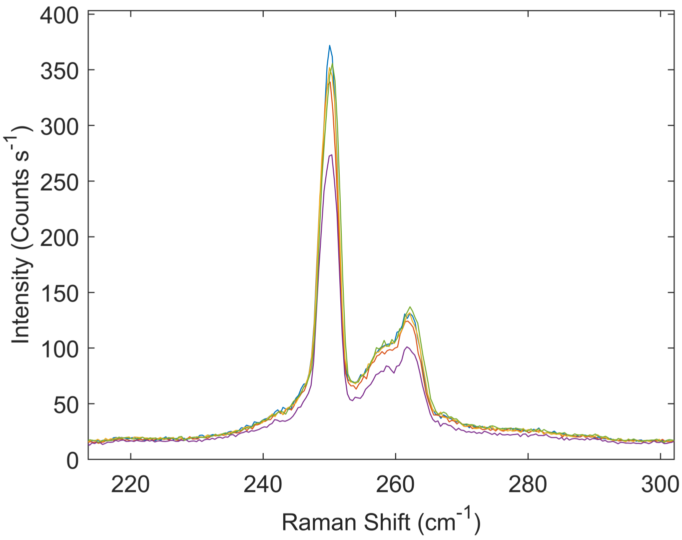

Figure 3.6: Repeat Raman spectra obtained on HS1 with an excitation energy of 1.766 eV during a resonance Raman experiment.

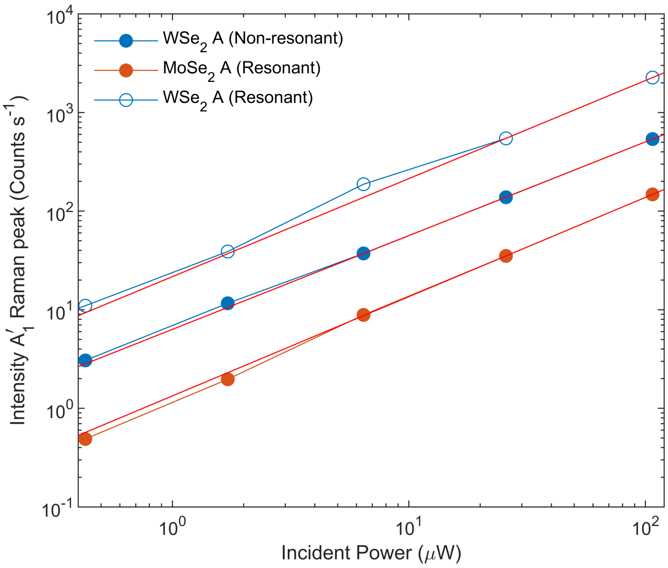

Figure 3.7: The intensity of the A$'_1$ Raman peaks as a function of incident power on sample HS1 using excitation energies of 1.73, 1.70, 1.65 eV. This corresponds to both resonant and near-resonant excitation of the WSe$_2$ A exciton, and resonant excitation of the MoSe$_2$ A exciton respectively. For each case the data has been fitted using a power law with the fitted lines shown in red. To allow for comparison of the different power curves axes shown are logarithmic.

Table 3.2: Coefficients obtained from fitting the power dependent data for sample HS1. Three datasets were obtained using excitation energies of 1.73, 1.70 and 1.65 eV corresponding to a resonant (R) and near-resonance (NR) excitation of the WSe$_2$ A exciton and resonant excitation of the MoSe$_2$ A exciton respectively. Errors given for the coefficients are a standard deviation obtained from the fitting process.

Coefficient	WSe$_2$ A (R)	WSe$_2$ A (NR)	MoSe$_2$ A
a	32.46±0.53	6.324±0.111	1.336±0.077
b	0.996±0.003	0.951±0.004	1.007±0.006

$$F(x) = ax^b \tag{3.1}$$

To determine a suitable power for the Raman measurements a series of spectra were obtained using powers from 0.4 to 110 μW on sample HS1. Although, higher powers above 110 μW are possible with our system, an upper limit was chosen to prevent irreversible damage to the sample. The power dependent measurements were performed using both resonant and near-resonant excitation energies with the WSe$_2$ and MoSe$_2$ A excitons. The intensity of the A$'_1$ Raman peak was obtained by fitting the spectra using a summation of Lorentzian line shapes. To compare the power dependence at different excitation energies the data has been plotted using logarithmic axes and is presented in Figure 3.7. For each excitation energy the power dependence has been fitted using a

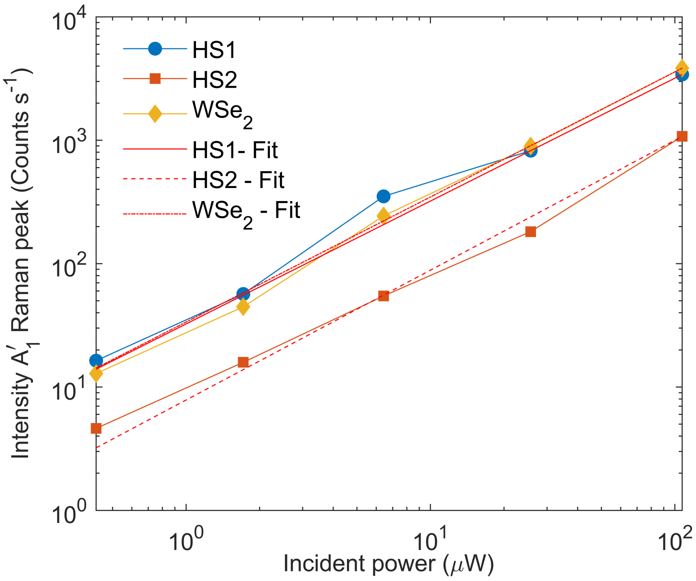

Figure 3.8: The intensity of the A'_1 Raman peak as a function of incident excitation power is presented for three sample areas HS1, HS2 and WSe_2, using an excitation energy of 1.73 eV. The power dependence in each case has been fitted to a power law with the resulting fit shown by the red lines. For comparison of the different sample regions the axes used are logarithmic.

power law of the form given in Eq 3.1. The fits to Eq 3.1 are shown by the red lines in Figure 3.7 and the obtained coefficients are provided in Table 3.2. At resonance with both the WSe_2 and $MoSe_2$ A excitons the exponent for the power law is ~ 1 indicating that the power dependence when resonant follows a linear relationship. For the case of near resonant excitation of the WSe_2 A exciton the exponent from the fit is 0.951 and so is sub-linear. However, if this is the result of laser heating we would expect the resonance energy to redshift and broaden with increasing temperature. The excitation energy of 1.70 eV for the near-resonant excitation is below the energy of the WSe_2 A exciton and so laser heating should result in a super-linear behaviour. Likewise if the increased laser power did result in a shift of the resonance energy or quenching of the different excitonic states we would expect these effects to be apparent in the power dependent data both near-resonance and at resonance with the WSe_2 and $MoSe_2$ A exciton. Therefore, the linear nature of the Raman intensity as a function of power when resonant with the A excitons suggests that there is no significant modification of the sample properties at higher powers.

To ensure that this behaviour is consistent for the different sample regions measured in our experiments the power dependent data for HS1, HS2 and monolayer WSe_2 when resonant with the WSe_2 A exciton is shown in Figure 3.8. The red lines shown in 3.8 show the resulting fits from using a power law with the fitted coefficients provided in Table 3.3. For HS1 and monolayer WSe_2 the exponents from fitting in Table 3.3 suggest a linear power dependence. In the case of HS2 the obtained exponent of 1.033 ±

Table 3.3: Coefficients obtained from fitting the power dependence data obtained on HS1, HS2, WSe_2 sample regions using an excitation energy of 1.73 eV. Errors given for each value are the standard deviation obtained from the fitting process.

Coefficient	HS1	HS2	WSe_2
a	32.46±0.53	7.844±1.749	33.64±5.39
b	0.996±0.003	1.033±0.024	1.014±0.018

0.024 may suggest a super-linear power dependence. However, the large uncertainty in the exponent for HS2 is likely the result of a lower signal to noise ratio for this sample, which overall has a lower Raman intensity at this excitation energy. This is evident from the lower y intercept in Figure 3.8. Therefore, from these results it seems reasonable to conclude that the power dependence for all three sample regions when resonant with the WSe_2 A exciton are linear. The linearity of the power dependence behaviour suggests there is no significant laser induced heating or modification of the sample properties in this regime. As a result for the Raman measurements in this thesis we choose to use the highest power in this linear regime of 110 μW in order to maximise the measured Raman signal.

3.3 Fitting Procedures

The following section discusses the fitting procedures used when analysing the Raman spectra obtained in our experiments and allows the amplitude, width and position of the Raman peaks to be extracted. This requires the use of background subtraction techniques to remove unwanted Rayleigh scattered light and photoluminescence peaks; calibration of the Raman spectra to eliminate systematic variation in the peak frequencies, and fitting of the peaks to appropriate line shapes to extract their parameters. This allows the intensity profiles of different Raman peaks to be extracted as a function of excitation energy. The fitting of the resonance Raman profiles is discussed and includes definitions of the different Raman scattering models and coefficients used in this analysis.

3.3.1 Background Subtraction

A common challenge when measuring Raman spectra is the appearance of photoluminescence features which in non-resonant experiments is avoided by careful selection of the excitation energy. However, in RRS the use of a range of excitation energies inevitably results in photoluminescence features appearing in the Raman spectra. For TMDC monolayers and heterobilayers the photoluminescence emission is an issue when probing the A excitons, which produce relatively intense photoluminescence. In addition, when measuring low frequency Raman peaks a significant background signal can also appear in the spectra due to the Rayleigh scattered laser light. Therefore, background subtraction techniques are required to fully utilise the Raman spectra. For the measurements presented in this thesis we make use of both polarisation resolved measurements and fitting to higher order polynomials to eliminate the unwanted background signal.

To eliminate the photoluminescence background signal in our Raman spectra we have made use of polarisation resolved measurements. The samples are excited with a linearly polarised laser, which is horizontal relative to the optical bench, and the Raman spectra are measured with the analyser set to both horizontal and vertical polarisations. As Raman scattering is a coherent process the observed Raman peaks are polarised, whereas the photo-luminescence is generally incoherent in nature and so is unpolarised. This is shown in Figure 3.9 panel a) which presents an exemplar Raman spectra for both parallel (XX) and crossed (XY) polarisations. In the parallel spectra there are several narrow features associated with Raman peaks, which are suppressed in the crossed spectra indicating these peaks are linearly polarised. Whereas the broader peaks in the spectra have equal intensities for both polarisations indicating they are unpolarised. Therefore, subtraction of the two polarisation resolved Raman spectra can remove the unpolarised photoluminescence background. This is demonstrated in Figure 3.9 panel b) which shows the resulting background subtracted spectra. This process can introduce artefacts into

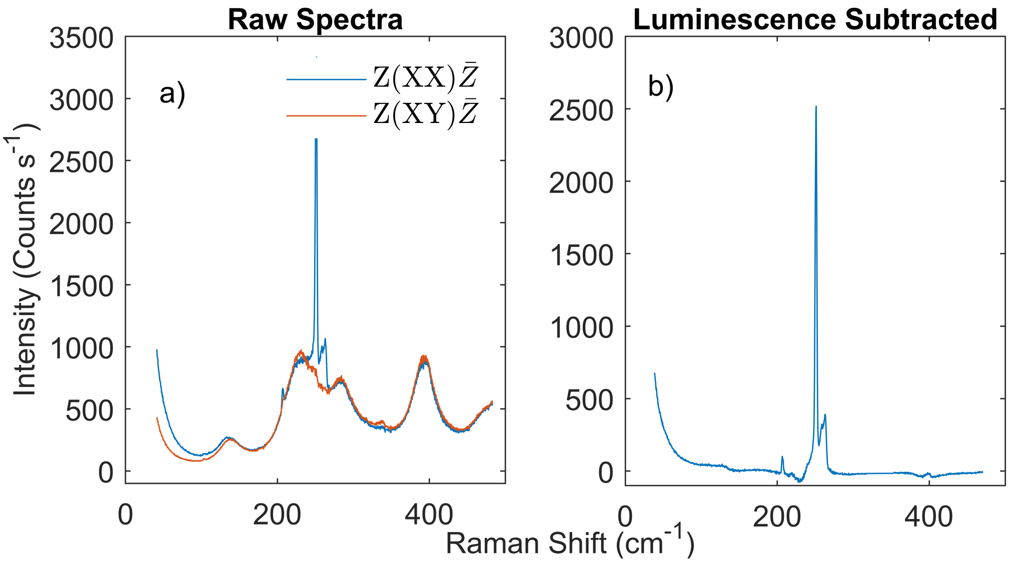

Figure 3.9: Panel a) Raman spectra obtained on HS1 using both parallel and crossed polarisations with an excitation energy of 1.727 eV near resonance with the WSe_2 A exciton. The Raman peaks appear linearly polarised while the luminescence peaks are unpolarised. Panel b) shows the result of luminescence subtraction using the parallel and crossed polarised Raman spectra shown in panel a).

the spectrum if the intensities of the PL features do not match perfectly and may occur due to fluctuations in the incident laser power. However, these features are typically narrower than the photoluminescence and are not observed consistently in the Raman spectra and so are easily rejected during the fitting process.

From Figure 3.9 panel b) the subtracting of the polarised spectra is unable to remove the Rayleigh scattered light from the laser as this is also linearly polarised. The Rayleigh scattered light is an issue when measuring the low frequency Raman spectra below 50 cm^{-1} as these peaks are relatively weak. This can be seen in Figure 3.10 where the Raman spectra is clearly superimposed onto a significant background. To remove this background a high order polynomial is fitted to the spectrum, whilst excluding the Raman peaks of interest from the fit. This process is demonstrated in Figure 3.10 panel a) where the excluded data points corresponding to Raman peaks are marked in red and the resulting polynomial fit is shown by the blue line. The background subtracted spectrum is then shown in Figure 3.10 panel b) and allows the low frequency Raman peaks to be easily resolved. The two background subtraction methods described here have been extensively used throughout this thesis and allow the resonance Raman data to be fully utilised.

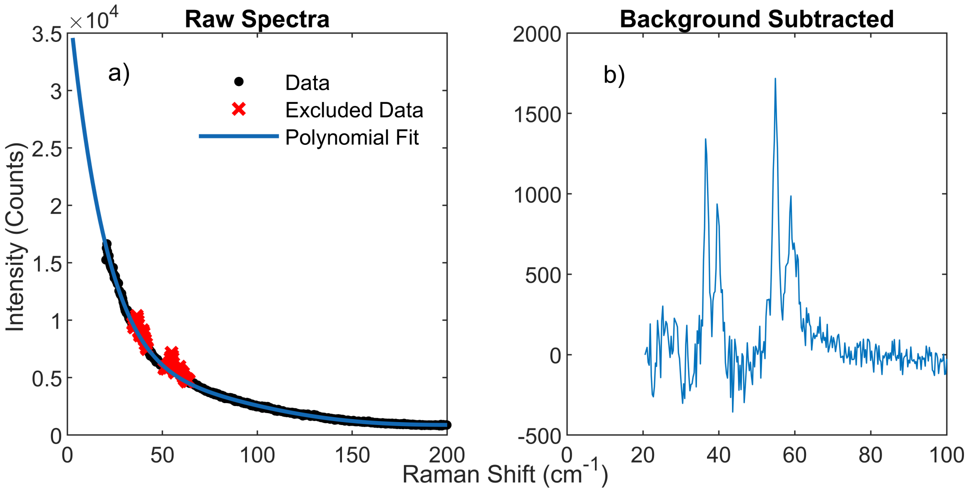

Figure 3.10: Panel a) Raman spectra obtained on HS1 with an excitation energy of 1.712 eV. When measuring low frequency Raman peaks below 100 cm^{-1} a significant background signal from the Rayleigh scattered laser light can be clearly seen in the spectra. In panel b) the Raman spectra obtained after background subtraction using a polynomial fit is shown and allows the low frequency Raman peaks to be clearly resolved.

3.3.2 Calibration of Raman Spectra

When measuring Raman spectra at different excitation energies there is some variation in the observed frequencies of the Raman peaks due to the uncertainty in the excitation energy of the laser. To correct for these systematic variations in the peak frequencies the Raman spectra are calibrated using an internal reference. For the samples investigated in this thesis the underlying substrate is a silicon wafer with 300 nm thick SiO_2. The Silicon Raman peak at 520 cm^{-1} appears in all spectra and provides a convenient reference signal. When fitting the Raman spectra the frequency of the Silicon peak is obtained and each spectra is calibrated to ensure the Silicon peak appears at the accepted value of 520 cm^{-1}, and is a standard reference used in Raman studies of TMDCs [148, 52, 194, 141, 144]. The dispersion of the spectrometer gratings is dependent on wavelength and so in some cases multiple spectra are required to obtain the desired spectral range from 10 to 1000 cm^{-1}. In these cases the silicon peak may only be observed in one of the obtained spectra and so the calibration is applied to the spectra where the 520 cm^{-1} peak is visible, and the calibrated frequencies of the TMDC peaks are then used to correct the adjacent spectra.

3.3.3 Fitting Raman Spectrum

There are a number of line shapes which can be used when fitting Raman spectra these include Gaussian, Lorentzian, Breit-Wigner Fano, and Voigt line shapes [240, 241]. From theory we expect the Raman peaks to have a Lorentzian line shape [38]. As a result a summation of Lorentzian line shapes has been used to fit the Raman spectra obtained during our experiments.

The fitting procedure for the Raman spectra was carried out following the background subtraction and calibration to the Silicon Raman peak. The model used to fit the data consisted of a summation of n Lorentzian line shapes with a quadratic background of the form given in Eq 3.2. Where a_i is the amplitude b_i is the width and c_i is the position of the Lorentzian, and $\mathrm{p}_{0,1,2}$ are the coefficients for the quadratic background. For each resonance the number of peaks and their positions was initially estimated by inspection of the Raman spectra. Fitting of the Raman peaks was then achieved using a least squares regression algorithm applied to the model in Eq 3.2. An exemplar spectra showing the resulting fit along with the individual Lorentzian line shapes is shown in Figure 3.11. In total for the fitted spectra in Figure 3.11 required a total of 17 Lorentzian line shapes to fit the Raman peaks and obtained an R-square value of 0.981 indicating a good fit to the data. The residuals appear randomly distributed around the zero line and suggests 17 Lorentzians are sufficient to fully describe the spectra. Although, near several of the intense Raman peaks there are clear contributions in the residuals indicating the Lorentzian line shape may not be the ideal fit for these peaks. However, these variations do not significantly alter the obtained amplitude from the fit and so are considered acceptable for our analysis.

$$f(x, p_0, p_1, p_2, a_1, b_1, c_1.....a_n, b_n, c_n) = (p_0 + p_1 x + p_2 x^2) + \sum_{i=1}^{n} a_i \frac{b_i^2}{(x - c_i)^2 + b_i^2} \tag{3.2}$$

3.3.4 Fitting Resonance Raman Profiles

To quantitatively analyse the resonance Raman profiles requires fitting to an appropriate Raman scattering model. As discussed in Chapter 2 Section 2.6 Raman scattering can involve both single phonon or multiphonon processes. For the TMDC monolayers in Chapters 4 & 5 Raman peaks are observed with frequencies up to 600 cm^{-1} and so can involve three or even four phonon processes. These higher order scattering processes become particularly complicated if they occur sequentially as opposed to simultaneously due to the addition of multiple resonance conditions and matrix elements in the Raman intensity expression. For higher order sequential processes where the underlying phonons are not explicitly known it is increasingly difficult to obtain useful fits to these models

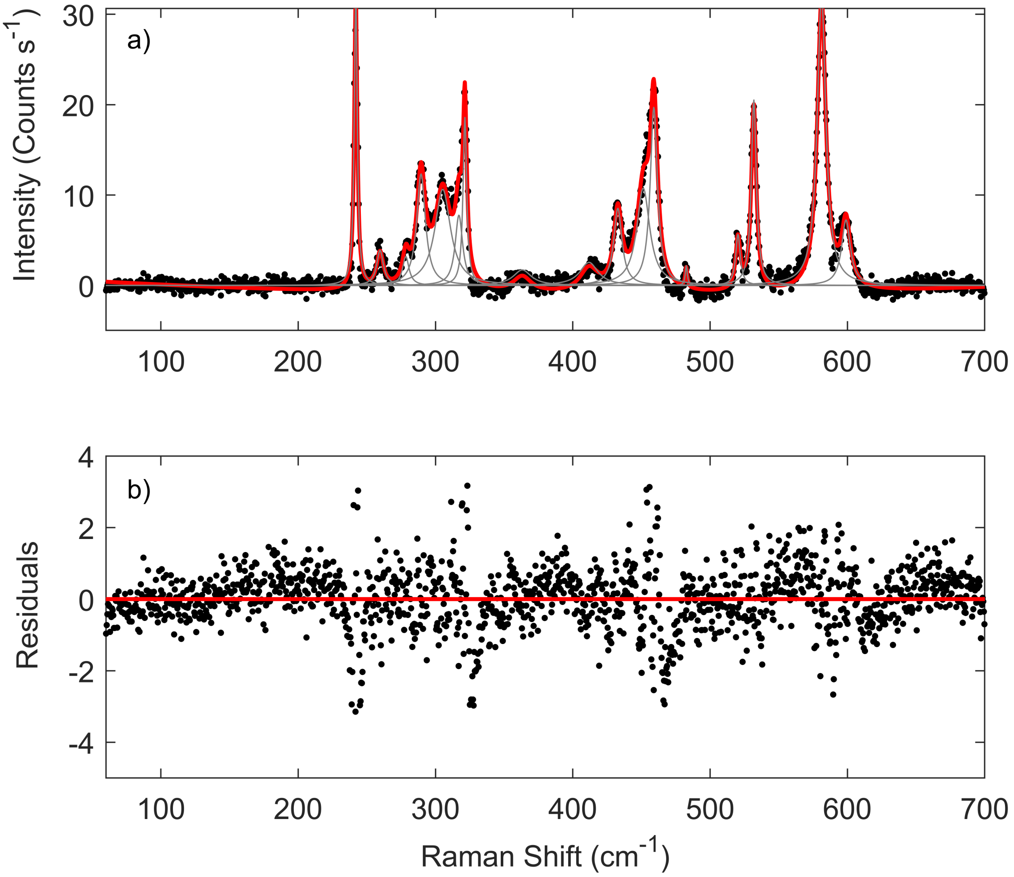

Figure 3.11: Panel a) presents an exemplar fitted Raman spectra and was obtained on an encapsulated monolayer of MoSe2$_2$ using an excitation energy of 1.878 eV corresponding to resonance with the MoSe$_2$ B exciton. The resulting fit required a total of 17 Lorentzian line shapes and is given by the red line with the individual line shapes also shown in grey. The residuals determined for the fitted model and data are presented in panel b).

due to the large number of unconstrained parameters and so requires the use of DFT predictions [141]. This approach is beyond the scope of this thesis and so we confine our Raman scattering models to those which occur from simultaneous Raman processes involving multiple excitonic states. For a simultaneous Raman scattering process the Feynman diagram is almost identical to the simplest model for single phonon Raman scattering and involves the emission of all phonon during a single scattering event. When referring to these models in the experimental chapters we describe them as a single phonon scattering event model.

$$f(x) = |\sum_{i,j} \frac{a_{i,j}}{(x - E_{i,j} - ib_{i,j})\,(x - E_{p1} - E_{i,j} - ib_{i,j})}|^2. \tag{3.3}$$

The fitted models are of the form given in Eq 3.3 where a$_{i,j}$ is the complex amplitude associated with the scattering channel, $b_{i,j}$ is the width of the resonance, $E_{i,j}$ is the energy of the underlying excitonic state involved in the process and $E_{p1,2}$ is the energy of the emitted phonon. For multiple excitonic states the Raman scattering model involves a summation over the states i and j and involve complex amplitudes allowing for interference between the different Raman scattering channels. In the experimental chapters three Raman scattering models are used when analysing the data assuming a single electronic excitation, two electronic excitations with no scattering between the i and j states (referred to as two independent electronic state model) and two electronic excitations with interstate scattering allowed. When reporting the amplitude coefficients for the models with two electronic states the amplitudes are labelled $a_{1,2,3}$. These labels are used consistently throughout all experimental chapters so that a_1 and a_2 refer to the amplitudes for scattering with the individual electronic excitations and a_3 is the interstate scattering amplitude. The strength of these amplitudes provides an indication of which scattering channel dominates the resonance Raman behaviour. This model for the Raman scattering was applied successfully in the work presented in ref [37] when investigating monolayer WS_2.

Chapter 4

Resonance Raman Spectroscopy of encapsulated Monolayer $MoSe_2$

4.1 Motivation

The experiments presented in this chapter explore the Raman scattering of encapsulated monolayer $MoSe_2$. There are several studies that have reported resonance Raman measurements on $MoSe_2$ [194, 155, 242, 144], and investigated the response of bulk material, effect of layer number and the higher energy C exciton. In general these studies use non-tunable lasers and were performed at room temperatures. As a result detailed studies of the A and B excitons have yet to be reported. Recent advances in the fabrication of encapsulated monolayers has allowed the effects of extrinsic defects to be overcome, and allows excitons and trions to be observed with narrow line widths ~ 5 meV [235]. PLE experiments of monolayer $MoSe_2$ at low temperatures have demonstrated enhancement of the photoluminescence peaks at energies consistent with the underlying phonons [243]. However, a study of the resonance Raman behaviour in $MoSe_2$ at low temperatures has not been reported and should provide additional information on the exciton-phonon coupling. Exciton-phonon interactions in monolayer TMDCs play an important role in valley depolarization and the ultrafast charge transfer [103, 204]. The use of Resonance Raman spectroscopy to study these materials can allow information on the exciton-phonon scattering to be elucidated and has yet to be fully exploited to probe the underlying physics of TMDC monolayers. Finally, the resonance Raman behaviour of monolayer $MoSe_2$ is of interest due to the availability of several $WSe_2/MoSe_2$ heterostructures, as such it is necessary to first understand the behaviour of the constituent monolayers before investigating these novel heterobilayers.

4.2 Photoluminescence of Monolayer MoSe$_2$

For initial characterisation PL spectra were obtained on the monolayer MoSe$_2$ sample region using an excitation energy of 2.33 eV (532 nm) with an incident power of 50 μW. The PL spectra is presented in Figure 4.1 and shows several peaks with energies in the range of 1.6 to 1.66 eV, corresponding to the A exciton in monolayer MoSe$_2$ [225]. The energies of the PL peaks were determined by fitting the spectra using five Lorentzian line shapes. The coefficients from fitting are provided in Table 4.1. The two most intense peaks in the spectra are assigned to the exciton and trion with energies of 1.649±0.001 and 1.622±0.001 eV respectively. The energies and separation of the exciton and trions peaks are in good agreement with those reported in similar encapsulated MoSe$_2$ samples [244, 245]. However, the origin of the additional peaks in the PL spectrum is not clear as both unencapsulated and encapsulated MoSe$_2$ monolayers typically contain only two peaks associated with the exciton and trion [225, 244].

These additional features may result from the small size of the monolayer MoSe$_2$ regions used in this sample which has dimensions of 2-3 μm, and is commensurate with the size of the laser spot (see Chapter 3). The overlap of the laser spot with the WSe$_2$ layers may allow for contamination of the MoSe$_2$ PL spectra by neighbouring heterostructure or monolayer WSe$_2$ regions. Although, this is unlikely as Raman measurements on the MoSe$_2$ monolayer region spectra at energies resonant with the WSe$_2$ A exciton contained no signal associated with the WSe$_2$ layer. In addition, spatial measurements across the sample region demonstrate a clear transition from the heterostructure PL to the monolayer MoSe$_2$ PL spectrum. To further explore these additional peaks would require similar samples containing larger area encapsulated monolayers of MoSe$_2$ and were not readily available during these experiments. Overall the assignment of these extra PL peaks is of interest but is not required for the discussion of the results presented in this chapter.

Table 4.1: Coefficients from fitting PL spectra for monolayer MoSe$_2$

Amplitude	Width (meV)	Energy (eV)
1698.5±84.5	10.1±0.4	1.618±0.001
18292.0±103.2	5.8±0.1	1.623±0.001
881.4±34.6	3.8±0.3	1.631±0.001
8011.4±58.3	4.2±0.1	1.649±0.001
2361.1±48.5	7.9±0.5	1.655±0.001
943.9±66.0	4.1±0.4	1.660±0.001

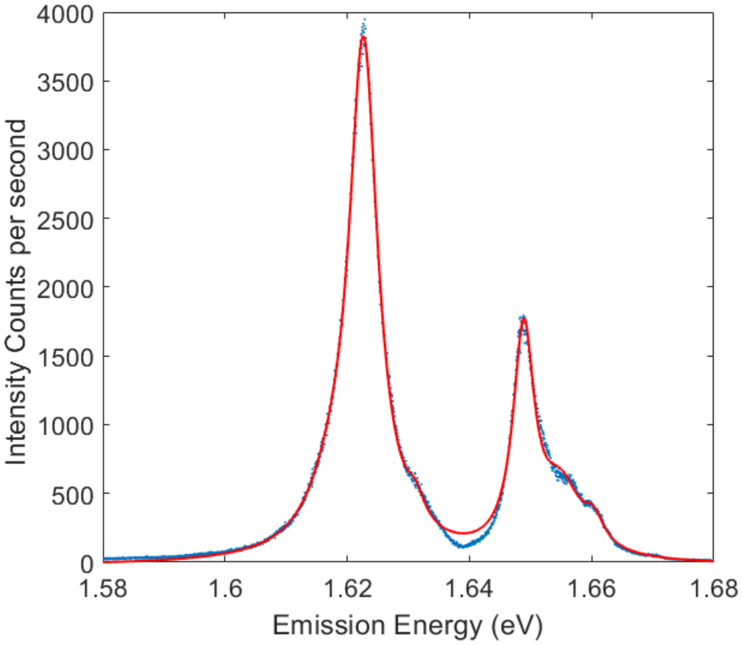

Figure 4.1: Photoluminescence spectrum taken on monolayer MoSe$_2$ region using 2.33 eV (532 nm) excitation. The spectrum was fitted to a summation of Lorentzian line shapes as shown by the red line.

4.3 Resonance Raman Spectroscopy of monolayer MoSe$_2$

4.3.1 Raman Peak Assignment

To understand the Raman data for monolayer MoSe$_2$ it is necessary to consider the assignment of the peaks in the Raman spectrum to their underlying phonons. The spectra obtained for monolayer MoSe$_2$ were measured from ~ 20 to 1000 cm^{-1}, however Raman peaks associated with MoSe$_2$ are only observed between 200 to 700 cm^{-1} and so data outside this range is not presented. To remove systematic variations and allow comparison of our Raman spectra to those in literature the spectra were calibrated to the silicon peak at 520 cm^{-1}. An exemplar spectra when resonant with the MoSe$_2$ B exciton is shown in Figure 4.2, and 13 Raman peaks associated with the MoSe$_2$ layer are observed. To assign these peaks to their underlying phonons we have make use of both previous Raman studies and phonon dispersion relations for monolayer MoSe$_2$.

Several resonance Raman studies of both monolayer and few layer MoSe$_2$ are reported in literature the most comprehensive of which are those by Bilgin et al. and Soubelet et al. [144, 194, 242, 155]. The resonance Raman behaviour when resonant with the C exciton has been studied extensively, with a particular focus on the effect of layer number on the Raman spectra. These studies observed a strong resonance enhancement at the C exciton in agreement with similar reports for MoS$_2$, WS$_2$ and WSe$_2$ [36, 193] along with the shifts in the peak positions and changes in intensity as a function of layer

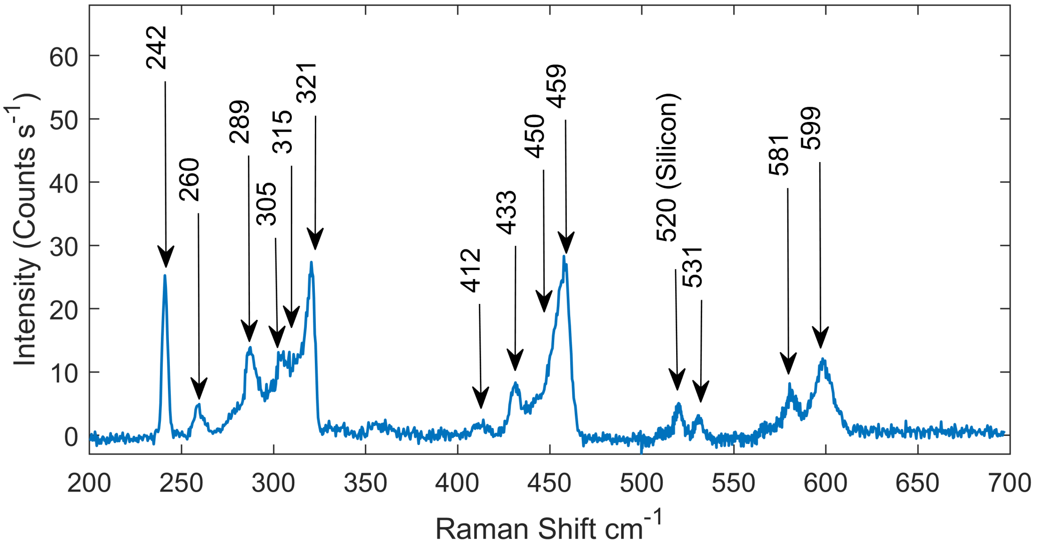

Figure 4.2: Raman spectra on monolayer $MoSe_2$ when resonant with the $MoSe_2$ B exciton at 4 K using an excitation energy of 1.829 eV. The spectra was calibrated using the silicon peak at 520 cm^{-1} as an internal reference.

number [144, 155, 242]. The resonance Raman enhancement of the A and B excitons was also reported, but a quantitative analysis of the resonance profiles was not presented [194]. Furthermore, these studies were only carried out at room temperature, which can complicate the Raman spectra as both absorption (Anti-Stokes) and emission (Stokes) of phonons can occur resulting in additional peaks in the spectra. In addition, at Room temperature the line widths of the excitons are significantly broader and prevents the investigation of other excitonic states e.g. trions [246]. These studies presented various mode assignments for the observed Raman peaks. These assignments were considered when assigning the peaks observed in our spectra. Although, as will be demonstrated there are several differences between our spectra and those previously reported, including several peaks absent from our spectra, new peaks with anomalous resonance behaviour and the observation of dispersive Raman peaks.

The assignment of the Raman spectra is performed using DFT calculated phonon dispersion relations. Several phonon dispersion relations are reported in literature for monolayer $MoSe_2$ [62, 247, 144]. For the assignments presented in this thesis the phonon dispersion relation calculated by Bilgin et al. [144] was used and is shown for reference in Figure 4.3. This phonon dispersion was chosen as the predicted frequency of the $A'_1(\Gamma)$ phonon and is in agreement with the position of the A'_1 peak in our spectra at 241.5 cm^{-1}. However, a comparison of the different reported $MoSe_2$ phonon dispersion relations demonstrates significant variation in the predicted values for the different phonon branches. In particular the frequency of the $A'_1(\Gamma)$ phonon was found to be repeatedly underestimated when compared to our experimental results [247, 248, 62]. This variation in predicted frequencies is not confined to only a single phonon branch,

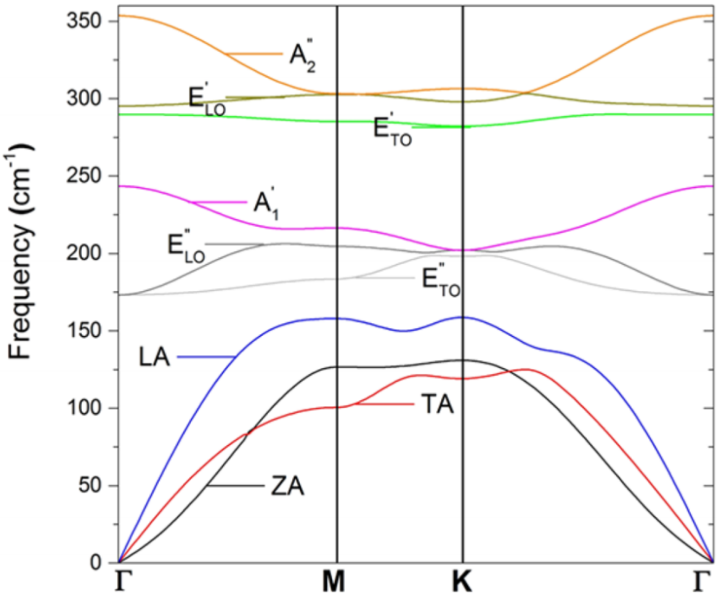

Figure 4.3: The phonon dispersion relation for monolayer MoSe$_2$ calculated using DFT by Bilgin et al.. The phonon branches are labelled according to the irreducible representations for a TMDC monolayer. Reprinted with permission from [144]. Copyright 2019 American Chemical Society.

for example the LA (M) phonon is predicted to have a frequency between 153 cm^{-1} to 161 cm^{-1} depending on the chosen dispersion relation. To account for this variation values were extracted for the A$'_1$(Γ) phonon from several phonon dispersion relations and a mean value and standard deviation were obtained [248, 249, 247, 144, 62]. The resulting standard deviation provides a measure of the uncertainty of the peak frequencies and was found to be 3 cm^{-1}. Therefore, when performing the peak assignments all possible modes are considered that have predicted frequencies within 3 cm^{-1} per phonon of the peak position.

As seen from the phonon dispersion relation in Figure 4.3 the highest possible Raman shift for a single phonon is $\sim$ 352 cm^{-1} and so all peaks observed at higher frequencies are multi phonon Raman peaks. To ensure all possible mode assignments are considered combination modes for up to fourth order Raman scattering processes were determined. However, to simplify the assignment process only phonons with frequencies at the high symmetry points were considered i.e. the Γ, M and K points. This is reasonable given the electronic band structure for monolayer TMDs which have conduction band minima at the K points and the midpoint between Γ and K known as the Q point. This allows for scattering by both M and K point phonons and has been reported experimentally in resonance Raman measurements on MoS$_2$ [141]. The frequencies and widths of the Raman peaks in our spectra were obtained by fitting multiple spectra at different excitation energies to a summation of Lorentzian line shapes. The peak widths and positions and proposed assignments are provided in Table 4.2 and where possible the mode assignments reported literature are also given.

Table 4.2: Mode assignments for monolayer $MoSe_2$ Raman peaks when resonant with the B exciton. Raman Shifts and errors given are mean and standard deviation obtained from fitting multiple spectra at different excitation energies. The order of the listed assignments was determined using the difference between the predicted frequencies and experimental values.

Raman Shift (cm^{-1})	Widths (cm^{-1})	Reported Assignment	Assignment	Predicted Shift (cm^{-1})
241.5±0.1	2.6±0.1	$A'_1(\Gamma)$	$A'_1(\Gamma)$	240.5
260.7±1.3	6.9±1.4		2ZA(K)	257.8
			LA(M) + TA(M)	253.8
288.6±0.5	4.4±1.1		$E'_{TO}(\Gamma)$	288.4
304.6±0.2	13.1±0.6		E'_{LO}(M)+TA(M)	300.6
			E'_{TO}(M)+ZA(M)	305.7
			2LA(M)	310.8
			2LA(K)	312.9
			3TA(M)	295.1
314.6±0.3	5.3±2.5	E_{1g}(M)+LA(M)	2LA(M)	310.8
			2LA(K)	312.9
			E''_{LO}(K)+TA(K)	316.9
			E''_{TO}(K)+TA(K)	312.9
321.4±0.2	2.9±0.2	Unassigned	E''_{LO}(K)+TA(K)	316.9
			E''_{LO}(K)+ZA(K)	329.2
			E''_{TO}(K)+ZA(K)	325.1
			2TA(M)+ZA(M)	321.0
412.2±0.4	15.9±0.1	2LA(M)+TA(M)	E'_{LO}(K)+TA(K)	412.2
			LA(K)+2ZA(K)	414.3
			2LA(M)+TA(M)	409.2
			ZA(K)+E'_{TO}(K)	409.2
432.5±0.1	7.7±0.7	E'(M)+LA(M) & 2LA(M)+ZA(M)	A''_2(K)+ZA(K)	433.6
			E''_{LO}(K)+2TA(K)	433.6
			E''_{TO}(M)+2ZA(M)	430.1
			2LA(M)+ZA(M)	435.2
			2LA(K)+TA(K)	429.6
			$2A'_1$(M)	429.0
450.4±1.3	11.2±0.2	3LA(M)	E''_{LO}(K)+LA(K)	452.0
			2ZA(K)+ E''_{TO}(K)	454.0
458.5±0.3	5.8±0.8	3LA(M)	A'_1(K)+2ZA(K)	458.1

Table 4.2 continued from previous page

Raman Shift (cm^{-1})	Widths (cm^{-1})	Reported Assignment	Assignment	Predicted Shift (cm^{-1})
			E$''_{LO}$(K)+2ZA(K)	456.0
			A$''_2$(M)+LA(M)	461.1
			3LA(M)	466.2
			3LA(K)	469.0
481.5±0.5	3.0±1.4	Unassigned	A$''_2$(M)+E$''_{TO}$(M)	482.0
			E$''_{TO}$(M)+ E$'_{LO}$(M)	482.0
			E$'_{TO}$(K)+A$'_1$(K)	480.5
			E$'_{TO}$(K)+E$''_{LO}$(K)	480.5
			E$'_{TO}$(M)+2TA(M)	479.5
531.2±0.2	3.9±0.2	Unassigned	E$'_{TO}$(M)+2ZA(M)	531.5
			2E$''_{LO}$(K)+ZA(K)	529.4
			E$'_{LO}$(K)+2TA(K)	528.9
			A$'_1$(M)+2LA(M)	525.3
581.1±0.1	7.4±0.6	E$'$(M)+2LA(M)	E$'_{TO}$(M)+A$''_2$(M)	583.4
			E$'_{LO}$(M)+E$'_{TO}$(M)	583.4
			E$'_{TO}$(K)+A$''_2$(K)	584.7
			5TA(K)	584.7
598.7.6±0.2	10.9±0.2	4LA(M)	E$'_{LO}$(K)+A$''_2$(K)	600.2
			E$'_{LO}$(M)+A$''_2$(M)	601.2
			2 E$'_{LO}$(M)	601.2
			2A$''_2$(M)	601.2
			E$'_{LO}$(M) +2LA(M)	608.4
			E$'_{LO}$(K) +2LA(M)	593.6
			4LA(M)	621.7
			4LA(K)	625.7

The first assignments to consider are those arising from single phonon processes. The lowest frequency peak observed in our spectra is at 241.5 cm^{-1} and is unambiguously assigned to the $A'_1(\Gamma)$ phonon. This assignment to the A'_1 mode is in good agreement with reported assignments in literature [194, 144]. As seen in Table 4.2 this is the only peak with a single assignment with all other peaks having multiple possible assignments. There is also only one other assignment to a Γ point single phonon process for the peak at 288.6 cm^{-1}. This peak has a possible assignment to the $E'_{TO}(\Gamma)$ phonon. However, this peak is also observed to be degenerate with a dispersive Raman peak which complicates the assignment process. As a result this peak will be discussed further when considering the dispersive Raman peaks in Section 4.3.1.1. The remaining single phonon modes predicted at the Γ point are the A''_2 and E'' phonons, and are reported in literature with frequencies of $\sim$ 356 and 309 cm^{-1} respectively [194] . However, in our spectra we do not observed any peaks at these frequencies. This is not unexpected as the A''_2 phonon is Raman inactive in monolayer and the E'' peak is forbidden in backscattering geometry [143].

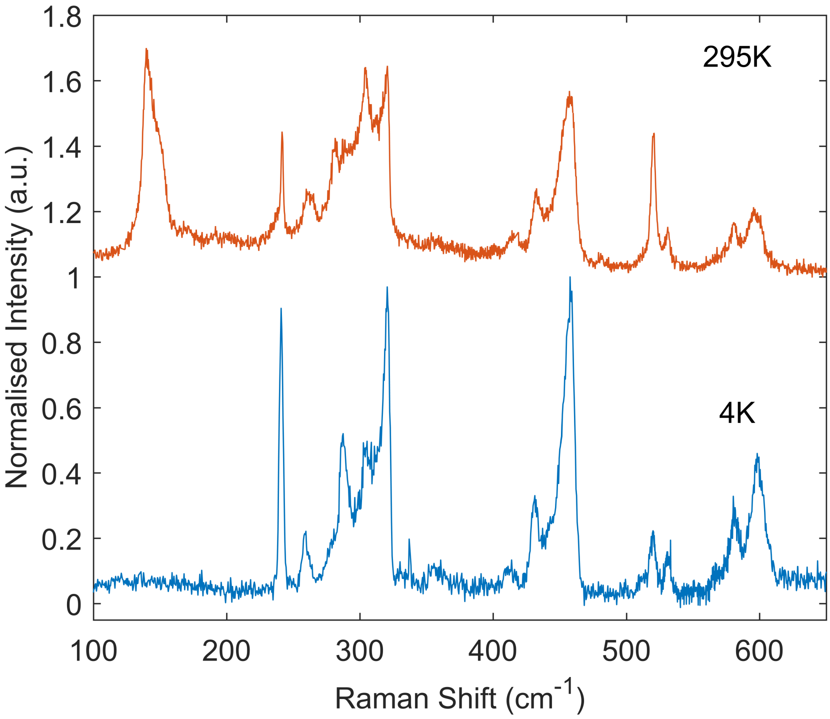

Figure 4.4: Raman Spectra on monolayer $MoSe_2$ when resonant with the B Exciton at both 4 K and 295 K using excitation energies of 1.829 and 1.777 eV respectively. The excitation energies were chosen to be near resonance with the $MoSe_2$ B exciton at each temperature. At 295 K there are several additional Raman peaks at $\sim$ 150 cm^{-1} which are not observed at 4 K.

Before considering the higher frequency peaks we present a discussion of several low frequencies peaks reported in literature, which are only observed in our sample at room temperature. These peaks can be seen near $\sim$ 250 cm^{-1} in the spectra shown in Figure

4.4. From fitting the spectra to Lorentzian line shapes the Raman shifts of the peaks were determined to be 140.4 and 149.1 cm^{-1}. This is in agreement with the spectra reported by Soubelet et al. and Bilgin et al. who observed two peaks at 141 and 152 cm^{-1}, and assigned these peaks to the E$'$(M)-LA(M) and the LA(M) respectively [194, 144]. As seen in Figure 4.4 these peaks are absent in our spectra at 4K. The temperature dependence of these peaks can be naturally explained if both combination modes involving Stokes and anti-Stokes phonons. The probability of absorption (anti-Stokes) and emission (Stokes) of a phonon when scattering with an electronic state is proportional to N$_{ph}$ and N$_{ph}$+1 respectively [38]. Where N$_{ph}$ is the phonon occupation number given by the Bose-Einstein distribution: $N_{ph}=(\exp[\frac{\hbar\omega}{k_bT}]-1)^{-1}$. Consequently, the probability of emitting a phonon tends to zero at low temperatures. The temperature dependence of the peaks at 140.4 and 149.1 cm^{-1} suggests they involve both emission and absorption of phonons. This suggests the reported assignment of the peak at 149.1 cm^{-1} to the LA(M) is incorrect. Whilst the justification for the peak assignments reported in literature is not explicitly stated, it is possible that the assignment of the peak at 149 cm^{-1} to the LA(M) mode was used to constrain the assignment of other Raman peaks to combination modes involving the LA(M) and other M point phonons. As a result there may be several erroneous assignments for not only the 149 cm^{-1} peak but higher frequency Raman peaks as well. Therefore, we consider all possible combinations modes and have not constrained our peak assignments.

Given the erroneous assignment of the LA(M) point Raman peak at 151 cm^{-1} it is useful to consider if the assignments in literature to overtones of the LA phonon are reasonable. These are the 2LA(M), 3LA(M) and 4LA(M) and are reported in literature at 304, 455 and 598 cm^{-1} respectively. In our spectra (see Figure 4.2) there are several Raman peaks at similar frequencies. The 2LA(M) mode has several possible assignments to the peaks at 304.6 and 314.6 cm^{-1}. In this case the 314.6 cm^{-1} peak is closest to the predicted frequencies of the 2LA modes. However, for both peaks there are alternative assignments to other two phonon combination modes and so it is not clear which peak should be assigned to the 2LA mode, if any. Similarly the peak attributed to the 3LA phonon at $\sim$ 455 cm^{-1} is best fit by two Lorentzian line shapes. This peak is composed of at least two Raman peaks at 450.4 and 458.5 cm^{-1} but is only treated as single peak in other studies. In this case the assignment of the 3LA can be made to the 458.5 cm^{-1} peak but again there are other assignments to two or three phonon modes which cannot be dismissed. The additional complexity of these higher order combination modes is not surprising with similar analysis by Carvalho et al. for monolayer MoS$_2$ revealing that the assigned 2LA peak is actually the result of at least 5 separate Raman peaks [141]. Further evidence that these higher frequency modes have not been fully addressed in literature is the Raman peak at 321.4 cm^{-1} which is visible in reported spectra [194, 144], but has not been assigned.

A useful quantity when evaluating the peak assignments are the widths of the Raman peaks. The width of the peak may indicate if a peak is composed of multiple underlying peaks, that are not clearly separated. The line width of the 241.5 cm^{-1} Raman peak is 2.6 cm^{-1} and is the narrowest Raman peak in our spectra. This peak is due to a single phonon process ($A'_1(\Gamma)$) and so provides a lower limit for the single phonon peak line widths. The peaks at 481.5 and 532.2 cm^{-1} are relatively narrow and are likely the result of single combination mode due to their symmetric appearance. In addition these peaks must be multiphonon peaks and so provide a limit for width of a single multiphonon Raman peak between 3.0 to 3.9 meV. The peak at 321.4 cm^{-1} has a width of 2.9 cm^{-1} and so is comparable in width to the 241.5 $cm-1$ and 481.5 cm^{-1} peak. This peak has possible assignments to two phonon combination modes and is likely the result of single mode due to its narrow line width. All other peaks observed on $MoSe_2$ are significantly broader with widths from 5.5 to 15.9 cm^{-1}. This indicates that these peaks are likely due to the presence of multiple underlying phonon modes which are almost degenerate. As demonstrated the similar line widths of the 241.5 (A'_1) and multiphonon 481.5 and 532.2 cm^{-1} peaks suggests it is not possible to distinguish between a single phonon or multiphonon process using the line width alone. The line width of the Raman peaks is also dependent on several factors including the coherence lifetime, homogeneity, quality of the sample material, and the effects of phonon confinement. Therefore, a rigorous analysis of the line widths would paradoxically require knowledge of the underlying phonons assignments. As a result the width of the peak is used primarily as a tool to optimise the fitting.

There are multiple Raman peaks which are observed in both Soubelet and Bilgin et al, but are not seen in our spectra. These include several peaks between 350 and 370 cm^{-1} which are assigned to the $A''_2(\Gamma)$ at 354 cm^{-1} and the $A'_1(M)+LA(M)$ at 364 cm^{-1}. These peaks are not clearly observed in our spectra but there is a weak broadband feature (see in Figure 4.2) in our spectra. However, due to its broad appearance and low intensity it is not possible to clearly resolve these peaks. An additional peak is also observed at 250 to 252 cm^{-1} and given an assignment to the 2ZA(M), but is reported only when resonant with the C exciton. It is possible that the differences in the number of peaks observed when probing the different excitons a result of variation in electron-phonon couplings when probing different excitonic states.

We also observe three new Raman peaks at 481.5, 531.0 and 581.1 cm^{-1}, which are of particular interest due to their anomalous resonance behaviour. The peaks at 481.5 and 531.0 cm^{-1} are only observed when resonant with this anomalous state and have not been previously reported in Raman studies of $MoSe_2$. Whereas, the 581.1 cm^{-1} peak is significantly enhanced when resonant with the anomalous state, but is also resonant with the $MoSe_2$ B exciton. The participation of the 581.1 cm^{-1} peak with both the $MoSe_2$ B and anomalous resonance may be due to a differences in the electron phonon coupling for the underlying phonons or the presence of a degenerate Raman peak. For all three of these Raman peaks there are multiple possible combination modes as seen in Table 4.2, although, the enhancement of only these three Raman peaks at the anomalous resonance suggests a similar underlying mechanism. This may require the underlying phonons to have a specific energy or wavevector to couple to the anomalous resonance. A set of modes which may explain these peaks are the $E'_{TO}(M)$ + 2ZA(M)/2TA(M)/2LA(M) combination modes. Whilst these assignments may be coincidental the similarity of these combination modes offers an intriguing possibility to explain the anomalous resonance behaviour and will be discussed again in Section 4.3.3.

Overall for the Raman peaks observed in monolayer $MoSe_2$ consideration of the mode assignments has demonstrated that this is a non trivial process. Whilst it is possible to assign several Raman peaks to single phonon modes and establish the origins of remaining peaks as due to multiphonon processes, the unambiguous assignments of these multiphonon peaks to a particular combination of phonons is not possible. In general these peaks do not have a single possible assignment but are likely the result of multiple combination modes which are nearly degenerate, and so attributing these peaks to a particular mode only confuses the situation. It is unlikely that the assignment of these modes will be resolved in future measurements due to the accuracy of predicted dispersion relations and the variations in both the samples and experimental setups resulting in slight changes to the spectrum. Experimentally there are numerous reasons for differences in the spectrum presented by Soubelet et al., Bilgin et al, and the results presented in this chapter. The frequency of the observed Raman peaks can be shifted due to a variety of factors including: the effect of encapsulation and use of different substrates [219]; differences in sample temperature [159]; effect of strain on material [250] and by the density of defects [157]. As will be demonstrated in Section 4.3 when discussing the resonance behaviour an understanding of the possible phonons associated with the observed Raman peaks can be very helpful.

4.3.1.1 Dispersive Raman peaks

In addition to the $MoSe_2$ Raman peaks presented in Figure 4.2 and Table 4.2 there are two additional Raman peaks observed between 277 to 279 cm^{-1} and 284 to 288 cm^{-1} respectively. The Raman shift of these peaks is not well defined by a single value, but varies continuously as a function of excitation energy. As a result these peaks are classified as dispersive Raman peaks. This behaviour can be seen in Figure 4.5 panel a) where two black arrows have been added to indicate the positions of the two dispersive peaks. For the Raman peak near 278 cm^{-1} there is a clear decrease in peak frequency with increasing excitation energy, which is visible in both the Raman spectra and colourmap in Figure 4.5. For the Raman peak at 288 cm^{-1} it is more difficult to resolve the dispersive peak as it is degenerate at energies below 1.86 eV with the Raman peak at 288.6 cm^{-1}. However, careful examination of Figure 4.5 panel a) shows a clear change in shape of the Raman peak as a function of excitation energy with the peak broadening significantly at 1.871 eV and implies the presence of multiple peaks at similar Raman shifts. This is also seen in Figure 4.5 panel b) where for energies above 1.86 eV there is a splitting of the peaks. The simplest explanation for this change in shape of the Raman peak is the presence of two underlying Raman peaks that are accidentally degenerate at low excitation energies. This requires a Raman peak fixed at 288 cm^{-1} with a dispersive peak which shifts to lower frequencies at higher excitation energies.

The observation of dispersive Raman peaks in monolayer $MoSe_2$ is not unexpected as dispersive peaks have been reported by Carvalho et al. [141] for monolayer MoS_2. In monolayer $MoSe_2$ both Soubelet et al. and Bilgin et al. also report a discrete shift in the frequency of the Raman peak near 288 cm^{-1} when comparing spectra near resonance

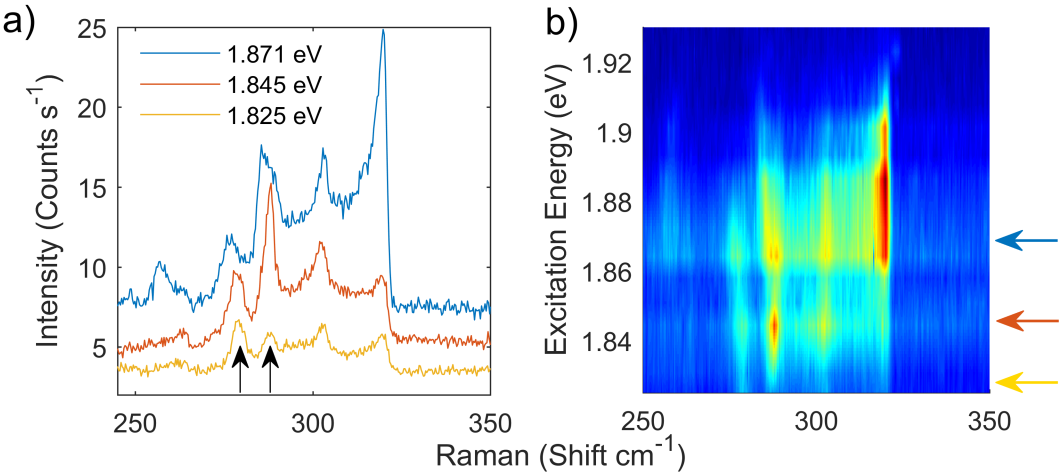

Figure 4.5: a) Raman spectra are shown for three different excitation energies when resonant with the $MoSe_2$ B exciton. The two arrows at 279 and 288 cm^{-1} indicate these peaks are dispersive in nature. b) Colourmap of resonance Raman data with arrows indicating the energy of the spectra shown in panel a).

with the A, B and C excitons and assign this peak to the E$'$(Γ) phonon [194, 144]. They propose that this is due to a difference in the coupling of LO/TO E$'$ branches to the A, B and C excitons. From the spectra shown in Figure 4.5 the separation of the two dispersive modes in our spectra is $\sim$ 9 cm^{-1}. Whereas, the expected splitting of the $\mathrm{E}'_{LO/TO}(\Gamma)$ modes from Bilgin et al. and Horzum et al. is $\sim$ 6 cm^{-1}. As a result it is possible these two peaks are due to the LO/TO splitting. However, Soubelet et al. and Bilgin et al. observed only a discrete shift in peak frequency, whereas our spectra show a continuous change in the phonon frequency with excitation energy. Therefore it is unlikely that the dispersive behaviour is simply due to differences in the coupling of the LO/TO phonons as this would produce only a discrete difference in frequency. The continuously varying nature of the peak indicates that these peaks involve large wavevectors. Consequently, from conservation of wavevector the dispersive peaks must involve either defect mediated or two phonon Raman scattering. Inspection of the phonon dispersion (see Figure 4.3) reveals the most likely wavevectors if the dispersive peak are the result of E$'$ LO/TO branches are those between theΓ and K points, as both branches show significant dispersion. Alternatively there are several two phonon peaks which could be involved in these processes such as the LA(M)+ZA(M) or the $\mathrm{E}''_{TO}(M)$+TA(M) which are predicted to appear at 279.8 cm^{-1} and could correspond to the peak observed between 277 to 279 cm^{-1}. The peak between 284 to 288 cm^{-1} may also be due to two phonon combination mode for the LA(K)+ZA(K) phonons. As a result it is not possible to precisely identify the underlying phonons, although this analysis has identified all likely possibilities. However, it is clear that the dispersive Raman peaks allow both a mapping of the phonon dispersion relations and reveal the presence of additional large wavevector dark states at the B exciton.

Overall the dispersive Raman peaks observed when resonant with the MoSe$_2$ B exciton show truly dispersive behaviour with a continuous change in frequency with excitation energy. This result demonstrates the need for more comprehensive Raman studies of monolayer MoSe$_2$ to enable a more complete understanding of both phonons and the electronic band structure. These dispersive modes when identified can act as a convenient probe of large wavevector states which are not accessible via the standard optical spectroscopy techniques employed on TMDCs.

4.3.2 Resonance Raman Spectroscopy

In this section the resonance Raman data obtained on a MoSe$_2$ monolayer using excitation energies from 1.80 to 1.98 eV is presented. A resonant enhancement of the MoSe$_2$ Raman peaks is observed at $\sim$ 1.86 eV, which corresponds to 211 meV above the PL peak assigned to the A exciton at 1.649 eV. This is in agreement with the energy of the B exciton reported by Han et al. [251] and with theoretical predictions for the valence and conduction band splitting in monolayer MoSe$_2$ $\sim$ [75]. For this sample, attempts to measure the resonance Raman behaviour for the A exciton were not successful due to the intense PL from the A exciton and trion. This is a result of the lowest energy states in monolayer MoSe$_2$ being optically bright and the high quality of the encapsulated samples resulting in intense PL [75, 235].

The resonance Raman data for MoSe$_2$ at the B exciton is presented in the colourmap and waterfall plots in Figure 4.6 & 4.7. The colourmap in Figure 4.6 shows a clear resonance enhancement near 1.86 eV which is relatively broad with a width of $\sim$ 100 meV. It is also evident that the majority of Raman peaks show similar resonance behaviour, although the higher frequency peaks have broader resonances. This can be seen by considering the Raman peak at 456.8 cm^{-1} which appears significantly broader than the resonance for the 241.5 cm^{-1} Raman peak. This indicates the presence of both incident and outgoing resonances with at least a single electronic state. The exceptions to this are the Raman peaks at 481.5, 531.2 and 581.1 cm^{-1} which demonstrate an anomalous resonance behaviour with a significant enhancement near 1.865 eV and are only strongly resonant between 1.850 to 1.885 eV. These anomalous resonances are significantly narrower than the other MoSe$_2$ Raman peaks. The anomalous Raman peaks can be clearly seen in Figure 4.7 for excitation energies from 1.851 to 1.878 eV. The presence of these anomalous resonance suggests the involvement of multiple excitonic states in the Raman scattering process at the B exciton. Further evidence of multiple states can be seen by comparing the peaks between 240 and 325 cm^{-1}, which demonstrate significant changes in their relative intensities as a function of excitation energy. The energies of these peaks are between 30 to 40 meV. As a result if the underlying resonance conditions are the same we would expect the resonance profiles to be almost identical and so changes in the relative intensity of these peaks would not be expected. A clear example of this is the behaviour of the 304.6 and 321.4 cm^{-1} where initially the 304.6 cm^{-1} peak is more intense at 1.851 eV but at 1.878 eV this has reversed with the 321.4 cm^{-1} having a significantly greater intensity. This behaviour combined with the anomalous resonances for the 481.5, 531.2 and 581.1 cm^{-1} peaks clearly indicates a more complex resonance at the B exciton possibly involving multiple excitonic states.

To understand the resonance Raman behaviour the spectra were fitted using Lorentzian line shapes to extract the resonance Raman profiles. A total of 16 Raman peaks are discussed in Section 4.3.1 during mode assignment, however it is not possible to obtain

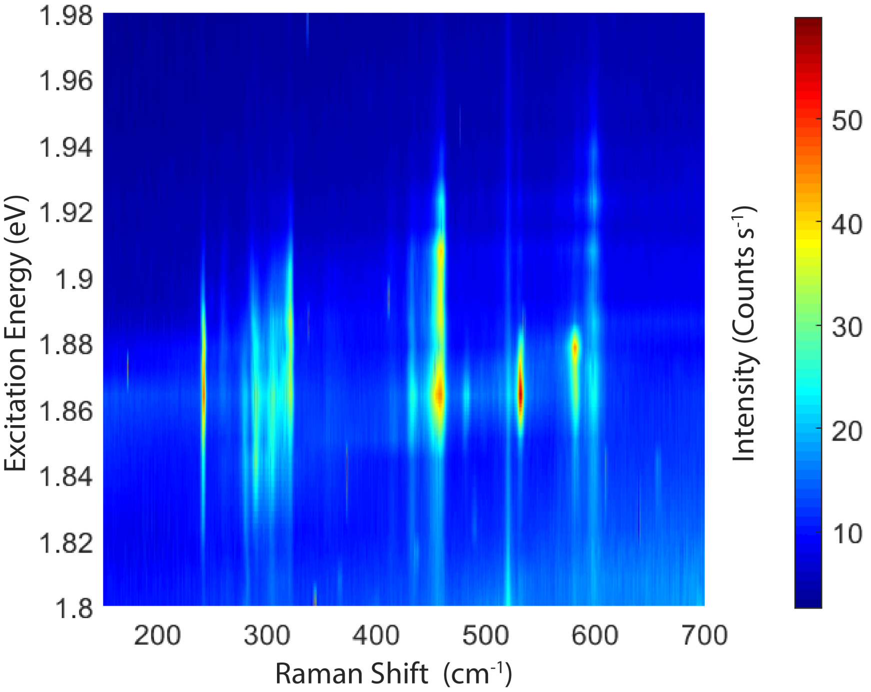

Figure 4.6: Colourmap showing resonance Raman data obtained on encapsulated MoSe$_2$ at 4 K with excitation energies from 1.8 to 1.98 eV probing the MoSe$_2$ B exciton.

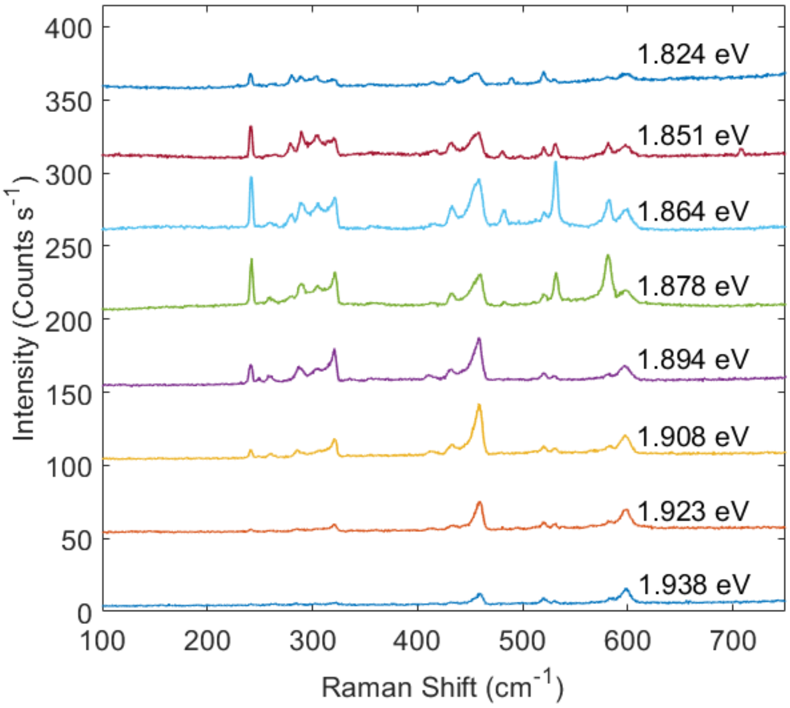

Figure 4.7: Raman spectra obtained during resonance Raman on encapsulated MoSe$_2$ at 4 K with excitation energies from 1.8 to 1.98 eV probing the MoSe$_2$ B exciton. For ease of comparison spectra have been offset.

resonance profiles for all of the observed peaks. This includes the peaks at 260.1 and 412.2 cm^{-1} that have a relatively low intensity, which prevents useful resonance profiles from being extracted. Each resonance profile was fitted to a Raman model assuming a single phonon scattering event involving a single underlying electronic excitation. The resonance profiles and obtained fits are presented in Figure 4.8 and the coefficients from the fitting process are provided in Table 4.3. The resulting fits for the single phonon model appear to be in reasonable agreement with the resonance profiles. Although, for several of the higher frequency peak profiles such as the 432.5, 450.4 and 458.5 cm^{-1} peaks there are several instances where the data and fitted model are in disagreement, and may indicate the presence of additional electronic states. The energies obtained from fitting are between 1.847 to 1.865 eV and appears to be clustered around two different energies. The peaks at 288.6, 304.6, 432.5 and 450.4 cm^{-1}, and are all in agreement to within the errors from fitting with a mean value of 1.848± 0.002 eV. The remaining peaks at 321.4, 458.5 and 598.6 cm^{-1} are also in agreement with a mean value of 1.864 ± 0.002 eV. The ability to separate the energies from fitting into two groups suggests the presence of multiple electronic excitations when resonant with the MoSe$_2$ B exciton.

To investigate the potential for multiple underlying excitonic states the resonance profile of the A$'_1$ Raman peak at 241.5 cm^{-1} was fitted to a single phonon event models for two electronic states. This peak was chosen as it is unambiguously assigned to a single phonon mode and so should be well described using our single phonon event models. In addition, the 241.5 cm^{-1} resonance profile has a low energy shoulder which is not well

Table 4.3: Coefficients from fitting the Resonance profiles for the Raman peaks observed on monolayer MoSe$_2$ when resonant with the B exciton. Each resonance profile was fitted to a single phonon event model assuming a single electronic state. The peak at 288.6 cm^{-1} has been highlighted as it is degenerate with a dispersive Raman peak and may show atypical resonance behaviour. Errors given are the standard deviation from fitting. For ease of presentation amplitude coefficients were scaled by a factor of 10^3 and have units of 10^{-3} $\sqrt{Counts\ s^{-1} \cdot eV^2}$.

Raman Shift cm^{-1}	Amplitude	Width (meV)	Energy (eV)
241.5	2.9±0.4	27.5±2.6	1.855±0.001
288.6	6.3±1.0	40.3±4.3	1.847±0.002
304.6	8.1±0.8	43.6±2.9	1.847±0.001
314.6	3.3±0.7	32.2±4.8	1.857±0.002
321.4	2.8±0.7	24.5±4.8	1.865±0.002
432.5	6.9±1.8	45.1±8.4	1.847±0.003
450.4	8.2±2.3	41.1±8.6	1.851±0.003
458.5	6.5±2.4	29.7±9.7	1.865±0.003
598.6	6.1±0.8	22.9±3.3	1.862±0.002

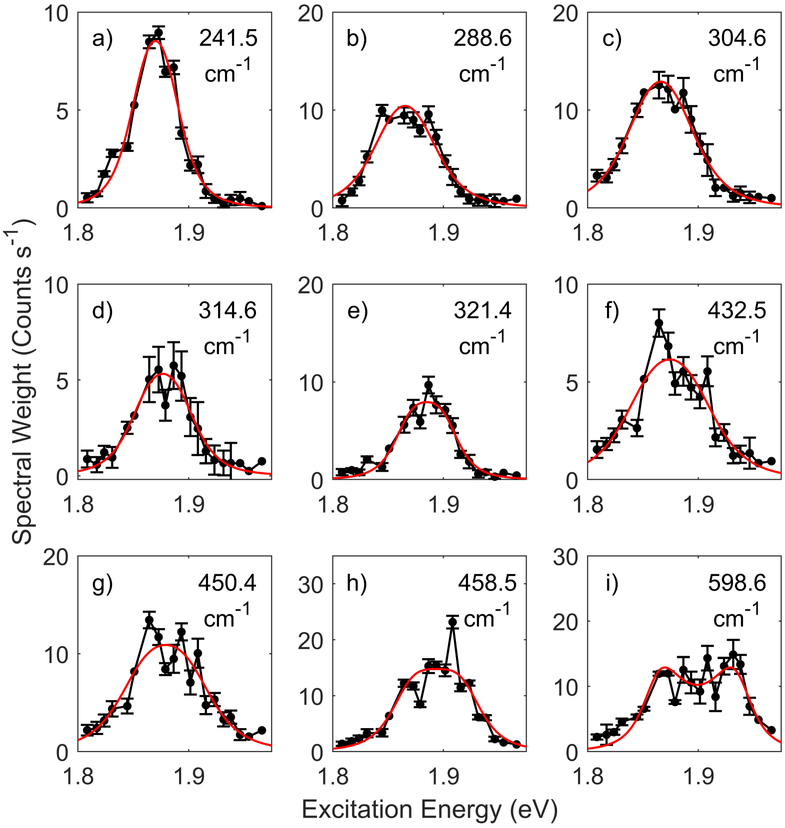

Figure 4.8: Resonance profiles are presented for the Raman peaks observed on monolayer MoSe$_2$ when resonant with the MoSe$_2$ B Exciton. In each case the resonance profiles have been fitted to single phonon event model shown assuming a single underlying electronic state with the fitted profile given by the red line. The error bars shown are a standard deviation determined from the fitting process.

fitted (see Figure 4.8) and may indicate the presence of an additional excitonic state. The resonance profile was fitted to two additional models assuming two independent electronic states and two electronic states with interstate scattering allowed. The resulting fits to the 241.5 cm^{-1} peak for all three Raman models are shown in Figure 4.9 with the adjusted r-square values and coefficients provided in Table 4.3. A visual comparison of the fits presented in Figure 4.9 clearly shows that the best fit to the data is obtained from the two state models shown in panels b) & c) with the both fits able to account for the low energy shoulder observed in the profile. This is reflected in the adjusted r-square values which are higher for both the two state models with the two state model assuming the electronic states are independent returning the highest r-square value of 0.986. Although, the difference between these two fits is negligible. This is also apparent in the coefficients obtained from fitting with the energies and widths for both the two state models in excellent agreement to within the errors. The similarity of the two models is suggests that the interstate scattering channel is relatively weak. This is obvious from the fitted amplitude where A_3 corresponds to the interstate scattering term. and A_1 and A_2 indicate the strength of scattering for the two states at E_1 and E_2 respectively. From the amplitude coefficients we can conclude that the higher energy state is the dominant scattering channel in the resonance profile. Therefore, when resonant with the $MoSe_2$ B exciton there are at least two electronic states involved with energies of 1.828±0.002 and and 1.862±0.001 eV respectively, but not significant scattering between these two states.

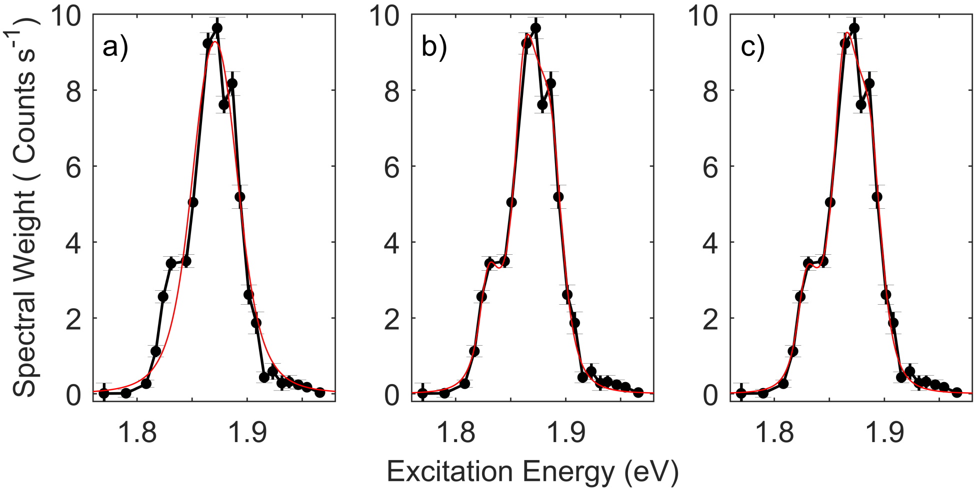

Figure 4.9: Resonance Raman profile for the peak at 241.5 cm^{-1} when resonant with the $MoSe_2$ B exciton. This profile was fitted to three single phonon event models assuming a) a single electronic state b) two independent electronic states and c) two electronic states with interstate scattering allowed.

		Model		
		Single State	Two State	Two State with scatter
Adjusted R-square		0.945	0.986	0.985
Amplitude	A_1	-	1.0 ± 0.1	0.8±0.2
	A_2	3.1±0.5	1.7±0.2	1.6±0.3
	A_3	-	-	0.1±0.3
Width (meV)	Γ_1	-	12.0±1.2	12.1±2.1
	Γ_2	28.3±3.2	16.4±1.9	16.0±2.3
Energy (eV)	E_1	-	1.828±0.002	1.827±0.003
	E_2	1.856 ± 0.001	1.861±0.001	1.862±0.002

Table 4.4: Adjusted R-square values and coefficients from fitting the 241.5 cm^{-1} peak resonance profile when resonant with the B exciton. The resonance profile was fitted to three separate single phonon event models assuming a single electronic state, two independent electronic states and two electronic states with interstate scattering allowed. Errors are the standard deviation from the fitting process. For ease of presentation amplitude coefficients were scaled by a factor of 10^3 and so have units of $10^{-3}\ \sqrt{Counts\ s^{-1} \cdot eV^2}$.

4.3.3 Anomalous Resonances

When resonant with the $MoSe_2$ B exciton the peaks at 481.5, 531.2 and 581.1 cm^{-1} demonstrate anomalous resonance behaviour. These peaks are clearly visible in Figures 4.6 & 4.7 between 1.855 and 1.880 eV. Compared to the other $MoSe_2$ Raman peaks in Figure 4.6 the resonances for the anomalous Raman peaks are significantly narrower and at lower energy. The resonance profiles for these peaks are presented in Figure 4.10. In each case the profiles appears to be the result of a single peak with a width of ~ 30 meV. In comparison the energy of the peaks at 481.5, 531.2 and 581.1 cm^{-1} are 59.7, 65.9 and 72.0 meV peaks respectively and so are a factor of 2 greater than the width of the observed resonances. Therefore, a single phonon event model assuming a single electronic excitation is cannot explain this resonance behaviour as it does not satisfy both the incoming and outgoing resonance conditions.

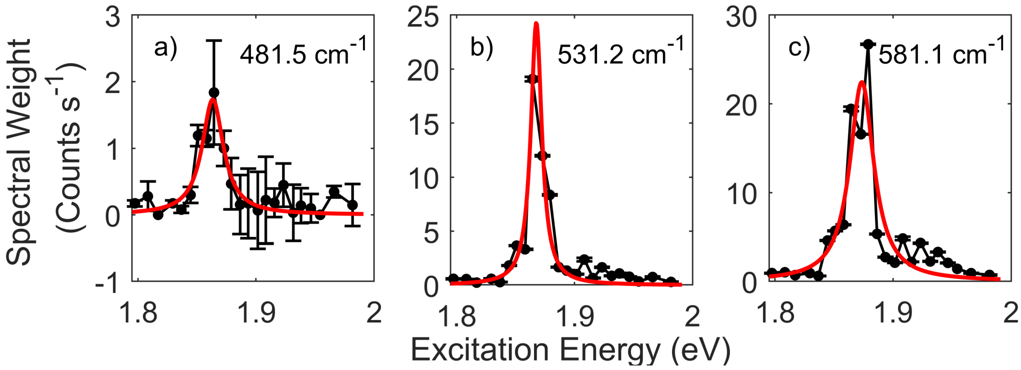

Figure 4.10: Resonance Raman profiles for the anomalous peaks at 481.5, 531.2 and 581.1 cm^{-1} are presented in panels (a-c). The anomalous behaviour of the resonance prevents fitting using the typical Raman models and so the profiles were fitted using a Lorentzian line shape. Errors given are a standard deviation from the fitting process.

To quantify the anomalous resonance behaviour the resonance profiles were fitted to single Lorentzian line shape. The resulting fits and resonance profiles are shown in Figure 4.10 and the coefficients from fitting are provided in Table 4.5. From fitting the energies of the resonance profiles are not identical and increase as a function of the Raman peak shift. The difference in energy between each of the resonance profiles is ~ 6 meV and is in agreement with the difference in energies of the Raman peaks. Therefore, the anomalous resonance profiles appear consistent with an outgoing resonance with an unidentified lower energy excitonic state. Assuming these resonance profiles are the result of an outgoing resonance the energy of the involved excitonic state should be given by $E\text{-}E_{ph}$. For each of the fitted profiles the value of $E\text{-}E_{ph}$ is provided in Table 4.5. For all three anomalous resonances the energy of the lower energy state is in excellent agreement with a mean value of 1.802 ± 0.001 eV. However, inspection of the Raman spectra near 1.802 eV shows no enhancement of any $MoSe_2$ Raman peaks. Therefore, there is no evidence for an incident resonance with this lower energy state.

The analysis of the Raman peak at 241.5 cm^{-1}, which has a more typical resonance behaviour, identified a electronic state at 1.862 eV and is close to the observed outgoing resonance for the anomalous peaks. This suggests a double resonance between the states at 1.802 and 1.862 eV and can explain the absence of a strong resonance when incident with this anomalous electronic state. In addition the coupling of this lower energy state only to the anomalous Raman peaks suggests that the underlying mechanism for these peaks is similar and may reveal further information regarding this new excitonic state. A further discussion of the potential origin of this anomalous state will be continued in the discussion presented in below.

Table 4.5: Coefficients from fitting Lorentzian line shapes to the resonance profiles for the anomalous Raman peaks at 481.5, 531.2 and 581.1 cm^{-1} when resonant with the $MoSe_2$ B exciton. Errors given for coefficients are a standard deviations from the fitting process. For ease of presentation amplitude coefficients are scaled by a factor of 10^3 and have units of 10^{-3} $\sqrt{Counts\ s^{-1} \cdot eV^2}$.

Raman Shift (cm^{-1})	Amplitude	Width (meV)	Energy (eV)	E_{ph} (meV)	E-E_{ph} (eV)
481.5	1.7 ± 0.2	11.0 ± 2.1	1.863 ± 0.001	59.7	1.803
531.2	24.3 ± 3.7	6.3 ± 1.4	1.868 ± 0.001	65.9	1.802
581.1	22.5 ± 2.8	12.1± 2.3	1.874 ± 0.002	72.0	1.802

Overall analysis of the resonance Raman data indicates the presence of multiple electronic states at the $MoSe_2$ B Exciton at 1.828 and 1.862 eV. The resonance behaviour of several anomalous Raman peaks was analysed and indicates this behaviour is due to an outgoing resonance associated with an unidentified excitonic state at 1.802 eV. The coincidence of the outgoing resonance term for this anomalous state near the state at 1.862 eV suggests this is a double resonance condition between these states. Therefore the resonance Raman behaviour for monolayer $MoSe_2$ is the result of scattering with at least three different excitonic states.

4.4 Discussion

The previous sections presented both the potential mode assignments for the $MoSe_2$ Raman peaks and an analysis of their resonance profiles. This section will address in more detail the possible origins of the excitonic peaks identified and the underlying phonons involved in the anomalous resonance profiles.

Analysis of the resonance Raman data for monolayer $MoSe_2$ when resonant with the $MoSe_2$ B exciton has revealed at least three different states involved in the resonance behaviour. From fitting to a model assuming a single electronic state revealed two clusters of energies were identified. Fitting of the 241.5 cm^{-1} resonance profile determined the energies of these two states to be 1.828 and 1.861 eV. The Raman peaks at 481.1, 532.2 and 581.1 cm^{-1} which demonstrate an anomalous resonance behaviour were also analysed and found to be involved with an outgoing resonance associated with an unidentified state at 1.802 eV.

The $MoSe_2$ B exciton is predicted by DFT calculations to have a separation of 216 meV relative to the A exciton resulting from the valence band and conduction band spin splitting [252], and has been verified by PL and reflectivity measurements performed on monolayer $MoSe_2$ [251, 133]. From the PL spectra obtained for our monolayer $MoSe_2$ sample the peak at 1.649 eV was attributed to the neutral $MoSe_2$ A exciton. Using this result the expected energy of the B exciton is predicted to be 1.865 eV using the predicted separation of 216 meV. In comparison to the energy of the states identified from our resonance Raman measurements this predicted is in agreement with the state at 1.862 eV. Therefore it is likely that the state at 1.862 eV is the neutral B exciton.

In addition, both positively and negatively charged trions have been reported in monolayer $MoSe_2$ at the A exciton. It is also possible for trions to form at the B exciton. These B trions have been predicted and are expected to have a smaller binding energy than their counterparts at the A exciton [88]. However, there are only a few experimental reports of B trions in literature [253, 254] with only the work of Wang et al. able to unambiguously distinguish between the trions and neutral B excitons [255]. Fortunately they report the observation of B trions in both monolayer $MoSe_2$ and WSe_2 and so we can use their results to identify the likely energy ranges for the neutral excitons and trions. From their results the energy of the neutral exciton is expected between 1.845 to 1.87 eV, whilst the negatively and positively charged trions are expected between 1.815 to 1.845 and 1.8 to 1.84 eV respectively. These results are also in agreement with gated photocurrent spectroscopy measurements which observe a state 30 meV below the neutral B exciton [256], although they propose that this could result from either the B trion or the spin forbidden B exciton. Considering then our experimental results the separation of the states at 1.862 and 1.828 eV of 34 meV is in reasonable agreement with the expected separation of the exciton and trion. Therefore, it seems reasonable to conclude that the state at 1.828 eV is due to a charged B exciton and the 1.862 eV state is the neutral B exciton. Although without the use of gated measurements it is not possible to identify unambiguously if the trion is positively or negatively charged. Future gated measurements would also clarify if this state is the result of a spin forbidden B exciton which would also have an energy 20 to 30 meV below the B exciton [75, 252].

The final state to consider is the electronic state at 1.802 eV which is observed only for the Raman peaks at 481.5, 531.2 and 581.1 cm^{-1}. The resonance in this case was observed to shift in energy in agreement with the change in phonon energy is due to an outgoing resonance with a lower energy state. The coincidence of this resonance near 1.862 eV suggests a double resonance between the neutral $MoSe_2$ B exciton and the lower energy anomalous state and explains the lack of incident resonance for the lower energy state at 1.802 eV. This anomalous resonance is 60 meV below the neutral B exciton and is unlikely to be associated with either B trions or spin forbidden B excitons. It is possible that this lower energy state could be the result of biexcitons which have been observed at the A exciton in several TMDCs [92]. However, biexcitons have not been reported for monolayer $MoSe_2$ at the A exciton and so it seems unlikely that these states are present at the B exciton. A more likely possibility is that the state at 1.802 eV is an excited state of the $MoSe_2$ A exciton. Both 2s and 2p states have previously been reported for monolayer $MoSe_2$ [133, 252, 251]. In particular Renucci et al. reported the energy the excited A 2s state in encapsulated monolayer $MoSe_2$ to be $\sim$ 150 meV above the A exciton, which corresponds to an energy 55 meV below the B exciton [251] and is close to our observed separation of the neutral B exciton and anomalous state. It is possible that there is another explanation for this low energy state however a thorough search of the literature has not produced any viable alternatives. Therefore we conclude that the anomalous state observed at 1.802 eV is due to the excited 2s A exciton.

If the anomalous state is the result of an excited A exciton this would suggest the phonon assisted scattering between the B and A excitonic states. In the electronic band structure of monolayer $MoSe_2$ the spin orbit splitting requires the states at the K and K′ valleys to have opposite spins. Whilst the spin of the excitonic states is zero the energies of these states at a particular valley are not degenerate. For a B exciton to scatter to the A exciton in the same valley must involve a change in the spins of the exciton. Recent work by Guo et al. describes an intra-valley mixing of the excitons in TMDCs arising due to the intra-valley exchange interaction and allows for the mixing of the A and B excitonic states [257]. Alternatively, the scattering of a B exciton at the K(K′) valley to an A excitonic state at the opposite K′(K) valley does not require a change spin. Therefore, the scattering of a B exciton to an excited A excitonic state could be mediated via large wavevector phonons scattering.

The coupling of only three Raman peaks to the anomalous resonance suggests this process requires a particular set of phonons. For the the Raman peaks at 481.5, 531.2 and 581.1 cm^{-1} there are multiple possible assignments to different multiphonon Raman peaks. However, all three Raman peaks could be explained by the E'_{TO}(M)

+ 2LA(M)/2TA(M)/2ZA(M) combination modes which have predicted frequencies of 479.5, 531.5 and 593.6 cm^{-1}. Whilst this may be a fortuitous coincidence the ability to explain all three anomalous Raman peaks as arising from similar multiphonon combination modes is an enticing proposition. The phonons involved in these peak are all large wavevector and so could allow for scattering between the B exciton and an excited A exciton. A inter-valley scattering process seems more likely to allow coupling between the A and B excitons as it does not require a change in spin via exchange interactions. However, it is not possible to fully clarify the underlying process due to the uncertainty in the peak assignment and the nature of the lower energy excitonic state. While an exact mechanism for the coupling between a B exciton and excited A state has yet to be elucidated this result may allow further information on intra and inter-valley scattering processes which can couple between the B and A excitonic states. At present the energies from resonance Raman spectroscopy suggests the involvement of both the neutral B exciton and excited state of the A exciton in the Raman scattering processes. Whilst excited states have been observed through other spectroscopy techniques our method provides additional information on scattering between excitonic states and the involvement of dark intermediate states. Further measurements using high resolution one photon and two phonon PLE may also allow for a direct measurement of the A excited state in this sample and confirm our proposed assignment.

4.5 Conclusion

In conclusion this chapter has presented the results of resonance Raman spectroscopy on an encapsulated monolayer of $MoSe_2$ and reports a thorough study of the resonance behaviour with the B exciton. A detailed assignment of the Raman peaks to possible phonon combination modes has been presented. Only the 241.5 cm^{-1} peak can be unambiguously assigned to a single phonon mode. The majority of Raman peaks instead have multiple possible assignments to multi-phonon combination modes and cannot be attributed to a particular mode. This is in contrast to the proposed assignments in literature which assign a single phonon mode to each Raman peak. In addition this analysis reveals an unexpected temperature dependence of a Raman peak observed at 150 cm^{-1} which is assigned in literature to the LA(M) phonon. This peak is not visible at 4 K but is clearly visible at room temperature. The temperature dependence of this peak can be explained if it is the result of a multiphonon process involving both emission and absorption of phonons. This is supported by the assignment of a similar peak at 140 cm^{-1} to the E' - LA(M) in literature [194]. The potential erroneous assignment of the LA(M) peak throws into doubt the reported assignment of overtones of the LA phonon and further emphasises that these multiphonon Raman peaks should not be assigned to a single set of underlying phonons. These results also reveal the presence of continuously dispersive Raman peaks at $\sim$ 288 cm^{-1}, which indicates the scattering of the E' phonon with large wavevector dark states.

The analysis of the resonance behaviour has demonstrated the presence of two excitonic states when resonant with the $MoSe_2$ B exciton and assigned these to a trion at 1.828 and neutral exciton at 1.862 eV. This is the first reported observation of B trions on monolayer $MoSe_2$ using resonance Raman spectroscopy. In addition an anomalous Raman resonance is observed for the three multiphonon Raman peaks at 481.5, 531.2 and 581.1 cm^{-1}. The mode assignment of these peaks have been considered and multiple possible assignments are available for each peak. However, we propose that these peaks arise due to the E'_{TO}(M) + 2LA(M)/2TA(M)/2ZA(M) combination modes and may imply a particular set of phonons are required to couple to the anomalous resonance. The anomalous resonance is attributed to a double resonance between the $MoSe_2$ B exciton and the excited 2s A exciton at 1.802 eV. A combination of the relaxation via scattering with the phonons and the intra-valley exchange interaction could allow for the coupling between a B exciton and excited A state in the same valley. Further investigation of this anomalous resonance with both gated resonance Raman measurements, PLE and polarisation resolved PL could provide confirmation that this peak is the 2s state. This would also allow further information on the mechanism for scattering between the A and B excitonic states and may provide additional information regarding valley depolarisation.

Chapter 5

Resonance Raman Spectroscopy of Encapsulated Monolayer WSe_2

This chapter presents a study of the excitonic transitions in encapsulated monolayer WSe_2 via resonance Raman spectroscopy using excitations energies between 1.6 and 2.25 eV. This allows both the A and B excitons at 1.742 and 2.16 eV respectively to be probed. We also report the presence of an additional resonance at ~ 1.866 eV, which is referred to as the A*, and is attributed to an excited Rydberg state of the A exciton.

5.1 Motivation

The experiments in this chapter explore Raman scattering in an encapsulated monolayer of WSe_2. Previous Raman studies of WSe_2 were only carried out at room temperature, did not made use of continuously tuneable lasers and focused on investigating the C exciton [35, 36, 193]. Consequently, the behaviour of the A and B excitons has yet to be fully explored by resonant Raman scattering. Recent studies of encapsulated monolayers of WSe_2 have demonstrated coupling between the TMDC and substrate phonons associated with a previously unobserved resonance in encapsulated WSe_2 [198, 199]. The underlying mechanism behind this process has yet to be fully understood. The lack of a complete study of the resonance Raman behaviour of monolayer WSe_2 means there is a wealth of physics still to be explored. Furthermore the sample utilised in these measurements also contains several novel heterobilayers composed of $MoSe_2$ and WSe_2. In order to understand the resonance Raman behaviour of these heterobilayers we first require a firm understanding of the Raman response of the constituent monolayers.

5.2 Photoluminescence of monolayer WSe_2

To characterise the sample a PL spectrum was acquired using an excitation energy of 2.33 eV with an incident power of 50μW. The obtained spectrum is shown in Figure 5.1 and reveals an abundance of peaks between 1.55 and 1.75 eV. To quantify these peaks the spectrum was fitted to a total of 10 Lorentzian line shapes. The coefficients from fitting are provided in Table 5.1. The highest energy peak is observed at 1.742 eV and assigned to the neutral A exciton, and is in agreement with the energies reported for similar samples [93, 199]. The next two peaks in the spectrum at 1.712 and 1.704 eV and are assigned to the inter and intra-valley negatively charged trions. The separation of 8 meV between these trionic states is in good agreement with reported values in literature [92, 258]. The remaining peaks below 1.70 eV are more difficult to assign due to the large number of peaks observed in this energy range, which have possible assignments to dark excitons, additional charged excitons, biexcitons, charged biexcitons, localised excitons and defect states [92, 259, 260, 261]. A precise assignment of these lower energy peaks would require both gated and power dependent measurements and is beyond the scope of this study. The results presented in this chapter show no resonant Raman enhancement of the WSe_2 modes below 1.7 eV. Therefore, a complete assignment of these lower energy peaks is not required for interpreting our Raman data. The lack of Raman resonances with these lower energy peaks is not surprising as these states typically exhibit a low oscillator strength and are not observed in reflectivity or absorption measurements [259, 132]. In addition we also observe an additional higher energy peak at 1.873 eV which is attributed to the A* resonance and is discussed in more detail in Section 5.3.2.2.

Table 5.1: Coefficients from fitting the WSe2 PL spectrum shown in Figure 5.1. Errors given are the standard deviation from the fitting process.

Amplitude	Width (meV)	Energy (eV)
322.6±7.7	6.9±0.3	1.742±0.001
462.8±12.8	5.9±0.3	1.712±0.001
568.3±8.1	10.0±0.4	1.704±0.001
370.7±9.8	4.3±0.2	1.693±0.001
874.6±8.8	5.0±0.1	1.679±0.001
1551.6±4.0	26.7±0.1	1.658±0.001
402.0±9.6	6.3±0.3	1.623±0.001
2192.0±7.8	12.1±0.1	1.612±0.001
884.6±20.2	11.0±0.4	1.600±0.001
443.3±14.5	23.0±0.6	1.589±0.001

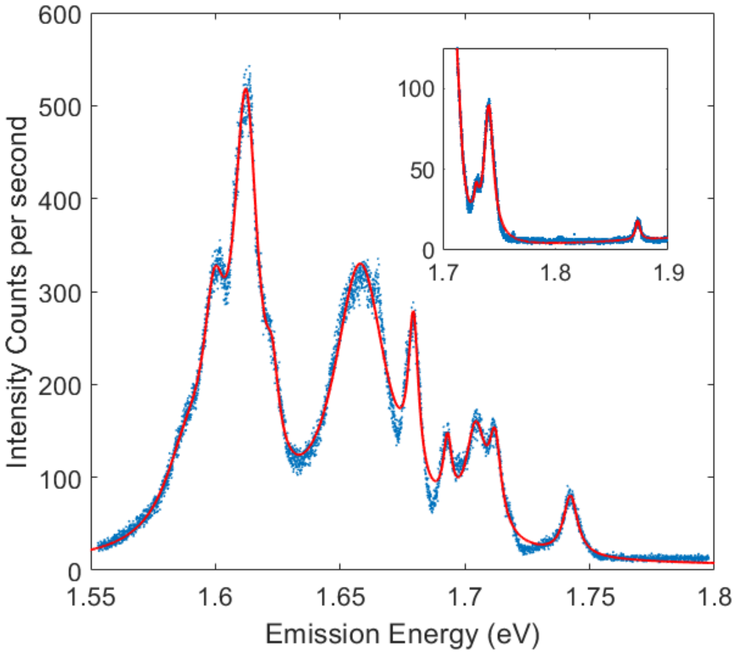

Figure 5.1: Photoluminescence spectrum taken on monolayer WSe$_2$ region using 2.33 eV (532 nm) excitation. The spectrum was been fitted to a summation of Lorentzian line shapes with the resultant fit indicated by the red line. Inset panel shows an additonal PL spectra obtained with an excitation energy of 1.968 eV and shows an additional state at 1.873 eV and is attributed to the A* state.

5.3 Resonance Raman Spectroscopy of monolayer WSe_2

For our WSe_2 monolayer resonance enhancement is observed with three different excitonic states labelled as the A, A* and B respectively. Resonance with the A exciton shows a clear enhancement near ~ 1.74 eV and is consistent with the neutral A exciton identified from PL measurements. The resonance with the WSe_2 B exciton is observed at ~ 2.16 eV with a separation between the A and B excitons of ~ 418 meV. This is in agreement with reflectance contrast measurements [132] and in line with theoretical predictions for the valence band splitting in WSe_2 which is estimated by Zhu et al. to be ~ 453 meV [66]. In addition a third unexpected resonance is observed at ~ 1.866 eV. The proximity of this peak to the A exciton has led to this resonance being labelled as the A* state. The following sections present a discussion of the mode assignment of the WSe_2 Raman spectra at each resonance followed by a detailed analysis of the resonance Raman data for the A, B and A* states.

5.3.1 Mode Assignment

In this section the WSe_2 Raman spectra are presented and an assignment of the Raman peaks to their underlying phonons is proposed. In total three separate Raman resonances identified for monolayer WSe_2 labelled as the A, A* and B excitons with energies of $\sim$ 1.74, 1.86, 2.16 eV respectively. Exemplar spectra at each resonance are presented in Figure 5.2 and were calibrated to the silicon signal at 520 cm^{-1}. To allow for a qualitative comparison the spectra were normalised to the maximum peak intensity and offset. From the spectra presented in Figure 5.2 there are clear differences between the Raman spectra when resonant with the different excitonic states. These include variations in the number of Raman peaks observed and changes in the relative peak intensities. Of the three resonances the A and A* spectra are similar in appearance. However there are several differences including an additional peak at ~ 495 cm^{-1} that is only observed for the A* spectra, and dispersive peak at ~ 207 cm^{-1} when resonant with the A exciton. Comparing the A and A* spectra to those at the B exciton there is a clear changes in the spectra, which include the appearance of new peaks between 200 to 250 cm^{-1} and an additional Raman peaks near ~ 400 cm^{-1}. There is also a significant change in the relative intensity of the Raman peaks. This can be seen by considering the dominant peak in the spectra at both the A and A* states the 250 cm^{-1} peak dominates the spectrum, however at the B exciton the dominant peaks are those at ~ 260 cm^{-1}. The differences in the Raman spectra when exciting the B exciton were previously reported but not considered in detail due to the lack of data at the A and B excitons [193].

To quantify the number of Raman peaks at each resonance the spectra were fitted to a summation of Lorentzian line shapes. For each resonance at least three spectra

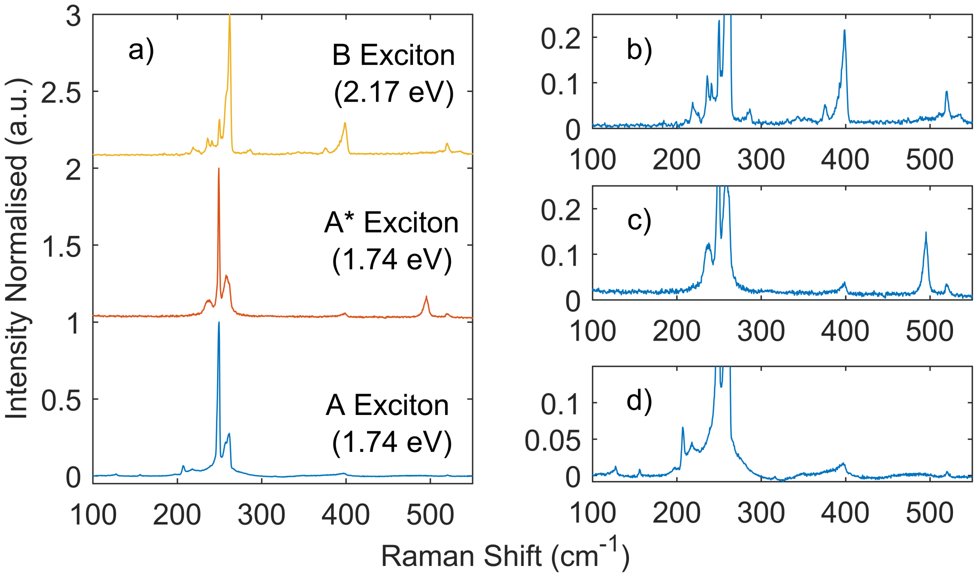

Figure 5.2: Raman spectra obtained when resonant with the A, A* and B excitonic states using 1.74, 1.87 and 2.17 eV excitation energy respectively are presented. All spectra are shown together in panel a) and have been normalised to the peak intensity in each case and offset to allow visual comparison. Panels (b-d) then show the individual spectra when resonant with B, A* and A excitons respectively and in each case the y-axis limits have been adjusted to allow easier inspection of the lower intensity Raman peaks.

at different excitation energies were fitted to determine a mean value and a standard deviation for each peak position. The Raman shifts from fitting spectra at the A, A* and B resonances are presented in Table 5.2, and reveals that there are several peaks which are only observed at a particular resonance, and indicate a difference in the underlying scattering processes. The peaks at ∼ 235, 241, 250, 258, 262 and 397 cm^{-1} are seen at all three resonances with their Raman shifts in agreement to within the error. At the WSe$_2$ A exciton we observed a dispersive Raman peak, with a frequency between 207.0 and 210 cm^{-1}, which is not observed at the A* or B resonances. The absence of this peak at the other resonances is not unexpected due to it's dispersive behaviour and is discussed in more detail in Section 5.3.1.1. At the WSe$_2$ A* resonance a new peak is observed at 494.6 cm^{-1} and is not seen at either the A or B resonances. For the B resonance there are several new peaks which are not observed for either of the other resonances at 197.8, 225.0, 230.5, 375.6 and 393.1 cm^{-1}. For the 375 to 400 cm^{-1} peaks there is evidence that these peaks are present at the A and A* resonance but are too weak to be resolved. For the A exciton in particular there are several instances where background subtraction of luminescence from the A exciton makes it difficult to resolve weaker peaks. Overall the significant differences in appearance of the Raman spectra at each resonance combined with the observation of Raman peaks exclusive to each resonance indicates a change in either the electron-phonon coupling or the nature of the underlying electronic states contributing to each resonance.

Table 5.2: Raman spectra at A, A* and B resonances were fitted to obtain the positions of the Raman peaks. The presented values are the mean and standard deviation from fitting several spectra at different excitation energies.

Raman Shift (cm^{-1})		
A	A*	B
-	-	197.8±0.3
207.0±1.4	-	-
219.2±0.7	-	219.1±0.3
-	-	230.5±0.5
234.5±0.3	236.2±0.5	235.2±0.1
241.5±0.7	240.2±0.3	241.0±0.2
249.5±0.1	249.0±0.1	249.7±0.1
257.7±0.2	257.4±0.1	258.1±0.1
261.9±0.2	261.6±0.1	262.0±0.1
-	286.7±0.5	285.9±0.4
-	-	375.6±0.3
-	-	393.1±0.5
396.6±0.4	397.4±0.4	398.6±0.1
-	494.6±0.1	-

The resonance Raman behaviour of monolayer WSe_2 has been reported previously in literature [35, 153, 193, 156, 190]. These studies demonstrated resonance enhancement at the C exciton, Davydov splitting of the Raman peaks and the changes in the Raman spectra as a function of layer number. A detailed resonance Raman study of the WSe_2 A exciton has not been previously reported, although the B exciton was studied by Del Corro et al. [193]. The lack of detailed investigations of the A and B exciton is due to the use of discrete lasers as opposed to a continuously tunable system, and limits the resolution of these experiments. All previous resonance Raman measurements were also conducted at room temperature, whilst our experiments are at 4 K. This is advantageous as the line widths of the excitons in the WSe_2 are significantly narrower at low temperatures and it is possible to resolve the detailed structure of the resonances, such as, the contributions from both excitons and trions [37, 262]. In addition there are numerous reports addressing the assignment of the WSe_2 Raman spectra using only a single excitation energy [263, 52, 163, 177, 264]. These studies have allowed the layer dependent behaviour of the A_1' and E' Raman peaks to be addressed and confirmed via polarisation resolved measurements that these peaks are degenerate in the monolayer limit [52, 163].

The assignment of the Raman peaks in our spectra to their underlying phonons requires the use of an appropriate phonon dispersion relation. We chose to use the phonon dispersion calculated by Terrones et al. for monolayer WSe_2 [153]. The WSe_2 dispersion phonon relation is provided for reference in Figure 5.3. As previously discussed when considering the mode assignment for monolayer $MoSe_2$ in Chapter 4 the predicted values for the different phonon branches can vary significantly between the reported phonon

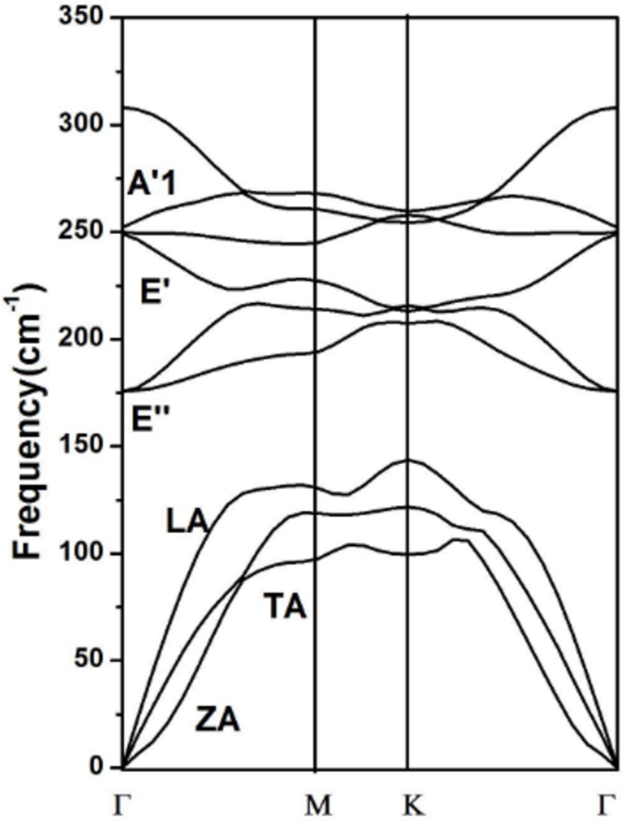

Figure 5.3: The predicted phonon dispersion relation for monolayer WSe$_2$ calculated by Terrones et al. using DFT. WSe$_2$ phonon dispersion by Terrones et al. [153] this work is licensed under a Creative Commons Attribution-NonCommerical NoDerivs 3.0 Unported License https://creativecommons.org/licenses/by-nc-nd/3.0/.

dispersion relations. In addition the experimentally measured Raman shift can also vary due to the effects of temperature, strain, and substrate choice [265, 218, 266]. As a result all possible phonon mode assignments are considered to within 3 cm^{-1} per phonon to account for the uncertainty in the predicted dispersion relations. The results of this assignment process are presented in Table 5.3 and for several of the assigned Raman peaks a more detail discussion of their assignments is provided. Where possible the assignment given in literature for these peaks is also provided. To simplify the mode assignments we constrain the available phonons in our analysis to those at the high symmetry points of the Brillouin zone i.e the Γ, K and M points.

Table 5.3: Mode assignments of the monolayer WSe_2 Raman peaks when resonant with the A, A* and B excitons. Assignments given in literature are provided along with the following superscripts corresponding to [a][199], [b][190], [c] [143], [d] [163] and [e] [153]. Where there are multiple possible peak assignments the difference between the predicted and experimentally frequencies were used to rank the assignments.

Raman Shift (cm^{-1})	Widths (cm^{-1})	Reported Assignment	Assignment	Predicted Shift (cm^{-1})
197.8±0.3	3.9±2.6		E''_{TO}(M)	195.5
			2TA(M)	195.5
			2TA(K)	201.8
			E''_{TO}(K)	209.2
207.0±1.4	2.6±0.4	Unassigned	E''_{TO}(K)	209.2
219.2±0.7	4.6±1.0	LA(M)+TA(M)[a,b]	TA(M)+ZA(M)	217.0
			E''_{LO}(K)	216.5
			E''_{LO}(M)	214.9
230.5±0.3	5.2±1.8		E'_{TO}(M)	228.6
			TA(M)+LA(M)	229.1
234.5±0.3	5.8±2.6		2ZA(M)	238.6
			TA(M)+LA(M)	229.1
241.5±0.7	2.7±0.4	LA(M)+ZA(M)[a,b]	2ZA(M)	238.6
			LA(K)+TA(K)	245.2
			E'_{LO}(M)	246.0
			2ZA(K)	246.0
249.5±0.1	2.8±1.4	A'_1(Γ) and E'(Γ)[e]	$E'_{LO/TO}$(Γ)	250.6
			A'_1(Γ)	250.6
			LA(M)+ZA(M)	250.7
257.7±0.2	4.6±1.0	A''_2(M)[c]	E'_{LO}(K)	259.1
			A'_1(K)	261.7
			A''_2(M)	262.2
261.9±0.2	3.14±0.8	2LA(M)	A'_1(K)	261.7
			A''_2(M)	262.2
			2LA(M)	262.8
			LA(M)+ZA(M)	267.5
			A'_1(M)	269.1
285.9±0.4	3.8±1.2	Unassigned	2LA(K)	289.0
			3TA(M)	293.3
375.6±0.3	4.8±1.0	E'_{LO}(M)+LA(M)	A''_2(K)+ZA(K)	377.9
			A''_2(M)+ZA(M)	381.5

Table 5.3 continued from previous page

Raman Shift (cm^{-1})	Widths (cm^{-1})	Reported Assignment	Assignment	Predicted Shift (cm^{-1})
			E'_{LO}(M)+LA(M)	377.3
393.1±0.5	8.2±1.4	3LA(M)^{b,c}	A''_2(M)+LA(M)	393.6
			3LA(M)	394.1
			3TA(M)	391.0
			2E''_{TO}(M)	391.0
			2LA(K)+TA(K)	389.9
			A'_1(M)+ZA(M)	388.4
			A''_2(K)+LA(K)	399.4
			A'_1(K)+ZA(K)	384.7
398.6±0.1	7.2±2.6	A'_1(M)+LA(M)^{b,c,d}	A''_2(K)+LA(K)	399.4
			A'_1(M)+LA(M)	400.5
			3LA(M)	394.1
			E'_{LO}(K)+LA(K)	403.6
			4TA(K)	403.6
			4TA(M)	391.0
			3TA(M)	391.0
			2E''_{TO}(M)	391.0
			A'_1(M)+LA(M)	406.2
494.6±0.1	5.3±0.2	2A'_1(Γ)^{a}	4ZA(K)	491.9
			2LA(M)+TA(M)	491.9
			2E'_{LO}(M)	491.9
			E'_{TO}(M)+A'_1(M)	497.7
			2LA(K)+E''_{TO}	498.2
			E'_{TO}(M)+A''_2(M)	490.8
			2ZA(M)+LA(M)	489.3
			2TA(M)+E''_{TO}(M)	488.7
			2E''_{TO}(M) +TA(M)	488.7
			2TA(K)+A''_2(K)	500.8
			2LA(K)+E'_{TO}	502.9
			2TA(K)+E'_{LO}(K)	505.0
			A'_1(M)+E''_{LO}(M)	484.0

First we consider the assignment of our observed Raman peaks to single phonon processes. At the Γ point in the phonon dispersion there are only three possible frequencies for single phonon Raman peaks due to the degeneracy of the A_1', E' and E'' phonon branches. The A_2'' branch is predicted at ~ 307 cm^{-1} at the Γ point but is Raman inactive in monolayer WSe_2 [153]. Likewise the E'' branch is predicted at ~ 176 cm^{-1} at the Γ point, but is also not expected to be visible in our spectra as this mode is forbidden in backscattering geometry [143]. However, under resonance Raman conditions these selection rules are not necessarily valid and these peaks are reported when resonant with the C exciton in other TMDC monolayers [194]. In our Raman measurements there are no peaks observed at these frequencies for either the A, A* or B exciton resonance and so we can conclude that the E'' and A_2'' peaks are not present in our spectra. As a result only one Raman peak in our spectra assigned to Γ point A_1' and E' phonons. These peaks are predicted to be degenerate at the Γ point for monolayer WSe_2 and has been confirmed experimentally [52, 163]. In our experiments the peak at 249.5 cm^{-1} is assigned to the A_1'/E' phonons and is in agreement with assignments reported in literature [52, 163, 193]. Although, we acknowledge that a combination mode arising from the LA(M)+ZA(M) is predicted in our analysis to appear at this frequency and so it is not possible to be absolutely certain of the peak assignment.

The resulting assignments in Table 5.3 also include potential assignments to single phonon processes with large wavevectors. To observe these large wavevector single phonon Raman peaks, an additional elastic scattering event with a defect state is required to satisfy the conservation of wavevector [267]. Defect scattering in TMDCs has been demonstrated using samples with increasing defect densities and results in an increase in the intensity of the Raman peak assigned to the LA phonon [168, 141, 170]. The effect of defect scattering on the Raman selection rules is unclear and may alter the symmetries allowed in the scattering processes, as such all possible phonons including the E'' and Raman inactive A_2'' phonons are considered in the assignment process. A consequence of defect scattering processes should be the appearance of Raman peaks associated with the acoustic phonons. The dispersion of the acoustic phonon branches allows for Raman peaks at the high symmetry points with frequencies in the range of 95 to 150 cm^{-1}. However, as seen from the results of Table 5.3 & 5.2 there are no Raman peaks observed at these lower frequencies in any of our spectra. Therefore, there is no evidence of single phonon scattering of large wavevector acoustic phonons in our experiments. As seen in Table 5.3 there are numerous possible assignments to large wavevector single phonon optical modes. However, in all cases there are also assignments to two phonon or higher order combination modes for these Raman peaks and so it is not possible from these results to distinguish between the two processes. An exception to this is the dispersive Raman peak at ~ 207 cm^{-1} at the A exciton which has a single assignment to the E''_{TO} phonon. The dispersive nature of this peak clearly indicates the involvement of phonons with different wavevectors and is evidence of large wavevector single phonon peaks due to optical phonons. Therefore, there is evidence for single phonon peaks due to large wavevector optical phonons, although for the majority of Raman peaks the possibility of degenerate assignments to other Raman peaks prevents a precise assignment of these large wavevector processes.

Our discussion so far has been limited to single phonon mode assignments, however there are several Raman peaks observed when resonant with the WSe_2 excitons that must originate from higher order multiphonon scattering processes. The phonon dispersion relation for monolayer WSe_2 provides a maximum frequency for a single phonon process of 307 cm^{-1}, predicted for the $A_2''(\Gamma)$ point phonon. Therefore, the Raman peaks observed at 375.6, 393.1, 398.6 and 494.6 cm^{-1} must result from higher order multi-phonon scattering processes. In our analysis multiphonon combination modes were considered up to 4th order when assigning the Raman peaks. As seen in Table 5.3 the assignment of these Raman peaks to a particular combination mode is not possible due to the large number of multiphonon modes with predicted frequencies that are almost degenerate. Therefore, it is likely that each of these Raman peaks are the result of several different underlying combination modes. For example the 2LA(M) mode in monolayer MoS_2 was shown by Carvalho et al. to result from at least five different multiphonon combination modes that were almost degenerate [141].

A method which may allow us to determine if a Raman peaks is composed of multiple combination modes is to consider the peak widths given in Table 5.3. The Raman peak assigned to the single phonon $A_1'/E'(\Gamma)$ mode at 249.5 cm^{-1} has a width of 2.8 cm^{-1}, and provides an estimate of the expected line width for a single phonon Raman peak. Comparing those peaks above 350 cm^{-1} which must be multiphonon peaks, their widths vary from 4.8 to 8.2 cm^{-1}. In particular the peaks at 393.1 and 398.6 cm^{-1} have widths of 8.2 and 7.2 cm^{-1} and so are 2-3 cm^{-1} broader than the peaks at 375.6 and 494.6 cm^{-1}. This may suggest that the 393.1 and 398.6 cm^{-1} peaks are composed of multiple combination modes which are almost degenerate. Although, the difference in width may result from the different order of the multiphonon processes. Likewise the lower frequency Raman peaks, which may be the result of multiphonon or large wavevector single phonon modes, have widths from 2.6 to 5.8 cm^{-1}. The peaks at 207.0, and 241.5 cm^{-1} both have similar widths to the 249.5 cm^{-1} peak. This may suggest that these peaks are also due to single phonon processes and could be assigned to the E''_{TO} and E'_{LO} phonons. However, the line width of the Raman peaks is dependent on other factors including the coherence lifetime, homogeneity, quality of the sample material, and effects of phonon confinement. For large wavevector processes the scattering via off zone centre phonons may also result in broadening due to a range of allowed wavevectors. A thorough analysis of the line widths would require the underlying phonons be more precisely known. Therefore, the width of the peak should be considered only as a metric when optimising the fits to the spectra. Overall there are several Raman peaks observed which must be the result of multiphonon Raman peaks due to their high frequency, but a precise assignment of these peaks to a particular set of underlying phonons is not possible due to the large number of peaks predicted to be almost degenerate for these peaks.

It is also interesting to compare the higher frequency peaks at the different resonances, particularly those observed between 375 and 400 cm^{-1} when resonant with the WSe_2 B exciton. For the A and A* resonance only the Raman peak at 398.6 cm^{-1} peak is seen in the Raman spectra presented in Figure 5.2 with only a weak broadband feature visible when resonant with the A exciton below the 398.6 cm^{-1} peak. However, when probing the A exciton there is also a significant PL background which has been removed by subtraction of co-linearly and cross-linearly polarised Raman spectra, and so it is difficult to clearly resolve the weaker Raman peaks in the spectrum. It is possible that the broad contribution seen in the spectra is due to a residual component of the background subtraction and not the result of Raman scattering. The lack of these peaks in the Raman spectra at the WSe_2 A and A* resonance is likely due to their low intensity, which prevents them being resolved from the noise in the spectra. The relative intensity of these peaks at the B exciton however clearly implies a change in the underlying process enhancing the strength of scattering from these high frequency multiphonon peaks. The differences between the different resonances is further demonstrated by the appearance of a Raman peak at 494.6 cm^{-1}, which is only observed when resonant with the A* state and has an unusual resonance behaviour.

The Raman spectra when resonant with the WSe_2 B exciton is significantly different when compared to the A and A* resonances. From Table 5.2 there are at least two peaks at 225.0 and 230.5 cm^{-1} which are exclusive to the WSe_2 B resonance. The assignments presented in Table 5.3 for these peaks indicate they are likely due to two phonon combination modes. It is also clear that at the WSe_2 B exciton the Raman peak at 249.5 cm^{-1} is no longer the dominant peak as was the case for the A and A* resonances. Instead the peaks at 257.7 and 261.9 cm^{-1} dominate the spectrum. The appearance of new peaks likely arising from two phonon processes and apparent increase in the relative intensity of the peaks at 257.7, 261.9, 375.6, 393.1 and 398.6 cm^{-1} suggests that multiphonon scattering processes are enhanced at the B exciton. This suggests the availability of large wavevector states allowing for an increase in multiphonon Raman scattering. However, it is also possible that this is the result of fundamental differences in the exciton phonon coupling similar to the mechanism proposed for monolayer MoS_2 [36].

5.3.1.1 Dispersive Mode

The Raman peaks discussed so far all have constant frequencies with the peak positions in agreement to within 1 cm^{-1} when comparing the spectra at the A, A* and B resonances. The exception to this is the Raman peak at $\sim$ 207.0 cm^{-1} which is observed only when resonant with the WSe$_2$ A exciton and shows a shift in frequency of $\sim$ 3 cm^{-1} as a function of excitation energy. This dispersive behaviour is visible in Figure 5.4 panel a) near the A exciton resonance. To quantify the shift in frequency of this peak the fitted positions are presented in Figure 5.4 panel b) as a function of excitation energy. The Raman shift of the peak is found to range from 205.5 to 208.6 cm^{-1}. The dispersive nature of this Raman peak indicates this Raman peak is associated with large wavevector intermediate states accessible via defect mediated single phonon scattering or multiphonon Raman processes. The proposed assignment for this peak in Table 5.3 is to the E$''(K)$ phonon. Considering the phonon dispersion relation for the E$''_{TO}(K)$, it is apparent that the dispersion near the M point is relatively flat whereas the frequency between the K and M point increases significantly. This appears to be in agreement with the change in frequency observed for the Raman peak and indicates the assignment to the E$''_{TO}(K)$ could result in the observed dispersion. The observation of this dispersive Raman peak is a clear indication that there are large wavevector excitonic dark states present at the WSe$_2$ A exciton.

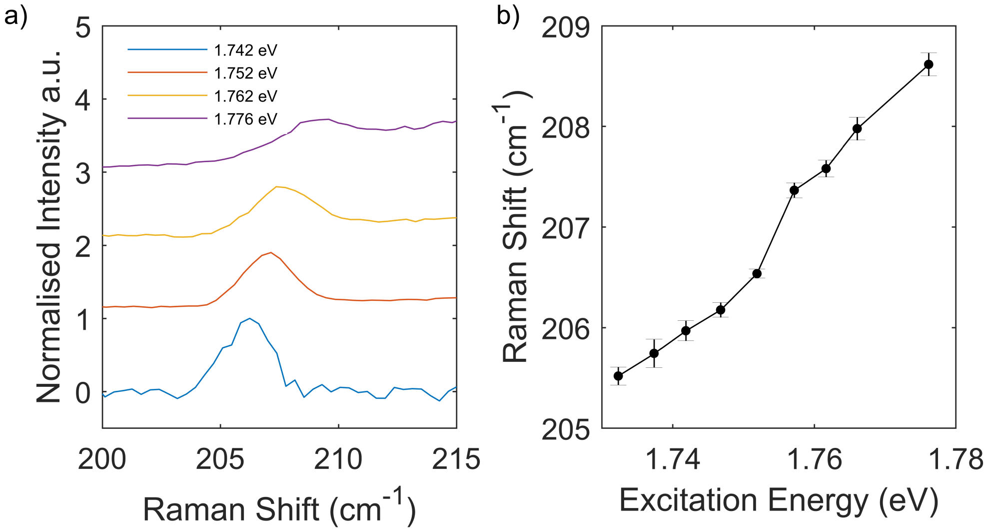

Figure 5.4: Panel a) Raman spectra showing dispersive Raman peak at $\sim$ 207 cm^{-1} for excitation energies of 1.742, 1.752, 1.762 and 1.776 eV when resonant with A exciton. Panel b) Fitted Raman shift for the dispersive peak as a function of excitation energy. Error bars shown are the standard deviation obtained from the fitting process.

5.3.1.2 Hexagonal Boron Nitride Modes

In addition to the Raman peaks associated with he WSe_2 monolayer, several higher frequency modes are observed at $\sim$ 800 cm^{-1} and 1000 cm^{-1} when probing the WSe_2 A* resonance, and are shown in Figure 5.5. These peaks are only observed near resonance with the WSe_2 A* state. The high frequency of these peaks suggests they are not typical WSe_2 modes as the highest frequency peaks on WSe_2 is at 494.6 cm^{-1}. These modes were previously reported by Jin et al. for an encapsulated monolayer of WSe_2 [198], who proposed that these peaks are due to coupling of hBN phonons to electronic states in the WSe_2 layer. These peaks were assigned to the hBN ZO phonon at $\sim$ 800 cm^{-1} and a combination mode arising from the ZO + A_1' phonons at $\sim$ 1060 cm^{-1} and so involve both hBN and WSe_2 phonons. Jin et al. also probed the resonance behaviour for these Raman peaks, which revealed a double resonance between the WSe_2 A exciton and a new electronic state accessible in WSe_2 due to the encapsulation in hBN. However, they were unable to determine the precise nature of this new electronic state. These results are also supported by a PLE study of encapsulated WSe_2 by Chow et al., which reported enhancements in the PL spectra due to coupling of surface phonons to electronic states in the WSe_2 layer via coupling of the out of plane phonons in the two materials. In particular for a hBN/WSe_2/hBN structure they observed two Raman peaks at 99 and 131 meV (or 798 and 1056 cm^{-1}). Therefore, the Raman peaks observed in our spectra at 800 and 1060 cm^{-1} are in agreement with these reported in literature, and are due to hBN phonons.

To date reports of these hBN modes are unable to identify the electronic state involved in the resonance Raman process but associate it with the WSe_2 layer. Our data indicates that these modes are due to a double resonance between the A* and A excitons in WSe_2. Our results are in good agreement with Jin et al. and demonstrate that the A* is a electronic state in WSe_2 due to the observed resonance enhancement of the WSe_2 Raman peaks [198]. As such these modes are discussed in relation to the A* state. However a complete set of resonance Raman data for these hBN related Raman modes is not presented here and is proposed as an area of future study. In particular the line shapes of these modes show significant asymmetry which has yet to be addressed and requires further investigation.

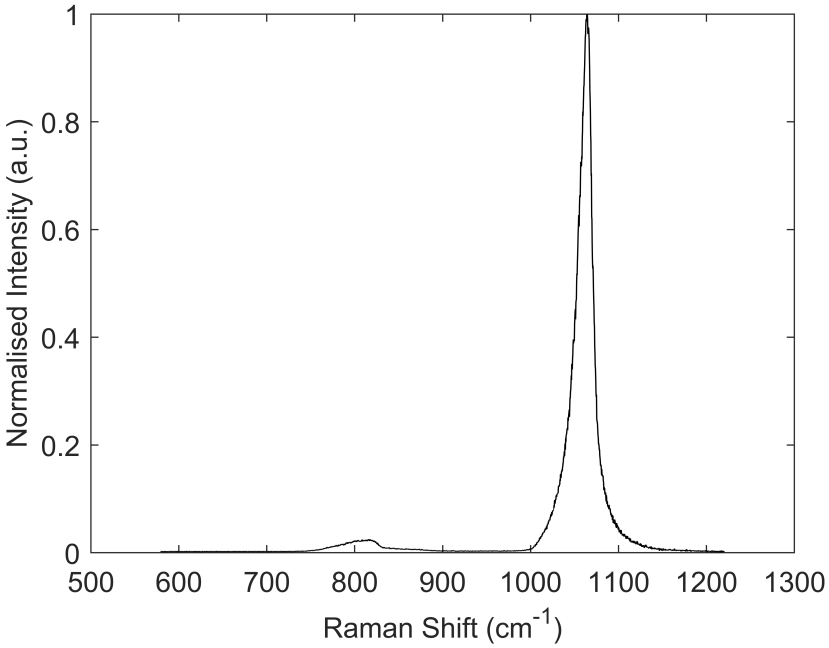

Figure 5.5: Raman spectra on monolayer WSe$_2$ when resonant with the WSe$_2$ A* using an excitation energy of 1.876 eV. Two peaks are observed near 800 and 1060 cm^{-1} and attributed to hBN phonons.

5.3.2 Resonance Raman Spectroscopy of WSe_2

In this section the resonance Raman data for on monolayer WSe_2 is presented for excitation energies in the range of 1.6 to 2.25 eV. In total three different resonances are observed at ∼1.74, 1.87 and 2.16 eV and are attributed to the A, A* and B excitonic states. The origins of the A* resonance at 1.87 eV is not immediately clear as it has not been previously reported in resonance Raman measurements but is most likely an excited state of the A exciton. The resonance Raman data will be presented and a qualitative comparison provided of the three different resonances. This is followed by three separate sections presenting a quantitative analysis of the resonance profiles for the A, A* and B excitons.

The Raman data for all three WSe_2 resonance is presented in the colourmaps and waterfall plots shown in Figures 5.6 & 5.7 and provides an overview of the resonance Raman data at the A, A* and B resonances respectively. Resonance Raman data was obtained between the A* and B resonances in the range of 1.96 to 2.1 eV, however no additional resonances were observed and so this data is not shown. There are clear differences in the resonance behaviour for the A, A* and B excitons as seen in Figure 5.6. In particular for the A and A* resonances each Raman peak shows similar resonance behaviour with enhancement at two different energies. This is visible when comparing the 249.5 cm^{-1} peak at the A exciton with two peaks at ∼ 1.747 and 1.776 eV and at the A* resonance with two peaks visible between 1.867 and 1.897 eV. The separation of these two resonant peaks are 29 and 30 meV at the A and A* respectively. These separations are in agreement with the energy of the 249.5 cm^{-1} Raman peak (31 meV) and indicates these two peaks are due to incoming and outgoing resonances. Further evidence supporting the observation of both the incoming and outgoing resonances can be seen by comparing the 249.5 cm^{-1} peaks to the higher frequency Raman peaks. For the higher frequency Raman peaks the separation of the peaks in their resonance behaviour is observed to increase as a function of Raman peak frequency. This behaviour is expected for an outgoing Raman resonance. In contrast for the WSe_2 B exciton resonances shown in Figure 5.6 panel c) the Raman peaks all have a single broad resonance. Comparing the resonances for the peaks near ∼ 260 cm^{-1} and those at ∼ 400 cm^{-1} there is no obvious evidence of outgoing resonance condition. This indicates a clear difference in resonance behaviour for the B exciton when compared to the A and A* with no clear separation of the incoming and outgoing resonances.

For each resonance exemplar Raman spectra as a function of excitation energy are shown in Figure 5.7. For the WSe_2 A and A* resonances it is useful to compare the relative intensities of the Raman peaks near ∼ 250 cm^{-1}. The relative intensities of the peaks appear to be constant for these peaks and indicates that they all have similar resonance behaviour. Therefore, the Raman resonances at the A and A* excitons are likely the result of a single narrow excitonic state. For the WSe_2 B resonance the spectra in

Figure 5.6 also appear to have relatively constant intensities between the Raman peaks. Although it is evident at higher excitation energies that the intensity of the 249.5 cm^{-1} peak relative to the peaks at $\sim$ 260 cm^{-1} is increasing. This suggests that the resonance behaviour at the B exciton is likely to involve multiple excitonic states. Overall it is clear that a more quantitative analysis of the resonance profiles is required and is presented for each resonance in the following sections.

5.3.2.1 Resonance Raman with the WSe_2 A exciton

This section presents a quantitative analysis of the resonance Raman behaviour when resonant with the WSe_2 A exciton. An initial comparison of the resonance data suggests that the Raman behaviour when resonant with the WSe_2 A exciton is due to a single excitonic state with clearly separated incoming and outgoing resonances. The energy of the incident resonance is at $\sim$ 1.747 eV is in agreement with the energy of the neutral A exciton observed in PL spectra at 1.742 ± 0.001 eV. To further investigate the resonance behaviour the resonance Raman profiles were extracted by fitting the spectra at each excitation energy to a summation of Lorentzian line shapes. This allowed resonance profiles to be obtained for the peaks at 207.0, 219.2, 249.5, 250.7, 257.7 and 261.9 cm^{-1}. However, it is not possible to obtain a complete resonance profile for the higher frequency peak at 398.6 cm^{-1} as this peak has a relatively low intensity and is difficult to resolve due to photoluminescence from the A exciton. To investigate the resonance Raman behaviour the profiles were fitted using a Raman model for a single phonon scattering event.

The resonance profile for the Raman peak at 249.5 cm^{-1} is considered first as it is the only peak which is unambiguously assigned to a single phonon process with either the $A'_1(\Gamma)$ or the $E'_{LO/TO}(\Gamma)$ phonons and so should be well described by our single phonon model. The resonance profile for this peak is presented in Figure 5.8 and features two clear peaks at $\sim$ 1.742 and 1.776 eV with similar intensities. The fitted profiles shown in Figure 5.8 are the result of fitting to three separate single phonon event models assuming a single electronic excitation, two independent electronic excitations and two electronic excitations with interstate scattering allowed. The resulting coefficients and adjusted r-square values obtained from fitting are provided in Table 5.4.

A visual comparison of the fitted profiles in Figure 5.8 shows that all of the fits are able to reproduce the two peaks attributed to the incoming and outgoing resonance conditions. However, the single state and two independent state fitted profiles shown in Figure 5.8 panels a) & b) do not provide the best fit. The energies from fitting to the different models are all in agreement with the higher energy state between 1.741 and 1.746 eV in agreement with the PL for the neutral A exciton. Therefore, the resonance Raman behaviour of the 249.5 cm^{-1} Raman peak is dominated by a resonance with the WSe_2 neutral A exciton. This is supported by the amplitude coefficients which show

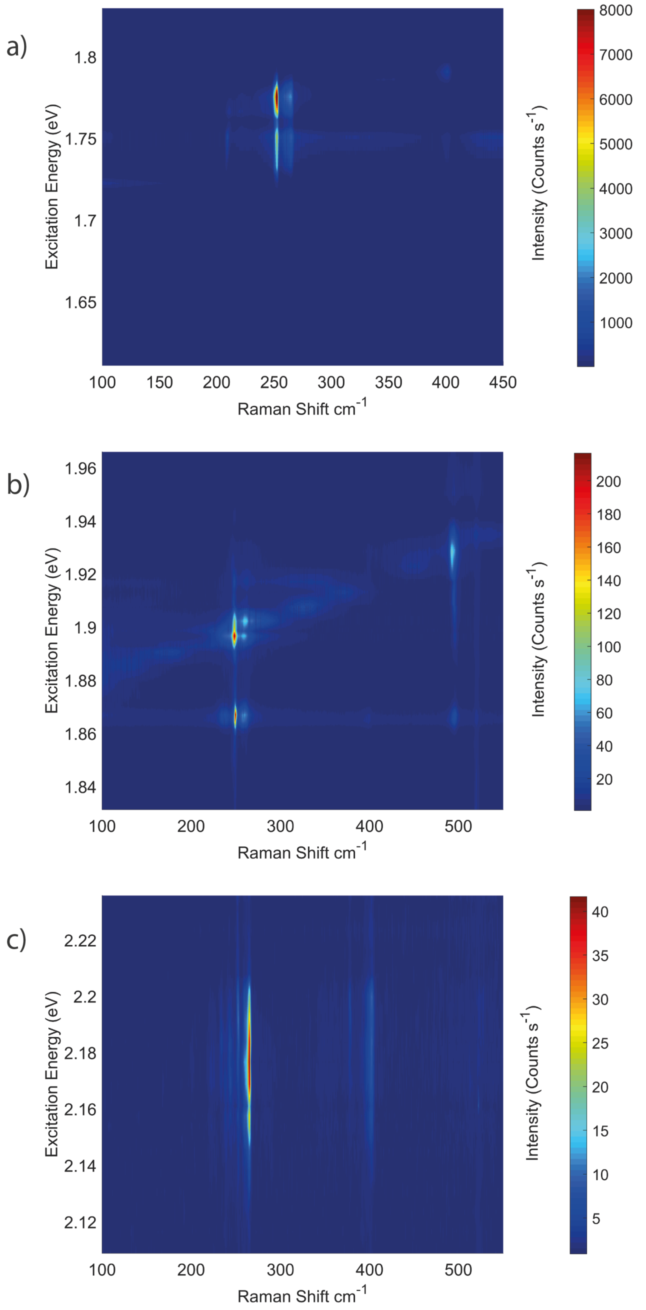

Figure 5.6: Colourmaps are presented showing the resonance Raman data obtained on monolayer WSe_2 when resonant with the WSe_2 A, A* and B excitonic states and are shown in panels a) ,b) and c) respectively.

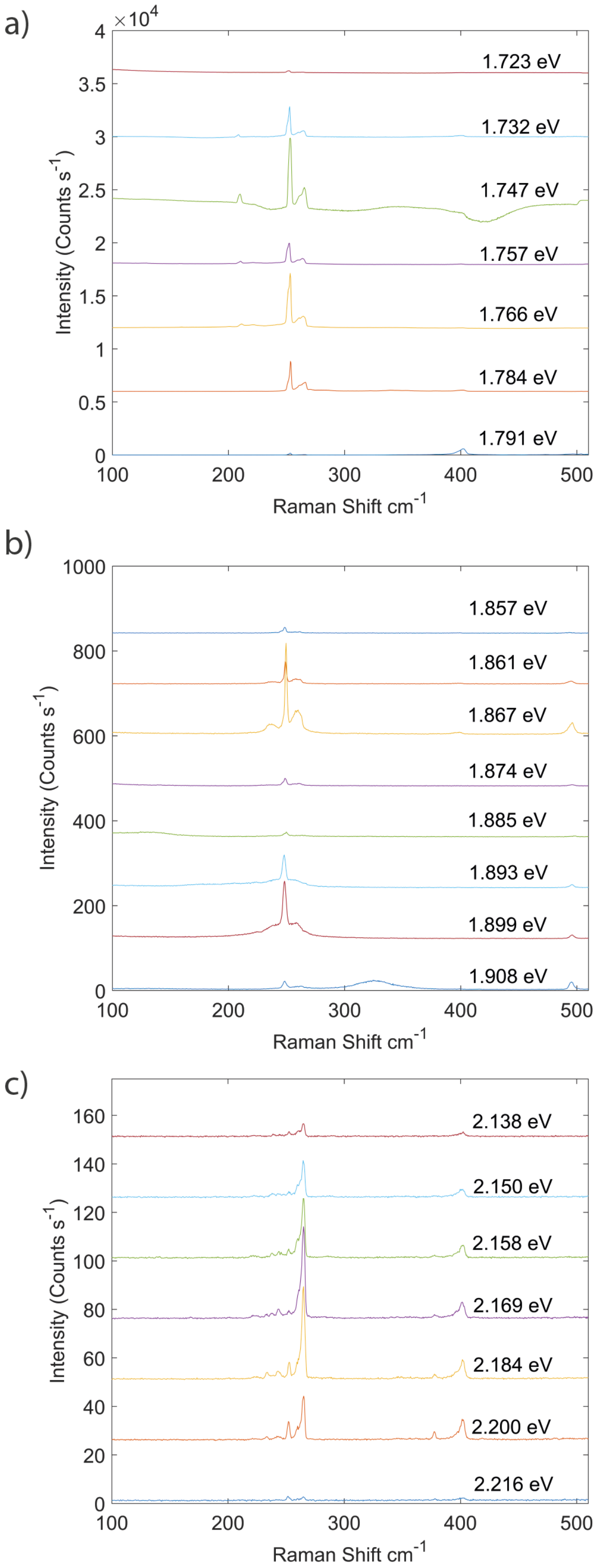

Figure 5.7: Waterfall plots are provided showing exemplar Raman spectra when resonant with the WSe$_2$ A, A* and B excitonic states in panels a,b and c respectively. In each case spectra have been offset to allow for easier visual comparison. For the WSe$_2$ A exciton data in panel a) the 1.747 eV spectra shows a large depression at 450 cm^{-1} this is an artefact of the background subtraction and is not real. Similar in panel b) at 1.908 eV there is some residual broadband luminescence peak appearing at $\sim$ 330 cm^{-1}.

Table 5.4: Coefficients and adjusted r-square values from fitting the 249.5 cm^{-1} peak resonance profile to single phonon event models assuming a single electronic state, two independent electronic states and two electronic states with interstate scattering allowed. The errors given for each coefficient are the standard deviation from fitting. The units for the amplitude coefficients are 10^{-3} $\sqrt{Counts\ s^{-1} \cdot eV^2}$.

		Single	Two	Two w/ scatter
Adjusted R Square		0.9362	0.844	0.979
	A_1	-	2.6±3.4	1.9±1.2
Amplitude	A_2	18.7±1.1	20.2±1.4	14.8±1.0
	A_3	-	-	4.9±0.8
Width (meV)	Γ_1	-	6.1±1.8	3.6±0.5
	Γ_2	4.3±0.5	5.3±0.5	4.1±0.4
Energies (eV)	E_1	-	1.715±0.008	1.709±0.002
	E_2	1.742±0.001	1.741±0.001	1.746±0.001

that the A_2 is significantly stronger than either the A_1 or A_3 coefficients, where A_2 is the amplitude component corresponding to scattering only with the E_2 state. The two state model with interstate scattering appears to give the best fit when considering the adjusted r-square values. The lower energy state predicted by this model is at 1.709 eV and is in agreement with the PL peak assigned to the negatively inter-valley trion. However, a careful inspection of the fitted profile for the two state model with interstate scattering in Figure 5.8 panel c) reveals a low energy peak at the incident energy of the E_1 state is predicted, but is not observed in the experimental data. Whilst the two state model with interstate scattering produces the best fitted profile in terms of visual appearance and adjusted r-square value, the asymmetry of the fit and predicted peak at the incident energy of trion state is not consistent with the experimental data. The same issues are also apparent in the fitted profiles using the two independent electronic states.

Due to the inconsistencies in the fitted profiles using two excitonic states it is useful to reconsider the model for a single underlying electronic excitation. For the 249.5 cm^{-1} resonance profile there are two peaks which are at energies consistent with the incoming and outgoing resonances and appear to have symmetric intensities. A symmetric resonance profile is the expected shape when resonant with a single electronic state as the amplitude coefficient is the same for both the incoming and outgoing resonance conditions. The lack of a lower energy peak at energies expected for the incident resonance with the trion in the data is also strong evidence that the amplitude coefficients for the trion and interstate scattering in the other fitted models were overestimated. However, the main issue with the fitted profile for the single state is a disagreement between the predicted and measured positions of the outgoing resonance. In the fitting process the energy of the phonon was fixed to 31 meV in agreement with the Raman shift of the peak at 249.5 cm^{-1}. However, by allowing the phonon energy to vary by 1-2 meV it is possible to obtain a significant improvement in the fitted profile. This change in the

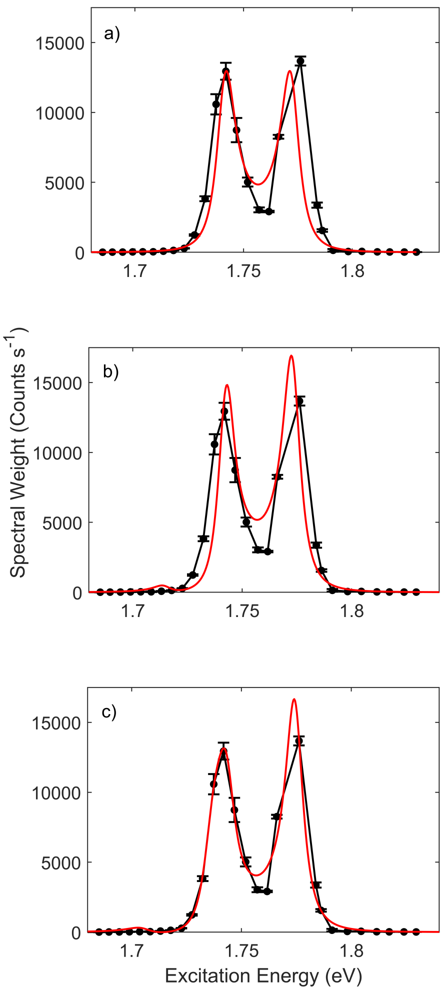

Figure 5.8: The resonance Raman profile for the 249.5 cm^{-1} is along with the resultant fits obtained from using a single phonon event model assuming a) single excitonic state, b) two independent states and c) two states with inter state scattering allowed. The errors bars shown are the standard deviation obtained from the fitting process for each spectra.

phonon energy would require a difference in the Raman peak shift of at least 25 cm^{-1}. Our measured Raman spectra are in agreement to literature values for the WSe$_2$ Raman peaks to within 1-2 cm^{-1} and so is not the cause of this difference in energy of the outgoing resonance. There are several possible experimental issues which may allow for the observed difference in the position of the incoming and outgoing resonances. The line width of the neutral A exciton from fitting the resonance profiles is between 4 to 6 meV and is in agreement with similar high quality monolayer samples [235]. A consequence of this narrow line width is that any change in the energy of the excitonic state due to sample inhomogeneity could result in a shift of several meV. As a result variations in the sample position could introduce a difference in the observed energy of the outgoing resonance. Furthermore, the data for the WSe_2 A exciton is the result of two separate experiments using our CR 599 and Mira 900 laser systems whilst overlapping spectra were in reasonable agreement the overlap between the two data sets occurs near the outgoing resonance. As a result, it is likely that the difference in separation of the incoming and outgoing resonances is due to variation our position on the sample leading to shifts in the energy of the excitonic state.

Overall the fitting of the 249.5 cm^{-1} peak resonance profile to multiple Raman scattering models reveals that the best fit is a single excitonic state model. The observed resonance is due to the neutral A exciton at 1.741 eV in agreement with PL spectra. Following this analysis the resonance profiles for the Raman peaks at 207.0, 219.2, 257.7 and 261.9 cm^{-1} were obtained and fitted to a single phonon model assuming a single electronic state. The resonance profiles and fits for the peaks at 219.2, 249.5, 257.7 and 261.9 cm^{-1} and are shown in Figure 5.9 along with the resonance profile for the dispersive peak at $\sim$ 207 cm^{-1} which is presented separately in Figure 5.10. The coefficients from fitting are presented in Table 5.5. For the peaks at 219.2, 257.7 and 261.9 cm^{-1} Figure 5.9 panels b,d & e) the resonance profiles are similar to the profile for the 249.5 cm^{-1} Raman peak with two peaks in the profiles between 1.725 to 1.75 eV and 1.76 to 1.79 eV. Overall the fits appear are in agreement with the resonance profiles for the Raman peaks at 257.7 and 261.9 cm^{-1}. For the 219 cm^{-1} peak the fitted model does not provide the best fit to the width of the incoming and outgoing resonances and appears to overestimate the amplitude of the resonance profile. However, in our Raman spectra at the WSe_2 A exciton this peak is relatively weak and is difficult to resolve this peak in all spectra as indicated by the large error bars for several data points. Considering the energies for these fitted resonance profiles the values are in agreement to within the fitted error and have a mean value of 1.742 ± 0.002 eV. This result is in excellent agreement with the energy of the neutral A exciton which was determined to be 1.742 ± 0.001 eV from the PL spectra. Therefore, the resonance profiles for the peaks at 219.2, 249.5, 257.7 and 261.9 cm^{-1} can all be explained due to resonance with the neutral A exciton at 1.742 eV.

Table 5.5: Coefficients obtained from fitting the Raman resonance profiles for the Raman peaks observe when resonant with the WSe_2 A exciton to a single phonon event model assuming a single underlying electronic state. The errors given for each coefficient are a standard deviation obtained from fitting. The units for the amplitude coefficients are $10^{-3}\ \sqrt{Counts\ s^{-1} \cdot eV^2}$.

Raman Shift (cm^{-1})	Amplitude	Width (meV)	Energy (eV)
207.0	9.5 ± 5.1	13.9 ± 6.4	1.733 ± 0.004
219.2	3.7 ± 0.3	3.6 ± 0.6	1.744 ± 0.001
249.5	18.7 ± 1.1	5.3 ± 0.5	1.741 ± 0.001
257.7	8.1 ± 0.4	5.2 ± 0.3	1.742 ± 0.001
261.9	11.1 ± 0.6	5.4 ± 0.3	1.742 ± 0.001

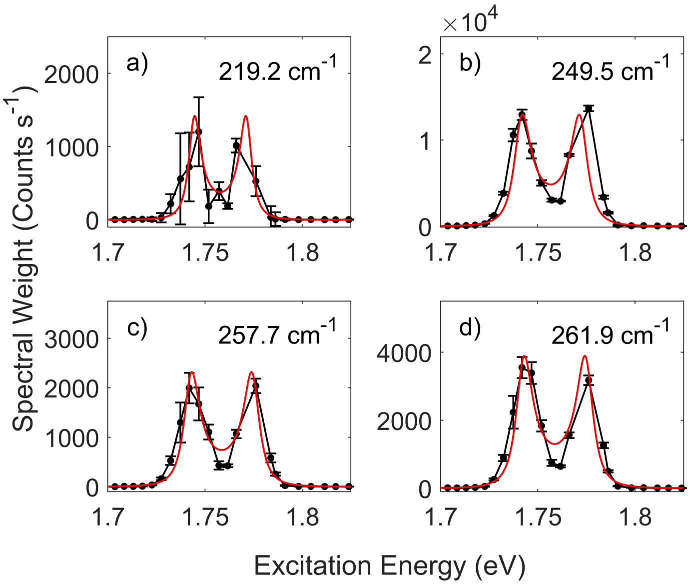

Figure 5.9: Resonance Raman profiles for the Raman peaks at 219.2, 249.5, 257.7 and 261.9 cm^{-1} observed on monolayer WSe$_2$ when resonant with the A exciton. In each case have been fitted to a single phonon event model assuming a single underlying electronic state.

The resonance profile for the 207 cm^{-1} dispersive Raman peak is presented in Figure 5.10 and a fit was attempted using a single phonon event model assuming a single electronic excitation. The resonance profile for this peak shows a distinct behaviour when compared to the other resonance profiles in Figure 5.9. In this case the resonance is dominated by a single peak appearing at $\sim$ 1.742 eV and with a possible higher energy shoulder/asymmetry at $\sim$ 1.77 eV. Therefore, it is clear that a single phonon event model assuming a single electronic state can not describe the observed resonance behaviour. This is not surprising as this dispersive Raman peak is either likely a defect mediated single phonon or two phonon combination mode. The dispersive nature of the peak indicates that the wavevector of the involved phonon is changing as a function of excitation energy. This indicates that the Raman peak is resonant with additional large wavevector electronic states and that there are a continuum of electronic states available allowing for the dispersion of the Raman peak. Fitting this resonance profile is non-trivial requiring additional intermediate excitonic states and should include a summation over all the phonon branches contribution to the peak. The additional complexity of this model has prevented further analysis at present as a more rigorous theoretical consideration is required. However, the presence of this dispersive Raman peak in the WSe$_2$ spectra at the A exciton, which is not observed for either the A* or B resonance, indicates there are additional large wavevector electronic states at the WSe$_2$ A exciton satisfying the resonance conditions for this dispersive Raman peak.

Overall analysis of the resonance profiles obtained between 1.6 to 1.825 eV reveals that

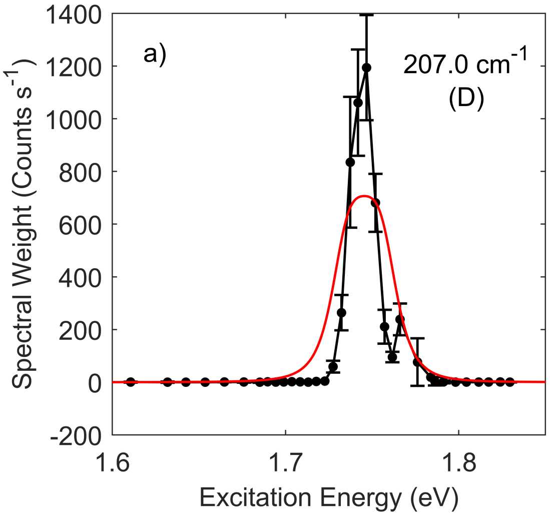

Figure 5.10: The Resonance Raman profile for the dispersive Raman peak at 207.0 cm^{-1} is presented. To illustrate the differences between this resonance and the other Raman peaks at the WSe_2 A exciton the profiles has been fitted to a single phonon event model assuming a single underlying electronic state.

the resonance is dominated by the neutral A exciton with an energy of 1.742 ± 0.001 eV. The two peaks observed in the majority of the resonance profiles are the result of incident and outgoing resonances which are clearly resolved due to the narrow width of the A excitonic transition ($\sim$ 5 meV). There is also no resonance observed with either the intra or inter-valley trions or any other lower energy states. Although the lower energy states assigned to the negatively charged trions are observed in PL spectra, these measurements are an indicator of the population of the state and not the oscillator strength. As a result the lower energy states can be populated by the relaxation of excited A excitons to these states by non-radiative processes and so are visible in PL measurements but not in resonance Raman. In addition a dispersive Raman peak is observed which shows only a strong resonance near the incident energy. The dispersive nature of this peak is evidence for the scattering to large wavevector dark states.

5.3.2.2 Resonance Raman with the WSe_2 A*

An unexpected resonance is observed between 1.85 and 1.95 eV and is labelled as the A* state. This resonance has not been reported in previous resonance Raman studies of monolayer WSe_2. As seen in Figure 5.6 there is a striking similarity between the behaviour of both the A and A* states, with each showing two resonant peaks associated with the incoming and outgoing resonance conditions. From the initial PL spectra (see Figure 5.1) there were no obvious PL peaks at energies above the neutral A exciton at 1.742 eV. However, upon discovery of this additional resonance a PL spectra was obtained using an excitation energy of 1.968 eV and is shown in Figure 5.11. In this case a higher energy PL peak is clearly visible in the spectrum at $\sim$ 1.87 eV and is in agreement with the A* resonance observed in the Raman measurements. Comparing the Raman spectra for the A* state to the spectra observed at the A exciton, the spectra have a similar the number of peaks and relative peak intensities. Although, there are clear differences including a broader peak observed at 234.5 cm^{-1} and a new peak exclusive to the A* resonance at 494.6 cm^{-1}, which has a different resonance behaviour compared to the other Raman peaks.

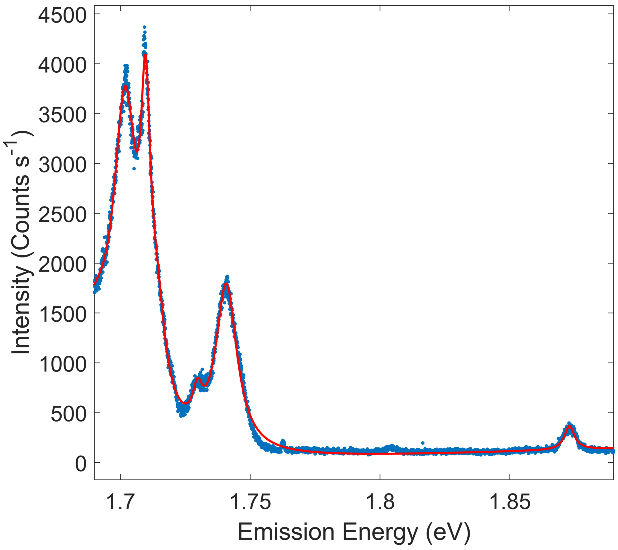

Figure 5.11: PL spectrum on WSe_2 region using 630 nm excitation wavelength. An additional feature is observed at 1.873 eV and attributed to the A* state.

The resonance profiles for the A* state were obtained for the peaks at 234.5, 249.5, 257.7, and 261.9 cm^{-1} and fitted to a single phonon model assuming a single electronic state. The resonance profiles and fits are shown in Figure 5.12 with the coefficients from fitting provided in Table 5.6. The resonance profiles for the Raman peaks at 236.1, 249.0, 257.4 and 261.6 cm^{-1} all have a similar appearance with two peaks in the profile between 1.86 to 1.87 eV and 1.89 to 1.9 eV. The separation of these peaks is in agreement with the phonon energies of the Raman peaks. Therefore, the two peaks in each resonance profile are due to incoming and outgoing resonances. This is obvious in Figure 5.6 when comparing the peaks near $\sim$ 250 cm^{-1} to the 494.6 cm^{-1} peak whose higher energy resonance peak is shifted by 30 meV as expected for an outgoing resonance. Visually there is some asymmetry between the incoming and outgoing peaks in the resonance profiles. However, we attribute this to the narrow line width of the A* resonance profile of $\sim$ 3 meV, which is approaching the step size between data points of $\sim$ 2.79 meV. As a result the asymmetry is likely due to the width of the resonance approaching the resolution of our resonance Raman measurements. The energies and widths from the fitted coefficients are in agreement for the peaks at 234.5, 249.5, 257.7 and 261.9 cm^{-1} with a width in the range of 2.1 to 3.3 meV and with an energy between 1.865 to 1.867 eV. Therefore the resonance profiles for the peaks at 234.5, 249.5, 257.7, and 261.9 cm^{-1} are the result of a single electronic state at 1.866 eV with a line width of 2.5 meV.

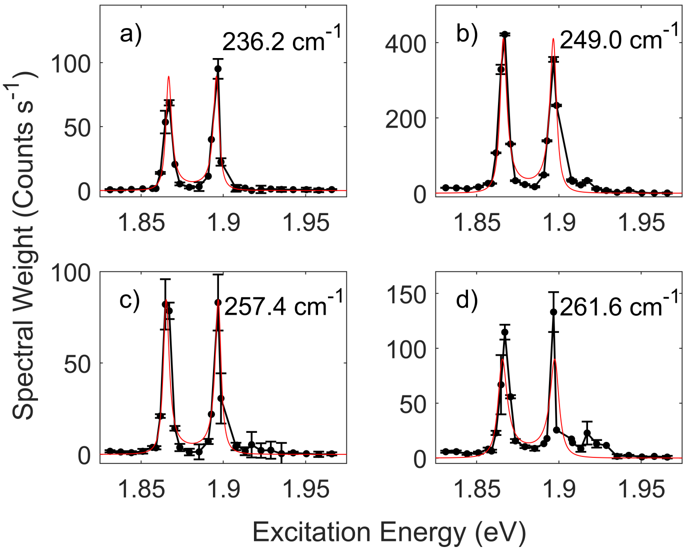

Figure 5.12: Resonance Raman profiles when resonant with the A* state on monolayer WSe_2 are presented. In each case the profiles were fitted to a single phonon event model assuming a single underlying electronic state.

Table 5.6: Coefficients from fitting the resonance profiles for the Raman peaks at 234.5, 249.5, 257.7 and 261.9 cm^{-1} using a single phonon event model assuming a single underlying electronic state. The errors for each coefficient are the standard deviation from fitting. The units for the amplitude coefficients are $10^{-3}\ \sqrt{Counts\ s^{-1} \cdot eV^2}$.

Raman Shift (cm^{-1})	Amplitude	Width (meV)	Energy (eV)
234.5	0.6 ±0.1	2.1 ±0.2	1.867 ±0.001
249.5	1.5 ±0.1	2.4 ±0.2	1.866 ±0.001
257.7	0.6 ±0.1	2.2 ±0.3	1.865 ±0.001
261.9	1.0 ±0.2	3.3 ±0.7	1.865 ±0.001

The resonance Raman profile for the 494.6 cm^{-1} peak are presented in Figure 5.13 with panel a) showing the resonance profile as a function of excitation energy and panel b) showing the resonance profile as a function of the energy difference relative to the A* state at 1.866 eV. From Figure 5.13 the resonance profile for this peak is asymmetric with the outgoing resonance at 61.4 meV is significantly stronger than the incident resonance at 1.866 eV and also has a low energy shoulder at $\sim$ 1.9 eV. The asymmetry of the resonance profile requires the presence of multiple electronic states to be explained by our Raman models. Fitting the 494.6 cm^{-1} was attempted using both two state models for two independent electronic states and two electronic states with interstate scattering allowed. However, the two independent state fit did not converge and so is not shown. The two state fit with interstate scattering allowed is able to fit to the data and is shown in Figure 5.13 panel a) and the fitted coefficients are provided in Table 5.7. Although the fit overestimates the intensity of the outgoing resonance peak this is likely due to the resolution of the resonance Raman measurements. The resulting fit requires a lower energy state E$_1$ which is in agreement with the other fitted resonance profiles with an energy for the A* state of 1.866 eV. The line width of the A* state at 1.866 eV is also in agreement with the fitted values in Table 5.6. This model predicts an additional electronic state with an energy of 1.904 eV and a line width a factor of 2 greater than the A* state. Therefore, the 494 cm^{-1} peak couples to both the A* at 1.866 eV and an additional higher energy excitonic state at 1.904 eV.

Table 5.7: Coefficients from fitting the resonance profile for the 494.6 cm^{-1} Raman peak to a single phonon event model assuming two underlying electronic states with interstate scattering allowed. The errors given for each coefficient are the standard deviation from fitting. The units for the amplitude coefficients are $10^{-3}\ \sqrt{Counts\ s^{-1} \cdot eV^2}$.

Amplitude	A$_1$	1.3±0.2
	A$_2$	1.7±0.4
	A$_3$	0.9±0.1
Width (meV)	Γ_1	3.4±0.5
	Γ_2	7.0±2.8
Energy (eV)	E$_1$	1.866±0.001
	E$_2$	1.904±0.002

From the mode assignment in Section 5.3.1 the peak at 494.6 cm^{-1} must be a multiphonon combination mode. The single phonon event model used in fitting the resonance profiles maybe valid for multiphonon Raman peaks if the phonon events occur simultaneously. Whereas, a sequential scattering process results in additional matrix elements and resonance conditions with intermediate states for each scattering event. To explore this further, fits were attempted using a two phonon event model with a single underlying electronic state. However, the fitting process was unable to account for the asymmetry or the lower energy shoulder in the resonance data for the 494.6 cm^{-1} peak and did not produce good fits to the data. Therefore it is clear that multiple excitonic states are required to explain the behaviour of the 494.6 cm^{-1} peak. A complete two phonon model assuming two electronic states was considered, however the number of coefficients required by this model is close to the number of data points and so does not produce

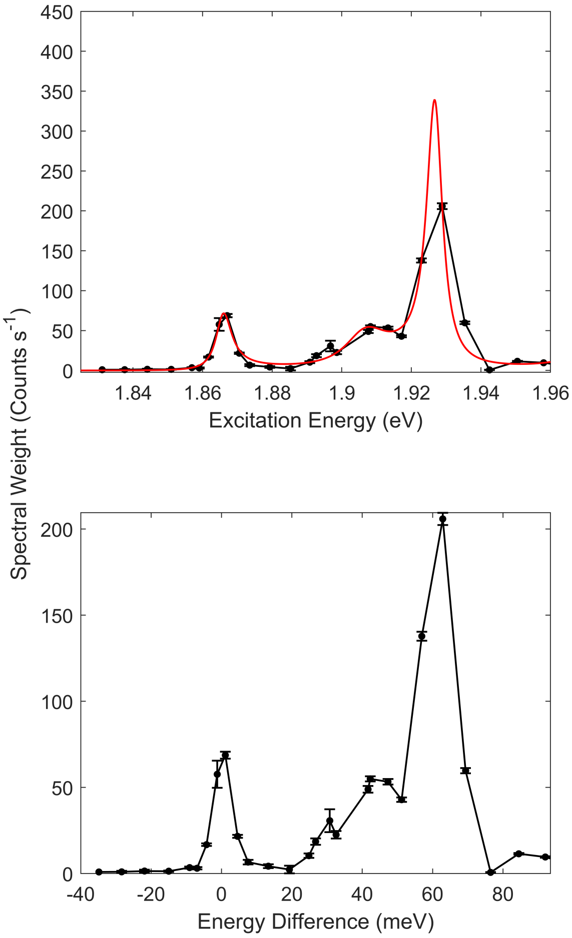

Figure 5.13: The resonance Raman profile for the peak at 494.6 cm^{-1} when resonant with the A* state on monolayer WSe$_2$ is presented in panel a). Panel b) presents the resonance profile but with the x axis showing the difference in energy relative to the A* state at 1.866 eV.

reliable fits to the data. As a result it seems reasonable to accept the results of fitting to a single phonon event model assuming two underlying electronic states. Although, this model is likely only an approximation of the resonance behaviour which is more complex, requiring a two phonon model with multiple excitonic states. Therefore the resonance behaviour for the WSe$_2$ Raman peaks at the A* resonance reveals the presence of two electronic states at energies of 1.866 and 1.904 eV. The potential origin of both the A* and this additional higher energy state are discussed further in Section 5.4.

5.3.2.3 Resonance Raman at WSe_2 B Exciton

The WSe_2 B exciton was observed in our resonance Raman measurements with a clear enhancement between 2.12 and 2.22 eV as seen in Figure 5.6. The resonance is centred at ~ 2.16 eV and has a separation relative to the neutral A exciton at 1.741 eV of 418 meV. This is in agreement with reflectance contrast, upconversion PL and PLE measurements of monolayer WSe_2 [132, 251, 268] and confirms this resonance is due to the WSe_2 B exciton. As discussed during the mode assignment the Raman spectra at the B exciton shows significant differences when compared to the A and A* resonant spectra with both the observation of additional Raman peaks and changes in the relative peak intensity. The resonance behaviour at the B exciton also appears different when compared to the A and A* with the resonance appearing significantly broader with no clear separation of the incoming and outgoing resonances.

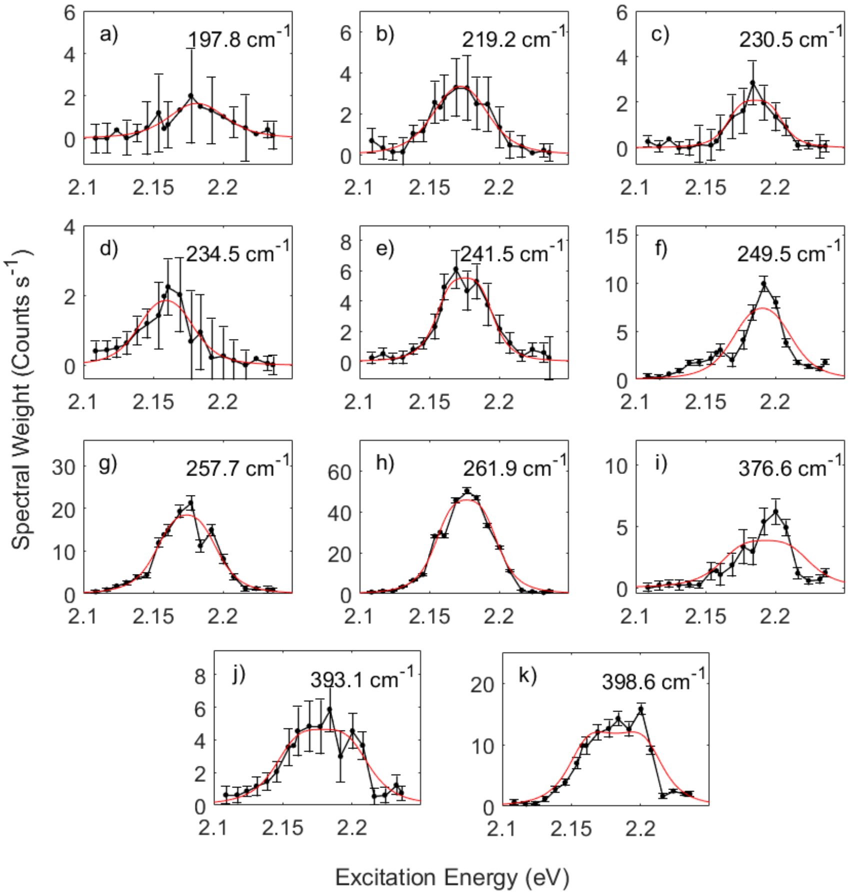

Figure 5.14: Resonance profiles when resonant with the WSe_2 B exciton are presented. All profiles were fitted to a single phonon event model assuming a single underlying electronic state. The error bars given are the standard deviation from fitting the Raman spectra.

In total the resonance profiles for 11 different Raman peaks were obtained when resonant with the WSe_2 B exciton. Whilst additional Raman peaks were identified in the mode assignment section these peaks are weak and it is not possible to extract useful resonance profiles. To quantify the resonance behaviour each profile was fitted using a single phonon event model assuming a single underlying electronic state. The resonance profiles and are presented in Figure 5.14 and the coefficients from fitting are provided in Table 5.8. The majority of the resonance profiles in Figure 5.14 are well described by a single broad resonance with no significant asymmetry. There are several exceptions to this with the peaks at 249.5 and 376.6 cm^{-1} demonstrating asymmetric resonance profiles with a low energy tail. For the peaks at 197.8, 219.2, 230.5, 241.5, 257.7 and 261.9 cm^{-1} the fitted profiles are in agreement with the experimental data. Therefore, the resonance behaviour of these peaks can be explained by a resonance with a single excitonic state. However, the profiles for the peaks at 249.5, 376.6, 393.1 and 398.6 cm^{-1} are asymmetric and so a single phonon model with a single electronic state is unable to produce the best fit to the data. This indicates the presence of additional electronic states at the B exciton.

In order to further investigate the presence of multiple electronic states at the WSe_2 B exciton, the Raman peak at 249.5 cm^{-1} was fitted to single phonon event models for two independent electronic states and two electronic states with interstate scattering allowed. The resultant fits are presented in Figure 5.15 and the adjusted r-square values and coefficients from fitting are provided in Table 5.9. A visual comparison of the fitted resonance profiles shows a significant improvement between the fit and the Raman data for both models involving two electronic states. A comparison of the adjusted r-square

Table 5.8: Coefficients from fitting the resonance profiles for the Raman peaks at the WSe_2 B exciton. In each case the resonance profiles were fitted to a single phonon event model assuming a single underlying electronic state. The errors for the coefficients are the standard deviation from fitting. The units for the amplitude coefficients are $10^{-3}\ \sqrt{Counts\ s^{-1} \cdot eV^2}$.

Raman Shift (cm^{-1})	Amplitude	Width (meV)	Energy (eV)
197.8	1.5 ± 0.4	31.5 ± 4.8	2.169 ± 0.002
219.2	1.7 ± 0.3	27.2 ± 2.9	2.159 ± 0.001
230.5	0.7 ± 0.2	15.9 ± 4.3	2.171 ± 0.002
234.5	1.2 ± 0.3	23.9 ± 5.1	2.144 ± 0.002
241.5	1.2 ± 0.2	16.6 ± 2.7	2.160 ± 0.001
249.5	2.3 ± 0.8	24.6 ± 6.4	2.175 ± 0.002
257.7	3.2 ± 0.7	22.1 ± 3.9	2.158 ± 0.001
261.9	4.3 ± 0.7	19.1 ± 2.6	2.160 ± 0.001
376.6	2.4 ± 1.5	25.9 ± 14.1	2.169 ± 0.004
393.1	2.7 ± 0.8	25.5 ± 6.5	2.154 ± 0.002
398.6	3.8 ± 0.9	21.9 ± 4.8	2.157 ± 0.002

values suggests that the best fit is to two electronic states with interstate scattering. The coefficients from fitting demonstrate that the 249.5 cm^{-1} peak is resonant with two electronic states at 2.139 and 2.165 eV with a separation of 26 meV. This indicates that the asymmetry observed for the 249.5 cm^{-1} peak can be well described by a single phonon event model assuming two electronic states with interstate scattering allowed. The obtained amplitudes indicate that the two dominant scattering channels are for the higher energy state (A_2) and for interstate scattering (A_3). The two state model with interstate scattering was also applied to the Raman peak at 376.6 cm^{-1}. The fitted profile is shown in Figure 5.16 and the coefficients from fitting are provided in Table 5.10. The energies from fitting are 2.133 and 2.159 eV. Comparing the results for both the 249.5 and 376.6 cm^{-1} the lower energy states are in agreement to within the errors determined from fitting. The higher energy states are similar but not in agreement to within the errors. Therefore the asymmetry of the 249.5 and 376.6 cm^{-1} is due to resonance with electronic states between 2.133 and 2.139 eV and 2.159 to 2.165 eV.

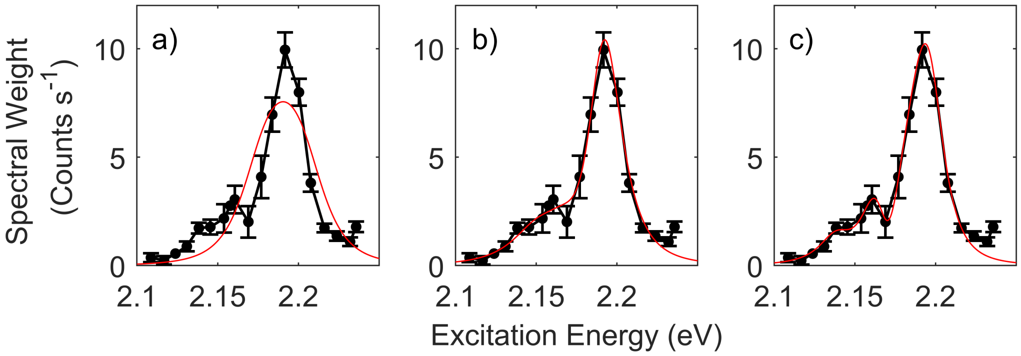

Figure 5.15: Resonance Raman profile for the 249.5 cm^{-1} peak is presented and is fitted to single phonon event model assuming a) a single electronic state b) two independent electronic states and c) two electronic states with interstate scattering allowed.

Table 5.9: Coefficients and adjusted R-square values from fitting the 249.5 cm^{-1} Raman peak to three single phonon event model assuming a single electronic state, two independent electronic states and two electronic states with interstate scattering allowed. The errors for each coefficient are the standard deviation from fitting. The units for the amplitude coefficients are 10^{-3} $\sqrt{Counts\ s^{-1} \cdot eV^2}$.

		Single State	Two State	Two State scatter
Adjusted R-Square		0.779	0.972	0.985
	A_1	2.3±0.8	5.5±3.8	0.8±0.4
Amplitude	A_2	-	3.8±4.9	3.9±1.7
	A_3	-	-	2.1±1.6
Width (meV)	Γ_1	24.2±6.2	24.5±12.4	15.6±6.1
	Γ_2	-	14.9±4.5	15.0±2.2
Energy (eV)	E_1	2.175±0.002	2.153±0.007	2.139±0.003
	E_2	-	2.160±0.004	2.165±0.001

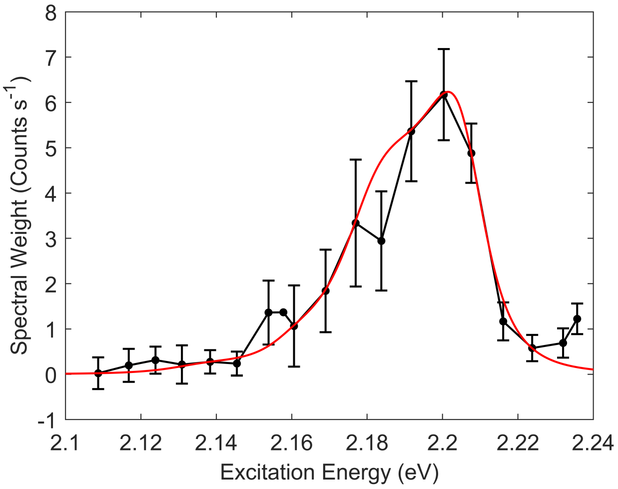

Figure 5.16: Resonance Raman profile for the 376.6 cm^{-1} is presented and is fitted to a single phonon event model assuming two underlying electronic states with interstate scattering allowed.

Table 5.10: Coefficients from fitting the resonance Raman profile for the 376.6 cm^{-1} peak to a two state model with interstate scattering between the states allowed. The errors for each coefficient are the standard deviation from fitting. The units for the amplitude coefficients are $10^{-3}\ \sqrt{Counts\ s^{-1} \cdot eV^2}$.

	Amplitude		Width (meV)		Energy (eV)	
A_1	A_2	A_3	Γ_1	Γ_2	E$_1$	E$_2$
1.0±0.4	2.1±0.4	1.3±0.4	11.9±4.0	9.9±1.8	2.133±0.004	2.159±0.001

Having determined that there are two possible excitonic states contributing to the WSe$_2$ B exciton resonance it is useful to revisit the result of fitting to a single state. The single state fits were able to well describe the data for the Raman peaks at 197.8, 219.2, 230.5, 234.5, 241.5, 257.7 and 261.9 cm^{-1} and may suggest that these phonons preferentially couple to only one of the excitonic states. In particular the peaks at 230.5 and 234.5 cm^{-1} are resonant at 2.171 and 2.144 eV with a separation of 27 meV. The resonance profiles for these peaks are shown in Figure 5.17 panel b) with the two peaks clearly resonant at different energies. Therefore, the Raman peaks at 230.5 and 234.5 cm^{-1} are observed to couple to different excitonic states. The energies of these resonance are also close to those obtained for the 249.5 and 376.6 cm^{-1} profiles and provide further evidence of two excitonic states at the WSe$_2$ B exciton. Considering the other resonance profiles it is also possible that the peaks involve contributions from two excitonic states. The obtained widths from fitting provide evidence supporting this assertion that the other resonances involve contributions from multiple electronic states. The widths from fitting using the two state models to the 249.5 and 376.6 cm^{-1} are between 10 to 15 meV, whereas the single state fitted profiles are significantly broader with widths ranging from 16 to 32 meV. As a result it is possible that the broader single state resonance profiles are due to the presence of multiple electronic states.

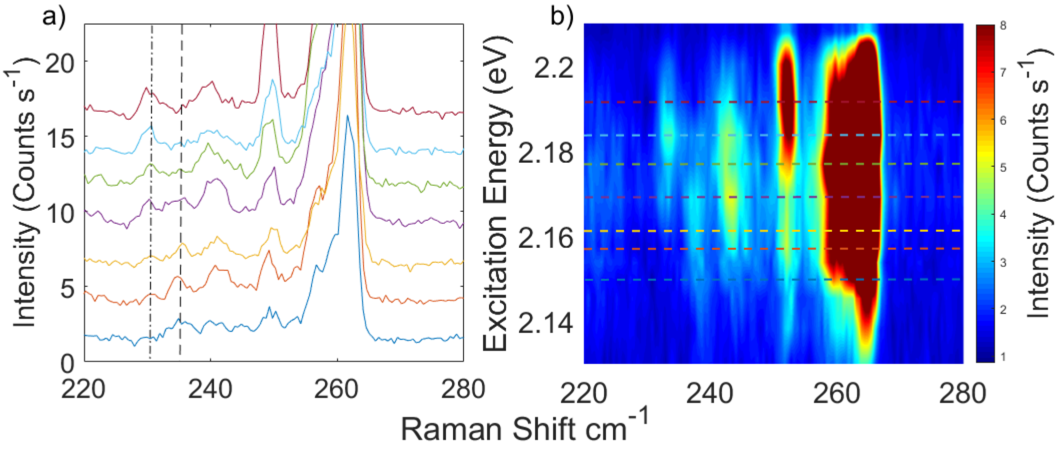

Figure 5.17: a) Raman spectra when resonant with the WSe$_2$ B exciton in the frequency range of 200 to 280 cm^{-1} . Panel b) shows a colourmap of all the resonance data in this frequency range. The dashed and dotted lines superimposed on the colourmap correspond to the energies of the Raman spectra shown in panel a).

Overall analysis of the resonance Raman behaviour for the WSe$_2$ B exciton has revealed the presence of two excitonic states contributing to the resonance behaviour. Fitting of the 249.5 and 376.6 cm^{-1} peaks indicate the energies of these states is between 2.133 to 2.139 and 2.159 to 2.165 eV with a separation of $\sim$ 26 meV. In addition the resonance profiles for the Raman peaks at 230.5 and 234.5 cm^{-1} are clearly resonant at different energies of 2.171 and 2.144 eV. Although the energy of these two resonances is $\sim$ 4 to 5 meV greater than those determined from the two state fits the separation and in all cases appears to be relatively constant between 26 to 27 meV. The line widths suggest that the other resonance profiles that were well fitted by the single state model might also involve two excitonic states. The observation of the peaks at 230.5 and 234.5 cm^{-1} coupling only to a single excitonic states suggests that these states couple selectively to different phonons. A discussion of the origins of these two excitonic states at the WSe$_2$ B exciton will be presented in the following sections.

5.4 Discussion

The nature of the excitonic states involved particularly at the A* and B excitons has yet to be discussed and will be presented in the following sections. However, before proceeding with a discussion of the particular excitons it is useful to compare the resonance profiles. The intensity of the our spectra indicate that the A exciton resonance is an order of magnitude more intense than the A* state and three orders of magnitude stronger than the B exciton. A comparison of the intensities of the A and B excitons in monolayer WSe$_2$ has not been previously reported. Although Del Corro et al. probed the B and C excitons and proposed that the strength of the A and B excitons was negligible and indicate a significantly different electron-phonon interaction when compared to other TMDC monolayers [193]. Whilst our results are unable to comment regarding the intensity the resonance enhancement of the A exciton is clearly significant and so suggests the resonance behaviour when comparing the A, B and C excitons is inline with those for other TMDC monolayers.

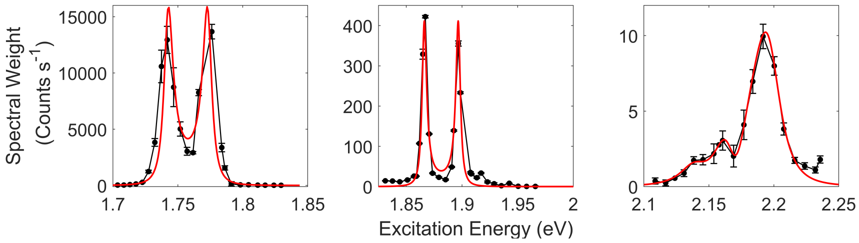

Figure 5.18: Resonance Raman profiles for 249.5 cm^{-1} Raman peak at the A, A* and B resonances along with the fitted resonance profiles.

5.4.1 Origin of A* Resonance

The resonance Raman data for monolayer WSe$_2$ has probed the A and B excitons and revealed an additional resonance at 1.866 eV, which is referred to as the A* state. The Raman spectra when resonant with the WSe$_2$ A and B excitons show clear differences in both the relative intensity and number of observed peaks. Comparing the Raman spectra for the A and B excitons to those when resonant with the WSe$_2$ A* state establishes a clear similarity between the A and A* Raman spectra. Although the Raman peak at 494.6 cm^{-1} is only observed when resonant with the WSe$_2$ A* state, whereas all other Raman peaks are seen at both the A and B excitons. The A* resonance profiles were analysed for the Raman peaks at 236.2, 249.0, 257.4 and 261.6 cm^{-1} and are all resonant with a single electronic state at 1.866 eV with a line width of $\sim$ 2.5 meV. The resonance behaviour of the 494.6 cm^{-1} peak is more complex showing a clear asymmetry between the incoming and outgoing resonance peaks and an additional shoulder in the resonance profile at $\sim$ 1.900 eV. The asymmetry of this profile can be explained by the presence of two electronic states at 1.866 and 1.904 eV. Therefore the resonance behaviour of the

A* state is due to at least two excitonic states at 1.866 and 1.904 eV and are labelled as the A* and A** states. In addition two Raman peaks were also observed near resonance with the A* state at $\sim$ 800 and 1050 cm^{-1} and are the result of combinations modes of WSe_2 and hBN phonons [198].

To compare our results to those published in literature the separations of the A* and A** states are determined to be 125 and 163 meV above the neutral A exciton at 1.741 eV. These states do not appear to be associated with the WSe_2 B exciton which is observed in our experiments at 2.16 eV. This is 419 meV above the A exciton. The similarity of the spectra to those observed at the WSe_2 A exciton and the separation of these states relative to the A indicates these are likely related to the WSe_2 A exciton. A possibility is that the A* and A** states are excited states of the A exciton. In monolayer TMDCs the large binding energy of the excitons also allows excited excitonic states, or Rydberg states to be observed in several TMDCs [80, 82, 269, 270, 271]. However, the observation of the Raman peaks at 800 and 1050 cm^{-1} associated with involving both WSe_2 and hBN phonons further complicates the assignment of these higher energy states as this may indicate that the A* and A** states are the result of the coupling between the hBN and WSe_2 layers.

For monolayer WSe_2 encapsulated in layers of hBN there are several reports of Raman peaks observed at 800 and 1050 cm^{-1} [198, 199, 190]. Investigation of these modes have shown that these peaks only arise for WSe_2 encapsulated between layers of hBN [199]. These peaks are proposed to arise due to the coupling of the out of plane ZO phonons in hBN to electronic states and phonons in the WSe_2 layer [198, 199]. The resonance Raman behaviour of these peaks indicate they are involved in a double resonance with the neutral WSe_2 A exciton and a higher energy state near 1.85 eV [198]. However, the nature of the electronic state involved has not been clearly established in literature and there is some confusion regarding the possibility that these hBN modes are the result of a composite exciton-phonon resonance or exciton-phonon replicas [272, 270]. Our results are in agreement with Jin et al. with the Raman peaks at 800 and 1050 cm^{-1} resonant with the outgoing resonance of the WSe_2 A exciton and with the A* state at 1.866 eV. Our observation of the resonance enhancement of the WSe_2 Raman peaks with the A* state at 1.866 eV indicates that this state is an excitonic state in the WSe_2 layer. The hBN related peaks are then the result of a double resonance between the incident resonance at the A* and the outgoing resonance of the A exciton. The A* state is clearly the result of an additional electronic state in the TMDC as indicated by its resonance with the TMDC Raman peaks showing the typical incoming and outgoing resonance behaviour expected for a single state resonance. There is some concern that the electronic state observed above the A exciton is only reported in encapsulated samples and may imply that the electronic state is only accessible in encapsulated samples. However, it is well established that the line width of transitions in encapsulated samples is significantly narrower [235]. As a result, if the higher energy state above the A exciton has a lower oscillator strength in lower quality samples with broader line widths this state unlikely to be observed.

There have been a number of reports in recent years of excited (Rydberg) states in encapsulated monolayers of WSe_2 using various optical spectroscopy techniques including reflectance contrast, PLE and upconversion PL [80, 132, 268, 82, 269, 271]. Recently magneto-luminescence measurements have observed up to the 4s excited state of the A exciton for an encapsulated monolayer of WSe_2 [272, 270]. The A* state identified from our resonance Raman measurements is 125 meV above the A exciton. This is consistent with the separation of the 1s and 2s exciton reported for monolayer WSe_2 with a separation of 130 meV reported reported by Stier et al. [272]. The observation of excited 3s and 4s states in WSe_2 samples may also explain the A** state observed at 1.904 eV. The 3s state has been reported with a separation relative to the A exciton of 157 meV [269], this is close to the separation of 163 meV for the A** state in our measurements. The difference between our observed separation of the A** state and the 3s state could be explained by the involvement of both the 3s and 4s state. The reported separation of the 3s and 4s excited states reported in literature are $\sim$ 10 meV. As a result it is possible that the higher energy of the A** state could be due to contributions from both the 3s and 4s excited states. The A** state is only observed in the 494.6 cm^{-1} peak resonance profile. The appearance of the A** for only the 494.6 cm^{-1} peak can be explained due to the energy of the outgoing resonance for the A* state coupling via interstate scattering to the A** state. Therefore, scattering between the A* and A** states is only observed when the energy of the outgoing resonance with the A* is above the energy of the A** state.

The interpretation that the A* and A** states are the result of resonance with excited states of the A exciton is compelling due to the agreement between our Raman resonances and the reported energies of the excited states in literature [272, 269, 270]. However, the widths of the excited states have been reported and shown to increase for the higher quantum number excited states [270]. From the resonance Raman results presented here the widths of the A exciton was determined to be $\sim$ 4.3 meV, and the width of the A* state is between 2.1 to 3.3 meV and the A** state width is 7.0 meV. For the A** the uncertainty in the width is significant with a standard deviation from fitting of 2.8 meV and so the width of this state is not well constrained. However, our results indicate that the A* state is narrower than the neutral A exciton in our resonance Raman measurements. This result contradicts the observed behaviour in magneto-luminescence measurements [270]. The expected increase in the line widths is proposed to result from the increase in the number of decay channels for the higher quantum number excited states. Therefore, if correct our results suggest that the number of decay channels is greater for the A exciton than the A* excited state. For these two states this maybe possible due to the potential for the ground state exciton to scatter to trion and lower energy states resulting in a larger number of decay channels than the 2s excited state[201]. However, when fitting the A exciton resonance an increased separation between the incident and outgoing resonance profiles was required. This was attributed to possible inhomogeneity in the sample or due to the use of two different laser sources for the resonance measurements. As a result it is possible that the observed width of the neutral A exciton is overestimated from these experiments or is evidence of more complicated behaviour at the neutral A exciton. Therefore, further measurements of other encapsulated monolayers of WSe_2 would be required to further investigate and clarify the line widths of the A, A* and A** states.

Overall the origins of the A* and A** states observed from our resonance Raman measurements of monolayer WSe_2 are in agreement with the energies of excited states of the A exciton. A report by Del Corro et al. of resonance Raman on monolayer WSe_2 proposed their results demonstrated resonance Raman enhancement with excited excitonic states [35], but in a later work concede that these proposed excited states were more likely the transitions associated with the C exciton [193]. As a result our observation of the A* and A** states is the first report of excited states in a TMDC monolayer using resonance Raman spectroscopy. These result indicate that the 2s state is likely coupled via the hBN phonons through a double resonance process to the neutral A exciton. This result provides clarity as to the behaviour of the hBN Raman peaks and is in agreement with Jin et al. The assignment of the A* is compatible with the double resonance process involving the hBN phonons. The lack of similar hBN related Raman peaks in other monolayer TMDCs is likely due to the lack of a suitable excitonic state above the A exciton to facilitate this double resonance.

5.4.2 Origin of multiple excitonic states at the B exciton resonance

Investigation of the WSe_2 B exciton has revealed a significant difference in the Raman spectra when compared to the A and A* excitons with additional Raman peaks and changes in the relative peak intensities. This may occur due to changes in the exciton-phonon coupling at the B exciton or due to the presence of large wavevector electronic states allowing for stronger large wavevector and multiphonon Raman scattering. Analysis of the resonance data has also revealed the presence of at least two excitonic states at the WSe_2 B exciton. The energies of these states were determined by fitting to both single and two state models. These two states have energies between 2.133 and 2.144 eV and 2.159 to 2.171 eV.

A possible assignment for the two states observed at the B exciton is to the B excitons and trions. The B trions are predicted to have binding energies of $\sim$ 23 meV [88]. However, the large line width of the B excitons reported experimentally makes separation of the contributions of the B exciton and trions difficult [253, 254]. The work of Wang et al. has demonstrated the presence of both neutral and charge excitons at the B exciton in both $MoSe_2$ and WSe_2 monolayers using gated reflectance contrast measurements [255]. Their results resolved both positively and negatively charged excitons with energies between 2.10 to 2.145 eV and 2.12 to 2.145 eV for the positively charged and negatively charged trions respectively with the neutral exciton between 2.145 to 2.170 eV. This suggests that the state observed between 2.159 to 2.171 eV in our experiments is the neutral B exciton and the lower energy state is either the positively or negatively charged trions. This provides a natural explanation for the two excitonic states observed in our measurements. An obvious area for future work would be to probe the resonance Raman response as a function of gate voltage in a monolayer WSe_2 sample. These measurements would allow confirmation of these assignments and allow the trion state to be identified as positively or negatively charged.

The resonance Raman spectra for monolayer WSe_2 reveals significant variations in the number of the Raman peaks and relative intensity of the peaks when comparing the A and B resonance spectra. Similar spectra were reported by Del Corro et al. for monolayer WSe_2 with the Raman spectra at the WSe_2 B exciton significantly different compared to those observed at the C exciton. This is in agreement with our spectra at the B exciton. The difference in appearance of the WSe_2 spectra when resonant with the B exciton may arise due to the nature of the underlying excitonic states and the exciton phonon coupling. At the WSe_2 A exciton the 249.5 cm^{-1} Raman peak arising from the $A'_1(\Gamma)$ or $E'(\Gamma)$ is the dominant Raman peak. Whereas, at the B exciton the most intense peak are those at 257.7 and 261.9 cm^{-1} peaks which are either large wavevector or two phonon combination modes. An increase in intensity is also observed for the Raman peak at 398.6 cm^{-1} which must be a multiphonon peak. The observation of several other peaks at 375.6 and 393.1 cm^{-1} must also be multiphonon combination modes. The increase in intensity of the multiphonon and large wavevector Raman peaks suggest the availability of large wavevector excitonic states.

The A and B excitons in monolayer TMDCs arise from the spin splitting of the valence band at the K point resulting in states VB$_1$ and VB$_2$ [75]. The B exciton consists of a hole in the lower energy valence band state VB$_2$. Electronic band structure calculations predict a maxima in the valence band at the Γ point, which is close to the energy of VB$_2$ [273]. This maxima at the Gamma point has been experimentally confirmed in ARPES measurements of monolayer WSe$_2$ [274]. As a result the Γ point maxima in the valence band provides large wavevector states which are accessible large wavevector phonons. The availability of large wavevector states can explain the resulting increase in the Raman intensity for the large wavevector and multiphonon Raman peaks. Although this does not provide an obvious explanation for the difference in coupling of the 230.5 and 234.5 cm^{-1} Raman peaks which are clearly resonant at different energies at the B exciton. Both peaks are assigned to either large wavevector or two phonon combination modes and so both involve large wavevector phonons. However, the multiple possible assignments to these Raman peaks make it difficult to propose a precise mechanism for their different resonance behaviour. The energies of these two peaks are similar and suggests the difference in coupling to the excitonic states is likely due to the phonon wavevectors or symmetries of the excitonic states. The possible phonon assignments of the 230.5 cm^{-1} peak is to either the E$'_{TO}(M)$ or TA(M)+LA(M) and the 234.5 cm^{-1} peak has an assignment to the 2ZA(M). As the assignment for both of these peaks involve M point phonons this may suggest that the difference in coupling of these peaks to the excitonic states is a result of the symmetry of these states. This is similar to the proposed symmetry dependent coupling for the in plane and out of plane phonons in monolayer MoS$_2$ [36]. A precise mechanism for difference in coupling of these Raman peaks is yet to be determined. However, these results offer significant insight into the behaviour of the B excitons in monolayer WSe$_2$ which have yet to be significantly probed. The potential preferential coupling of certain phonons to the different excitonic states is intriguing and could provide a sensitive probe of the different excitons at the B exciton. Although further investigation of this coupling would require gated resonance Raman measurements which would confirm the assignment of the states at the B exciton to the neutral exciton and trion.

5.5 Conclusions

In conclusion this chapter has presented the results of resonance Raman spectroscopy on monolayer of WSe_2, and reports a detailed study of the A and B excitons for the first time. The Raman spectra were observed when resonant and a detailed consideration of the phonon assignments presented. Similar to the results for monolayer $MoSe_2$ only the Raman peak at 249.5 cm^{-1} is assigned to a single phonon process with either the A_1' and E' phonons at the Γ point which are accidentally degenerate in monolayer WSe_2. The other Raman peaks observed are assigned to large wavevector single phonons or to multiphonon combination modes. In each case there are multiple possible assignments which are almost degenerate and so highlights that these peak assignments are not as well defined as presented in literature. The Raman spectra at the A, A* and B excitons were compared revealing several peaks that are observed at each resonance. An exception to this is the Raman peak observed at 494.6 cm^{-1} which is observed only when resonant with the A* state. Likewise, the Raman spectra at the B exciton are significantly different compared to the A and A* spectra with changes in the relative intensity of the Raman peaks and the observation of multiple new Raman peaks. The change in relative intensity indicates that Raman scattering with large wavevector phonons is significantly enhanced and is attributed to the availability of large wavevector states at the Γ point.

The resonance Raman behaviour was probed in detail for the A and B exciton and revealed an unexpected resonance at 1.866 eV, the A* resonance. The resonance behaviour of the A exciton revealed that the resonance profiles can be well described by a single phonon event model with a single electronic state at 1.741 eV and demonstrates a narrow line width of $\sim$ 5 meV. This state was assigned to the neutral A exciton and is in good agreement with PL spectra and values reported in literature. The A* state is observed 125 meV above the neutral A exciton and is attributed to the 2s excited state of the A exciton. In addition the Raman peak at 494.6 cm^{-1} which is observed exclusively at the A* resonance requires fitting to a two state model and reveals an additional state (A**) at 1.904 eV. This higher energy state is attributed to the 3s and 4s excited states which are observed only for the 494.6 cm^{-1} due to a double resonance between the A* and A** states. In addition the resonance with A* state also demonstrated the presence of hBN related phonons at 800 and 1050 cm^{-1}, which appear when resonant with the A* state and are double resonant with the neutral A exciton. The observation of resonance for both the WSe_2 Raman peaks and hBN peaks provides further clarification that the hBN modes arise due to a resonance with the excited A* state in WSe_2 and is strong evidence that the hBN related Raman peaks are not exciton-phonon replicas. The assignment of the A* and A** to excited states of the A exciton is the first report of excited excitonic states in monolayer TMDCs using resonance Raman spectroscopy. This presents the opportunity to probe the scattering of these excited states and may reveal useful information regarding their exciton-phonon coupling and scattering processes.

The resonance Raman behaviour of the B exciton has been probed in detail and reveals the presence of at least two excitonic states with separations of $\sim$ 26 meV. These two states were determined from fitting the 249.5 and 376.6 cm^{-1} Raman peaks to a two state model and from the resonances for the Raman peaks at 230.5 and 234.5 cm^{-1} which are clearly resonant with two different states. The energies of these state are between 2.133 to 2.144 and 2.159 to 2.171 eV and are assigned to a trion and neutral exciton respectively. However, it is not possible without further gated measurements to determine if the trion is positively or negatively charged. This is the first observation of both neutral and charged B excitons in monolayer WSe$_2$ using resonance Raman spectroscopy. The Raman peak at 230.5 and 234.5 cm^{-1} appear to show resonance only with the exciton and trion respectively. The underlying mechanism behind this coupling is not obvious given the similar energies of the peaks and both having possible assignments to large wavevector phonons. Further investigation is required to fully understand the coupling of these phonons and to confirm the assignment of the B trion and neutral exciton.

Chapter 6

Resonance Raman Spectroscopy of Encapsulated $WSe_2/MoSe_2$ Heterostructures

This chapter presents the results of resonance Raman spectroscopy on heterobilayers fabricated from $MoSe_2$ and WSe_2. The measurements in this chapter were carried out using excitation energies from 1.6 to 2.25 eV and observed resonances with both the $MoSe_2$ and WSe_2 A and B excitons intralayer excitons. The samples used in this study have twist angles of 57 and 6 ° between the $MoSe_2$ and WSe_2 layers and are referred to as heterostructure region 1 (HS1) and heterostructure region 2 (HS2) throughout this chapter. For HS1 new low frequency modes are identified and attributed to the resulting moiré interference pattern in the heterobilayer. The resonance behaviour of these low frequency peaks is resolved and reveals two different sets of peaks associated with the $MoSe_2$ and WSe_2 materials respectively and a preferential coupling of these peaks to trions.

6.1 Motivation

Since the discovery of monolayer TMDCs there has been considerable work on the fabrication of heterostructures composed of different 2D materials. The ever expanding family of 2D materials provides a variety of materials for use in heterobilayer devices and stacked Van der Waals structures. For the heterobilayers discussed in this chapter the band alignment of the two layers allows for the formation of an interlayer excitons with a broadly tuneable energy [26]. These interlayer excitons have demonstrated long lifetimes, ultrafast charge transfer and tuning of both the valley polarisation and polarisation lifetimes via electrostatic gating [103, 275, 276]. Until recently a relatively unexplored aspect of these heterostructures was the effect of twist angle on their optical and electrical properties. However recent work on bilayer Graphene has shown that small changes in the relative twist angle can vastly alter the electronic properties, allowing for a transition to superconducting behaviour [28]. The importance of the twist angle is due to the effect of moiré interference on the crystal structure and the additional periodicity which gives rise to a moiré superlattice. In TMDC heterostructures the twist angles allows tuning of the energies of moiré excitons, can modulate the strength of interlayer coupling,tune the interlayer exciton PL efficiency and give rise to new Raman peaks due to zone folding of the Brillouin zone [123, 107]. This allows for an additional degree of freedom and has implications for the fabrication of heterostructures composed of 2D materials. Therefore, an understanding the underlying physics of these twisted heterostructures is vital to developing future applications of not just TMDCs but 2D heterostructures in general.

6.2 Photoluminescence of Heterostructure Regions

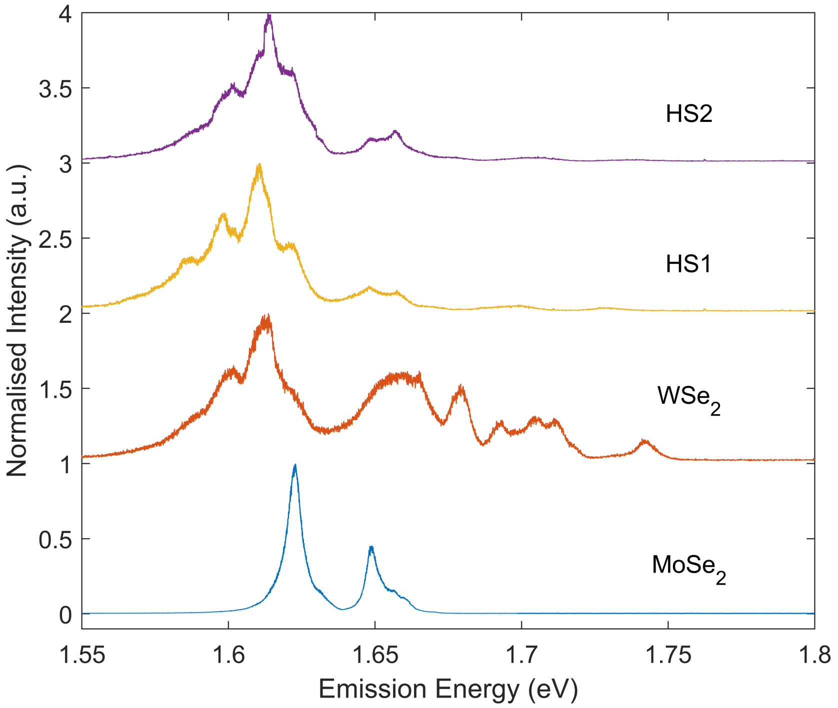

Figure 6.1: Photo-luminescence spectra were measured using a 2.33eV excitation energy at 4K and are presented for both heterostructures and monolayer regions. In each case the spectra have been offset and normalised to the maximum intensity to allow visual comparison between spectra.

Initial characterisation of HS1 and HS2 was carried out by measuring the PL spectra using a 2.33 eV (532nm) excitation energy at 4K. The spectra were fitted to a summation of Lorentzian line shapes to quantify the energies of the luminescence peaks. The

PL spectra and fitted profiles are presented in Figures 6.2 with the fitted amplitudes, widths and energies are provided in Table 6.1 & 6.2. As seen in the PL spectra for both monolayer $MoSe_2$ and WSe_2 in Chapters 4 & 5 there are a significant number of peaks in the PL spectra associated with neutral excitons, trions, biexcitons, localised and defect states. For heterostructures the PL spectra is more complex as it contains features from both of the constituent monolayers. There is also the possibility of new photoluminescence peaks arising from the moiré interference, and the formation of interlayer excitons [277, 122, 278, 279]. The intensity of peaks in the spectra can also be modified; this can occur due to changes in carrier density from charge transfer and for interlayer excitons the PL intensity is dependent on the twist angle of the samples [107, 103]. For the heterostructures presented in this chapter the spectra are further complicated by the accidental degeneracy of peaks in the PL spectra from the WSe_2 and $MoSe_2$ layers and can be seen in Figure 6.1.

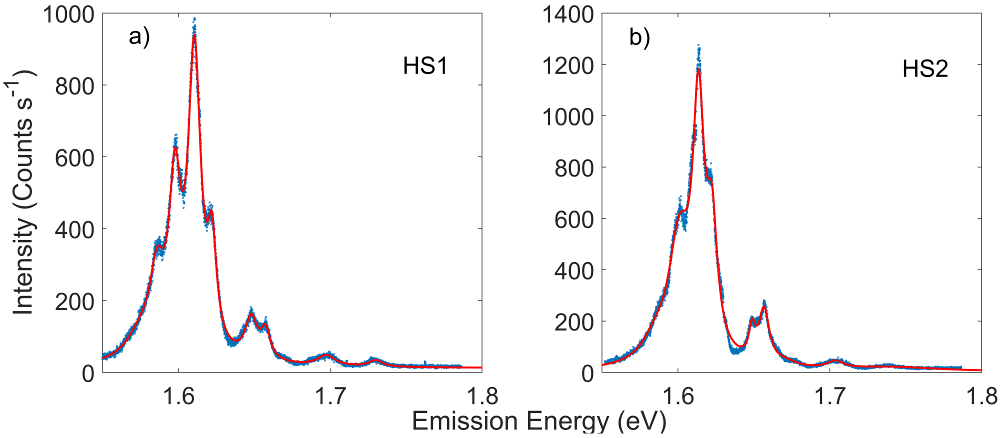

Figure 6.2: Photoluminescence spectra taken on HS1 (panel a) and HS2 (panel b) region using 2.33eV (532nm) excitation at 4K. Red line shown is a fitted profile obtained using a summation of Lorentzian lineshapes.

For HS1 the PL spectra were fitted to a total of eleven Lorentzian line shapes. The highest energy peak observed appears at 1.731 eV (see Table 6.1) and is assigned to the WSe_2 A exciton. The next assigned peaks are those at 1.691 and 1.700 eV and are attributed to the intra and inter-valley trions with separations of 31 and 40 meV. These are in agreement with the separations determined for the trions in monolayer WSe_2 (see Chapter 5) of 30 and 38 meV. The $MoSe_2$ neutral A exciton and trion are attributed to the peaks at 1.648 and 1.622 eV respectively. These assignments are in excellent agreement with the energies of the exciton and trion identified in monolayer $MoSe_2$ at 1.649 and 1.622 eV (see Chapter 4). The remaining peaks in the PL spectrum are not assigned, but a comparison to the constituent monolayer spectra in Figure 6.1 indicates these features are consistent with the peaks observed in monolayer WSe_2, and are likely due to, biexcitons, defects and localized states [132].

For HS2 the PL spectra in Figure 6.2 was fitted to a total of ten Lorentzian line shapes. The highest energy peak in the PL spectrum is at 1.739 eV (see Table6.2) and is in good agreement with the energy of the WSe_2 neutral A exciton, which was observed at 1.742 eV in the monolayer (see Chapter 5). The peak observed at 1.704 eV is also in good agreement with the energy of the WSe_2 intra-valley trion. The $MoSe_2$ A exciton and trion are attributed to the peaks at 1.649 and 1.622 eV respectively, and are in agreement with the values obtained for monolayer $MoSe_2$. As with HS1, the remaining peaks which have not been assigned appear to be related to those peaks observed on monolayer WSe_2.

Finally in $MoSe_2$ and WSe_2 heterobilayers the band alignment allows for the formation of interlayer excitons with electrons localised to the $MoSe_2$ conduction band and holes to the WSe_2 valence band. Figure 6.3 shows both the intralayer and interlayer PL emission observed in HS1 and HS2, with the interlayer exciton appearing near ~ 1.33 eV. Comparing the two spectra it is clear that the intensity of the interlayer PL for HS2

Table 6.1: Coefficients obtained from fitting PL spectra for HS1 using 2.33 eV excitation energy. Errors are a standard deviation obtained from the fitting process.

Amplitude (Counts s^{-1})	Width (meV)	Energy (eV)
26.7±0.7	14.8±0.6	1.729±0.001
30.7±1.1	5.9±0.3	1.704±0.001
15.5±1.3	4.8±0.5	1.691±0.001
63.5±0.9	2.9±0.1	1.658±0.001
112.4±0.9	6.8±0.1	1.648±0.001
270.5±1.4	3.6±0.04	1.622±0.001
832.4±1.2	5.0±0.02	1.611±0.001
439.2±1.7	4.7±0.04	1.598±0.001
208.3±3.7	6.0±0.2	1.586±0.001
61.8±3.0	11.4±0.4	1.574±0.001

Table 6.2: Coefficients obtained from fitting HS2 PL spectra to a summation of Lorentzian line shape. Errors given are a standard deviation obtained from the fitting process.

Amplitude	Width (meV)	Energy (eV)
15.5±10.0	37.5±7.6	1.739±0.001
27.6±10.3	6.4±0.8	1.704±0.001
16.6±2.1	8.0±1.8	1.677±0.001
41.3±2.6	5.7±0.1	1.664±0.001
207.2±2.6	4.2±0.1	1.657±0.001
133.3±3.4	2.6±0.1	1.649±0.001
456.8±3.7	4.3±0.1	1.622±0.001
933.4±6.0	4.6±0.1	1.614±0.001
461.0±6.0	8.7±0.2	1.601±0.001
76.0±5.6	10.8±0.8	1.585±0.001

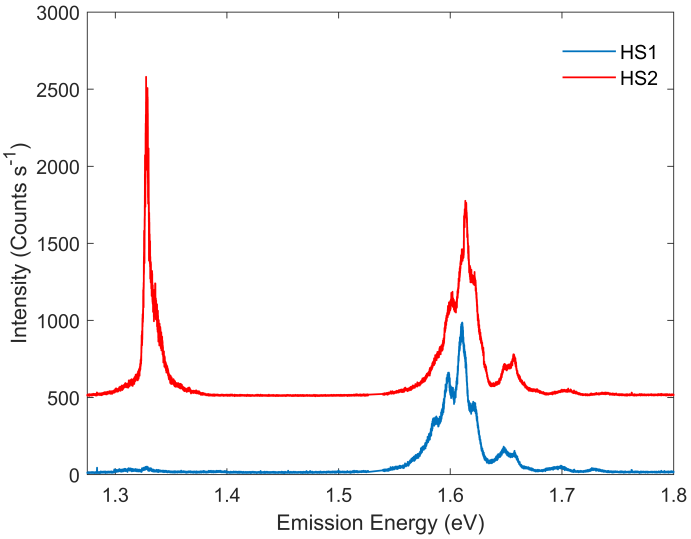

Figure 6.3: Photo-luminescence spectra for both HS1 and HS2 showing full spectral range from 1.275 to 1.8 eV obtained using 2.33 eV excitation energy at 4K. Both intralayer and interlayer exciton emission is visible for HS1 and HS2 at $\sim$ 1.34 eV For visual comparison spectra have been offset.

is several orders of magnitude greater than the emission from HS1. Studies of the PL spectra of TMD heterostructures as a function of twist angle have demonstrated that the efficiency of the interlayer PL is strongly dependent on the crystal alignment. However, the results in literature suggest that the intensity of the PL should be comparable for samples near alignment of the crystal lattices i.e close to 0° or 60°. However, this is not consistent with the results for HS1 and HS2. At present it is not clear if the difference in PL intensity from the samples is a consequence of twist angle or sample quality and requires further investigation.

6.3 Mode Assignment of Raman Spectra

The focus of the rest of this chapter are the results of resonance Raman spectroscopy on both HS1 and HS2 when probing the WSe$_2$ and MoSe$_2$ intralayer excitons. When resonant with the intralayer excitons the Raman spectra are similar to the spectra observed when probing the same exciton in the constituent monolayer. However, there are several differences including the appearance of new Raman peaks in both heterostructures. Of particular interest are the new low frequency Raman peaks which are only observed on HS1. The aim of this section is to present a comparison of the Raman spectra for the two heterostructures when resonant with the MoSe$_2$ and WSe$_2$ intralayer excitons. In addition, a detailed discussion of the new low frequency Raman peaks observed between 20 to 60 cm^{-1} on HS1 is also presented.

For HS1 and HS2 the Raman spectra contain peaks associated with both the $MoSe_2$ and WSe_2 layers, and new peaks unique to the heterostructures. As a result, a total of 45 different Raman peaks are observed. The majority of these peaks can be directly associated with the constituent monolayers. In Chapters 4 & 5 the Raman spectra for both monolayer $MoSe_2$ and WSe_2 were presented and the mode assignments discussed in detail. As a result, a complete discussion of the different possible phonon assignment to each peak observed in the heterostructures is unnecessary. Instead this section will establish which Raman peaks have been previously observed on the monolayers and those which are unique to the heterostructures.

Group	Subgroups	Abbreviation
Bulk	Bulk Anomalous	BA
	Bulk Dispersive	BD
	Bulk Standard	BS
Heterostructure	Heterostructure Anomalous	HS
	Heterostructure Dispersive	HD
	Heterostructure Low Frequency	HLF
	Heterostructure Standard	HS

Table 6.3: Table listing the different categories used when discussing the different Raman peaks in HS1 and HS2.

To allow for a more concise discussion of the different Raman peaks they have been classified into several different categories. The label for each category can be broken down into two parts and are split into two distinct groups. The first group is prefixed by the term Bulk (B) and identifies the Raman peaks which are observed in both heterostructures and monolayers. The second group is prefixed by the term Heterostructure (H) and referes to Raman peaks which are only observed in the heterostructures. Each group consists of several subcategories defined as: Dispersive (D) identifying any dispersive Raman peaks; Anomalous (A) which indicates that the Raman peak has a distinct resonance behaviour; and Low Frequency (LF) for peaks with a frequency below 100 cm^{-1}. Those Raman peaks not included in the above categories are labelled as Standard (S), and have well defined frequencies and resonance behaviour. For reference the different categories are summarised in Table 6.3.

6.3.1 $MoSe_2$ Resonant Raman Spectra

Exemplar Raman spectra for HS1, HS2 and both monolayers when resonant with the $MoSe_2$ A and B excitons are presented in Figures 6.4 & 6.5. In each case the spectra have been normalized and offset to aid visual comparison. From Figure 6.5 when resonant with the $MoSe_2$ B exciton the monolayer $MoSe_2$ and heterostructure spectra are clearly similar with the majority of peaks visible in all three Raman spectra. When resonant with the $MoSe_2$ A exciton Raman spectra are only presented for HS1 and HS2. For monolayer $MoSe_2$ no Raman spectra were obtained at the A exciton due to intense

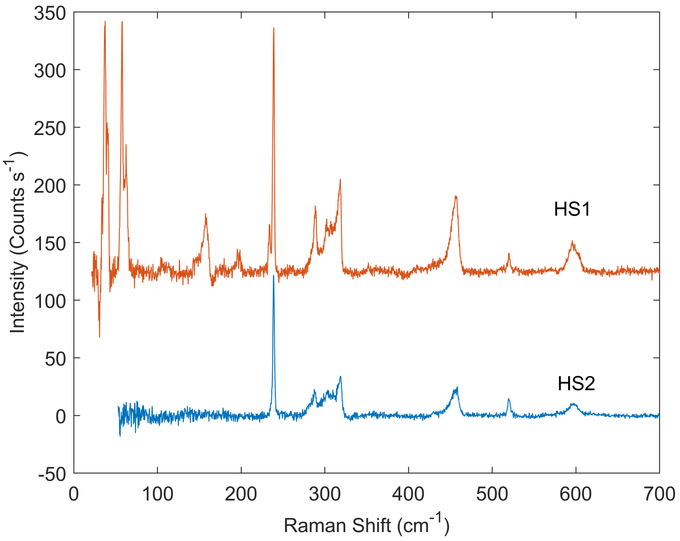

Figure 6.4: Raman spectra obtained using an excitation energy of 1.631 eV on both HS1 and HS2 are presented. It is clear that for HS1 there are a large number of additional peaks in the low frequency range 20 to 60 cm^{-1} along with a higher frequency peak at 235.8 cm^{-1}. Several peaks are also observed between 140 to 200 cm^{-1} however these are not seen in spectra at different excitation energies and so are considered to be unwanted luminescence.

photoluminescence. Comparing the Raman spectra for HS1 and HS2 in Figures 6.4 & 6.5 reveals that the spectra at the A and B excitons appear to be relatively similar.

To provide a quantitative comparison of the Raman spectra when resonant with the $MoSe_2$ intralayer excitons both monolayer and heterostructure spectra were fitted to a summation of Lorentzian line shapes. The Raman spectra in each case were calibrated to the silicon peak at 520 cm^{-1} which is used as an internal reference. For each sample the frequencies of the Raman peaks were determined by fitting multiple spectra at different excitation energies. The mean frequencies and standard deviation for each peak are provided in Table 6.4. Each peak has also been assigned a labelled using the categories defined in Table 6.3. Overall the majority of Raman peaks identified from fitting are observed on all three sample regions. There is some variation in the obtained frequencies when comparing the heterostructures and monolayers, but these are typically less than 1 cm^{-1} difference. These shifts in the peak frequencies are not unexpected as the Raman shift is sensitive to a range of factors including sample strain, dielectric environment and interlayer coupling [52, 157, 219]. It is also unlikely that these shifts are due to different Raman peaks being observed qs the shifts are significantly smaller than the widths of the Raman peaks, with the narrowest peaks having a width of ~ 2 cm^{-1} and suggest a single peak is responsible.

Inspection of Table 6.4 reveals that a total of 24 different Raman peaks are observed when resonant with the $MoSe_2$ intralayer excitons. Overall 14 of the peaks have been classified as bulk standard (BS) Raman peaks. This classification requires that the Raman peaks

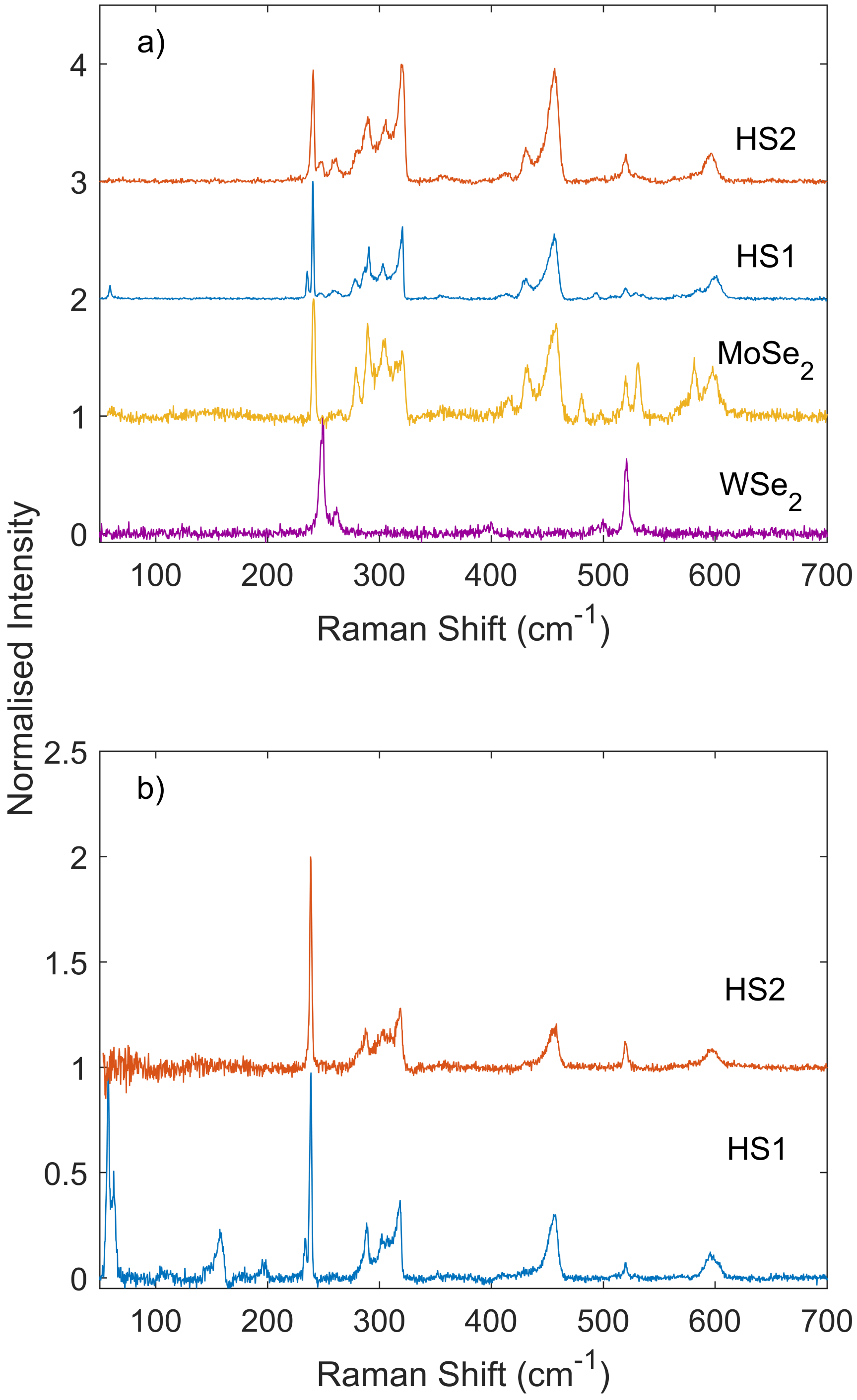

Figure 6.5: Panel a) Raman spectra obtained using an excitation energy of 1.851 eV when resonant with the $MoSe_2$ B exciton for both HS1 and HS2 are presented along with monolayer spectra for comparison. Panel b) presents Raman spectra on all sample areas from 50 to 700 cm^{-1}. Panel b) Raman spectra obtained using an excitation energy of 1.631 eV on both HS1 and HS2 are presented. For HS1 spectra there are several peaks in the range of 100 to 200 $cm^{-}1$ which are not observed in spectra at other excitation energies and so are likely unwanted luminescence.

are observed on the constituent monolayer and that their Raman resonances behave as expected. An exception is the peak at 357.9 cm^{-1}: as seen in Table 6.4 this peak is only observed for HS2 when resonant with the B exciton. However, close inspection of the Raman spectra for both monolayer $MoSe_2$ and HS1 reveals weak features in this frequency range in several spectra . As a result the peak at 357.9 cm^{-1} has been classified as a BS peak, as it is likely present in all samples. The next classification with a significant number of peaks are the low frequency modes (HLF), which are only observed for HS1, and results in 5 new Raman peaks. A more detailed discussion of the HLF peaks is presented in Section 6.3.3 due to the appearance of similar peaks when resonant with the WSe_2 intralayer excitons.

Of the remaining Raman peaks there are three BA peaks, two BD peaks, a HA peak and a HS peak identified when resonant with the $MoSe_2$ intralayer excitons. Considering first the bulk dispersive Raman peak at $\sim$ 288 cm^{-1}. In monolayer $MoSe_2$ two dispersive Raman peaks were identified near $\sim$ 280 and 288 cm^{-1} (see Chapter 4). In HS1 similar dispersive peaks are also observed with frequencies in the range of 278 to 280.5 cm^{-1} and from 285.9 to 287.7 cm^{-1}. However, for HS2 the Raman peaks in this range show no significant dispersion. In particular dispersive peaks between 284 and 288 cm^{-1} are observed on both monolayer $MoSe_2$ and HS1, but are not seen in the HS2. This is apparent in Figure 6.6 where the resonance data for HS1 and HS2 is presented. For HS1 a dispersive peak is visible as a shoulder to the peak at 290.9 cm^{-1}, whilst for HS2 there is no obvious dispersive peak near 289.2 cm^{-1} with the Raman peak appearing to be symmetric at all excitation energies. The lack of dispersive Raman peaks on HS2 suggests either a modification of the phonon dispersion or change in the availability of large wavevector electronic states to mediate these processes. Although as seen in Table 6.4 the frequencies of the Raman peaks are in reasonable agreement and suggests the phonon dispersion relation is not significantly different for either HS1, HS2 or monolayer $MoSe_2$. In Chapters 4 & 5 the dispersive Raman peaks in both $MoSe_2$ and WSe_2 also display a distinct resonance behaviour. Therefore, the most plausible explanation for the disappearance of the dispersive peak in HS2 is due to changes in the availability of electronic states required to satisfy the resonance conditions for these dispersive peaks.

The BA Raman peaks are observed at $\sim$ 481, 530, 581 cm^{-1} in HS1 and were also seen in monolayer $MoSe_2$. The results for monolayer $MoSe_2$ revealed these peaks had an anomalous resonance behaviour, which was attributed to a double resonance between the $MoSe_2$ B exciton and a lower energy electronic state at 1.802 eV (see Chapter 4). For HS1 these Raman peaks are also observed to exhibit an anomalous resonance behaviour with a lower energy state at 1.755 eV (see Section 6.4.3). From Table 6.4 it is also clear that the peaks at $\sim$ 481 and 530 cm^{-1} are not observed in HS2. Whilst the peak at $\sim$ 581 cm^{-1} is seen in both HS1 and monolayer $MoSe_2$ it also demonstrates an anomalous resonance behaviour. There are two possible explanations for the 581 cm^{-1} showing both BS and BA behaviours. Either the 581 cm^{-1} peak is able to satisfy both the resonance

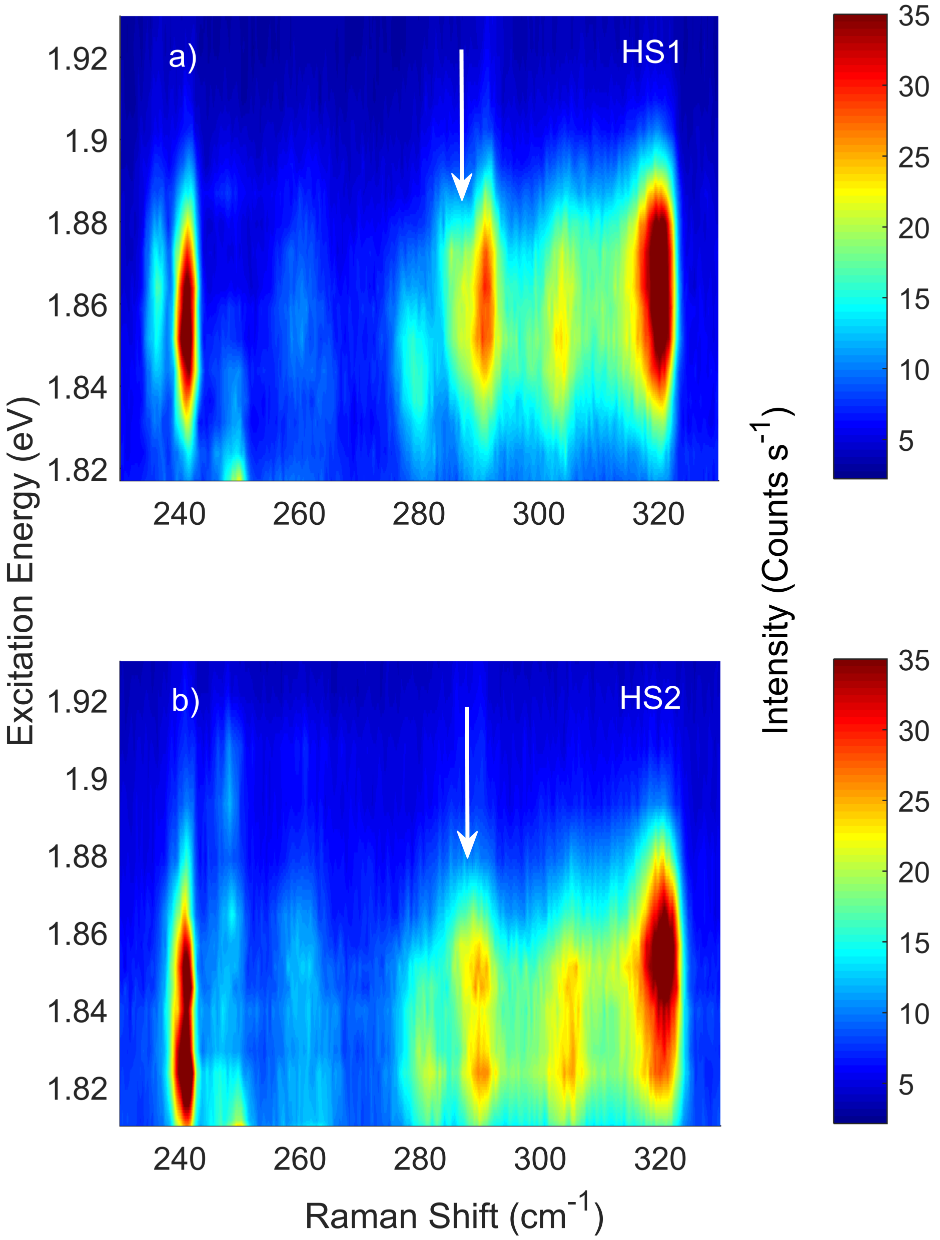

Figure 6.6: Colourmaps of the resonance Raman data for HS1 (panel a) and HS2 (panel b) are presented when resonant with the MoSe$_2$ B exciton. Raman peaks near 288 cm^{-1} are indicated by the white arrows. In HS1 a dispersive peak can clearly been seen as a shoulder on the peak, whereas in HS2 no dispersive Raman peaks are observed.

conditions with the anomalous resonance and B exciton, or the anomalous resonance is the result of another peak coincidentally degenerate with the 581 cm^{-1} peak. The energy of the anomalous resonance in HS1 and monolayer $MoSe_2$ is also shifted by $\sim$ 47 meV, and implies a difference in the underlying electronic states. The absence of the anomalous Raman peaks on HS2 suggests that there may be a difference in the electronic states present in HS1 and HS2. The behaviour of the anomalous Raman peaks may allow for the differences in the electronic states in monolayers and heterostructures to be probed. A more complete discussion of these anomalous resonances is presented in Section 6.5.1 following a thorough analysis of the resonance behaviour.

The Raman peak at 245.8 cm^{-1} has been classified as HA. This peak is only observed on HS2 near resonance with the $MoSe_2$ A and WSe_2 A excitons. As a result, it is not clear which layer this peak is associated with and so is included in Table 6.4 to allow for a comparison to the other $MoSe_2$ Raman peaks. This reveals that no other Raman peaks at this frequency are observed in either HS1 or monolayer $MoSe_2$. Due to this Raman peak only being observed near resonance with both the $MoSe_2$ and WSe_2 A excitons a comparison to the WSe_2 Raman peaks is required before discussing this peak further. Consequently, a detailed discussion of this Raman peak will be presented when discussing the WSe_2 Raman spectra.

Finally we consider the peak at 235.8 cm^{-1} which is classified as a HS peak. From Table 6.4 it is obvious that this Raman peak is only observed on HS1 when resonant with the $MoSe_2$ A and excitons. The $MoSe_2$ phonon dispersion relation indicates that there are no Γ point phonons expected at frequencies consistent with this new peak. The relatively low frequency of this new peak also limits the number of predicted multi-phonon modes. Two possibilities are the 2TA(K) at 233 cm^{-1} or the TA(M) + ZA(M) at 223 cm^{-1} (predicted shifts determined using dispersion relation from Bilgin et al.[144]). However, the absence of this peak in monolayer $MoSe_2$ implies it is intrinsic to the heterostructure. Likewise, the appearance of this peak on HS1 and not on HS2 suggests this new Raman peak is dependent on the sample twist angle. The appearance of HLF modes also supports this argument as the low frequencies of these peaks cannot be explained by phonons at the high symmetry points of the Brillouin zone. A clear possibility is that the peak at 235.8 cm^{-1} is the result of the moiré interference arising in the heterostructure. Moiré phonons have been previously reported for twisted MoS_2 homobilayers [123], and arise from zone folding of large wavevector phonon onto the Brillouin zone centre. For the 235.8 cm^{-1} Raman peak the only phonon branch that could give rise to this peak is the A_1' branch. The frequency of this branch decreases for small changes in wavevector away from the Γ point, and so it is possible that the 235.8 cm^{-1} peak is the zone folded A_1'. However, more detailed survey of heterostructures with different twist angles is necessary to confirm this proposed origin.

In summary the Raman spectra when resonant with the $MoSe_2$ intralayer excitons reveals the majority of Raman peaks observed on HS1 and HS2 are attributed to bulk peaks

Table 6.4: Raman shifts are presented for all peaks observed on HS1, HS2 and Monolayer MoSe$_2$ when resonant with the A and B excitons. The Raman spectra were fitted using a summation of Lorentzian line shapes and calibrated to the Silicon peak at 520 cm^1. The values presented are the mean and standard deviation obtained from fitting several spectra at different excitation energies. All presented values have units of cm^{-1}.

MoSe$_2$ A		MoSe$_2$ B			Peak Type
HS1	HS2	HS1	HS2	MoSe$_2$	
35.3±0.1	-	35.4±0.2	-	-	HLF
39.1±0.05	-	38.9±0.1	-	-	HLF
42.4±0.05	-	42.1±0.2	-	-	HLF
59.3±0.05	-	59.0±0.1	-	-	HLF
63.5±0.1	-	63.8±0.1	-	-	HLF
235.8±0.1	-	235.8±0.1	-	-	HLF
240.8±0.05	240.8±0.05	241.0±0.1	240.9±0.4	241.5±0.1	BS
-	245.8	-	-	-	HA
-	-	260.4±0.4	261.2±0.8	260.7±1.3	BS
-	-	277.7±1.2	280.1±0.4	277.4±1.2	BS/BD
288.3±0.1	287.0±0.2	286.0±0.6	-	288.6±0.5	BD
-	-	290.9±0.1	289.2±0.7	290.7±0.3	BS
303.4±0.4	303.5±0.3	304.2±0.6	304.9±0.8	304.6±0.2	BS
313.1±0.4	-	316.1±0.1	316.3±0.2	314.6±0.3	BS
319.8±0.1	320.5±0.1	320.2±0.1	319.6±0.6	321.4±0.2	BS
-	-	357.9±0.5	-	-	BS
-	-	410.6±0.8	413±0.7	412.2±0.4	BS
432.0±1.3	-	431.5±0.1	432.2±0.5	432.5±0.1	BS
455.3±0.1	455.3±0.1	450.2±0.05	447.5±0.4	450.4±1.3	BS
-	-	456.9±0.05	456±0.8	458.5±0.3	BS
-	-	480.6±1.4	-	481.5±0.5	BA
-	-	529.5±0.5	-	531.2±0.2	BA
-	-	581.7±0	580.2±0.8	581.1±0.1	BS/BA
596.7±0.4	596.9±0.4	599.8±0	596.0±0.5	598.7±0.2	BS

previously seen in monolayer MoSe$_2$. Although there are several differences between HS1 and HS2, such as the absence of BD and BA peaks on HS2, which suggests a difference in the electronic states available in the two samples. The new Raman peaks in HS1 classified as HLF and HS peaks are not seen in HS2 and maybe dependent on sample twist angle. These peaks are likely the result of moiré interference resulting in zone folding of off zone center phonons.

6.3.1.1 Observation of hBN phonons in Heterostructures

When near resonance with the $MoSe_2$ B exciton in both HS1 and HS2 two Raman peaks are observed at $\sim$ 800 and 1050 cm^1, and are only seen when using excitation energies in the range of $\sim$ 1.8 to 1.88 eV (see Figure 6.7). These peaks were previously reported for encapsulated monolayers of WSe_2 and arise due to coupling of hBN phonons to electronic states in the WSe_2 layer [198, 199, 190]. The resonance profiles for these peaks were investigated by Jin et al. and attributed to a double resonance with the A exciton and a higher energy state [198]. We also observed these peaks during resonance Raman measurements on monolayer WSe_2 (see Chapter 5). Our results are in agreement with the published literature and also require a double resonance process with the WSe_2 A outgoing resonance and the WSe_2 A* state. To confirm these are Raman peaks spectra were obtained for both crossed and parallel polarisations and demonstrate that the peaks are linearly polarised, and confirms that these features are Raman peaks and not unpolarised luminescence. Overall these peaks are of interest for future studies of encapsulated TMDCs, but are not investigated further in this thesis. Instead the aim of this section is to ensure the reader is aware of these peaks as they are visible in the Raman spectra presented for HS1 and HS2.

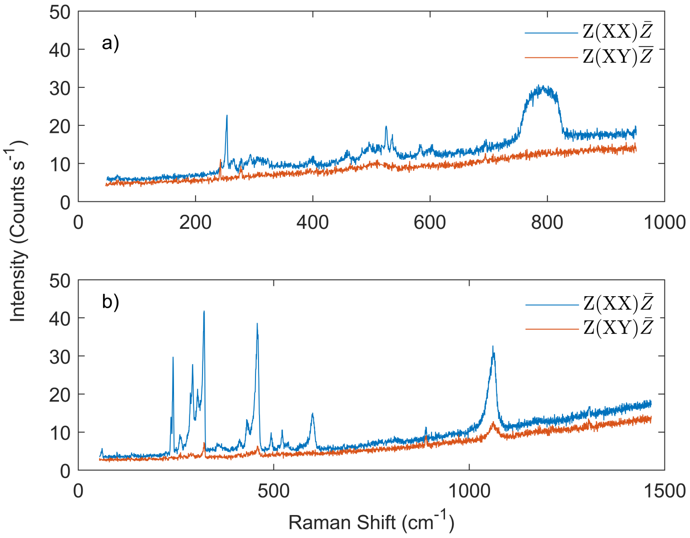

Figure 6.7: Raman spectra obtained on HS1 using excitation energies of 1.800 and 1.873 eV are presented in panels a) and b) respectively. For each excitation energy spectra polarisation resolved spectra are presented with the incident light linearly polarised and the scattered light measured in both parallel (Z(XX)$\overline{Z}$) and crossed configurations (Z(XY)$\overline{Z}$). Two additional peaks are observed at $\sim$ 790 and 1050 cm^{-1} which are both linearly polarised indicating these peaks are Raman peaks and not photoluminescence.

6.3.2 WSe_2 Resonant Raman Spectra

Exemplar spectra for both the heterostructures and monolayer WSe_2 when resonant with the A and B intralayer excitons are presented in Figure 6.8. In each case the Raman spectra have been normalised to the peak intensity and offset to allow for easier visual comparison. In Figure 6.8 panel a) when resonant with the WSe_2 A exciton, there is a clear similarity between the Raman spectra across all three sample regions. In each case the dominant peak in the spectra is located at $\sim$ 250 cm^{-1} with several weaker peaks appearing between 255 and 270 cm^{-1} and a weak peak also observed at $\sim$ 400 cm^{-1}. There are several Raman peaks between 200 and 250 cm^{-1}, and a dispersive Raman peak is seen at $\sim$ 208 cm^{-1} on all samples. The Raman spectra in Figure 6.8 panel b) also shows that when resonant with the WSe_2 B exciton the resulting spectra are clearly different for the three sample regions. The differences in these spectra can be characterised by changes in the relative intensity of the Raman peaks and the total number of observed peaks. In particular on HS1 three new Raman peaks appear between 280 and 360 cm^{-1}, and are not observed on either HS2 or monolayer WSe_2.

To quantify the positions of the Raman peaks the spectra have been fitted to a summation of Lorentzian lineshapes. To compare the peak frequencies across the different samples the Raman spectra were calibrated using the Silicon peak at 520 cm^{-1} as an internal reference. The mean values and standard deviation of the peak positions was obtained for each sample by fitting multiple spectra at different excitation energies. The peak positions are provided in Table 6.5 and each peak has been labelled using the classifications presented at the start of this section. The Raman peaks across all three sample regions have been compared and the equivalent Raman peaks in each sample are presented in the same row in Table 6.5. In general the frequencies of the peaks are found to be in agreement to within $\sim$ 1 cm^{-1} across the different sample regions. The shifts in the peak frequencies are not unexpected as the Raman shift is sensitive to a range of factors including sample strain, dielectric environment and interlayer coupling [280, 52, 219]. It is also unlikely that these shifts are due to differences in the Raman peaks as the shifts are significantly smaller than the widths of the Raman peaks, with the narrowest peaks having a width of $\sim$ 2 cm^{-1}.

From Table 6.5 21 different Raman peaks have been identified when resonant with the WSe_2 A and B intralayer excitons. Of these Raman peaks 13 peaks are bulk related with 12 classified as BS and one as BD. For the peaks associated with the heterostructure there are a total of 9 peaks which are separated into four HLF, a HD and 3 HA Raman peaks. Several of the Raman peaks between 370 and 400 cm^{-1} are not observed when resonant with the A exciton, but are seen on all sample areas at the B exciton. The lack of these peaks at the A exciton in monolayer WSe_2 is attributed to intense photoluminescence background observed when resonant. The assignments of the BS peaks has been considered in Chapter 5 and so are not discussed further in this section. The HLF

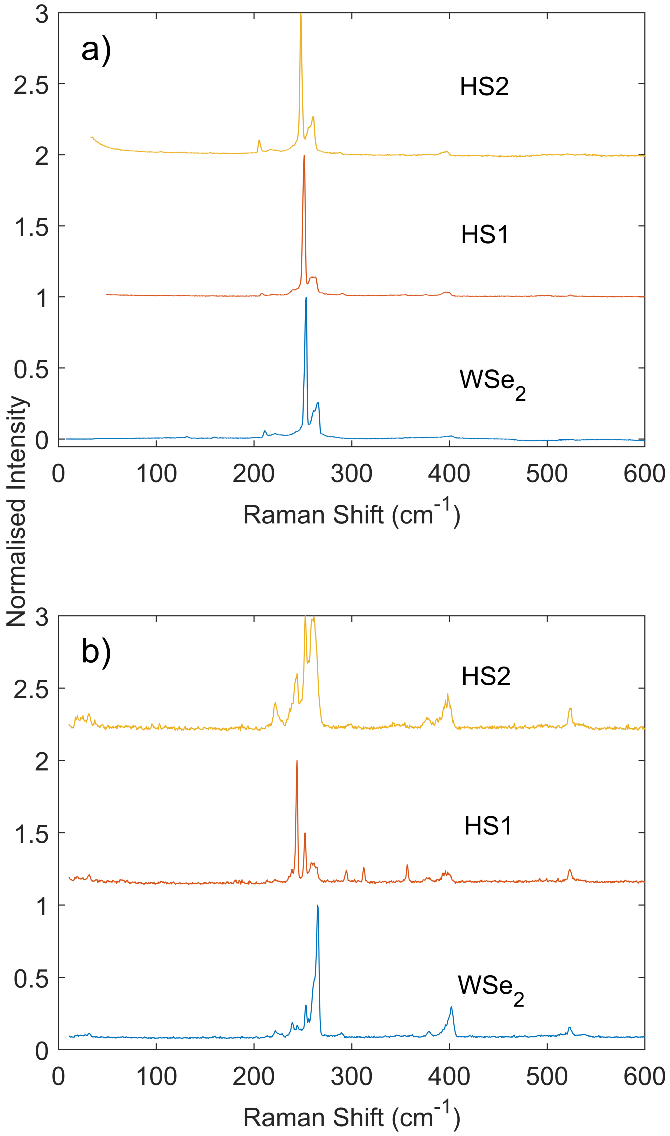

Figure 6.8: Raman spectra are presented for both heterostructures and monolayer WSe_2 when resonant with both the A and B intralayer excitons associated with the WSe_2 layer. Panel a) shows Raman spectra obtained when resonant with WSe_2 A exciton using an excitation energy 1.74 eV which is resonant with the A exciton. Panel b) Raman spectra obtained when resonant with WSe_2 B exciton using an excitation energy 2.14 eV and is resonant with the WSe_2 B exciton.

Raman peaks are observed when resonant with the WSe_2 A exciton and are exclusive to HS1. As previously seen in Section 6.3.1 a similar set of peaks is observed on HS1 at the $MoSe_2$ intralayer excitons and so a more detailed discussion and comparison of these peaks is presented in Section 6.3.3.

At the A exciton resonance a BD Raman peak is observed on all samples area near 208 cm^{-1}. The dispersive nature of this Raman peak indicates the involvement of large wavevector phonons. The resonance behaviour for these dispersive Raman peaks is distinct from the BS peak suggesting the involvement of large wavevector electronic states. The observation of this dispersive mode on both heterostructures and the monolayer indicates a similarity in the resonance behaviour at the WSe_2 A exciton and also suggests that the phonon dispersion in the heterostructures is not significantly modified relative to the constituent monolayer.

The HA peak at 245.8 cm^{-1} was observed only on HS2 when near resonance with the $MoSe_2$ and WSe_2 A excitons. The resonance behaviour of this peak is anomalous compared to the BS peaks associated with the $MoSe_2$ and WSe_2 layers respectively. As will be presented in Section 6.4.1, this peak is resonant with two excitonic states at 1.688 and 1.703 eV which may be associated with either the $MoSe_2$ or WSe_2 layers. As a result a clear assignment of this peak to a particular layer is not possible. Consideration of the $MoSe_2$ phonon dispersion relations indicate possible assignment peak to the 2ZA(M) or ZA(K)+TA(K) peaks with predicted frequencies of 248.7 and 245.6 cm^{-1} respectively. Likewise, this peak can also be assigned to WSe_2 2ZA(K) combination mode, which is predicted to appear at 245.9 cm^{-1}. The WSe_2 phonon dispersion also indicates that this peak maybe the result of zone folding of the E' branch and so could also be a moiré phonon. Although, there is no other evidence of zone folded moiré phonons in HS2. The final possibility for the origin of the 245.8 cm^{-1} peak is a multiphonon process involving both $MoSe_2$ and WSe_2 phonons. For both the $MoSe_2$ and WSe_2 layers the acoustic phonons have similar frequencies with the ZA phonons in the range of 119 to 129 cm^{-1}. As a result the peak at 245.8 cm^{-1} could be the result of a 2ZA peak involving a WSe_2 and $MoSe_2$ phonon with the M point mode having a predicted frequency of $\sim$ 243 cm^{-1}. However, from the Raman data presented in this thesis there is no clear evidence indicating which of these assignments is correct. Therefore, the assignment of the anomalous peak at 245.8 cm^{-1} is inconclusive and will require further investigation of other heterostructure samples.

The remaining heterostructure related peak exclusive to HS2 is the peak at 261.2 cm^{-1}, which is classified as both BS and HD. For both monolayer and WSe_2, the Raman peak near 261.2 $\sim$ is observed and is classified as BS. However in HS2 the 261.2 cm^{-1} peak is clearly a dispersive Raman peak. This dispersive behaviour can be seen in Figures 6.9 & 6.10. The assignment of the Raman peaks near $\sim$ 260 cm^{-1} is disputed in literature with most reports proposing that there are only two Raman peaks, whereas Du et al. propose this peak is composed of at least three separate Raman peaks. Similar results for monolayer MoS_2 by Carvalho et al. also demonstrated that the peak commonly assigned to the 2LA was actually the result of five almost degenerate Raman peaks some of which were dispersive in nature [141]. Therefore it is possible this dispersive behaviour could occur due to the presence of an new Raman peak near 262 cm^{-1}. However, for our results we find that only two Lorentzian line shapes are required to achieve a best fit to the Raman spectra. Therefore, we attribute this behaviour to a dispersive Raman peak. The lack of a dispersive Raman peak in monolayer WSe_2 and in HS1 implies either a change in the phonon dispersion or a difference in the underlying electronic states.

The final peaks to consider are the new Raman peaks seen exclusively on HS1 at 290.7, 309.1 and 353.8cm^{-1}. As seen in Figure 6.8 panel b) these Raman peaks are only observed for HS1 when resonant with the WSe_2 B exciton. From the fitted peak frequencies in Table 6.5 it is clear that the 290.7 cm^{-1} peak is close to peaks reported in both monolayer WSe_2 and HS2 between 286.5 and 288 cm^{-1}. As a result, we cannot discount the possibility that this Raman peak is a WSe_2 bulk related peak. Whereas, the peaks at 309.1 and 353.8 cm^{-1} are clearly only seen in HS1. The absence of these peaks in the monolayer spectrum and their appearance only in Raman spectra on HS1 suggests that these peaks are associated with the heterostructure and maybe dependent on the sample twist angle. As a result these peaks may arise from zone folding of off centre phonons due to the moiré interference in the heterostructure.

Considering the possibility that these new peaks are moiré phonons requires the use of the phonon dispersion relations for WSe_2 (see Figure 5.3 in Chapter 5). For WSe_2 the highest frequency single phonon peak is predicted to be the A_2'' at the Γ point with a frequency of $\sim$ 308 cm^{-1}. This could explain the 309.1 cm^{-1} Raman peak, and zone folding of the A_2'' branch could also explain the 290.7 cm^{-1} peak. However, Raman peak at 353.8 cm^{-1} must a multiphonon peak as there are no single phonon branches with frequencies predicted above 308 cm^{-1} in the WSe_2 phonon dispersion. As a result it is not possible to explain these new Raman peaks using only zone folded moiré phonons. In addition, the observation of these peaks at only the WSe_2 B exciton suggests that the underlying electronic states play a significant role in observing these peaks. Therefore, it seems unlikely that these Raman peaks are the result of moiré phonons.

An alternative explanation for the origin of these peaks becomes apparent from considering the reported Raman spectra for other heterobilayers in literature. For comparable $MoSe_2/WSe_2$ heterostructures a Raman peak has been reported at 309 cm^{-1} by Nayak et al. [107] and has also been observed in several other heterobilayers including WSe_2/WS_2 and WSe_2/MoS_2 [281, 282]. These reports propose an assignment of this Raman peak to the A_2'' phonon at the Γ point. The A_2'' peak is not expected to be Raman active in monolayer but is observed in bilayer and few layer WSe_2 [52]. In addition, the results of Nayak et al. also report a Raman peak at 353 cm^{-1} and assign this to the $A_2''(\Gamma)$ phonon associated with the $MoSe_2$ layer [107, 283]. Similarly the A_2'' phonon is not Raman active in monolayer $MoSe_2$, but is active in bilayer and few layer $MoSe_2$ [194]. Therefore, our results are in agreement with those reported in literature for $MoSe_2/WSe_2$ heterostructures and suggests that the peaks at 309.1 and 353.8 cm^{-1} may be assigned to the $A_2''(\Gamma)$ phonons.

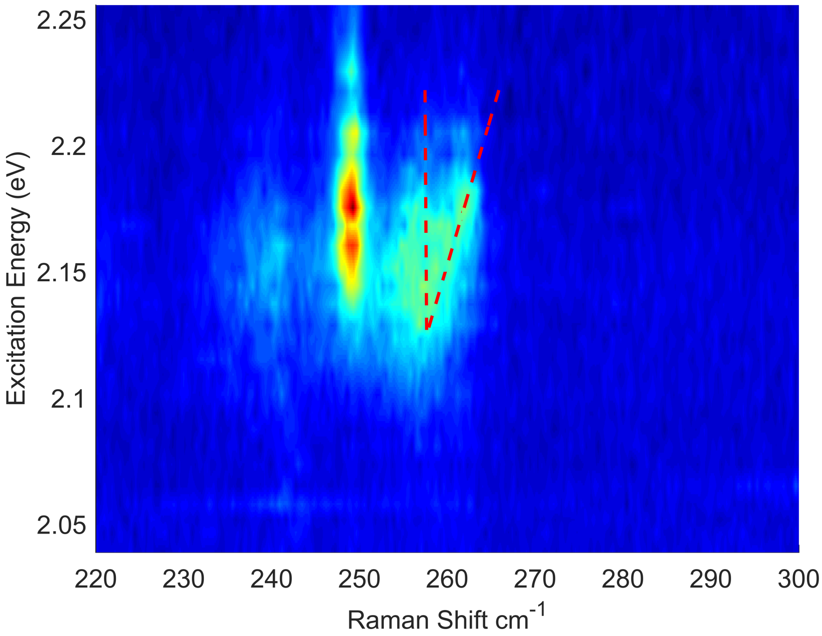

Figure 6.9: Colourmap showing resonance Raman data for HS2 when resonant with the WSe_2 B exciton from 200 to 300 cm^{-1}. As a visual aid red dashed lines have been added to indicate the location of the dispersive Raman peak observed for the peak at 261.2 cm^{-1}

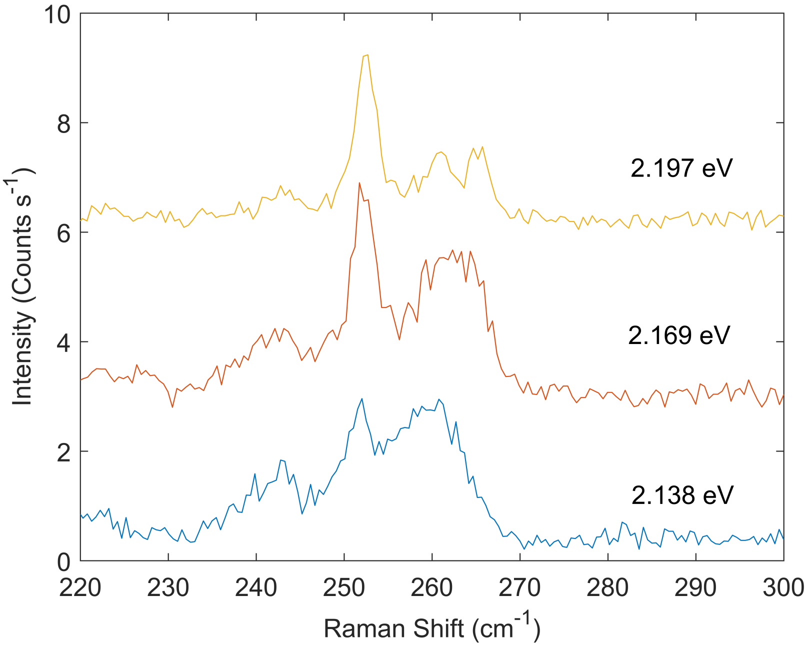

Figure 6.10: Exemplar Raman spectra for HS2 when resonant with the WSe_2 B exciton using excitation energies of 2.138, 2.169 and 2.197 eV. At 2.197 eV at least two Raman peaks near $\sim$ 260 cm^{-1}. At lower excitation energies the dispersive Raman peak in the range of 259 to 262 cm^{-1} then shifts in frequency and resulting in a broad peak near 260 cm^{-1}.

The possibility of $MoSe_2$ Raman peaks appearing at the WSe_2 B exciton resonance requires a revised analysis of the Raman spectra for HS1. In particular the Raman peak at 240.4 cm^{-1} was initially classified as BS/HA. In Figure 6.8 and Table 6.4 it is clear that peaks near $\sim$ 240 cm^{-1} are observed in all samples at both the WSe_2 A and B excitons. However, for HS1 at the WSe_2 B exciton the intensity of the 240.4 cm^{-1} peak is significantly enhanced relative to the other WSe_2 Raman peaks. Typically the most intense peaks in WSe_2 are those between 250-270 cm^{-1}, however in HS1 the 240.4 cm^{-1} is the dominant peak in the spectrum (see Figure 6.8 panel b). A natural explanation for the atypical intensity of the 240.4 cm^{-1} arises if it is the $MoSe_2$ $A'_1(\Gamma)$ phonon, which is observed at 240.8 cm^{-1} on HS1 when resonant with the $MoSe_2$ intralayer excitons. It is also possible to assign the new peak at 290.7 cm^{-1} to the $MoSe_2$ $E'(\Gamma)$ phonon. To confirm that these new peaks assigned to $MoSe_2$ phonons are not the result of an additional $MoSe_2$ resonance measurements were carried out on the monolayer $MoSe_2$ sample over the same energy range. However, no resonance Raman behaviour was observed in the monolayer $MoSe_2$ sample. Therefore, the observation of $MoSe_2$ Raman peaks at the WSe_2 B exciton, in HS1 is not due to an accidental degeneracy with a higher energy $MoSe_2$ state. The resonance Raman behaviour for these Raman peaks is discussed in Section 6.4.4 and reveals differences in the resonance behaviour of these new peaks, and may be the result of hybridisation of intralayer and interlayer excitons. This possibility is discussed in more detail in Section 6.5.1.1.

In summary the Raman spectra when resonant with the WSe_2 A and B intralayer excitons have been presented. The majority of Raman peaks observed in the spectra have been assigned to BS peaks. However, there are several Raman peaks which have been observed only in the heterostructures. For HS1 the HA peak at 245.8 cm^{-1} has been considered and it is concluded that an assignment of this peak to phonon associated with the $MoSe_2$ or WSe_2 layer is not possible. For HS1 three new Raman peaks are observed at 290.7, 309.1 and 353.8cm^{-1}. The peaks at 309.1 and 353.8 cm^{-1} are assigned to the $A''_2(\Gamma)$ phonon associated with the WSe_2 and $MoSe_2$ layer and are in agreement with reports in literature [107]. The participation of $MoSe_2$ Γ point phonons can also explain the Raman peaks at 290.7 cm^{-1} and the atypical behaviour of the 240.4 cm^{-1} peak if they are also the $E'(\Gamma)$ and A'_1 (Γ) phonons. Therefore, for HS1 both $MoSe_2$ and WSe_2 phonons are observed and suggests the hybridisation states between the two layers.

Table 6.5: Raman Peak positions are given for HS1, HS2 and WSe$_2$ monolayer when resonant with the A and B WSe$_2$ excitons respectively. Peak position obtained from fitting spectra at several excitation energies to Lorentzian line shapes. The values given are then the mean and standard deviation. In all cases spectra have been calibrated to the Silicon peak at 520 cm^{-1}.

	WSe$_2$ A			WSe$_2$ B		Peak Type
WSe$_2$	HS1	HS2	WSe$_2$	HS1	HS2	
-	34.6±0.1	-	-	-	-	HLF
-	38.8±1.1	-	-	-	-	HLF
-	52.9±0.1	-	-	-	-	HLF
-	57.8±0.5	-	-	-	-	HLF
206.3±1.7	206.2±0.7	207.3±0.6	-	-	-	BD
219.2±0.7	219±0.9	219.3±0.3	218.1±0.7	218.0±1.6	218.3±0.6	BS
-	-	-	224.6±1.3	-	-	BS
235.1±1.3	236.7±0.5	-	236.3±0.2	235.0±0.7	235.7±0.5	BS
-	245.8	-	-	-	-	HA
241.5±0.7	240.3±0.9	239.8±1.0	241.8±0.6	240.4±0.1	240.2±0.3	BS/HA
249.5±0.1	248.8±0.1	249.0±0.4	249.5±0.2	248.7±0.2	249±0.2	BS
-	-	-	255.2±0.2	255.2±0.8	255.8±0.6	BS
257.7±0.2	256.5±0.1	257.0±0.2	258.0±0.4	-	258.3±0.3	BS
261.9±0.2	260.4±0.2	261.2±0.2	262.0±0.1	260.4±0.5	261.2±0.2	BS/HD
-	287.2±0.1	288.0±1.7	286.5±1.4	-	-	BS
-	-	-	-	290.7±0.8	-	HA
-	-	-	-	309.1±0.6	-	HA
-	-	-	-	353.8±0.8	-	HA
-	373±0.9	372.3±1.2	374.1±3.6	374.5±0.4	372.7±1.3	BS
-	395.2±1.8	394.9±0.7	392.4±0.3	393.3±2.0	392.2±0.3	BS
396.6±0.4	399.1±0.8	398.6±0.5	398.7±0.3	398.2±0.9	396.3±0.5	BS

6.3.3 Low Frequency Raman Peaks

As presented in Sections 6.3.1 & 6.3.2 new low frequency Raman peaks in the range of 35 to 65 cm^{-1} are observed on HS1 when resonant with both the $MoSe_2$ and WSe_2 intralayer excitons. The appearance of these modes only on HS1 suggests that these peaks may be strongly dependent on the twist angle of the heterostructures. It is also apparent that the number of observed peaks and their Raman shifts are dependent on whether the exciton involved in the resonance process is associated with the $MoSe_2$ or WSe_2 layer. To demonstrate this Raman spectra for the low frequency modes are presented in Figure 6.11 when resonant with the WSe_2 A and $MoSe_2$ A and B excitons. When resonant with the $MoSe_2$ A and B excitons the number of Raman peaks and their positions appear to be in agreement with some variation in the relative intensity of the peaks. Whereas, the low frequency peaks seen when resonant with the WSe_2 A exciton appear at different shifts compared to those observed when resonant with the $MoSe_2$ A and B excitons.

To further investigate this for each resonance Raman spectra have been fitted for multiple excitation energies and calibrated to the silicon peak of the substrate at 520 cm^{-1}. The

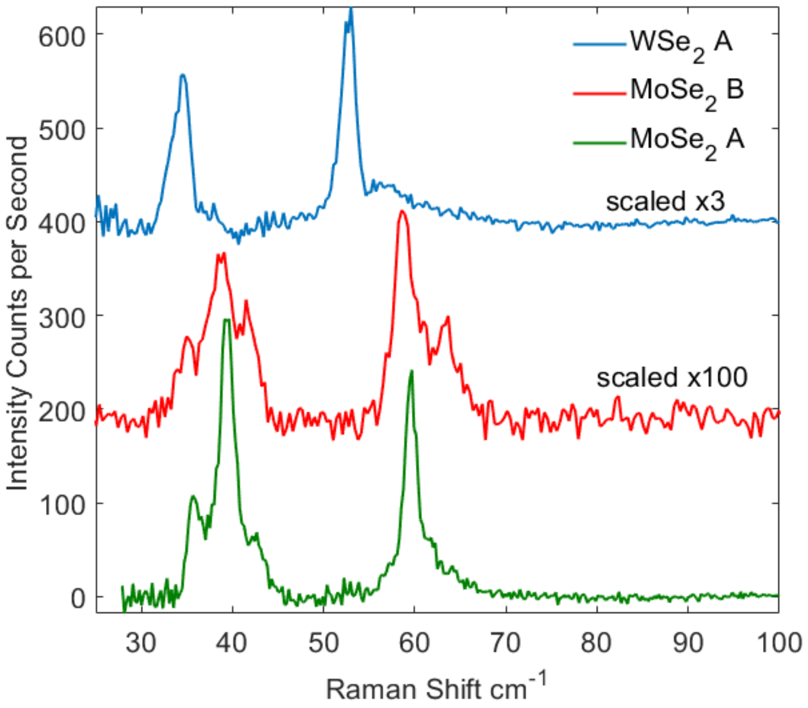

Figure 6.11: Raman Spectra were obtained on HS1 when resonant with the WSe_2 A exciton and $MoSe_2$ A and B excitons using excitation energies of 1.710, 1.625 and 1.848 eV respectively. In each case the Raman spectra have been calibrated using the Silicon peak at 520 cm^{-1} as an external reference, and have been scaled and offset for ease of comparison. For each resonance there are a series of low frequency modes that are only observed on HS1.

Table 6.6: Raman Shifts for low frequency peaks observed on HS1 when resonant with the WSe$_2$ A exciton were obtained from fitting. Values given are the mean and standard deviation obtained from fitting multiple spectra at several excitation energies.

	Raman Shift cm^{-1}			
	1	2	3	4
WSe$_2$ A	34.6±0.1	38.8±1.1	52.9±0.1	57.8±0.5

Table 6.7: Raman Shifts for low frequency peaks observed on HS1 when resonant with the MoSe$_2$ A and B excitons were obtained from fitting. Values given are the mean and standard deviation obtained from fitting multiple spectra at several excitation energies.

	Raman Shift cm^{-1}				
	1	2	3	4	5
MoSe$_2$ A	35.3±0.1	39.1±0.1	42.4±0.1	59.3±0.1	63.5±0.3
MoSe$_2$ B	35.4±0.3	38.9±0.4	42.1±0.2	59.0±0.2	63.8±0.9

resulting mean values and standard deviations obtained from fitting multiple spectra for each peak are provided in Table 6.7 & 6.6. For the low frequency modes when resonant with the MoSe$_2$ A and B excitons the resulting peak positions are in excellent agreement for all peaks. This confirms that the low frequency Raman peaks observed for the MoSe$_2$ A and B exciton are the same peaks with no significant shifts in the peak positions. For the low frequency peaks seen when resonant with the WSe$_2$ A exciton four separate Raman peaks are identified. Comparing the frequencies of these peaks to those in the MoSe$_2$ spectra it is clear that the peaks have different frequencies. The possible exception to this is the peak at 38.8 cm^{-1} which to within the error is in agreement with the peaks observed at 38.9 and 39.1 cm^{-1} when resonant with the MoSe$_2$ excitons. Whilst the Raman spectra clearly have different Raman shifts there is an obvious similarity to the spectra for the low frequency modes when resonant with the MoSe$_2$ and WSe$_2$ layers. In each case there are generally two dominant peaks with one in the range of 20 to 50 cm^{-1} and a higher frequency peak between 50 and 70 cm^{-1}. It also seems clear that the lower intensity peaks in the WSe$_2$ and MoSe$_2$ spectra have similar positions relative to the dominant peaks. A likely explanation is that the low frequency peaks at both the WSe$_2$ and MoSe$_2$ resonances have the same underlying physical mechanism with the Raman peaks shifted as a result of the difference in mass of the two TMDC layers. In this case the peaks associated with the heavier WSe$_2$ layer are expected to have lower frequencies than their MoSe$_2$ counterparts, which is in agreement with our experimental results.

Considering the origin of these peaks an obvious possibility is that they are the result of layer breathing or shear modes arising in the heterostructure. However, results reported by Nayak et al. for eight different twist angles on similar unencapsulated MoSe$_2$/WSe$_2$ heterostructures assigned the peaks associated with the layer breathing and shear modes to peaks in the range of 15 to 30 cm^{-1} [107]. In comparison the low frequency observed in HS1 have frequencies in the range of 34 to 65 cm^{-1} and are different depending on which layer is being excited. Therefore, it is not possible for these peaks to be the result of shear and layer breathing modes as these are collection motions of the two layers and are not dependent on which layer is excited. Another possible mechanism for these low frequency modes is zone folding of off centre acoustic phonons due to moiré interference. moiré phonons have previously been observed in twisted homobilayers of MoS$_2$ for all twist angles [123]. It is possible that the low frequency of the modes for HS1 are the result of moiré phonons, although the lack of similar peaks in HS2 is unexpected. In addition the resonance behaviour of the low frequency modes appears to demonstrate a preferentially coupling to the lower energy trion states. Therefore, to fully address the potential origins of these peaks requires a discussion of both the Raman spectra and the resonance data, and is presented later in this chapter in Section 6.5.2.

In summary, the Raman spectra of the low frequency modes are dependent on which layer is being resonantly excited, with a different characteristic spectrum observed when exciting either the WSe$_2$ or MoSe$_2$ excitons. The similarity of the low frequency modes in the MoSe$_2$ and WSe$_2$ spectra suggests that these peaks likely have the same origin, but are shifted due to the difference in mass of the Mo and W atoms.

6.4 Resonance Raman Spectroscopy of TMDC Heterostructures

The following sections present the resonance Raman data for both HS1 and HS2 using excitation energies from 1.60 to 2.24 eV. In total there are four separate resonances which are addressed corresponding to the $MoSe_2$ A and B excitons and the WSe_2 A and B excitons for each heterostructure.

6.4.1 Resonance Raman with $MoSe_2$ A Exciton

This section presents the resonance Raman data for both HS1 and HS2 using excitation energies from 1.6 to 1.75 eV when resonant with the $MoSe_2$ A exciton. For monolayer $MoSe_2$ it was not possible to observe resonance Raman scattering with the $MoSe_2$ A exciton due to the intense PL emission from the exciton and trions. For the heterostructures the intensity of PL is significantly lower and so resonance Raman data has been obtained for the $MoSe_2$ A exciton. However for both heterostructure regions there are several spectra when near resonance with the PL where it is not possible to resolve the Raman peaks.

6.4.1.1 HS1 Resonance Raman with $MoSe_2$ A Exciton

The Raman data for HS1 when resonant with the $MoSe_2$ A exciton is presented in the colourmap and waterfall plots shown in Figures 6.36 & 6.37 respectively. As seen in Figure 6.36 the resonance Raman data is presented from 1.6 to 1.75 eV, as a result both resonances associated with the $MoSe_2$ A and WSe_2 A excitons are visible in the data. From 1.68 to 1.75 eV the colourmap and spectra are dominated by the WSe_2 Raman peaks which are observed between 250 to 270 cm^{-1}. The resonance features associated with $MoSe_2$ A exciton are observed between 1.62 and 1.71 eV with an incident resonance at $\sim$ 1.64 eV. The outgoing resonance is visible between 1.65 and 1.71 eV with the energy of the resonance dependent on the energy of the phonons. For the Raman peaks near $\sim$ 460 cm^{-1} there is also a significant difference in the intensity of the outgoing resonance at $\sim$ 1.682 eV compared to the incident resonance at $\sim$ 1.636 eV. The asymmetry of these resonances suggests the presence of multiple excitonic states at the $MoSe_2$ A exciton. Another indicator for multiple excitonic states is the characteristic variation in the relative intensity of Raman peaks with similar shifts. This is visible in Figure 6.13 when comparing the Raman peaks between 280 to 320 cm^{-1} at 1.664 and 1.653 eV.

The resonance Raman profiles for eight different peaks at 240.8, 288.3, 303.4, 313.1, 319.8, 450.7, 455.3, 569.7 were obtained when resonant with the $MoSe_2$ A exciton. The Raman peak near 240 cm^{-1} was used to investigate which Raman model provides the

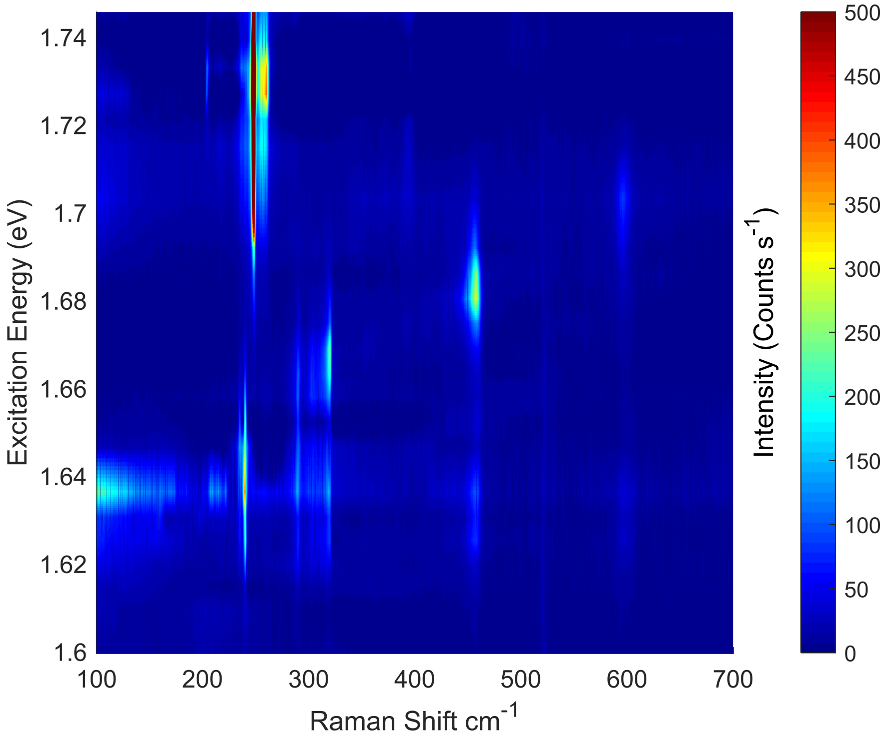

Figure 6.12: Colourmap presenting the resonance Raman data taken obtained on HS1 using excitation energies from 1.60 to 1.75 eV when resonant with the $MoSe_2$ A exciton.

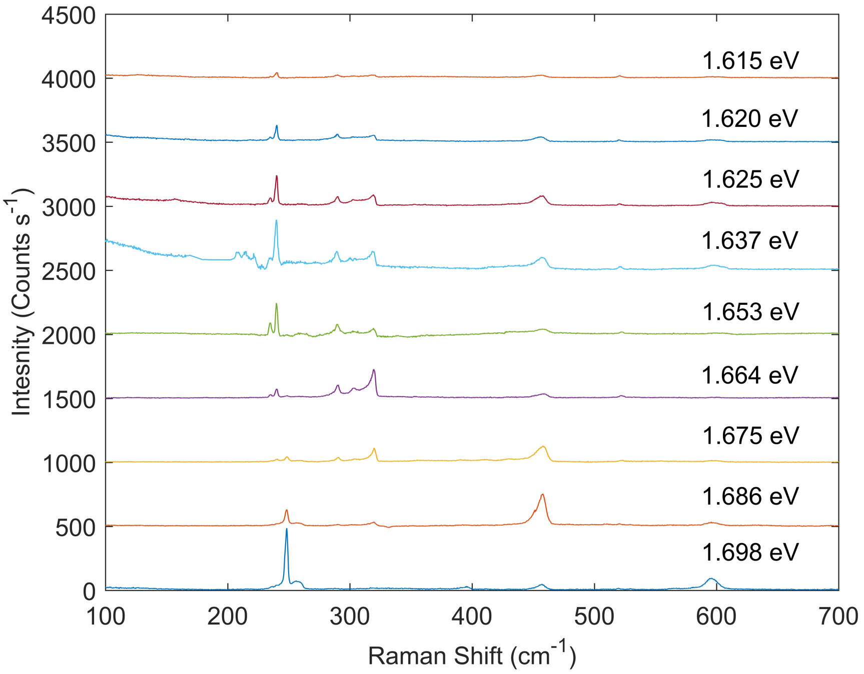

Figure 6.13: Waterfall plot presenting a Raman spectra obtained when resonant with $MoSe_2$ A exciton on HS1 using excitation energies from 1.60 to 1.75 eV.

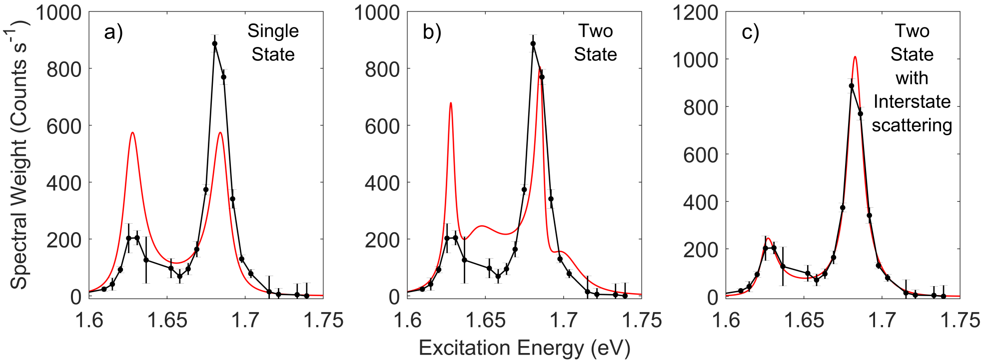

Figure 6.14: Resonance Raman profile for the Raman peak at 455.3 cm^{-1} when resonant with the MoSe$_2$ A exciton is shown and has been fitted to three single phonon event models for a) single electronic state, b) two independent electronic states and c) two electronic states allowing interstate scattering with the fits indicated by the red lines. Errorbars shown were determined from fitting the Raman spectra.

best fit to the data, before extending the process to other resonance profiles. This peak was chosen as it is unambiguously assigned to the $A_1'(\Gamma)$ phonon. Raman scattering by this mode is a single phonon process and so should be well described by the single phonon event models used in the fitting process. However, when resonant with the MoSe$_2$ A exciton intense photoluminescence from the neutral exciton and trion prevents useful Raman spectra being obtained at several excitation energies from 1.640 to 1.655 eV. As a result it is more convenient to consider the resonance behaviour for higher wave number Raman peaks as these profiles have a larger separation between the incoming and outgoing resonance conditions which allows for more complete resonance profiles to be obtained. Therefore, the Raman peak at 455.3 cm^{-1} has been fitted to three single phonon event models for a single electronic state, two independent electronic states and two electronic states with interstate scattering allowed.

The resonance profiles and fits are shown in Figure 6.14 and the adjusted R-square values and fitted coefficients are provided in Table 6.8. The resonance profile for the 455.3 cm^{-1} Raman peak in Figure 6.14 is composed of two peaks at $\sim$ 1.63 and 1.68 eV and has a clear asymmetry with the higher energy peak a factor of 4 more intense. Considering all of the fitted profiles shown in Figure 6.14 a visual comparison of the fits reveals that the best fit for the resonance data is obtained using a Raman model assuming two electronic states with interstate scattering allowed (see Figure 6.14 panel c). The energies from the fitting process are 1.626±0.001 and 1.649±0.009 eV. Comparing these energies to the PL spectra the results are in close agreement with the PL peaks at 1.622 and 1.648 eV which were assigned to the MoSe$_2$ A trion and neutral exciton respectively. Therefore, the resonance Raman behaviour of the 455.3 cm^{-1} Raman peak is due to scattering with both the neutral exciton at 1.648 eV and trion at 1.622 eV.

Table 6.8: Adjusted R-square values and coefficients obtained from fitting the resonance Raman profile for the 455.3 cm^{-1} Raman observed on HS1 when resonant with the MoSe$_2$ A Exciton. Resonance profile has been fitted to three single phonon event models assuming a single state, two independent states and two states with interstate scattering allowed. Errors given are a standard deviation from the fitting process. Amplitude coefficients have units of 10^{-3} $\sqrt{Counts\ s^{-1} \cdot eV^2}$.

		Single State	Two State	Two \w scatter
	Adjusted R-Square	0.528	0.579	0.996
	A$_1$	9.5±2.2	3.4±1.1	0±1.3
Amplitude	A$_2$	-	11.1±7.1	12.8±9.6
	A$_3$	-	-	7.9±1.1
Width	Γ$_1$	6.8±2.1	3±NaN	6.0±0.3
	Γ$_2$	-	15.5±12.2	22.6±13.4
Energy	E$_1$	1.627±0.002	1.628±0.001	1.626±0.001
	E$_2$	-	1.642±0.008	1.649±0.009

The resonance profiles for all Raman peaks were fitted to a single phonon event model assuming two electronic states with interstate scattering allowed. The resonance profiles and resulting fits are presented in Figure 6.15 with the coefficients from fitting provided in Table 6.9. The energies for the lower energy state E$_1$ are in good agreement with values between 1.624 to 1.628 eV and a mean value of 1.627±0.001 eV. The higher energy state E$_2$ is less well bounded with some coefficients having errors exceeding 10 meV. However the values for this energy still show a general agreement with energies between 1.644 and 1.655 eV and a mean value of 1.648 ±0.001 eV. Although the variation in the energies of the higher energy state may indicate the presence of multiple excitonic states. However, in this instance the variation in the energy of E$_2$ is likely due to the absence of several data points between 1.637 and 1.655 eV, which were excluded due to the intense photoluminescence from the MoSe$_2$ A exciton. Therefore, when resonant with the MoSe$_2$ A exciton on HS1 there are at least two electronic states present with energies of 1.627±0.001 and 1.648±0.005 eV respectively. These energies are in good agreement with the neutral exciton and trions peaks identified in photoluminescence spectra (see Figure 6.1), and are in agreement with reported energies in literature [244, 235, 245].

Table 6.9: Coefficients from fitting the resonance Raman profiles on HS1 when resonant with MoSe$_2$ A exciton. Resonance profiles have been fitted to a single phonon event model assuming two electronic states with interstate scattering allowed. Errors given are a standard deviation determined from the fitting process. Amplitude coefficients have units of $10^{-3}\ \sqrt{Counts\ s^{-1} \cdot eV^2}$.

	Amplitude			Width (meV)		Energy (eV)	
Raman Shift (cm^{-1})	A$_1$	A$_2$	A$_3$	Γ_1	Γ_2	E$_1$	E$_2$
240.8	6.9±1.2	20.8±11.6	8.2±2.3	6.6±4.3	43.2±26.5	1.624±0.001	1.641±0.007
288.3	3.3±0.6	3.3±2.2	1.2±0.9	12.6±1.5	20.7±12.6	1.623±0.001	1.654±0.008
303.4	5.1±0.6	0.3±0.1	0.9±0.2	10.5±1.3	4.9±3.1	1.627±0.001	1.651±0.001
313.1	3.3±0.2	2.1±0.4	1.3±0.2	8.1±0.6	8.2.7±2.1	1.626±0.001	1.652±0.011
319.8	0	9.5±2.2	6.3±1.0	6.7±0.7	19/7±9.1	1.628±0.001	1.650±0.006
450.7	0	10.7±3.6	6.8±1.4	6.5±0.4	24.1±3.0	1.626±0.001	1.646±0.007
455.3	0	13.2±2.4	8.0±0.9	6.1±0.3	21.1±9.1	1.626±0.001	1.649±0.002
599.7	0	13.7±4.2	9.8±1.6	7.4±0.7	19.4±11.7	1.626±0.001	1.649±0.002

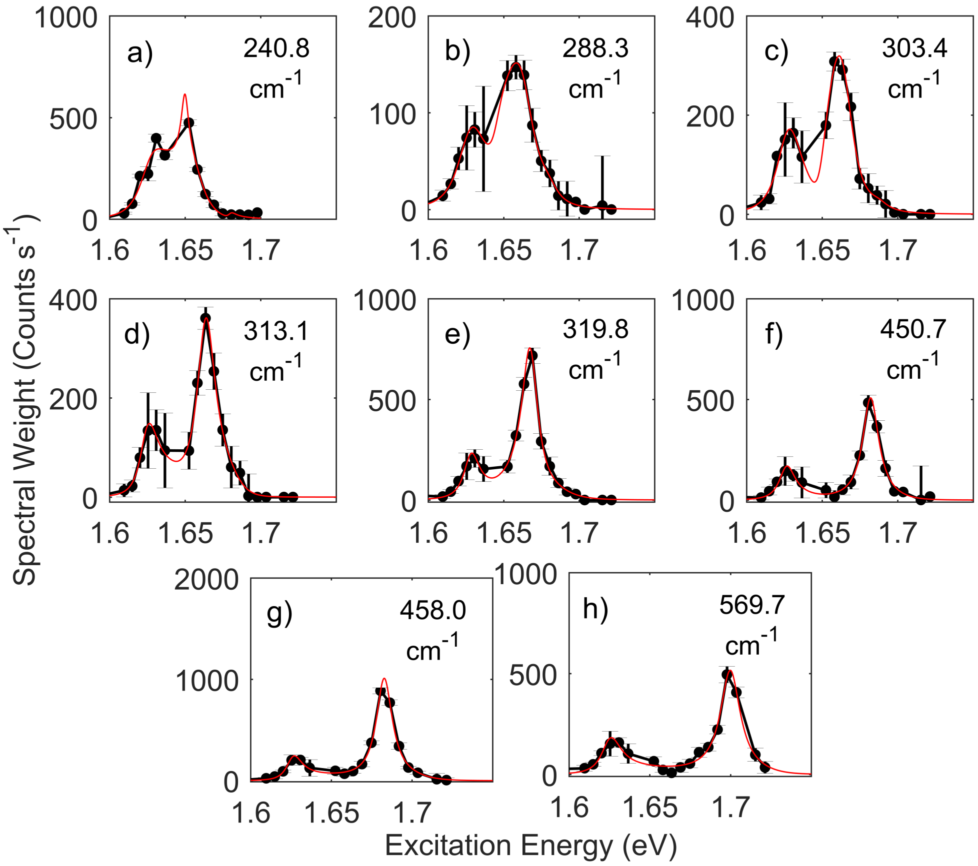

Figure 6.15: Resonance Raman profiles obtained for the Raman peaks observed on HS1 when resonant with the $MoSe_2$ A exciton are presented. In each case the resonance profiles have been fitted to a single phonon event model assuming two electronic states allowing interstate scattering with the fitted profiles indicated by the red lines. Error bars shown were determined from fitting the Raman spectra.

6.4.1.2 HS2 Resonance Raman with $MoSe_2$ A Exciton

The resonance Raman data for HS2 when resonant with the $MoSe_2$ A exciton using excitation energies from 1.6 to 1.75 eV is presented in this section. In this case the analysis of the data is more limited due to difficulty resolving the Raman signal from the PL background. Previously in this Chapter and those presenting the data for monolayer $MoSe_2$ and WSe_2 (Chapters 4 & 5) photoluminescence has been removed by subtracting crossed and parallel polarised Raman spectra. For the data presented in this section both polarisation resolved measurements and fitting of the background to a combination of a higher order polynomial and Gaussian line shapes were used. However, for several spectra when resonant with the $MoSe_2$ A exciton the PL is too intense to resolve the Raman peaks and so these spectra were excluded from the presented data.

Considering the colourmap and waterfall plot presented in Figures 6.16 & 6.17 both the WSe_2 A exciton and $MoSe_2$ A exciton resonances are clearly visible. In Figure 6.16 the WSe_2 A exciton is resonant between 1.67 to 1.72 eV and the $MoSe_2$ A exciton is resonant in the range of 1.6 to 1.7 eV. Considering the Raman peaks associated with the $MoSe_2$ layer there is an obvious resonance centred at $\sim$ 1.644 eV with peaks near 300 and 460 cm^{-1} also resonant at $\sim$ 1.683 eV. In general the higher energy resonance peaks observed in this thesis are typically associated with an outgoing resonance condition, with the energy of the peak dependent on the phonon energy. In this instance the higher energy resonance appears at the same energy for all of the Raman peaks and so does not appear to be an outgoing resonance. The Raman peaks near $\sim$ 460 cm^{-1} also have an asymmetric resonance behaviour. This asymmetry suggests that there are multiple excitonic states contributing to the resonance process. This is also apparent in the spectra presented in Figure 6.17 at 1.685 eV where the peaks near $\sim$ 460 cm^{-1} are significantly stronger than at lower energies.

As discussed in Section 6.3.2 an additional Raman peak at 245.8 cm^{-1} is observed on HS2 when near resonance with the $MoSe_2$ and WSe_2 A excitons. The assignment process revealed that is not possible to provide a definite assignment to either $MoSe_2$ or WSe_2 phonons for this peak. The exemplar spectra in Figure 6.18 show the typical spectra associated with the WSe_2 A and $MoSe_2$ A excitons at 1.757 eV and 1.632 eV along with an intermediate spectra at 1.685 eV. The spectra at 1.685 eV is of interest due to the presence of both $MoSe_2$ and WSe_2 Raman peaks and the emergence of the new peak at 245.8 cm^{-1}, which is not observed at any other resonance with either WSe_2 or $MoSe_2$ intralayer excitons. This peak is observed exclusively on HS2 and is not seen in HS1 or either of the monolayer samples. Whilst the origin of the 245.8 cm^{-1} Raman peak is uncertain in regards to which layer it is associated with the analysis of its resonance behaviour will be presented in this section.

In this case the resonance Raman profiles have been obtained for the Raman peaks at 240.8, 320.5, 455.3 cm^{-1} which are unambiguously associated with the $MoSe_2$ layer.

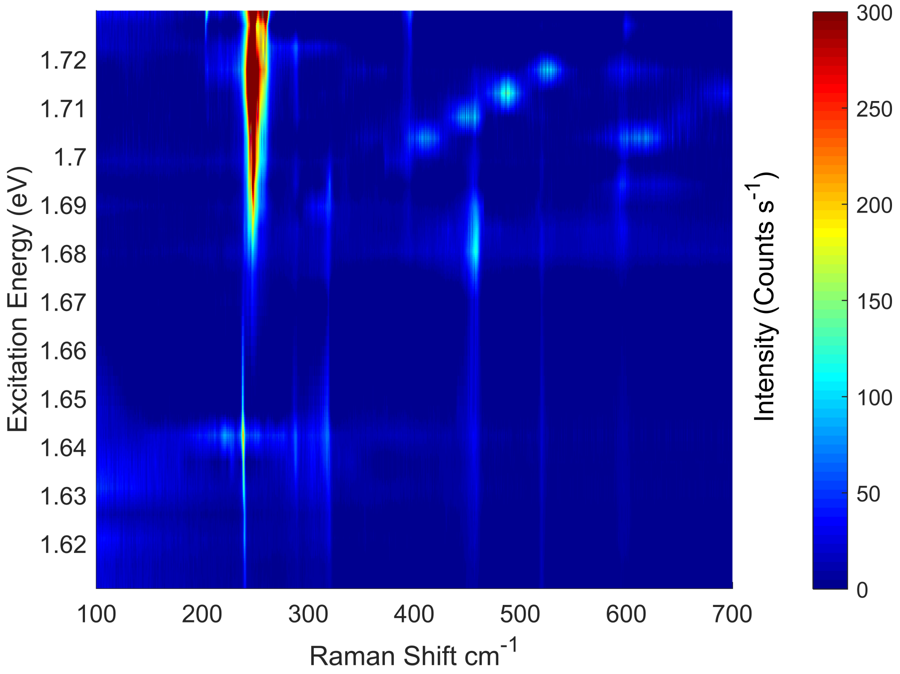

Figure 6.16: Colourmap presenting the resonance Raman data for HS2 using excitation energies from 1.60 to 1.75 eV and is resonant with the $MoSe_2$ A exciton.

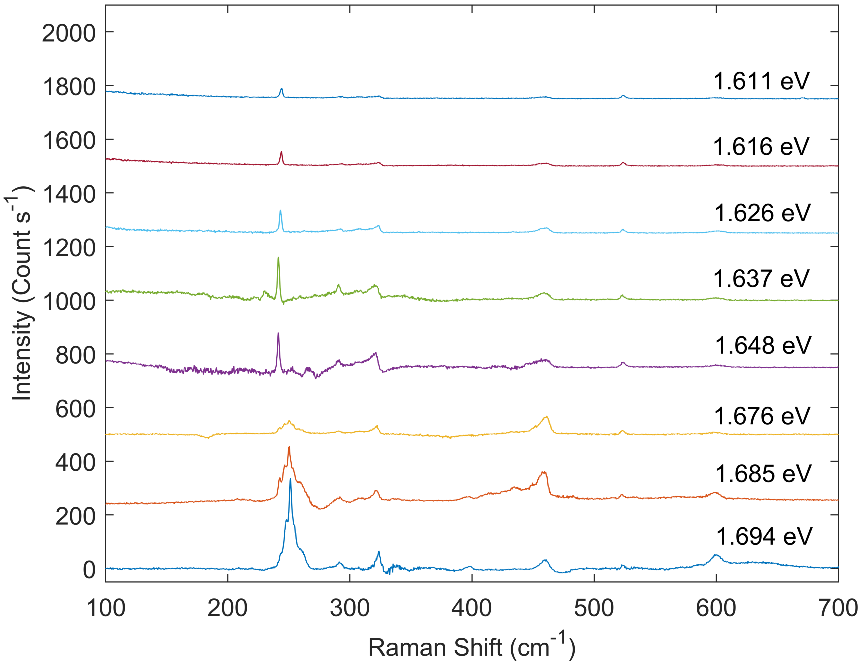

Figure 6.17: Waterfall showing Raman spectra obtained when resonant with $MoSe_2$ A exciton on HS2 using excitation energies from 1.60 to 1.75 eV.

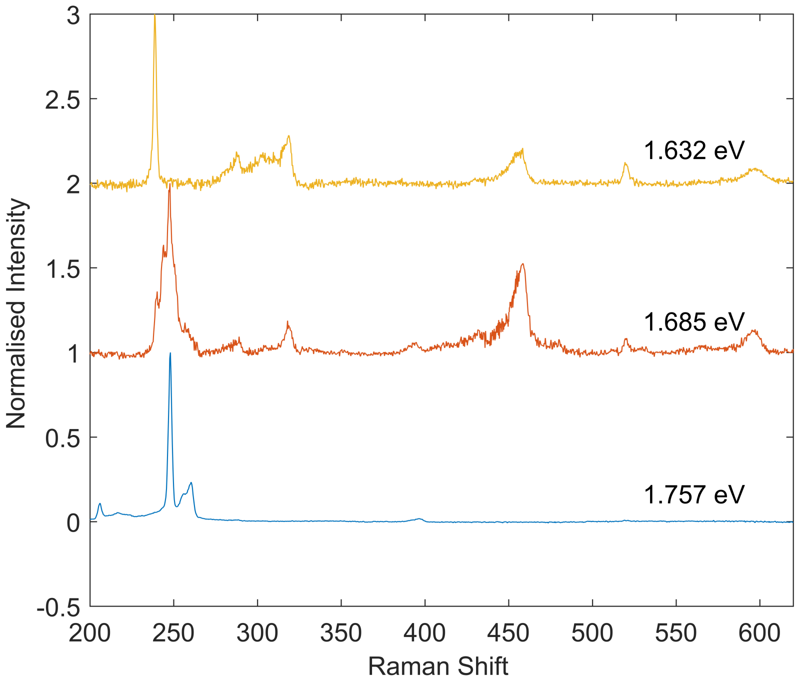

Figure 6.18: Raman spectra presented were obtained using excitation energies of 1.632, 1.685 and 1.757 eV and the spectra have been offset and normalised to the maximum intensity in each case. The spectra at 1.632 and 1.757 eV appear to show the spectra typically seen when resonant with the $MoSe_2$ monolayer and WSe_2 monolayer respectively. Whereas at 1.685 eV the spectra contains both $MoSe_2$ and WSe_2 Raman peaks with a new Raman peak appearing at 245.8 cm^{-1}.

Whilst, three additional peaks are observed on HS2 when resonant with the $MoSe_2$ A exciton (see Table 6.4), it is not possible to resolve their resonance profiles due to their low intensity. In addition the anomalous Raman peak at 245.8cm^{-1} resonance profile is also obtained. The resonance profiles are presented in Figure 6.19 and were all fitted using a single phonon event model. The obtained coefficients from fitting are provided in Table 6.10. Considering first the 240.8 cm^{-1} peak profile in Figure 6.19 panel a) in this case data is shown from 1.6 to 1.7 eV, but is not shown for higher energies due to the presence of the WSe_2 A exciton resonance and WSe_2 Raman peaks. The resonance profile for the 240.8 cm^{-1} peak is relatively broad and centred at $\sim$ 1.645 eV. In addition for several data points it is not possible to resolve the 240.8 cm^{-1} peak and so no data points are available 1.648 to 1.665 eV, which handicaps the fitting process. Nonetheless the resonance profile for the 240.8 cm^{-1} was fitted to a single phonon event model assuming a single electronic state. The energy from fitting for this peak is 1.627±0.003 eV. A comparison of the fitted profile in Figure 6.19 panel a) shows that the fit is not ideal as the width of the fitted profile is too broad and unable to describe the low energy shoulder near 1.624 eV. This suggests the resonance profile is the result of multiple excitonic states. However, attempts to fit the profile using two state models failed due

Table 6.10: Coefficients were obtained from fitting the resonance profiles for HS2 when resonant with the $MoSe_2$ A Exciton. Errors given are a standard deviation from the fitting process. Amplitude coefficients have units of 10^{-3} $\sqrt{Counts\ s^{-1} \cdot eV^2}$.

	Amplitude			Width (meV)		Energy (eV)	
Raman Shift (cm^{-1})	A_1	A_2	A_3	Γ_1	Γ_2	E_1	E_2
240.8	7.5±4.6	-	-	14.2±7.8	-	1.627±0.003	-
320.5	12.7±9.3	8.3±3.0	7.1±2.7	20.1±11.4	11.9.4±5.5	1.626±0.008	1.657±0.003
455.3	0.2±0.1	5.4±1.8	6.5±1.4	11.7±0.7	15.3±3.1	1.631±0.001	1.655±0.003
245.8	8.2±1.0	10.4±1.4	7.8±1.4	5.3±0.6	20.7±2.9	1.688±0.001	1.703±0.002

to the lack of data points between 1.65 to 1.665 eV. Therefore for the 240.8 cm^{-1} peak we conclude it is resonant with an electronic state at 1.627±0.003 eV but is also likely to be resonant with a higher energy state the energy of which cannot be determined from this dataset.

The remaining resonance profiles for the 320.5, 455.3 cm^{-1} and anomalous peak at 245.8 cm^{-1} in Figure 6.19 all show significant asymmetry. The profile for the 320.5 cm^{-1} Raman peak shows a broad resonance at $\sim$ 1.65 eV with a high energy shoulder at $\sim$ 1.69 eV, whereas, for the 455.3 cm^{-1} peak profile there is a significant peak at $\sim$ 1.68 eV with a low energy shoulder between 1.66 to 1.6 eV. The anomalous resonance then shows clearly different behaviour with a peak at $\sim$ 1.716 eV and a low energy tail from 1.675 to 1.700 eV. The asymmetry observed for each of the three resonance Raman profiles is then best fit by a two state model with interstate scattering allowed. The fitted profiles for the 455.3 and 245.8 cm^{-1} Raman peak show good agreement with the data and are able to reproduce the asymmetry and low energy shoulders. For the 320.5 cm^{-1} Raman peak the lower energy peak is well described by the fitted model although the higher energy shoulder at 1.69 eV is not reproduced by the fit.

For the Raman peaks at 320.5 and 455.3 cm^{-1} the energies obtained for lowest energy state are 1.633±0.003 and 1.625±0.001 eV with the higher energy state having values of 1.652±0.004 and 1.648±0.003 eV respectively. The energies for the higher energy state are in good agreement and consistent with the Raman peak identified in PL spectra at 1.649 eV and assigned to the neutral A exciton in $MoSe_2$. The energy of the lower energy state for the 455.3 cm^{-1} resonance is in agreement with the PL peak assigned to the $MoSe_2$ trion at 1.622 eV. This assignment is in agreement with the energies obtained from fitting the 320.5 cm^{-1} peak. Overall the resonance profiles for the $MoSe_2$ Raman peaks at 240.8, 320.5 and 455.3 cm^{-1} show clear evidence of multiple electronic states contributing to the resonance behaviour at the $MoSe_2$ A exciton. The higher energy state identified in fitting is in agreement with the observed energies of the neutral $MoSe_2$ A exciton, with the lower energy state attributed to the trion. Therefore the resonance behaviour for the $MoSe_2$ Raman peaks at the A exciton involves both the neutral exciton and trion.

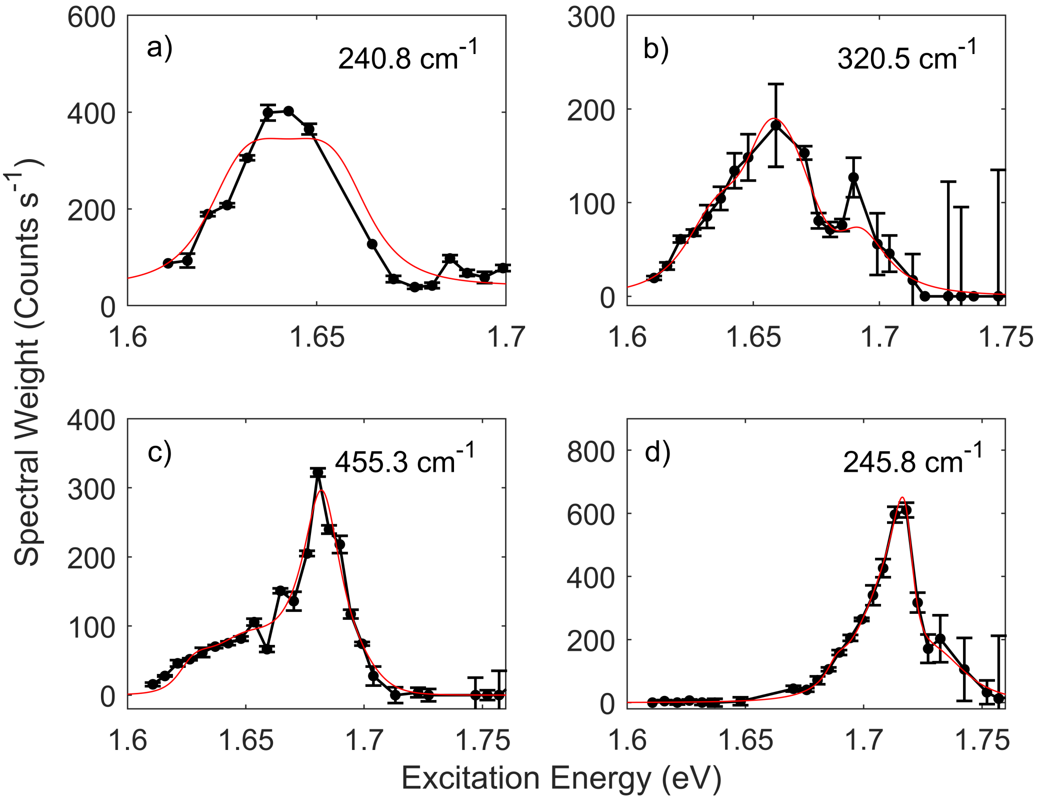

Figure 6.19: Resonance Raman profiles are presented for the Raman peaks observed on HS2 when resonant with the MoSe$_2$ A Exciton. Panel a) shows resonance profile for the 240.8 cm^{-1} peak along with the fitted profile given by the red line and obtained from fitting to a single phonon event model assuming a single electronic state. Panels c-d show the resonance profiles for the 320.5, 455.3 and 245.8 cm^{-1} Raman peaks and their fitted profiles indicated by the red line and were obtained from fitting to a single phonon model for a two state model with interstate scattering allowed. Error bars shown were determined from fitting the Raman spectra.

Finally the anomalous Raman peak at 245.8 cm^{-1} resonance profile is considered. The resonance profile contains significant asymmetry, but is well fitted by a single phonon event model assuming two electronic states with interstate scattering allowed. The energies obtained from fitting are then 1.688 and 1.703 eV. These energies are significantly higher than those observed for the MoSe$_2$ A exciton and trion. The higher energy state at 1.703 eV is in agreement with the energy of WSe$_2$ A intra-valley trion and so suggests the 245.8 cm^{-1} is resonant with the WSe$_2$ layer. The lower energy state at 1.688 eV may also be due to a state in the WSe$_2$ layer. As a result, to fully consider the behaviour of this Raman peaks requires a discussion of both the MoSe$_2$ and WSe$_2$ A exciton resonances on HS2 and will be presented in Section 6.5.1.

6.4.2 Resonance Raman with WSe_2 A Exciton

This section presents the resonance Raman data on both HS1 and HS2 using excitation energies from 1.7 to 1.8 eV. In the constituent monolayers resonances in this energy range were attributed to the WSe_2 neutral A exciton as presented in Chapter 5.

6.4.2.1 HS1 Resonance Raman with WSe_2 A Exciton

For HS1 the Raman data when resonant with the WSe_2 A exciton is shown in Figures 6.20 & 6.21 for excitation energies between 1.68 and 1.82 eV. Due to the proximity to the $MoSe_2$ A exciton (near $\sim$ 1.65 eV) there are several Raman peaks visible in Figure 6.20 which are associated with the the $MoSe_2$ A exciton. This can be seen between 1.68 and 1.71 eV with the $MoSe_2$ Raman peaks at 319.8, 455.3 and 596.7 cm^{-1} visible. The WSe_2 Raman peaks are resonant between 1.69 and 1.79 eV with the Raman peak at 248.8 cm^{-1} dominating the Raman spectra and is visible in Figures 6.20 & 6.21. There are also several weaker WSe_2 Raman peaks near $\sim$ 260 and 400 cm^{-1}, which are also resonantly enhanced. In addition to the BS Raman peaks a dispersive Raman peak near $\sim$ 207 cm^{-1} is observed. The low intensity of this peak relative to the 248.8 cm^{-1} makes is difficult to see visually in Figures 6.20 & 6.21, but is clearly evident in the Raman spectra shown in Figure 6.8. This peak appears to be resonant at lower energies that the other WSe_2 Raman peaks. For all of the WSe_2 Raman peaks the resonance behaviour seen in Figures 6.20 & 6.21 suggests a single broad resonance with no obvious signs of multiple electronic states.

Resonance profiles for the Raman peaks at 206.2, 219.0, 236.7, 240.3, 248.8, 256.5, 260.4 and 287.2 cm^{-1} were obtained when resonant with the WSe_2 A exciton on HS1. There are also several Raman peaks which were identified in Section 6.3.2, but were too weak to extract their resonance behaviour. To analyse the resonance Raman behaviour the resonance profile for the 248.8 cm^{-1} Raman peak was fitted to three single phonon event models assuming a single electronic state, two independent electronic states and two states with interstate scattering allowed. The resonance profile for the 248.8 cm^{-1} peak and the resultant fits are presented in Figure 6.22 with the adjusted R-square values and coefficients obtained from fitting provided in Table 6.11. As seen in Figure 6.22 the resonance profile for the 248.8 cm^{-1} Raman peak has a broad resonance characterised by two peaks at $\sim$ 1.713 and 1.732 eV and is asymmetric. The asymmetry of the resonance profiles suggests the involvement of multiple excitonic states. From the fitted profiles in Figure 6.22 it is clear that the single state model is unable to account for the asymmetry of the resonance profile. Therefore, a single state model cannot explain the resonance behaviour. Whereas, the two state models show improved fits to the resonance profile and are able to account for the asymmetry. The adjusted R-square values indicate the best fit for the 248.8 cm^{-1} peak profile is to a two state model assuming interstate

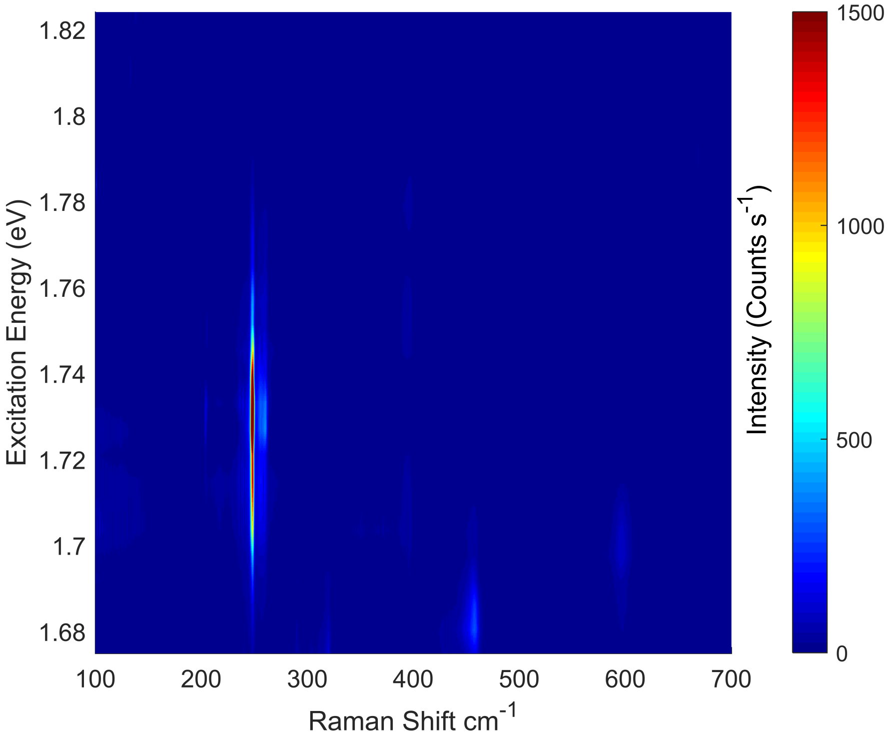

Figure 6.20: Colourmap presenting the resonance Raman data obtained for HS1 using excitation energies from 1.68 to 1.82 eV and is resonant with the WSe_2 A exciton.

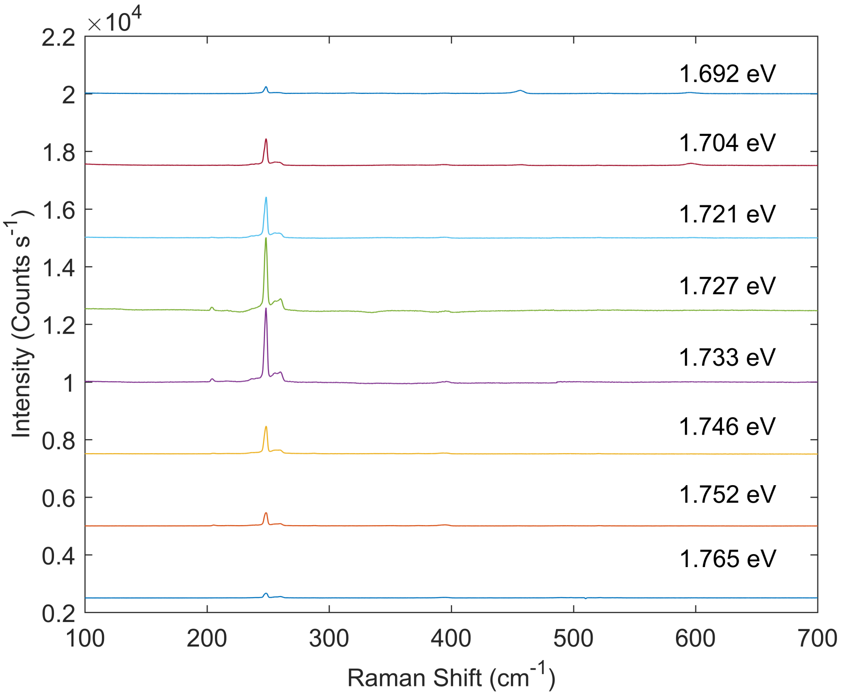

Figure 6.21: Waterfall plot showing Raman spectra obtained when resonant with WSe_2 A exciton on HS1 using excitation energies from 1.68 to 1.82 eV.

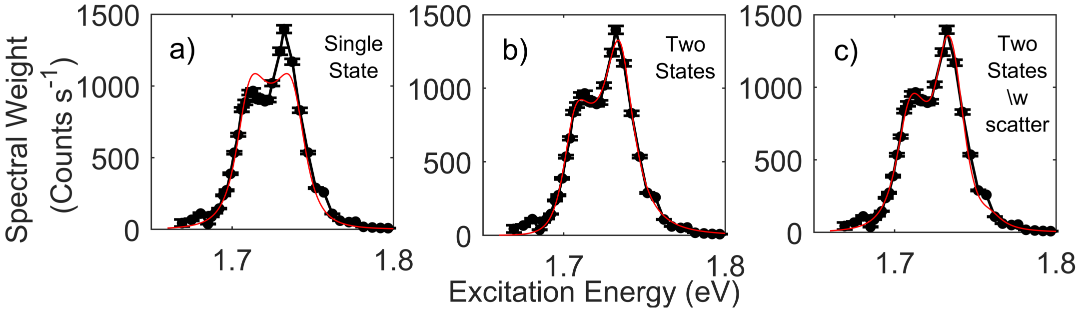

Figure 6.22: The resonance Raman profile obtained from fitting the 248.8 cm^{-1} Raman peaks observed for HS1 when resonant with the WSe_2 A exciton. The resonance profile has been fitted using three single phonon event model assuming a) a single electronic excitation, b) two independent electronic excitations and c) two underlying electronic excitations and with interstate scattering allowed.

		Single	Two States	Two States Scatter
	Adjusted R-Square	0.952	0.992	0.995
Amplitude	A_1	12.3±1.0	13.2±0.6	13.8±1.1
	A_2	-	25.5±2.1	8.8±2.2
	A_3	-	-	7.3±1.5
Width (meV)	Γ_1	12.0±1.1	11.1±0.4	11.7±0.5
	Γ_2	-	55.2±0.1	6.5±1.1
Energy (eV)	E_1	1.709±0.001	1.704±0.001	1.707±0.001
	E_2	-	1.705±0.001	1.728±0.002

Table 6.11: Adjusted R-square values and coefficients obtained from fitting the 248.8cm^{-1} Raman peak on HS1 when resonant with the WSe_2 A Exciton. Resonance profile has been fitted to three Raman scattering models assuming a single phonon event model for a single electronic excitation, two independent electronic excitations and two electronic excitations with interstate scattering allowed. The errors given for each coefficient are a standard deviation obtained from fitting. The units for the amplitude coefficients are $10^{-3}\ \sqrt{Counts\ s^{-1} \cdot eV^2}$.

scattering. Therefore, the resonance Raman behaviour of the 248.8 cm^{-1} Raman peak is the result of contributions from two electronic states at 1.707 and 1.728 eV.

Following the analysis of the 248.8 cm^{-1} resonance behaviour the resonance Raman profiles for the other Raman peaks have also been fitted to a single phonon event model assuming two electronic states with interstate scattering allowed. The resonance profiles and resulting fits for all Raman peaks are presented in Figure 6.23 and the coefficients obtained from fitting are provided in Table 6.12. The resonance profiles for the Raman peaks at 238.8, 243.2, 256.5, 260.4 cm^{-1} have a similar appearance to the 248.8 cm^{-1} resonance profile and are all well fitted by the two state model. Whereas, the resonance profiles for the peaks at 219.0 and 287.2 cm^{-1} show a more prominent peak at $\sim$ 1.74 eV and a low energy shoulder between 1.70 and 1.73 eV. The resonance profiles for these peaks are also well fitted by the two state model. The only Raman peak which does not produce a good fit to the two state model is the dispersive Raman peak near $\sim$ 207

Table 6.12: Coefficients obtained from fitting the resonance profiles for the Raman peaks observed on HS1 when resonant with the WSe$_2$ A exciton. Resonance profiles have been fitted to a single phonon event model for two electronic excitations with interstate scattering allowed. The errors given for each coefficient are a standard deviation obtained from fitting. The units for the amplitude coefficients are $10^{-3}\ \sqrt{Counts\ s^{-1} \cdot eV^2}$.

	Amplitude			Width (meV)		Energy (eV)	
Raman Shift (cm^{-1})	A$_1$	A$_2$	A$_3$	Γ_1	Γ_2	E$_1$	E$_2$
207.1	1.3±0.4	0.7±0.3	0.6±0.3	12.2±3.6	2.9±0.9	1.720±0.004	1.734±0.001
219.0	3.2±0.4	0.5±0.1	0.3±0.1	13.4±1.5	4.8±0.5	1.707±0.001	1.730±0.001
238.3	3.1±0.2	0.4±0.1	0.1±0.1	9.8±0.6	2.6±0.3	1.707±0.001	1.732±0.001
243.2	5.1±0.7	0.1±0.1	0.4±0.2	18.1±2.0	5.4±1.5	1.704±0.001	1.734±0.001
248.8	13.8±1.1	8.8±2.2	7.3±1.5	11.7±0.5	6.5±1.1	1.707±0.001	1.728±0.002
256.5	12.7±0.6	5.2±1.7	5.7±1.5	11.3±0.5	5.8±1.6	1.706±0.001	1.734±0.002
260.4	6.8±0.6	3.4±0.9	3.1±0.7	12.0±0.7	5.5±1.0	1.706±0.001	1.732±0.001
287.2	4.2±0.9	1.7±0.6	2.2±0.8	10.2±2.6	8.5±2.7	1.704±0.002	1.736±0.002

cm^{-1}. However, this is not unexpected as a dispersive Raman peak requires multiple scattering events and so should not be well described by a single phonon event model.

Considering the coefficients obtained from fitting in Table 6.12 the energies and widths appear to be in reasonable agreement. The lower energy states E$_1$ is in the range of 1.704 to 1.707 and is in agreement to within the errors from fitting with a mean value of 1.706±0.001 eV. For the higher energy state E$_2$ the energies are in also in agreement to within the errors with a mean value of 1.732±0.003 eV. The separation of these two electronic states is 26 meV. From photoluminescence measurements the neutral A exciton and trion were attributed to peaks at 1.729 and 1.704 eV with a separation of 25 meV. Therefore, the higher energy state at 1.732 eV is attributed to the WSe$_2$ neutral A exciton and the 1.707 eV peak to the trion. The widths obtained from fitting the resonance profiles are is close agreement for with the widths of the trion state between 9.8 to 18.1 meV and the width of the neutral exciton between 2.6 to 8.5 meV. This suggests that the trion state is $\sim$ a factor of two broader than the neutral exciton. A possible explanation is the trion state involves both the intra-valley and inter-valley trions in WSe$_2$, which are well separated in PL of monolayer WSe$_2$ [258, 92].

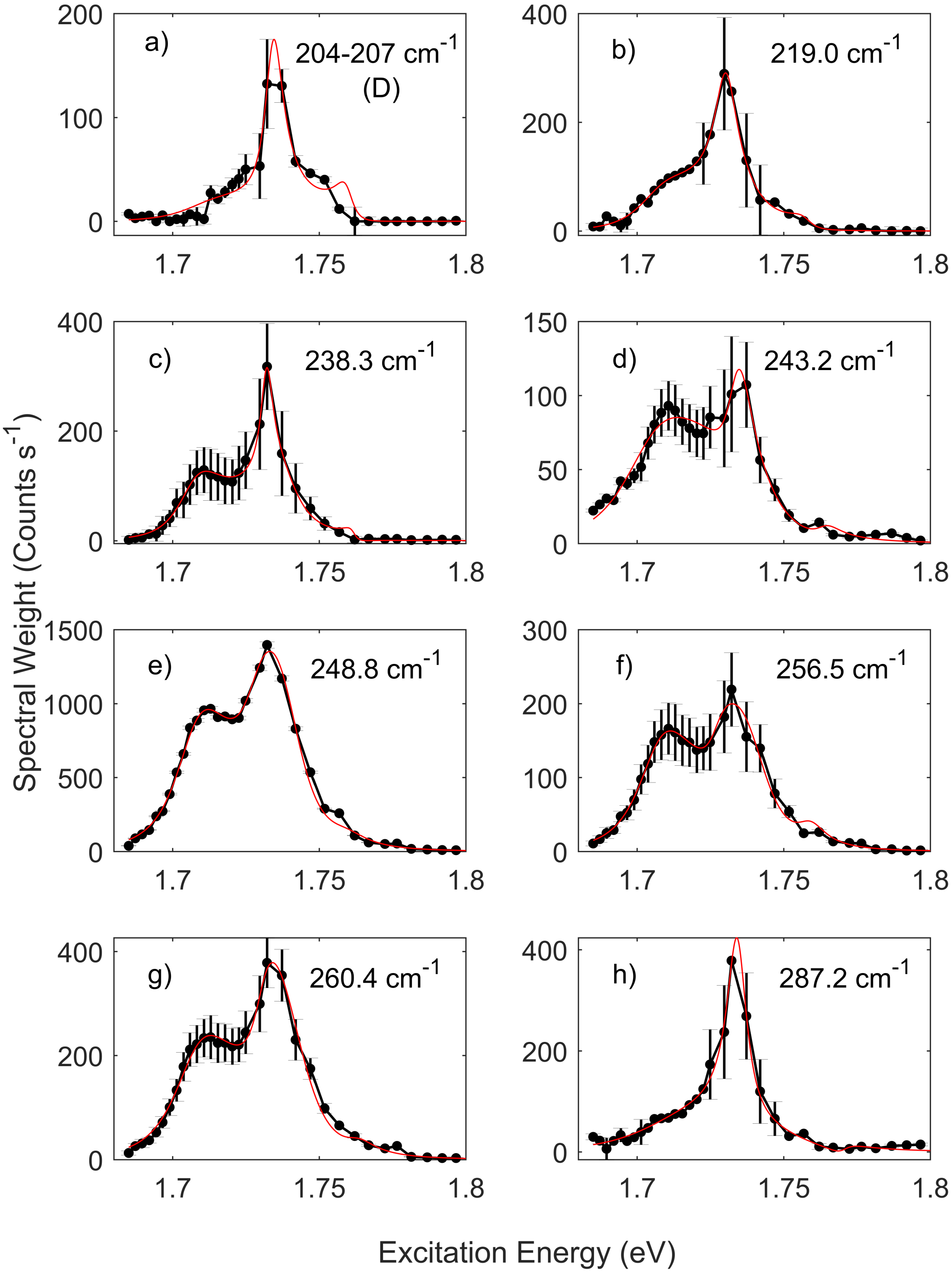

Figure 6.23: Resonance Raman profiles obtained from fitting Raman peaks observed for HS1 when resonant with the WSe_2 A exciton. Each profiles has been fitted using a single phonon event model assuming two underlying electronic excitations and allowing scattering between the two states.

6.4.2.2 HS2 Resonance Raman with WSe_2 A Exciton

The Raman data for HS2 when resonant with the WSe_2 A exciton is presented in Figures 6.24 & 6.25. In Figure 6.24 a clear resonance is observed between 1.73 to 1.77 eV with the peak at the 249.0 cm^{-1} the most intense. For the 249.0 cm^{-1} peak there is a splitting of the resonance with two peaks at $\sim$ 1.737 and 1.765 eV, along with a low energy tail from 1.73 to 1.68 eV. Similar resonance behaviour can also be seen for the peaks near $\sim$ 260 cm^{-1}. A dispersive Raman peak is also visible in the colourmap with a Raman shift ranging from 204 to 208 cm^{-1}, and is resonant between 1.73 and 1.76 eV. These features are visible in the Raman spectra presented in Figure 6.25 with the dispersive peak shifting as a function of excitation energy. A weak Raman peak is also observed near 400 cm^{-1}, however, this peak is difficult to resolve due to the photoluminescence background present when resonant with the WSe_2 A exciton.

To quantify the resonance behaviour profiles were obtained for the Raman peaks at 207.3, 249.0, 257.0 and 261.2 cm^{-1}. Although, there are several other peaks identified in the Raman spectra for HS2 when resonant with the WSe_2 A exciton (see Table 6.5) these peaks have a low intensity and so it is not possible to extract reliable resonance profiles. As with previous resonances the behaviour of the Raman peak at 249 .0cm^{-1} peak is investigated first to determine the best model for fitting. This peak was chosen due to its assignment to the A_1' or E' Raman peaks and so is the result of a single phonon process. As a result this peak should be well described by a single phonon event model. The resonance data has been fitted to three single phonon event models assuming a single electronic state, two independent electronic states and two electronic states with interstate scattering allowed. The resonance profiles and resulting fits are presented in Figure 6.26 with the adjusted R-square and coefficients from fitting provided in Table 6.13.

As seen in the resonance profile in Figure 6.26 there are two clear peaks at $\sim$ 1.733 and 1.766 eV that are asymmetric along with a low energy shoulder below 1.720 eV. Comparing the fitted profile in Figure 6.26 panel a) it is clear that a single electronic state is unable to account for the asymmetry of the peaks or the low energy shoulder. The fitted profiles obtained for the two state models in Figure 6.26 panels b & c produce show a significant improvement with each fit able to account for the asymmetry of the resonance and the low energy shoulder. The adjusted R-square values in Table 6.13 are unable to differentiate between the two fits in this case with both having a value of 0.984. To determine which of these models provides the best fit requires an examination of the coefficients obtained from fitting. An obvious difference between the two models is the widths obtained from fitting. The widths for the higher energy states are relatively consistent with values of 7.3 and 7.6 meV for the two independent state model and two state model with interstate scattering respectively. Whereas, the lower energy state has significantly different widths with values of 39.3 meV and 7.653 meV obtained for the

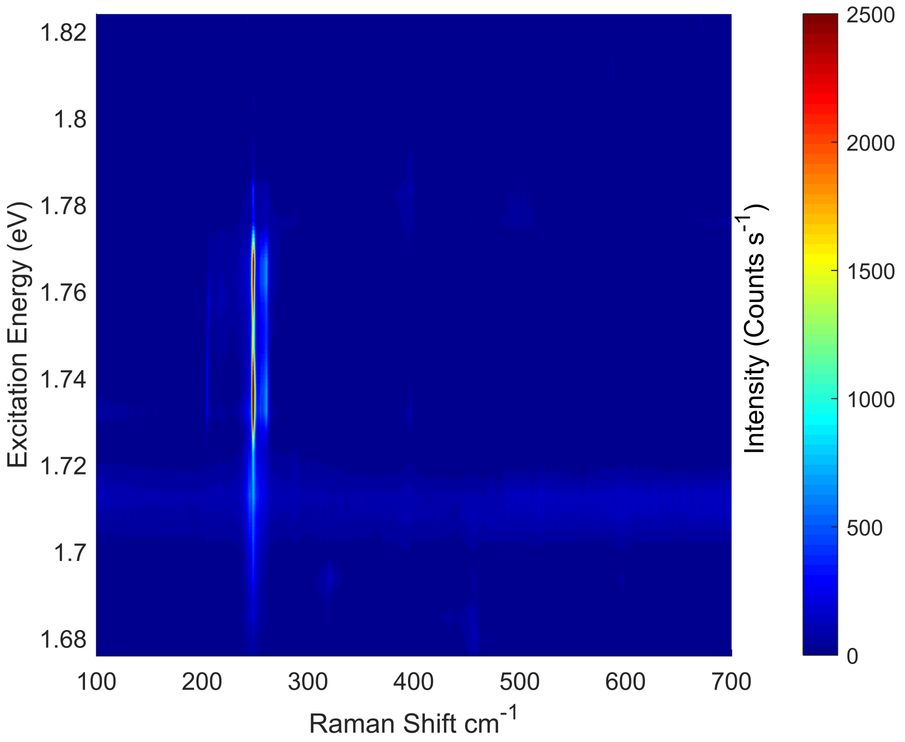

Figure 6.24: Colourmap showing resonance Raman data taken on HS2 using excitation energies from 1.68 to 1.82 eV probing the WSe$_2$ A exciton.

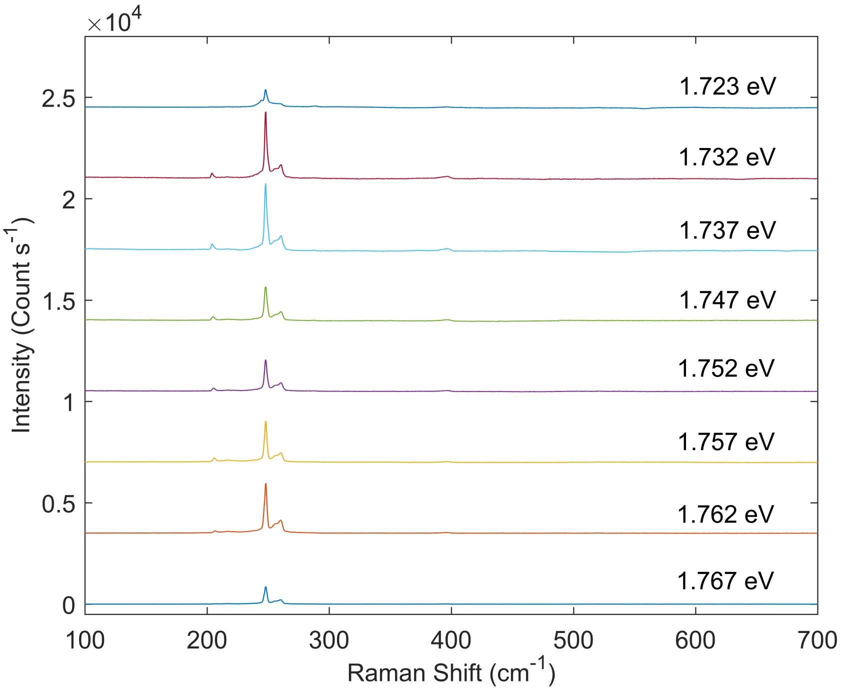

Figure 6.25: Raman spectra obtained when resonant with WSe$_2$ A exciton on HS2 using excitation energies from 1.68 to 1.82 eV.

Model	Single State	Two State	Two State with Scatter
Adjusted R-square	0.930	0.984	0.984
A_1	-	27.3±17.0	4.0±2.3
A_2	13.6±0.7	14.0±1.1	12.5±1.7
A_3	-	-	0.5±0.4
Γ_1	-	39.3±16.8	4.8±2.2
Γ_2	7.2±0.5	7.3±0.4	7.0±0.6
E_1	-	1.690±0.006	1.701±0.001
E_2	1.734±0.001	1.735±0.001	1.736±0.001

Table 6.13: Adjusted R-Square values and coefficients from fitting the resonance profile for the 249.0 cm^{-1} Raman peak observed on HS2 when resonant with the WSe_2 A exciton. Resonance profile has been fitted to three single phonon event models assuming a single electronic excitation, two independent electronic excitations and two electronic excitations with interstate scattering allowed.The errors given for each coefficient are a standard deviation obtained from fitting. The units for the amplitude coefficients are $10^{-3}\ \sqrt{Counts\ s^{-1} \cdot eV^2}$.

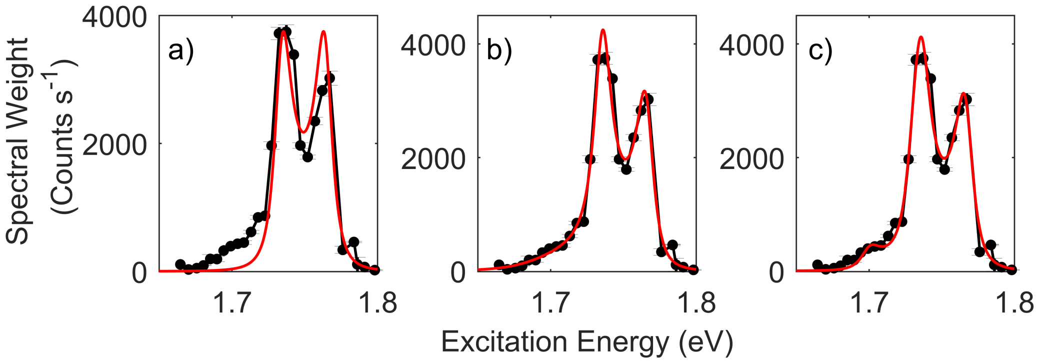

Figure 6.26: Resonance Raman profile obtained from fitting the Raman peak at 249.0 cm^{-1} on HS2 when resonant with the WSe_2 A exciton. Each profiles has been fitted to a different single phonon event model assuming a) a single electronic state, b) two independent electronic states and c) two underlying electronic states with interstate scattering allowed.

two models. It is possible that the width of 39.2 meV is correct, however this value is anomalously large when compared to the widths obtained for the WSe_2 A exciton on HS1 and monolayer WSe_2 which are between 5.1 to 12.2 meV and so we reject the two state model from our analysis. Therefore, the best fit is obtained assuming two electronic states with interstate scattering allowed and indicates the presence of two electronic states at 1.699±0.002 and 1.736±0.001 eV.

The two state model was then used to fit the resonance profiles for the Raman peaks at 257.0 and 261.2 cm^{-1}. The resonance profiles and fits are presented for these peaks along with the dispersive Raman peak at 205 cm^{-1} are shown in Figure 6.27 and the coefficients from fitting provided in Table 6.14. The resonance profiles for the two peaks at 257.0 and 261.2 cm^{-1} are both similar in appearance to the 249.0 cm−1 profile with two peaks at $\sim$ 1.738 and 1.766 eV along with a low energy shoulder between 1.680

Table 6.14: Coefficients obtained from fitting the resonance profiles for the Raman peaks observed on HS2 when resonant with the WSe_2 A exciton. Resonance profiles have been fitted to a single phonon event model with two electronic excitations with interstate scattering allowed. The errors given for each coefficient are a standard deviation obtained from fitting. The units for the amplitude coefficients are $10^{-3}\ \sqrt{Counts\ s^{-1} \cdot eV^2}$.

Raman Shift (cm^{-1})	Amplitude			Width		Energy	
	A_1	A_2	A_3	Γ_1	Γ_2	E_1	E_2
249.0	4.0±2.3	12.6±1.7	0.5±0.3	4.8±2.2	7.0±0.6	1.701±0.001	1.736±0.001
257.0	13.3±4.6	15.6±5.0	11.2±5.5	20.6±4.9	6.1±1.1	1.710±0.003	1.732±0.001
261.2	1.9±0.8	6.6±0.4	0.3±0.2	4.2±1.0	6.1±0.5	1.708±0.001	1.734±0.001

and 1.723 eV. In each case the fitted profiles using a two state model with interstate scattering are in good agreement with the data. Considering the coefficients for the three fitted profiles the higher energy states have values for E_2 in the range of 1.733 to 1.736 and are in agreement to within the errors obtained from fitting. The mean value and standard deviation of E_2 is 1.743±0.002 eV. The lower energy state for E_1 is varies with the values for the 257.0 and 261.2 cm^{-1} peaks in good agreement with values of 1.709 and 1.708 eV respectively. However, for the 249.0 cm^{-1} resonance the energy obtained is 1.699 eV and so is 10 meV lower in energy than the other Raman peak energies. However, it is possible to produce a good fit for 249.0 cm^{-1} resonance profile by constraining the energy of E_1 to 1.708 eV. Therefore, it is possible to explain all three resonance profiles using a two state model involving excitonic states between 1.708 to 1.709 eV and 1.733 to 1.736 eV. Comparing these energies to those obtained from fitting the PL spectrum for HS2 the higher energy state between the neutral A exciton and trion were attributed to the peaks at 1.739 and 1.704 eV respectively. Therefore we attribute the two states to the WSe_2 neutral A exciton and trion.

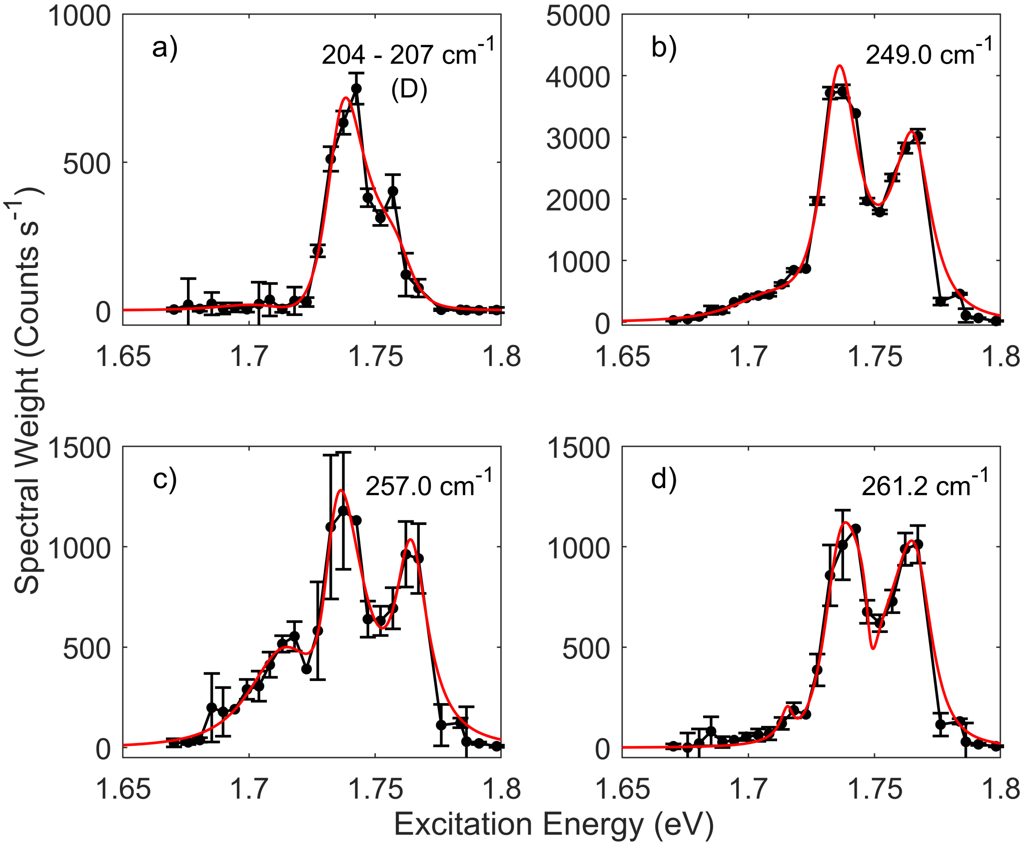

Figure 6.27: Resonance Raman profiles shown for all Raman peaks observed on HS2 when resonant with the WSe$_2$ A Exciton including the dispersive peak between 204 to 207 cm^{-1}. The resonance profiles for the Raman peaks at 249.0, 255.8 and 260.6 cm^{-1} have been fitted to a single phonon event model for two electronic states with interstate scattering allowed. Errors given on data points are a standard deviation obtained from the fitting process. Where shown (D) indicates the resonance profile shown is related to a dispersive Raman peak.

6.4.3 Resonance Raman with $MoSe_2$ B Exciton

This section presents the resonance Raman data for both HS1 and HS2 using excitation energies from 1.8 to 1.96 eV. As seen previously in Chapters 4 and 5 resonances are observed in this energy range for both $MoSe_2$ and WSe_2 monolayers. These resonances have been attributed to the $MoSe_2$ B Exciton and WSe_2 A* state respectively.

6.4.3.1 HS1 Resonance Raman with $MoSe_2$ B Exciton

The resonance Raman data for HS1 when resonant with the $MoSe_2$ B exciton is presented in Figures 6.28 & 6.29. From Figure 6.28 there is a clear resonance for the Raman peaks associated with $MoSe_2$ layer at $\sim$ 1.86 eV. In addition the resonances for different Raman peaks broaden as a function of Raman shift. This indicates the presence of both incoming and outgoing resonances with at least one electronic excitation. Between 1.78 to 1.82 eV in Figure 6.28 there is also significant Raman signal and Photoluminescence associated with the WSe_2 A exciton near $\sim$ 1.74 eV. There is also a Raman peak at $\sim$ 800 cm^{-1}, which is strongly resonant at $\sim$ 1.81 eV. As discussed in Section 6.3.1 this peak was previously reported in literature [190, 198] and attributed to coupling of the ZO phonon in hBN to a double resonance with the WSe_2 A exciton. The resonance behaviour of this feature is not considered further in this thesis. Considering the spectra shown in Figure 6.29 there are several Raman peaks near $\sim$ 300 cm^{-1}, which show significant variation in their relative intensities as a function of excitation energy. This behaviour suggests the presence of multiple electronic states contributing to the resonance process.

To further investigate the resonance behaviour the Raman spectra have been fitted to determine the spectral weight as a function of excitation energy and obtain the resonance profiles. In total resonance profiles were obtained for 17 Raman peaks associated with the $MoSe_2$ layer. Three of these Raman peaks at 480.6, 529.5 and 581.7 cm^{-1} demonstrate clearly anomalous resonance behaviour and are analysed separately. In addition resonance profiles were also obtained for the low frequency modes below 100 cm^{-1} and are presented later in Section 6.4.5.

Each resonance profile has been fitted to a Raman model for a single phonon event assuming a single electronic excitation. The resonance profiles and resultant fits are presented in Figure 6.30 and the coefficients obtained from fitting are provided in Table 6.15. For the Raman peaks in the range 235 to 320 cm^{-1} the resonance profiles all have a similar appearance characterised by a broad symmetric peak with the incoming and outgoing terms not clearly resolved. However, resonance profiles for peaks at higher frequencies (>350 cm^{-1}) (see Figure 6.30 panels i to n) are clearly different with two peaks appearing in the profiles near $\sim$ 1.85 and 1.89 eV. These peaks appear to be symmetric and the separation dependent on the Raman shift. Therefore, it is likely that the two peaks observed are the incoming and outgoing resonances for the $MoSe_2$

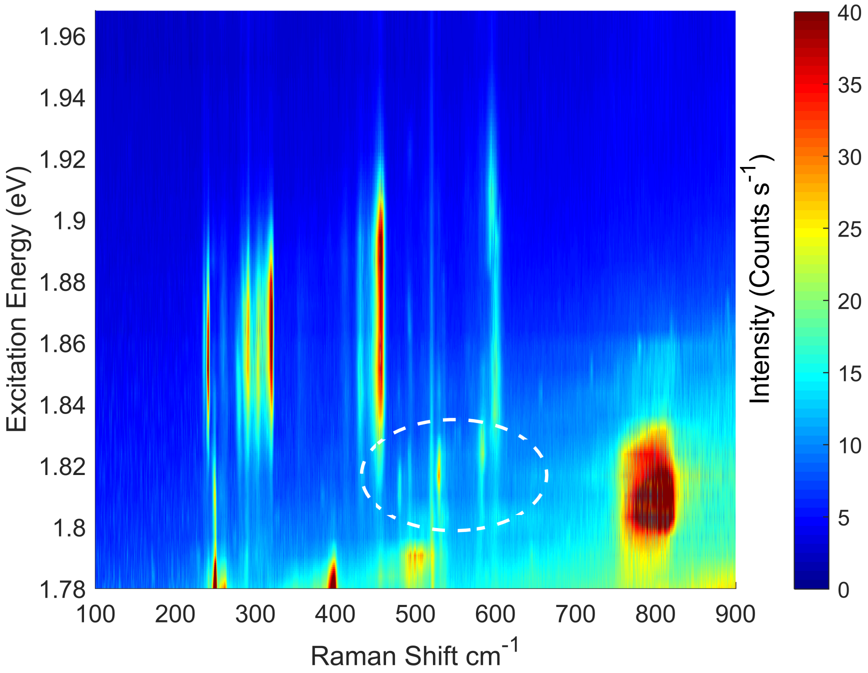

Figure 6.28: Colourmap showing resonance Raman data taken on HS1 using excitation energies from 1.8 to 1.96 eV probing the $MoSe_2$ B exciton. The white dashed circle indicates the location of the anomalous Raman peaks at 480.6, 529.5 and 581.7 cm^{-1}.

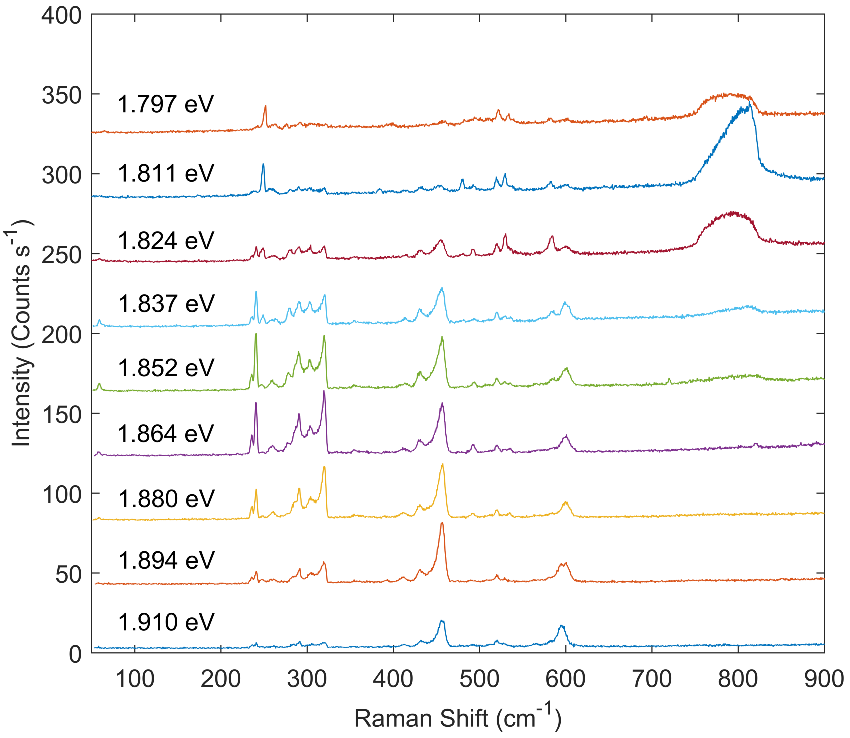

Figure 6.29: Raman spectra obtained when resonant with $MoSe_2$ B exciton on HS1 using excitation energies from 1.8 to 1.96 eV.

Table 6.15: Table of coefficients for fitting the resonance profiles for HS1 when resonant with the $MoSe_2$ B exciton using a single phonon event model assuming a single electronic state. Coefficients for the 277.7 cm^{-1} peak are highlighted in gray as this peak demonstrates dispersive behaviour. The errors given for each coefficient are a standard deviation obtained from fitting. The units for the amplitude coefficients are $10^{-3}\ \sqrt{Counts\ s^{-1} \cdot eV^2}$.

Raman Shift cm^{-1}	Amplitude	Width (meV)	Energy (eV)
235.8	2.5±0.4	32.6±3.4	1.850±0.001
241.0	2.2±0.3	21.1±2.2	1.843±0.001
277.7	1.6±0.3	19.4±3.4	1.828±0.001
286.0	2.1±0.4	23.5±3.5	1.853±0.001
290.9	4.8±0.6	33.3±3.1	1.846±0.001
304.2	6.3±0.7	31.1±2.5	1.842±0.001
316.1	3.2±0.6	24.2±3.5	1.845±0.001
320.2	3.0±0.2	19.3±1.3	1.846±0.001
357.9	1.4±0.1	14.5±1.6	1.847±0.001
410.6	1.8±1.4	14.2±1.6	1.846±0.001
431.5	2.6±0.2	15.6±1.6	1.843±0.001
450.2	4.0±0.3	17.8±1.3	1.843±0.001
456.9	5.8±0.9	20.6±3.4	1.848±0.002
599.8	7.4±0.8	24.7±3.2	1.845±0.002

B exciton. For the Raman peaks at 357.9, 410.6, 456.9 and 599.8 cm^{-1} there is a slight asymmetry, and may suggests the presence of multiple underlying electronic states. In this case fits were attempted using single phonon event models assuming two independent electronic states and two electronic states with interstate scattering allowed. However, for the two state models it was not possible to produce well constrained fits to the data Therefore, whilst the data maybe more complex and involving multiple excitonic states we limit our analysis to a single excitonic state model.

The coefficients from fitting to a single electronic state in Table 6.15 are in agreement with energy of the underlying state near $\sim$ 1.845 eV in almost all cases. An exception is the peak at 277.7 cm^{-1} which is a dispersive Raman peak. From Table 6.15 it is immediately obvious that this dispersive peak is resonant at a lower energy of 1.828 eV. In addition the Raman peak at 286.0 cm^{-1} is accidentally degenerate with another dispersive Raman peak at lower excitation energies and so its resonance profile may not be representative of a non-dispersive process. Excluding these two peaks from our consideration of the single state fits it is clear that the energies obtained from fitting are in good agreement with values from 1.843 to 1.850 eV. A mean value was obtained and suggests the electronic state involved in the $MoSe_2$ B resonance is at 1.845±0.002 eV. Therefore, for the BS Raman peaks observed in HS1 at the $MoSe_2$ B the resonance behaviour can be explained due to the presence of a single electronic state at 1.845 eV. The energy of this state is in agreement with the results of Wang et al. [255] and indicates this state is likely the neutral B exciton.

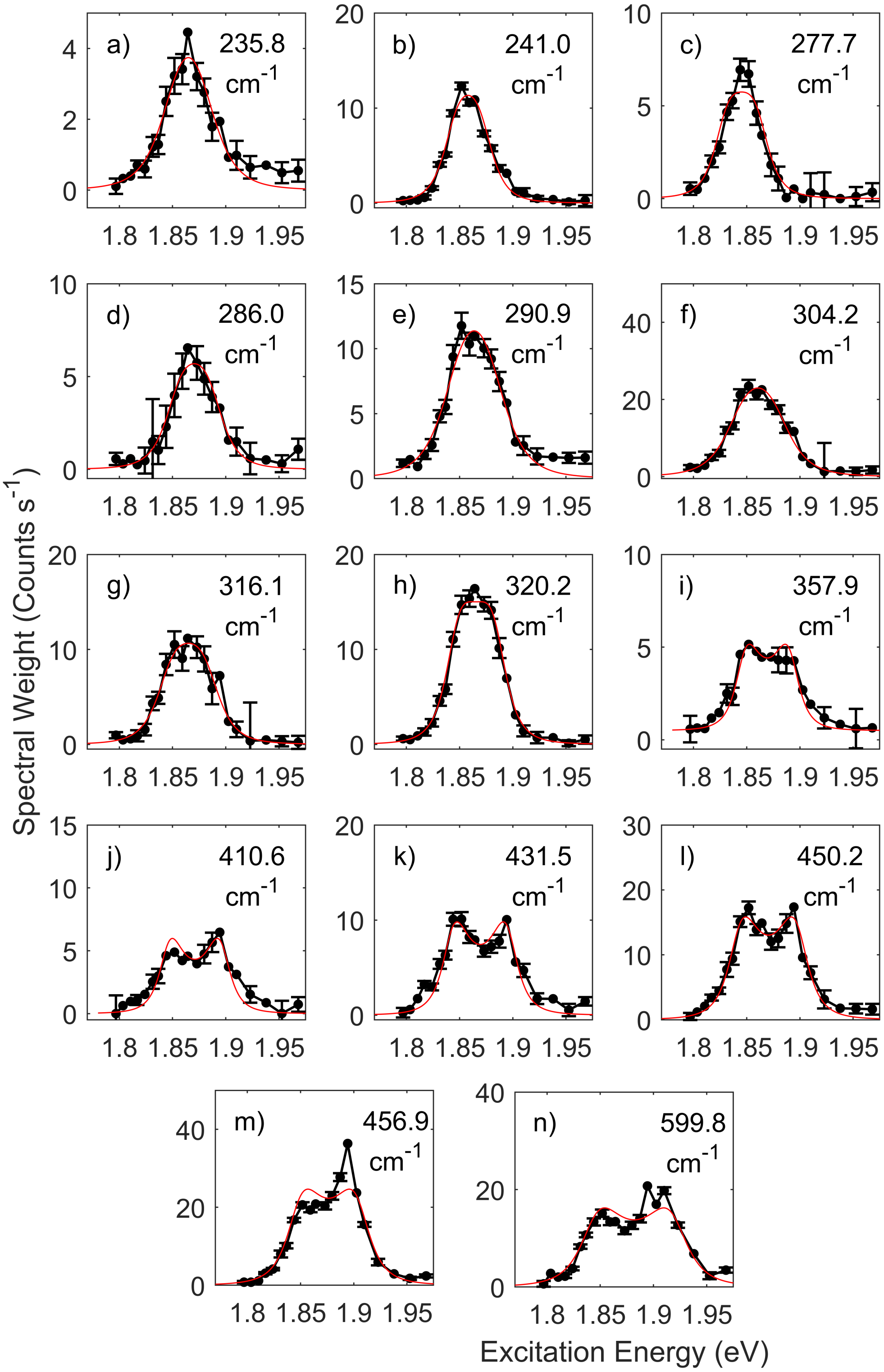

Figure 6.30: Resonance profiles have been obtained for 14 Raman different peaks on HS1 when resonant with the $MoSe_2$ B exciton. Each resonance profile has been fitted using a single phonon event model assuming a single underlying electronic excitation with the resultant fit shown in red. Error bars shown are a standard deviation obtained from the fitting process.

Table 6.16: Coefficients obtained from fitting the anomalous resonance profiles for the Raman peaks at 480.1, 530.4 and 483.3 cm^{-1} to a single Lorentzian line shape with a linear background. The errors given for each coefficient are a standard deviation obtained from fitting. The units for the amplitude coefficients are $10^{-3}\ \sqrt{Counts\ s^{-1} \cdot eV^2}$.

Raman Shift (cm^{-1}	Amplitude	Width (meV)	Energy (eV)	E$_{ph}$ (meV)	E-E$_{ph}$ (eV)
480.6	3.2±1.5	5.5±3.2	1.814±0.001	59.5	1.755
529.5	15.6±1.6	10.0±2.0	1.818±0.001	65.8	1.752
581.7	7.4±0.9	12.7±2.9	1.827±0.001	72.3	1.755

The Raman peaks observed at 480.6, 529.5 and 581.7 cm^{-1} demonstrate anomalous resonance behaviour. This can be seen in Figure 6.28 between 1.8 to 1.82 eV. The resonances associated with these Raman peaks are significantly narrower than the BS peaks and their energies are observed to increase with increasing phonon energy. This behaviour implies an outgoing resonance with a lower energy state and is similar to the anomalous peaks observed in monolayer MoSe$_2$ (see Chapter 4). The resonance profiles for these modes are presented in Figure 6.31 a comparison of these profiles to the resonance profiles shown in Figure 6.30 reveals that the anomalous peak profiles are significantly narrower and at lower energies with the widths of the anomalous resonances in the range of $\sim$ 20 to 30 meV. The energies of the Raman peaks are then 59, 66 and 72 meV for the peaks at 480.6, 529.5 and 581.7 cm^{-1} respectively. Therefore, the width of the anomalous resonances are too narrow to involve both incoming and outgoing resonances.

Due to the narrow width of the anomalous resonance profiles a single phonon event model assuming a single electronic state will not produce a good fit. As a result, each resonance profile was fitted to a single Lorentzian line shape as shown in Figure 6.31. The coefficients from fitting the resonance profiles are provided in Table 6.16 along with the energies of the Raman peaks. The energies from fitting confirms that the energy of the resonance increases as a function of Raman shift. This behaviour indicates that the anomalous resonances is due to an outgoing resonance condition. In Table 6.16 the energy of the lower energy state involved in the resonance was determined by calculating E-E$_{ph}$ for each resonance. For all three anomalous resonances the energy of the lower energy state is in good agreement with an average value of 1.754±0.002 eV. Raman spectra were also obtained at energies near 1.754 eV but no incident resonance with the anomalous Raman peaks was observed. Therefore, the anomalous resonances are likely the result of a double resonance between the MoSe$_2$ B exciton and the lower energy state at 1.754 eV.

In summary the resonance Raman behaviour at the MoSe$_2$ B exciton in HS1 has been investigated. The majority of Raman peaks can be explained by a resonance with a single electronic state at 1.845 eV, which is attributed to the neutral B exciton. Dispersive Raman peaks are also observed when resonant with the MoSe$_2$ B exciton and is resonant

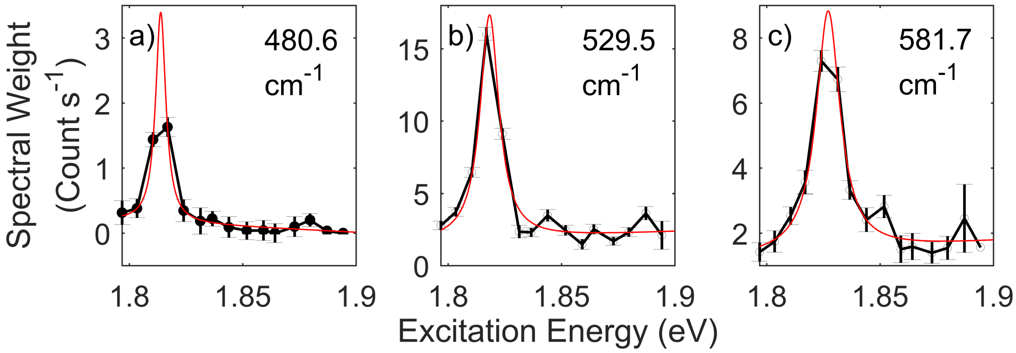

Figure 6.31: Resonance profiles obtained for peaks at 480.1, 530.4 and 583.3 cm^{-1} for sample HS1 when resonant with the MoSe$_2$ B Exciton are presented in panels a,b and c respectively. Comparing these profiles to those previously presented in Figure 6.30 these peaks demonstrate anomalous behaviour with only a sharp resonance between 1.8 to 1.84 eV and are narrower with widths ~ 10 meV. Profiles were fitted to a single Lorentzian line shape with a linear background to determine the energy of the resonance the fitted coefficients are shown in Table 6.16.

at lower energies this is similar to results for monolayer MoSe$_2$ and suggests the presence of large wavevector electronic states at the B exciton in HS1. The resonance profiles for the three anomalous peaks at 480, 530, 583 cm^{-1} were also observed and are similar to those seen on monolayer MoSe$_2$. Analysis of these resonance profiles suggests a double resonance between the MoSe$_2$ B exciton and a as yet unidentified lower energy state at 1.755 eV.

6.4.3.2 HS2 Raman Resonance with the MoSe$_2$ B Exciton

For HS2 the resonance Raman data when resonant with the MoSe$_2$ B exciton is presented in Figures 6.32 & 6.33. From Figure 6.32 the Raman peaks associated with the MoSe$_2$ layer are resonant between 1.82 and 1.86 eV. In this case the proximity of the MoSe$_2$ B and WSe$_2$ A excitons results in features associated with both resonances appearing in Figure 6.32 & 6.33. In particular there are several WSe$_2$ Raman peaks between 1.79 and 1.81 eV near ~ 250 and 400 cm^{-1}. There is also a prominent peak at ~ 800 cm^{-1} between 1.8 and 1.85 eV. As discussed in Section 6.3.2 this Raman peak was previously reported in encapsulated monolayers of WSe$_2$ and is attributed to the ZO phonon associated with hBN coupling to electronic states in the TMDC layer. Having identified the extraneous Raman features in the resonance data the Raman peaks associated with the MoSe$_2$ layers are strongly resonance from 1.81 to 1.92 eV. In Figure 6.32 it becomes obvious that the resonances for higher frequency Raman peaks are significantly broader with the width increasing as a function of Raman shift. This suggests the presence of both incoming and outgoing resonances with at least a single electronic state. The Raman spectra in Figure 6.33 also suggests the presence of multiple electronic excitations present at the MoSe$_2$ B exciton. This can be seen by comparing the relative intensities of the Raman peaks between 260 and 320 cm^{-1}. The energy of these Raman peaks are between 32 to 39 meV for such a small difference in the energy of the Raman peaks we would expect the peaks to have an almost identical resonance behaviour with only slight shifts in the energies of the outgoing resonance term. The significant variation in the relative intensities is then a clear indication of more complex resonance behaviour involving multiple electronic states.

The resonance profiles were extracted by fitting the Raman spectra and a total of 9 resonance profiles were obtained. The resonance Raman profiles were each fitted to a single phonon event model assuming a single underlying electronic state. The resonance profiles and results of fitting are presented in Figure 6.34 and the coefficients from fitting are provided in Table 6.17. The resonance Raman profiles shown in Figure 6.34 are reasonably similar with a single broad peak and no clear separation of the incoming and outgoing resonance terms. Although, there is a consistent asymmetry in all of the resonance profiles. In particular the profiles for the peaks between 240.9 and 304.9 cm^{-1} all show a rapid decrease in spectral weight at lower energies and a more gradual tail at higher energies. For the Raman peaks from 319.6 to 456.0 cm^{-1} this asymmetry manifests as a lower energy shoulder to the resonance between 1.8 and 1.83 eV. The asymmetry of the resonance Raman profiles requires the presence of at least two electronic states. However, fitting to a single state model does appear to produce reasonable fits to the resonance profiles.

Considering the fitted coefficients in Table 6.17 the energies obtained cover a broad range from 1.815 to 1.840 eV. However the Raman peak at 280.1 cm^{-1} appears to

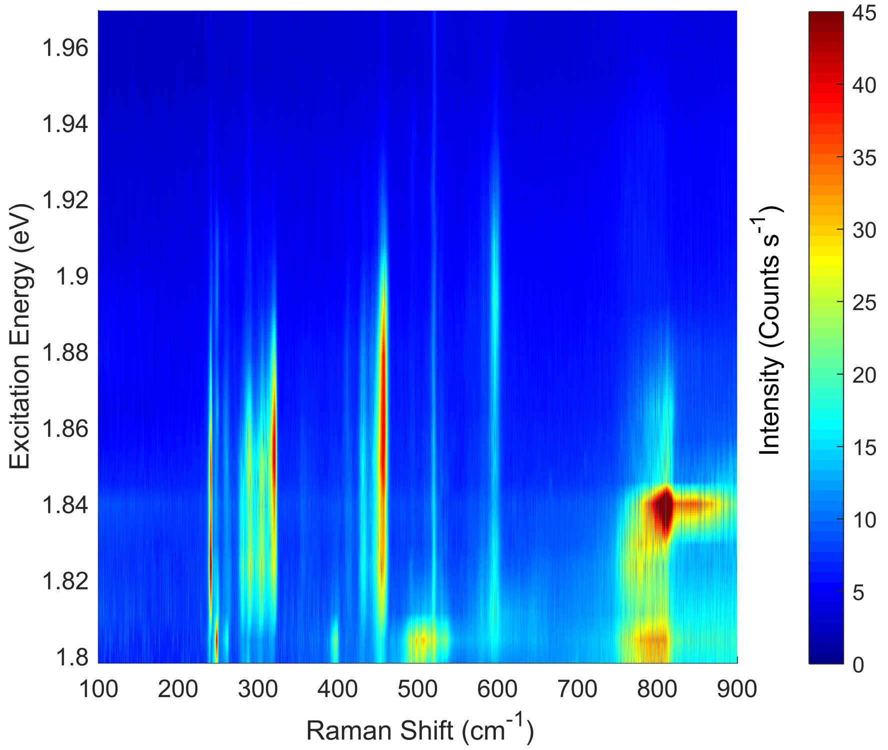

Figure 6.32: Colourmap showing resonance Raman data taken on HS2 using excitation energies from 1.8 to 1.96 eV probing the MoSe$_2$ B exciton.

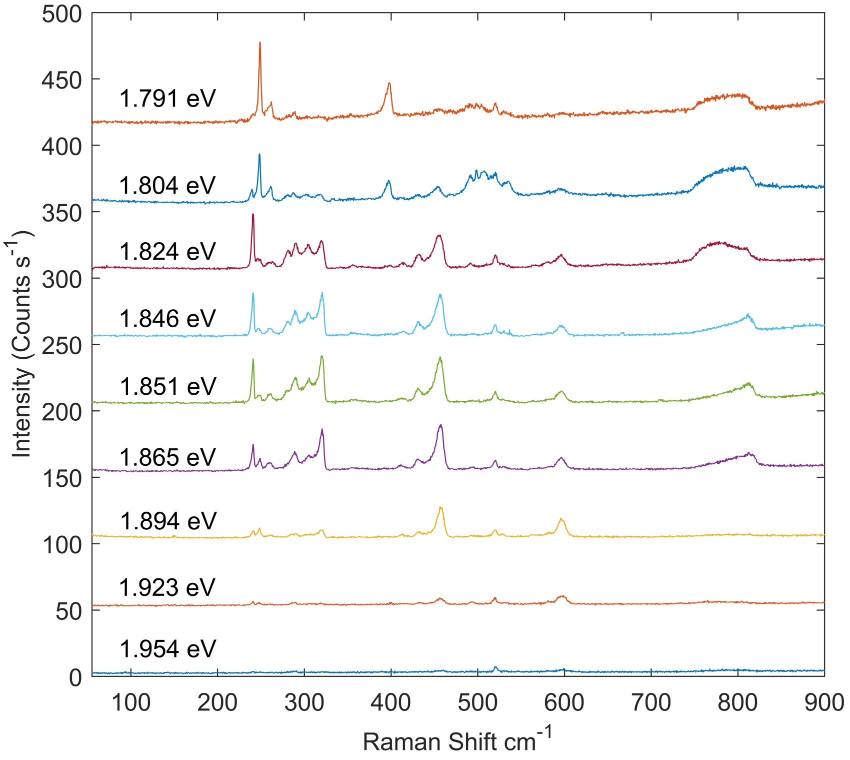

Figure 6.33: Raman spectra obtained when resonant with MoSe$_2$ B exciton on HS2 using excitation energies from 1.8 to 1.96 eV.

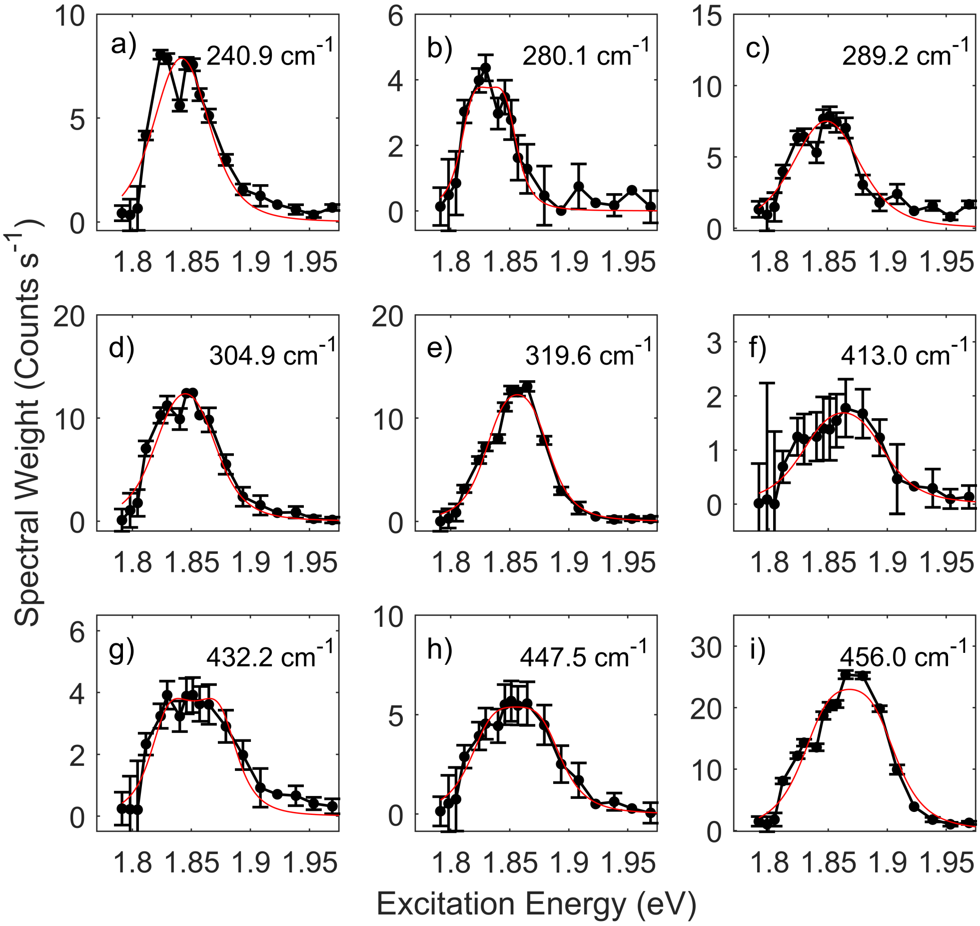

Figure 6.34: Resonance profiles for Raman peaks observed on HS2 when resonant with MoSe$_2$ B exciton.

Table 6.17: Table of coefficients obtained from fitting the resonance profiles for the Raman peaks observed when resonant with the MoSe$_2$ B Exciton on HS2. Coefficients from fitting with a single phonon event model assuming a single electronic state. The rows shaded grey indicate that the Raman peaks are dispersive or degenerate with dispersive Raman peaks and so are likely to exhibit different resonance behaviour. The errors given for each coefficient are a standard deviation obtained from fitting. The units for the amplitude coefficients are $10^{-3}\ \sqrt{Counts\ s^{-1} \cdot eV^2}$.

Raman Shift (cm^{-1})	Amplitude	Width (meV)	Energy (eV)
240.9	4.2±1.2	35.6±6.4	1.827±0.003
280.1	1.1±0.3	16.3±4.2	1.815±0.001
289.2	6.0±1.5	43.4±6.7	1.831±0.003
304.9	4.9±1.1	32.0±4.9	1.826±0.002
319.6	3.9±0.7	27.0±3.8	1.837±0.001
413.0	2.8±0.7	39.1±7.4	1.837±0.003
432.2	2.4±0.4	23.2±4.2	1.825±0.002
447.5	3.7±0.6	29.1±4.5	1.828±0.002
456.0	9.5±2.0	34.5±6.0	1.840±0.002’

be an outlier with a lower energy than the other peaks of 1.815 eV. For monolayer MoSe$_2$ and HS1 the Raman the peak at 280.1 cm^{-1} was classified as a bulk dispersive Raman peak. As presented in Section 6.3.1 there does not appear to be any significant dispersion in the Raman peaks between 270 and 290 cm^{-1} for HS2 when resonant with the MoSe$_2$ B exciton. However, the resonance behaviour of HS1 and monolayer MoSe$_2$ has consistently shown that the dispersive Raman peaks are resonant at lower energies. This is in agreement with the behaviour of the 280.1 cm^{-1} Raman peak in HS2. In addition the Raman peak at 289.2 cm^{-1} has been previously observed to be degenerate with a dispersive Raman peak in monolayer MoSe$_2$ and so when considering the results of fitting both the 280.1 and 289.2 cm^{-1} were excluded. The range of possible energies for the resonance profiles is then between 1.825 and 1.840 eV. From Table 6.17 the energies obtained from fitting also appear to be clustered near either $\sim$ 1.827 or 1.837 eV. This may indicate the presence of two distinct electronic states. Therefore, the range of different energies obtained from fitting along with the observed asymmetry in the resonance profiles suggests the presence of multiple electronic states contributing to the MoSe$_2$ B exciton resonance in HS2.

To further investigate the possibility of multiple electronic states involved in the resonance Raman data the profile for the 240.9 cm^{-1} Raman peak was fitted to a single phonon event model assuming two independent electronic states and two states with interstate scattering allowed. The resulting fits to all three fitted models for the 240.9 cm^{-1} are presented in Figure 6.35 with the adjusted r-square values and coefficients from fitting provided in Table 6.18. An inspection of the resulting fits for the two state models in Figure 6.35 panels b) & c) reveals the best fit to the data appears to be the two state with interstate scattering (panel c). However the fitted coefficients in Table 6.18 shows that these values are not well constrained and have large errors for the energies, widths and amplitudes. For example the energy for the higher energy state at 1.830 eV has an error of 83 meV. Therefore, despite the apparent improvement of the fit for the two state model with interstate scattering it is necessary to reject the fit obtained in this case. Considering the coefficients from fitting to the two independent electronic states we find the obtained errors are more reasonable with energies of 1.822±0.009 and 1.846±0.016 eV. This suggests the presence of two electronic states are involved when resonant with the MoSe$_2$ B exciton.

Previously the two state model has been considered in detail for a particular resonance profile and then extended to the other resonance Raman profiles. However, in this case fitting of the remaining resonance profiles to a two state model was attempted but unable to produce well constrained fits. However, the results of fitting to a single state model clearly suggest the presence of multiple excitonic states at the MoSe$_2$ B exciotn. The energy of the two states from fitting the 240.9 cm^{-1} peak profile are 1.822 and 1.846 eV. These are in agreement with the results of Wang et al. [255] for the B trion and neutral exciton. Therefore, the resonance Raman behaviour at the MoSe$_2$ B exciton in HS2 is

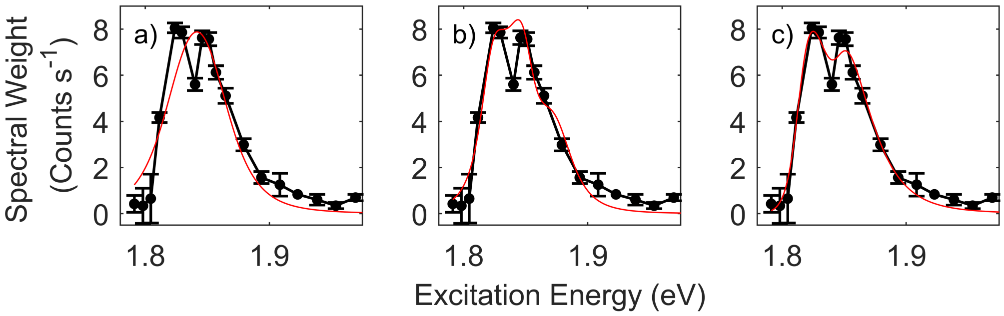

Figure 6.35: Resonance profiles for 240.9 cm^{-1} Raman peak observed on HS2 when resonant with $MoSe_2$ B exciton fitted to three single phonon event models assuming a) a single electronic state, b) two electronic states and c) two electronic states with scattering between states allowed.

Model	Single State	Two State	Two State with Scatter
Adjusted R-Square	0.8597	0.9434	0.9495
A_1	4.2±1.2	1.0±0.6	2.2±0.8
A_2	-	1.5±2.1	6.0±1.4
A_3	-	-	3.1±1.7
Γ_1	35.4±6.3	14.8±4.7	9.6±2.0
Γ_2	-	22.1±13.4	56.9±9.5
E_1	1.827±0.003	1.822±0.009	1.820±0.002
E_2	-	1.846±0.016	1.843±0.010

Table 6.18: Table of coefficients obtained from fitting the resonance profile for the 240.9 cm^{-1} Raman peak observed on HS2 when resonant with $MoSe_2$ B exciton. Resonance profile has been fitted to three single phonon event models assuming a) a single electronic state, b) two electronic states and c) two electronic states with scattering between states allowed. The errors given for each coefficient are a standard deviation obtained from fitting. The units for the amplitude coefficients are $10^{-3}\ \sqrt{Counts\ s^{-1} \cdot eV^2}$.

likely the result of resonance with the trion at 1.822 eV and the neutral B exciton at 1.846 eV.

Overall the resonance Raman behaviour of the $MoSe_2$ B exciton on HS2 has revealed the involvement of both excitons and trions with energies of 1.846 and 1.822 eV respectively. In addition the Raman peak at 280.1 cm^{-1} and has been associated with a dispersive Raman peak in monolayer $MoSe_2$ and HS1 is resonant at lower energies that the BS Raman peaks. Whilst, the Raman peak did not appear dispersive in HS2 the difference in resonance behaviour is in agreement with the dispersive peaks on monolayer $MoSe_2$ and HS1. The difference in dispersion of this peak suggests either a modification of the phonon dispersion in HS2 or a change in the excitonic dispersion.

6.4.4 Resonance Raman with WSe_2 B Exciton

This section presents the resonance Raman data for both HS1 and HS2 using excitation energies from 2.0 to 2.25 eV. In the constituent monolayers resonances in this energy range were attributed to the WSe_2 B exciton (see Chapter 5). In both HS1 and HS2 resonances are observed at similar energies however the Raman peaks are much weaker compared to monolayer WSe_2 with an order of magnitude decrease in the Raman intensity and so we are only able to extract resonance profiles for the most intense Raman peaks.

6.4.4.1 HS1 Resonance Raman with WSe_2 B Exciton

For HS1 the Raman data when resonant with the WSe_2 B exciton is presented in Figures 6.36 & 6.37. In Figure 6.36 the resonance behaviour is dominated by four Raman peaks at 240.4, 248.7, 255.2 and 260.4 cm^{-1}. There are also several weaker Raman peaks visible including peaks at 290.7, 309.1 and 353.8 cm^{-1} and the Raman peak at 398.2 cm^{-1}. The resonance behaviour of these peaks reveals three distinct behaviours. The 240.4 cm^{-1} peak can be seen in Figure 6.36 and has a lower energy resonance centred at 2.15 eV. The Raman peaks at 255.2 and 260.4 cm^{-1} demonstrate a similar behaviour to the 248.7 cm^{-1} with the resonances centred at $\sim$ 2.18 eV. However, the 248.7 cm^{-1} Raman peak also shows significant enhancement at energies above 2.2 eV and suggests this peak is resonant with higher energy states above the B exciton, that are not accessible with our experimental setup. These differences in the resonance behaviour can be seen in the exemplar spectra in Figure 6.37 by comparing the relative intensity of the Raman peaks. As a result the resonance Raman behaviour when resonant with the WSe_2 B exciton on HS1 likely involves multiple underlying electronic states.

The resonance Raman profiles were obtained for the peaks at 240.4, 248.7, 255.2 and 260.4 cm^{-1} and are shown in Figure 6.38. In the mode assignment in Section 6.3.2 there are additional Raman peaks present in the Raman spectra when resonant with the WSe_2 B exciton. However these peaks are too weak to allow their resonance profiles to be resolved. The resonance profiles for the different Raman peaks show significant variations with the peaks at 240.4, 255.2, 260.4 cm^{-1} dominated by a single broad peaks, whereas the 248.7 cm^{-1} peak shows two clear peaks near 2.11 and 2.18 eV and is also enhanced at 2.2 to 2.25 eV. To analyse the data the resonance profiles were fitted to a single phonon event model assuming a single electronic state. The resulting fits are shown in Figure 6.38 with the coefficients from fitting provided in Table 6.19. The single state model is able to reasonably fit the 240.4 cm^{-1} peak, however, for the peak at 248.7 cm^{-1} a single state model is clearly unable to describe the data. For the Raman peaks at 255.2 and 260.4 cm^{-1} the fits to a single state model are able to explain the main peak in the resonance near 2.17 eV, although there is a significant spectral weight at

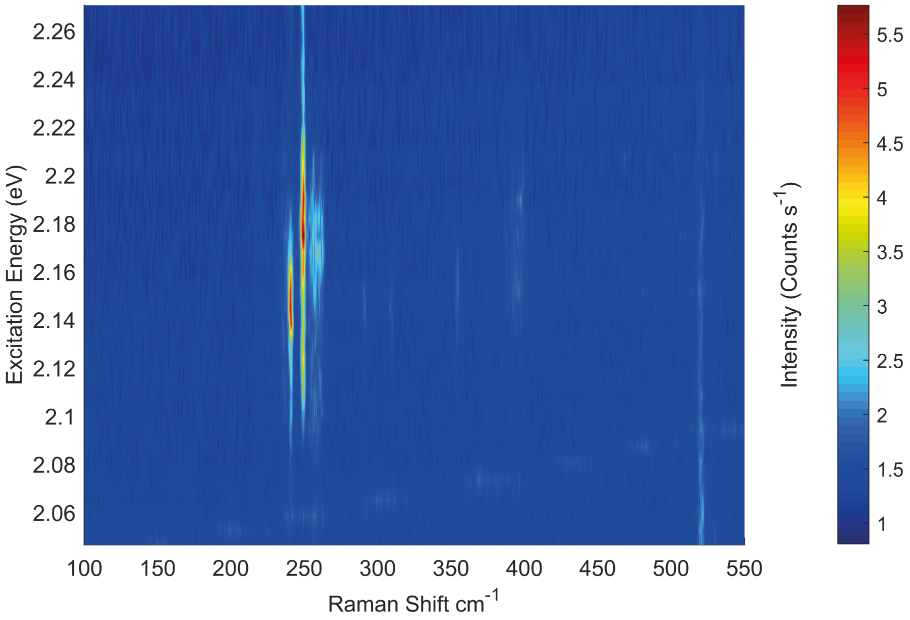

Figure 6.36: Colourmap showing resonance Raman data taken on HS1 using excitation energies from 2.05 to 2.25 eV probing the WSe$_2$ B exciton.

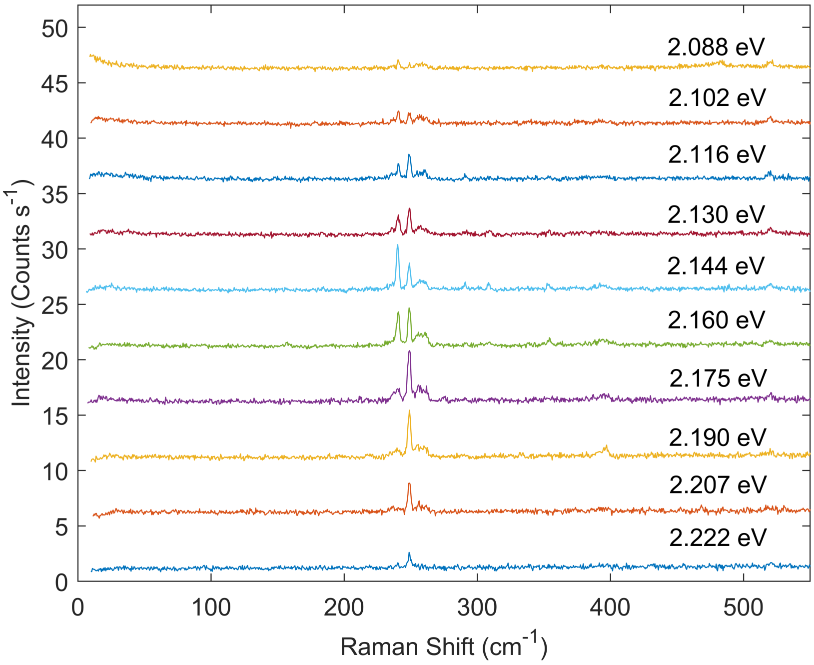

Figure 6.37: Raman spectra obtained when resonant with WSe$_2$ B exciton on HS1 using excitation energies from 2.05 to 2.25 eV.

Raman Shift (cm^{-1})	Amplitude	Width (meV)	Energy (eV)
240.4	3.2±0.6	29.8±4.1	2.135±0.002
248.7	11.1±1.8	70.6±6.5	2.162±0.003
255.2	4.1±1.1	38.2±6.4	2.154±0.003
260.4	2.4±0.6	28.7±5.2	2.164±0.002

Table 6.19: Coefficients obtained from fitting the resonance profiles for the Raman peaks observed on HS1 when resonant with the WSe_2 B Exciton. Resonance profiles were fitted to a single phonon model assuming a single electronic excitation. The errors given for each coefficient are a standard deviation obtained from fitting. The units for the amplitude coefficients are 10^{-3} $\sqrt{Counts\ s^{-1} \cdot eV^2}$.

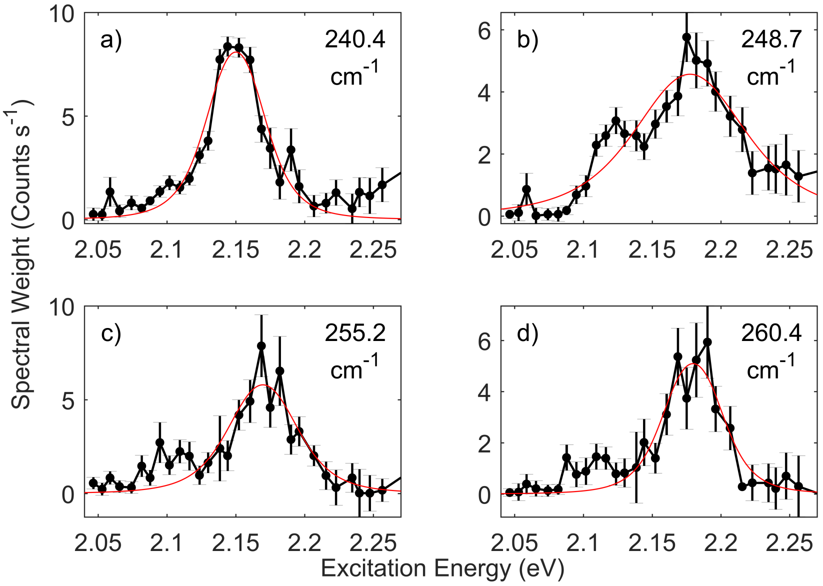

Figure 6.38: Resonance Raman profiles are presented for the Raman peaks at 240.4, 248.7, 255.2 and 260.4 cm^{-1} observed when resonant with the WSe_2 B exciton. Each profile has then been fitted to a single phonon model assuming an underlying electronic excitation.

lower energies which is not accounted for in this model. The complex nature of the 248.7 cm^{-1} Raman peak and clear differences in the energies obtained for the fitted profiles clearly indicates the presence of multiple electronic states.

The resonance profile for the 248.7 cm^{-1} Raman peak shows clear evidence of multiple excitonic states. To analyse this further the resonance profile has been fitted using a single phonon event models assuming two independent electronic states and two electronic states with interstate scattering allowed. In addition to account for the enhancement of the 248.7 cm^{-1} peak at energies above 2.2 eV a linear background was introduced into the fitted model. The resonance profiles for all three models with a linear background are presented in Figure 6.39 and the adjusted R-square values and coefficients are provided in Table 6.20. From Figure 6.39 there is a clear improvement in the fits for both

Table 6.20: Adjusted R-square values and coefficients from fitting the resonance profile for the 248.7 cm^{-1} Raman peak observed on HS1 when resonant with the WSe$_2$ B Exciton. In this case the resonance profile has been fitted to three Raman scattering models assuming a single electronic excitation, two independent electronic excitations and two electronic excitations with interstate scattering allowed. The errors given for each coefficient are a standard deviation obtained from fitting. The units for the amplitude coefficients are 10^{-3} $\sqrt{Counts\ s^{-1} \cdot eV^2}$.

		Single	Two	Two with scatter
	Adjusted R-Square	0.862	0.955	0.941
	A$_1$		1.3±0.6	0
Amplitude	A$_2$	10.0±4.5	2.7±1.1	3.6±1.5
	A$_3$	-	-	2.0±0.9
Width (meV)	Γ$_1$	-	17.4±4.6	12.9±4.2
	Γ$_2$	67.5±14.7	27.9±6.5	36.5±4.2
Energy (eV)	E$_1$	-	2.119±0.003	2.108±0.005
	E$_2$	2.159±0.004	2.164±0.003	2.169±0.002

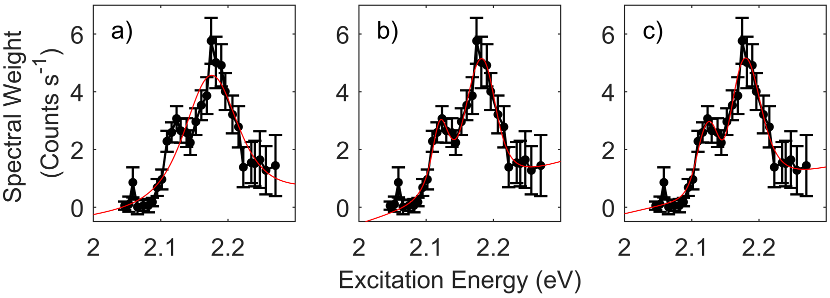

Figure 6.39: Resonance Raman profile for the 248.7 cm^{-1} Raman peak has been fitted to a single phonon event model assuming a) a single electronic excitation, b) two independent electronic excitation and c) two electronic excitations with scattering allowed between the states. In each case a linear background has also been included in the model.

of the two state models able, which are able to account for the multiple peaks in the resonance profile. The adjusted R-square values from Table 6.20 indicate that the best fit to the data is for the single phonon event model assuming two independent electronic excitations. The energies obtained using this model for the two electronic states are then 2.119±0.003 and 2.164±0.003 eV. It is useful to compare these energies to those obtained from fitting a single electronic state to the resonance profiles for the peaks at 240.4, 255.2 and 260.4 cm^{-1}. The higher energy obtained for the two state model is in good agreement with the energy of the 2.164 eV obtained for the Raman peak at 260.4 cm^{-1} and is close to the value of 2.154 eV obtained for the Raman peak at 255.2 cm^{-1}. The presence of an additional electronic state at 2.119 eV can also explain the spectral weight seen in both the 255.2 and 260.4 cm^{-1} resonance profiles. Therefore, the resonance profiles for the Raman peak at 248.7, 255.2 and 260.4 cm^{-1} can be explained by the presence of two electronic states at 2.119 and 2.164 eV.

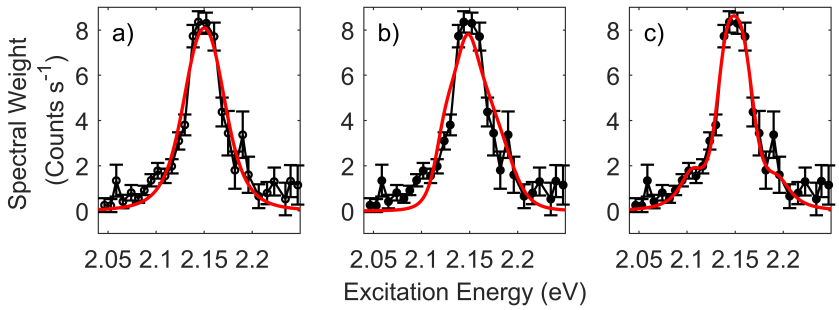

Figure 6.40: The Resonance Raman profile for the Raman peak observed at 240.4 cm^{-1} on HS1 when resonant with the WSe$_2$ B Exciton is presented and has been refitted to single and two state Raman models. a) Single state Raman model for a single phonon event process, b) Two independent state model and c) Two states with interstate scattering allowed. For the case of the Two independent state model the values for the energies and widths of the states were fixed to those obtained from fitting the 248.7 cm^{-1} peak. Error bars shown are standard deviation obtained from fitting each spectra.

The resonance profile for the 240.4 cm^{-1} peak is centred at 2.148 eV and so it is not obvious if this resonance profile can be explained by a two electronic states at 2.119 and 2.164 eV. As a result further fitting of the 240.4 cm^{-1} resonance profile has been carried using a single phonon event model assuming two independent electronic states and two electronic states with interstate scattering allowed. The fitted resonance profiles for the 240.4 cm^{-1} Raman peak are presented in Figure 6.40 and the adjusted R-square values and coefficients from the fits are also provided in Table 6.21. When fitting using the two independent electronic state model it was found that the fitted energies and widths reached the limits of the defined bounds and so the fit was unable to converge. Therefore, the fitted profile presented for this model was obtained by fixing the widths and energies to those obtained when fitting the 248.7 cm^{-1} leaving the amplitudes unconstrained.

From Figure 6.40 panels a) & c) the fitted profiles for the single state and two state with interstate scattering models are able to produce reasonable fits to the data. The adjusted r-square values indicate that the best fit for the resonance profiles is achieved using the two state model with interstate scattering. The coefficients from Table 6.21 reveal energies for the two electronic states in this model of 2.103 and 2.163 eV. Comparing these energies to those obtained for the 248.7 cm^{-1} peak the higher energy states are in excellent agreement with values of 2.163 and 2.164 eV. For the lower energy states there is a larger variation with values of 2.119 and 2.103 eV. Although a comparison of the two peaks using the values from the two state model with interstate scattering allowed produces better agreement between the lower energy states. Therefore, the resonance Raman behaviour of both the 240.4 and 248.7 cm^{-1} Raman peaks can be explained by the presence of two electronic states with a higher energy state at 2.164 eV and a lower energy state in the range of 2.103 to 2.119 eV.

		Single State	Two States	Two State with Scatter
	Adjusted R-square	0.927	0.879	0.983
	A_1	3.2±0.6	1.2±0.3	1.1±0.6
Amplitude	A_2	-	1.7±0.4	1.8±0.9
	A_3	-	-	3.4±1.5
Width (meV)	Γ_1	29.8±4.1	17.4	19.6±4.9
	Γ_2	-	27.9	20.0±5.1
Energy (eV)	E_1	2.135±0.002	2.119	2.103±0.003
	E_2	-	2.164	2.163±0.004

Table 6.21: Adjusted R-square values and coefficients are presented from fitting the 240.4 cm^{-1} Raman peak observed on HS1 when resonant with the WSe_2 B Exciton to single state and two state Raman models. For the case of the two independent state model it was not possible to obtain a good fit within the constrains for the widths and energies and so these values were fixed to those obtained for the Raman peak at 248.7 cm^{-1} to allow for comparison.

There are several additional Raman peaks which are visible in Figure 6.37 but whose resonance profiles were not resolved due to their low intensity. However, it is possible to discuss the resonance behaviour of these additional peaks by using the colourmap presented in Figure 6.41. To aid in visual comparison of the different resonance behaviour the intensity of the peaks has been scaled emphasize the weaker Raman peaks. In Figure 6.41 the Raman peaks at 290.7, 309.1, 353.8 and 398.2 cm^{-1} are clearly visible. The peak at 398.2 cm^{-1} has been observed at both the WSe_2 A and B resonance on monolayer WSe_2 and is classified as a BS peak. The energies of the electronic states obtained from fitting the 248.7 cm^{-1} resonance profile at 2.119 and 2.164 eV are indicated in Figure 6.41 by the blue lines, with a red line also showing the centre of the 240.4 cm^{-1} peak resonance at 2.148 eV. Comparing the resonance behaviour of the 398.2 cm^{-1} peak we find it is in good agreement with the energy of the state at 2.119 and 2.164 eV. For the peaks at 290.7, 309.1 and 353.8 cm^{-1} it is apparent that these peaks are resonant at energies below 2.164 eV and have a resonance behaviour similar to the 240.4 cm^{-1} peak.

From this qualitative analysis there are two clear groups of Raman peaks with similar resonance behaviour. The peaks at 248.7, 255.2, 260.4 and 398.2 cm^{-1} all show similar behaviour and are also observed when resonant with the WSe_2 A exciton in HS1. The second group contains the Raman peaks at 240.4, 290.7, 309.1 and 353.8 cm^{-1}, which are not observed at the A exciton in either HS1, HS2 or monolayer WSe_2. The 309.1 and 353.8 cm^{-1} peaks have been assigned to the A_2'' phonons in WSe_2 and $MoSe_2$ respectively, which are Raman inactive in monolayers. As a result we propose the assignment of the 240.4 and 290.7 cm^{-1} peaks to $MoSe_2$ Γ point phonons. A potential explanation for the observation of $MoSe_2$ Raman peaks to $MoSe_2$ at a WSe_2 B exciton resonance is the hybridisation of the WSe_2 B exciton with $MoSe_2$ states. Whilst, it is possible that the anomalous resonance behaviour of the 240.4 cm^{-1} peak can be explained due to resonance with the electronic states at 2.119 and 2.164 eV. The hybridisation of the WSe_2 B exciton resonance with $MoSe_2$ states can explain both the anomalous resonance

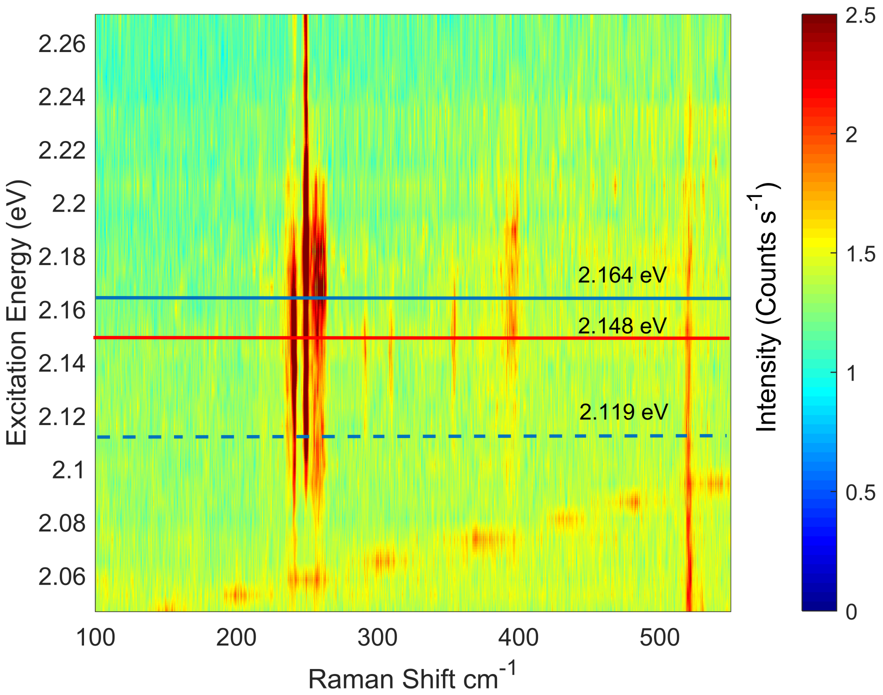

Figure 6.41: Colourmap showing resonance Raman data taken on HS1 using excitation energies from 2.05 to 2.25 eV probing the WSe$_2$ B exciton. Intensity data has been adjusted to emphasise the resonances for the Raman peaks that were too weak to be resolved for fitting. Coloured lines have been added to indicate the energies obtained from fitting the resonance profiles for the 240.3 and 249 cm^{-1} peaks.

behaviour and the appearance of the Raman peaks at 240.4, 290.7, 309.1 and 353.8 cm^{-1}. A more thorough discussion of the hybridisation of the WSe$_2$ B exciton is presented in Section 6.5.1.1.

In summary the resonance Raman behaviour for HS1 when resonant with the WSe$_2$ B exciton has been presented. The resonance Raman data demonstrated several different resonance behaviours with the 240.4 cm^{-1} peak profile showing a resonance at lower energy of 2.148 eV. Fitting of the 248.7 cm^{-1} resonance profile revealed the presence of two electronic states at 2.119 and 2.164 eV. The anomalous resonance behaviour of the 240.4 cm^{-1} was also fitted to a two state model and can be explained by resonance with two electronic states at 2.164 and 2.103 eV. A qualitative comparison of the resonance behaviour for the 290.7, 309.1 and 353.8 cm^{-1} Raman peaks revealed a similar behaviour to the 240.4 cm^{-1} peak. The proposed mode assignment for these Raman peaks to bilayer active and MoSe$_2$ Raman peaks suggests a likely explanation for the anomalous resonance behaviour of these Raman peaks is the hybridisation of the WSe$_2$ B exciton with MoSe$_2$ states.

6.4.4.2 HS2 Resonance Raman with WSe_2 B Exciton

For HS2 the Raman data when resonant with the WSe_2 B exciton is presented in Figures 6.42 & 6.43. From Figure 6.42 the resonance enhancement of several Raman peaks between 230 to 280 cm^{-1} is observed between 2.12 and 2.20 eV. As seen in HS1 the Raman peak at 249.0 cm^{-1} has a high energy tail, with the peak still showing significant intensity at the highest energies accessible with our experimental apparatus. This suggests that the 249.0 cm^{-1} Raman peak is also resonant with higher energy states above the B exciton. In addition there are several Raman peaks at 240.2, 258.3 and 261.2 cm^{-1} which are also clearly resonant at similar energies to the 249.0 cm,$^{-1}$ peak but are not strongly resonant above 2.22 eV. It is also clear from Figure 6.43 that there are several weak peaks near 400 cm^{-1} and below 240 cm^{-1}.

The Raman spectra were fitted and resonance profiles extracted for the Raman peaks at 240.2, 249.0, 258.3, 261.2, 392.2 and 396.3 cm^{-1}. The resonance profiles were then fitted to a single phonon event model assuming a single electronic state and are presented in Figure 6.44. Excluding the 249.0 cm^{-1} peak the resonance profiles all appear to be characterized by a single broad peak. For the Raman peaks at 240.2, 249.0, 258.3 and 261.2 cm^{-1} the resonance profiles appear to be in good agreement with the single state model. The coefficients from fitting are presented in Table 6.22 and show a significant variation in the energies obtained from the fitting process between 2.130 to 2.163 eV. The widths of the resonances are also relatively broad with values in the range of 42 to 68 meV. In comparison for HS1 the resonances have widths in the range of 17 to 38 meV and for monolayer WSe_2 (see Chapter 5) the widths are between 16 to 31 meV. Whilst it is possible that the resonances in HS2 are naturally broader a distinct possibility is the presence of multiple electronic states. The range of energies obtained from fitting the single state model between 2.130 and 2.163 eV also suggest the presence of multiple excitonic states.

Table 6.22: Coefficients obtained from fitting the resonance profiles for the Raman peaks observed on HS2 when resonant at the WSe_2 B exciton. Resonance profiles have been fitted to a single phonon event model assuming a single electronic excitation. The errors given for each coefficient are a standard deviation obtained from fitting. The units for the amplitude coefficients are 10^{-3} $\sqrt{Counts\ s^{-1} \cdot eV^2}$.

Raman Shift (cm^{-1})	Amplitude	Width (meV)	Energy (eV)
240.2	6.0±0.8	57.3±4.3	2.140±0.002
249.0	9.5±1.3	53.7±4.3	2.163±0.002
258.3	7.4±0.6	56.2±2.7	2.135±0.001
261.2	3.5±0.5	42.1±4.1	2.157±0.002
392.2	4.9±1.2	59.4±9.4	2.130±0.004
396.3	6.1±0.9	67.5±6.1	2.146±0.003

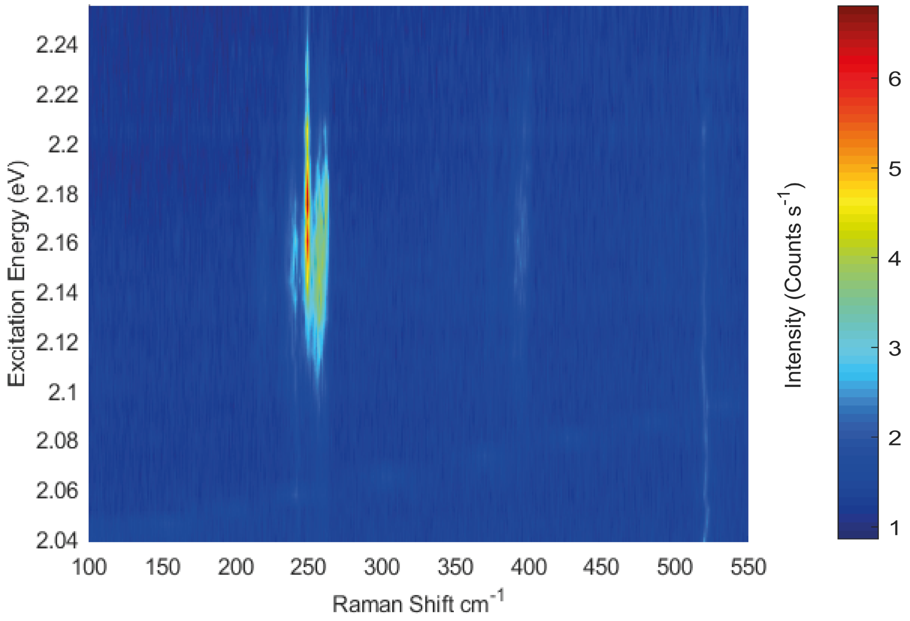

Figure 6.42: Colourmap showing resonance Raman data taken on HS2 using excitation energies from 2.05 to 2.25 eV probing the $MoSe_2$ B exciton.

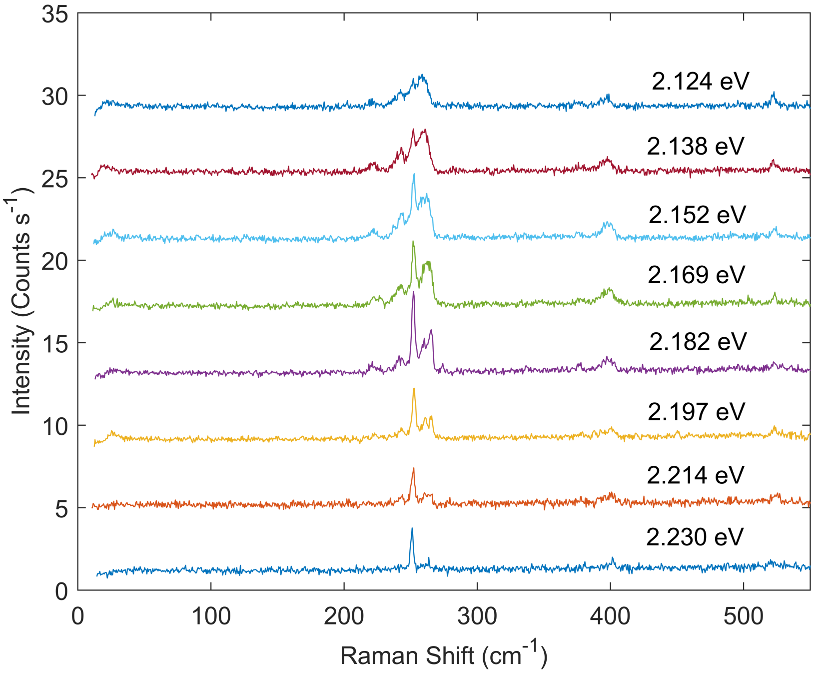

Figure 6.43: Raman spectra obtained when resonant with WSe_2 B exciton on HS2 using excitation energies from 2.05 to 2.25 eV.

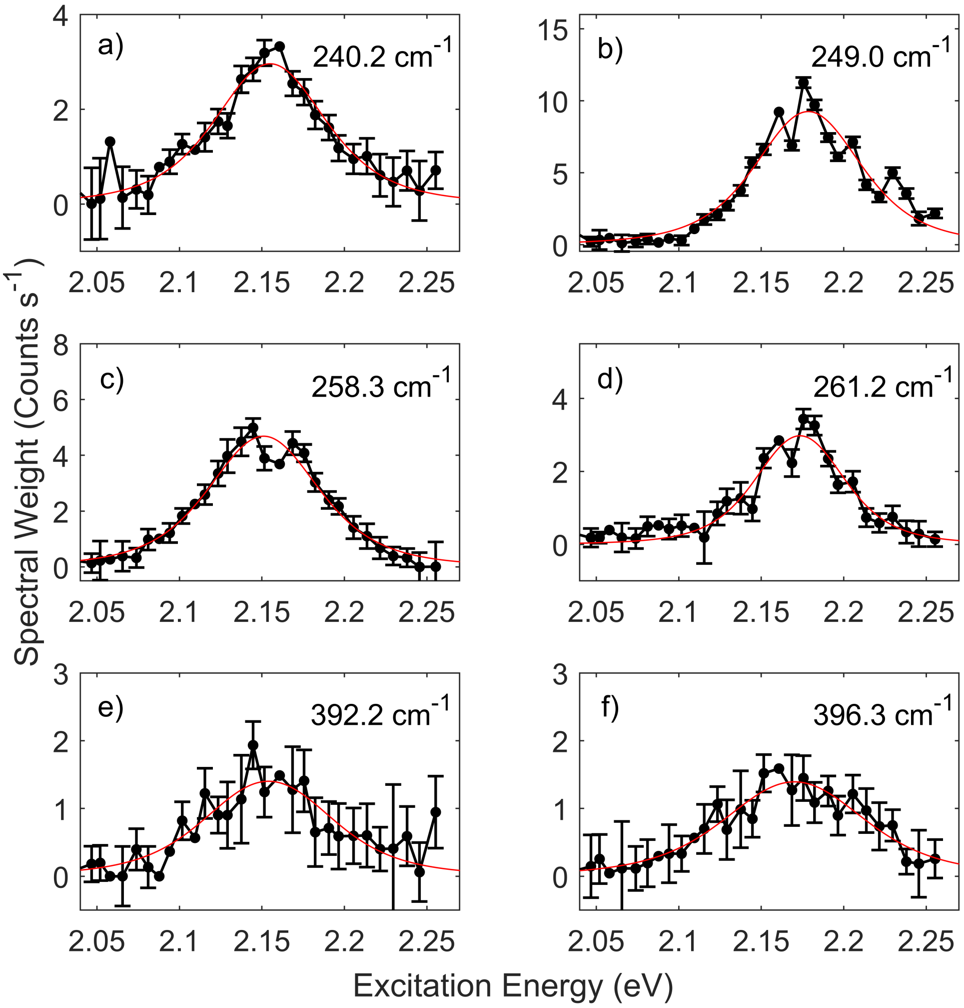

Figure 6.44: Resonance Raman profiles obtained for Raman peaks observed on HS2 when resonant with the WSe$_2$ B Exciton along with fits to a single phonon event model for a single electronic excitation.

Considering the energies from fitting in more detail the Raman peaks at 240.2, 255.8, 392.2 and 396.3 cm^{-1} all have energies in the range of 2.130 to 2.146 eV. Whereas, the energies for the Raman peaks at 249.0 and 261.2 cm^{-1} are significantly higher at 2.157 and 2.163 eV respectively. It is useful to consider if there is any justification for these two Raman peaks to act differently compared to the other Raman peaks. For the case of the 261.2 cm^{-1} peak the results presented in the mode assignment Section when resonant with the WSe$_2$ B exciton indicate this peak is dispersive. The dispersive nature of the 261.2 cm^{-1} peak can be seen upon a closer examination of the spectra presented in Figure 6.43 and is shown in Figure 6.9 in Section 6.3.2. In Figure 6.43 at 2.152 eV two clearly separated peaks are observed near 260 cm^{-1} whereas at 2.182 eV the dispersive nature of the 261.2 cm-1 peak results in a broader single peak. As previously stated dispersive Raman peaks require scattering to large wavevector intermediate states and so cannot be well approximated by the single phonon event models used in the fitting process. Therefore, the resonance energy for the 261.2 cm^{-1} should be omitted from the consideration of the resonance energies as it is unlikely to be representative of a discrete underlying electronic state. Considering the 249.0 cm^{-1} peak when comparing it's resonance profile to the remaining Raman peaks there is considerable spectral weight at energies above 2.25 eV, which is not observed in the other resonance profiles. Similar behaviour was also seen for the same peak in HS1. This implies that there are higher energy resonances which are not accessible for in our experiments and couple strongly to the 249.0 cm^{-1} peak. As a result it seems reasonable to consider this Raman peak as a separate case. For all the remaining Raman peaks observed on HS2 when resonant with the WSe_2 B exciton the energies obtained from fitting indicate the presence of an electronic state with a mean value and standard deviation of 2.138±0.007 eV.

Overall the resonance Raman profiles for HS2 when resonant with the WSe_2 B indicate the presence of an excitonic state at 2.138±0.007 eV. In addition the 249.0 cm^{-1} Raman peak has a distinct resonance profile and appears to be resonant with a state at 2.163 eV, but is also still resonant at higher energies above 2.22 eV. The exact behaviour of the 249.0 cm^{-1} peak is not resolved in these experiments, as 2.25 eV is the highest excitation available with our setup. These results suggest that the WSe_2 B exciton resonance for HS2 involves two electronic states at 2.138 and 2.163 eV. Comparing our results to those presented in Wang et al. [255] a likely assignment of these states is to the WSe_2 B trion at 2.138 eV and neutral exciton at 2.163 eV. The Raman spectra for HS2 at the WSe_2 B exciton also includes a dispersive Raman peak near $\sim$ 261.2 cm^{-1}. Peaks at similar frequencies in monolayer WSe_2 and HS1 have also been observed but are not obviously dispersive. A possibility is that this is a different Raman peak to those observed previously. This is supported by the work of Du et al. [190] who have suggested the presence of at least three Raman peaks near $\sim$ 260 cm^{-1}. For our results we find the best fit to the spectra only requires two peaks at 258.3 cm^{-1} and 261.2 cm^{-1}. The dispersion of this peak in HS2 and not HS1 or monolayer WSe_2 suggests either a modification of the WSe_2 phonon dispersion or difference in the underlying electronic states. A modification of the phonon dispersion seems unlikely due to the good agreement between the Raman peaks frequencies between HS2 and the other samples regions. Furthermore, the observation of a peak at 261.2 cm^{-1} at the WSe_2 A exciton in HS2 which is not dispersive suggests that the dispersion of this peak is a result of the electronic states available a the WSe_2 B exciton. Therefore, the dispersive behaviour of the 261.2 cm^{-1} is due to changes in the dispersion relation for excitons in HS2 compared to HS1 and monolayer WSe_2.

6.4.5 Resonance Raman of Low Frequency Modes

As presented in Sections 6.3.1 & 6.3.2 on HS1 there are several low frequency modes which are only observed for this sample region and have a different Raman spectra depending on if the resonant state is associated with the $MoSe_2$ or WSe_2 layer. This section presents the resonance Raman data for the low frequency modes observed in resonance Raman experiments. The low frequency modes are observed when resonant with the WSe_2 A exciton and for both the $MoSe_2$ A and B excitons.

6.4.5.1 Resonance with WSe_2 A Exciton

The resonance Raman data showing the low frequency modes when resonant with the WSe_2 A exciton is presented in Figure 6.45 with panel a) showing the resonance observed for the low frequency modes and panel b) showing the higher frequency WSe_2 Raman peaks near ~ 250 cm^{-1}. For the low frequency modes a resonance is clearly observed at $\sim$ 1.71 eV with four Raman peaks clearly visible at 35, 39, 53, 58 cm^{-1}. In comparison the BS peaks observed at higher frequencies on HS1 have much broader resonance profiles between 1.69 and 1.76 eV (see Section 6.4.1). The analysis of the higher frequency peaks demonstrated that the resonance profile was the result of resonance with two electronic states at 1.707±0.002 and 1.731±0.003 eV attributed to the trion and neutral exciton respectively. This suggests the low frequency peaks are only strongly resonant with the trion at the WSe_2 A exciton.

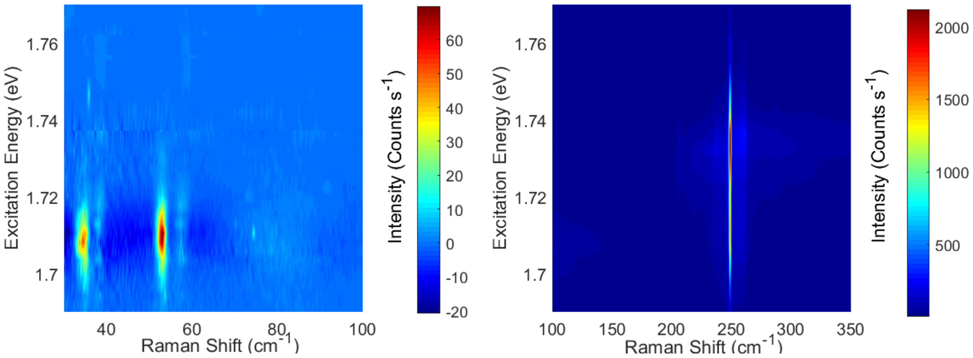

Figure 6.45: Colourmap shows resonance Raman data for the low frequency modes observed on HS1 when resonant with the WSe_2 A exciton.

The resonance profiles for the low frequency peaks are presented in Figure 6.46 and were fitted to a single phonon event model for a single electronic state. Overall the fits assuming a single electronic state are in good agreement with the data for the four low frequency Raman peaks. There is no visible asymmetry to the resonance profiles and so the low frequency peaks are likely resonant with a single electronic state. The coefficients from fitting are provided in Table 6.23. The energies obtained from fitting for all four Raman peaks are in agreement to within the errors with a mean value of

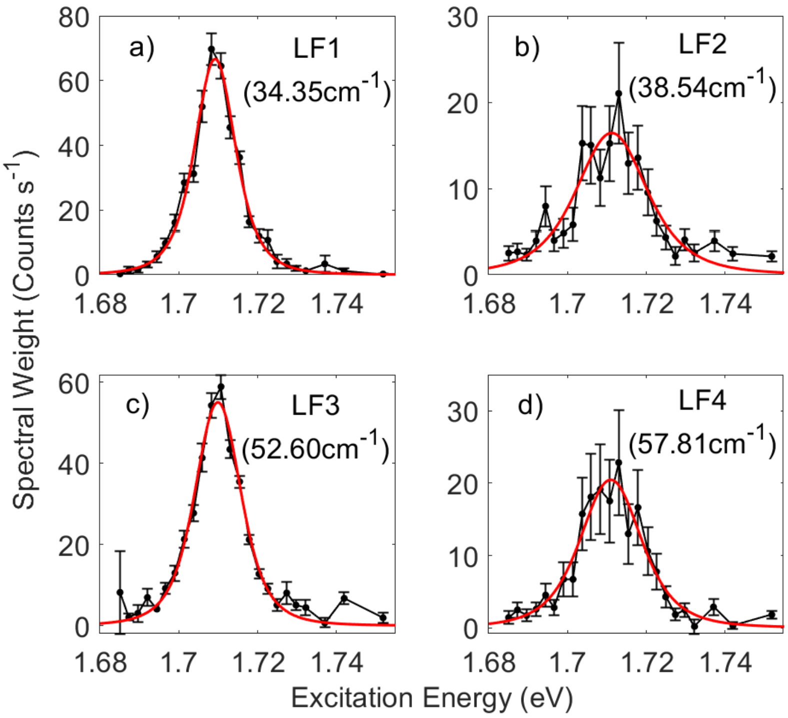

Figure 6.46: Fitted resonance profiles for all low frequency modes observed when resonant with WSe_2 A exciton and have been fitted using a single state Raman model.Error bars have been obtained from fitting and are given as a standard deviation.

1.708±0.001 eV. This is in excellent agreement with the lower energy state observed for the higher frequency WSe_2 modes. Therefore, the resonance Raman behaviour of the low frequency modes is due to resonance with the WSe_2 A trion.

Table 6.23: Coefficients from fitting the low frequency Raman peaks observed on HS1 when resonant with WSe_2 A exciton. Resonance profiles have been fitted to a single phonon event model for a single electronic excitation. The errors given for each coefficient are a standard deviation obtained from fitting. The units for the amplitude coefficients are $10^{-4}\ \sqrt{Counts\ s^{-1} \cdot eV^2}$.

Mode	Raman Shift (cm^{-1})	Amplitude	Width (meV)	Energy (eV)
LF1	34.4	0.7 ± 0.1	8.9 ± 0.3	1.707 ± 0.001
LF2	38.5	1.1 ± 0.2	16.2 ± 1.7	1.709 ± 0.001
LF3	52.6	0.7 ± 0.1	9.4 ± 0.4	1.707 ± 0.001
LF4	57.8	0.8 ± 0.1	13.1 ± 0.9	1.707 ± 0.001

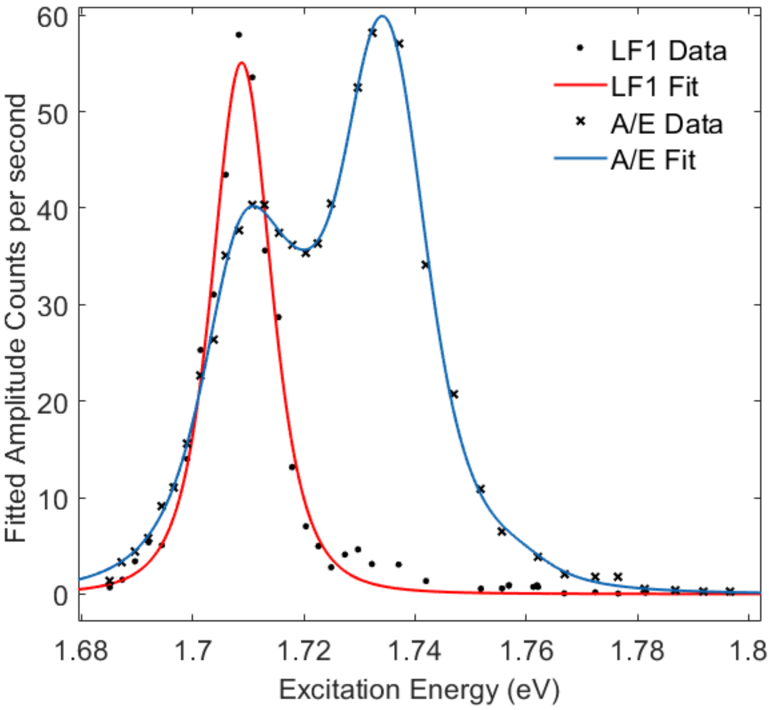

Figure 6.47: Comparison of the resonance profiles for the low frequency peak at 34.4 cm^{-1} (LF1) and 248.8 cm^{-1} (A/E) Raman peak when resonant with the WSe$_2$ A exciton. The best fit obtained from the analysis of both resonance profiles is also shown as indicated by the blue and red lines. In the case of the A/E resonance profile the fitted amplitude have been scaled by a factor of 37 for visual comparison.

6.4.5.2 Resonance with MoSe$_2$ B Exciton

The Raman data when resonant with the MoSe$_2$ B exciton is presented in Figure 6.48 with panel a) showing the low frequency range from 15 to 100 cm^{-1} and panel b) presents the higher frequency range from 100 to 350 cm^{-1} to allow a direct comparison with the typical MoSe$_2$ Raman peaks. The low frequency peaks at 39 and 58 cm^{-1} are resonant between 1.83 and 1.87 eV with the other low frequency Raman peaks also resonant but significantly weaker. In comparison the higher frequency MoSe$_2$ peaks are resonant from 1.83 to 1.89 eV and are significantly broader due to the larger separation of the incident and outgoing resonances.

Resonance profiles were obtained for the Raman peaks at 38.5 and 58.4 cm^{-1} and are presented in Figure 6.49. Whilst there are several other low frequency peaks visible these are relatively weak and it is not possible to extract their resonance profiles. Each resonance profile was fitted to a single phonon event model assuming a single electronic state and the resulting fits are shown in Figure 6.49 with the obtained coefficients are provided in Table 6.24 along with the phonon energies. Overall the coefficients for both peaks are in good agreement. The energies from fitting are 1.846±0.002 and 1.844±0.001

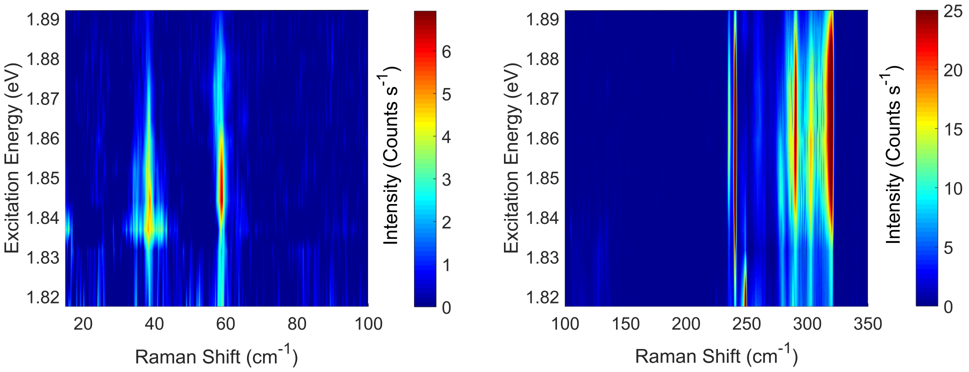

Figure 6.48: Colourmaps showing the resonance Raman data for HS1 when resonant with the MoSe$_2$ B Exciton. Panel a) Shows low frequency Raman from 15 to 100 cm^{-1} and panel b) show higher frequency range from 100 to 350 cm^{-1}. Colourbars shown have units of Counts per second.

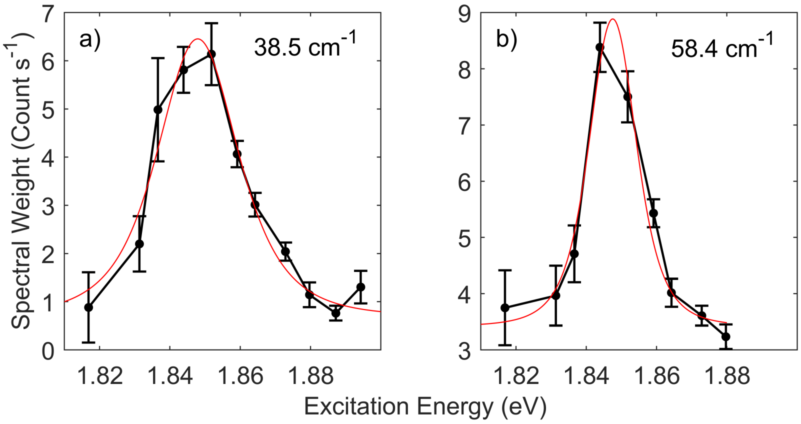

Figure 6.49: Resonance profiles for the low frequency Raman peaks at 38.5 and 58.4 cm^{-1} are presented in panels a) and b) respectively. In each case resonances have been fitted to a single phonon event model for a single electronic state with the resulting fit shown by the red line. The errors shown for the data are those obtained from fitting the Raman spectra.

eV for the 38.5 and 58.4 cm^{-1} peaks respectively and are in agreement to within the errors from fitting. In comparison the higher frequency TMDC Raman peaks (see Section 6.4.3) are also resonant with a state at 1.846±0.003 eV. Once again the energies obtained for the low frequency peak resonances are in excellent agreement with the energies of the higher frequency BS peaks.

Table 6.24: Coefficients obtained from fitting the resonance profiles for the low frequency modes at 38.5 and 58.4 cm^{-1} observed on HS1 when resonant with the MoSe$_2$ B Exciton. Resonance profiles have been fitted using a single phonon event model with a single electronic excitation. The errors given for each coefficient are a standard deviation obtained from fitting. The units for the amplitude coefficients are $10^{-3}\ \sqrt{Counts\ s^{-1} \cdot eV^2}$.

Raman Shift (cm^{-1})	Amplitude	Width (meV)	Energy (eV)	E$_{ph}$ (meV)
38.5	1.1±0.4	20.8±3.5	1.846±0.002	4.7
58.4	0.3±0.1	10.9±2.4	1.844±0.001	7.3

6.4.5.3 Resonance with the MoSe$_2$ A exciton

The resonance Raman data obtained for the low frequency Raman peaks observed on HS1 when resonant with the MoSe$_2$ A exciton is presented in Figure 6.50. From the colourmap in Figure 6.50 there are four low frequency Raman peaks at 39.1, 42.4, 59.3 and 63.5 cm^{-1} with a fifth Raman peak at 35.3 cm^{-1} appearing as a shoulder below the 39.1 cm^{-1} Raman peak. All the Raman peaks in this case are resonant between 1.62 and 1.635 eV although there appears to be some variation in the resonance energies for these peaks.

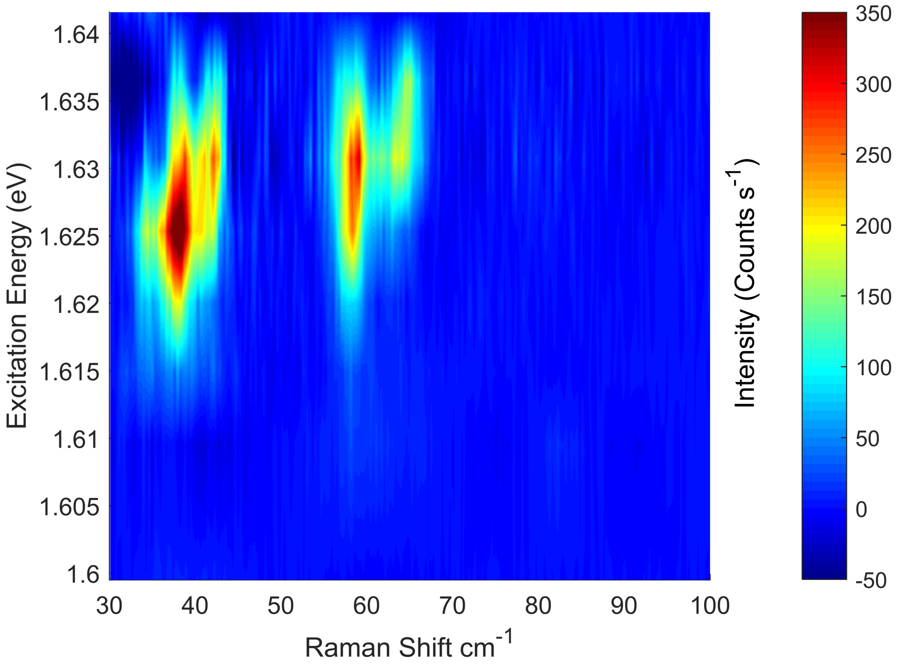

Figure 6.50: Colourmap presenting the resonance Raman data for the low frequency modes on HS1 observed when resonant with the MoSe$_2$ A exciton. Four of the Raman peaks are clearly resolved with a fifth Raman peak at 35.3 cm^{-1} appearing as a shoulder below the 38.9 cm^{-1} peak are observed and resonant at ~ 1.63 eV at 34.2 cm^{-1}.

Table 6.25: Coefficients obtained from fitting the resonance profiles for the low frequency modes observed on HS1 when resonant with the $MoSe_2$ A exciton. Resonance profiles were fitted to a single phonon event model assuming a single electronic excitation. The errors given for each coefficient are a standard deviation obtained from fitting. The units for the amplitude coefficients are 10^{-3} $\sqrt{Counts\ s^{-1} \cdot eV^2}$.

Raman Shift (cm^{-1})	Amplitude	Width (meV)	Energy (eV)
35.3	0.7±0.3	8.9±1.8	1.623±0.001
39.1	1.8±0.2	8.4±0.7	1.624±0.001
42.4	0.9±0.2	7.3±0.9	1.628±0.001
59.3	1.7±0.2	7.8±0.7	1.625±0.001
63.5	0.8±0.1	5.0±2.0	1.629±0.001

The resonance profiles for all five peaks were obtained and fitted to a single phonon event model assuming a single electronic excitation. The resonance profiles and obtained fits are presented in Figure 6.51 with the coefficients from fitting provided in Table 6.25. The resonance profiles data is shown for excitation energies between 1.6 and 1.65 eV. Measurements were made at higher excitation energies as shown in Section for the Bulk TMDC Raman peaks. However, no low frequency modes were observed at higher energies above 1.65 eV at the $MoSe_2$ A exciton resonance. The resonance profiles for all of the Raman peaks have a similar appearance characterised by a single symmetric peak. The fitted model for a single electronic state is in good agreement with the experimental data in each case. Considering the coefficients obtained from fitting in Table 6.25 the energies for all of the Raman peaks are between 1.623 to 1.629 eV, with a mean value and standard deviation of 1.626±0.003 eV. Closer inspection reveals that the energies appear to form two subsets with the Raman peaks at 35.3, 39.1 and 59.3 cm^{-1} all having similar energies between 1.623 and 1.625 eV. Whereas, the Raman peaks at 42.4 and 63.5 cm^{-1} both have slightly higher energies of 1.628 and 1.629 eV respectively. Whilst the differences between these energies is relatively small 4-5 meV a clear difference in the resonance energy is also apparent in Figure 6.50. It is therefore possible that the resonances for the low frequency modes requires two electronic excitations separated by 4-5 meV. However, at present the nature of these states is not clear. For the BS Raman peaks the analysis of the resonances at the $MoSe_2$ A exciton demonstrated the involvement of the $MoSe_2$ A trion at 1.627 eV and the neutral exciton at 1.648 eV. Therefore, the low frequency modes on HS1 appear to be only resonant with the $MoSe_2$ A trion. These results may suggest a fine structure to the trion with a separation of $\sim$ 5 meV, and requires further investigation.

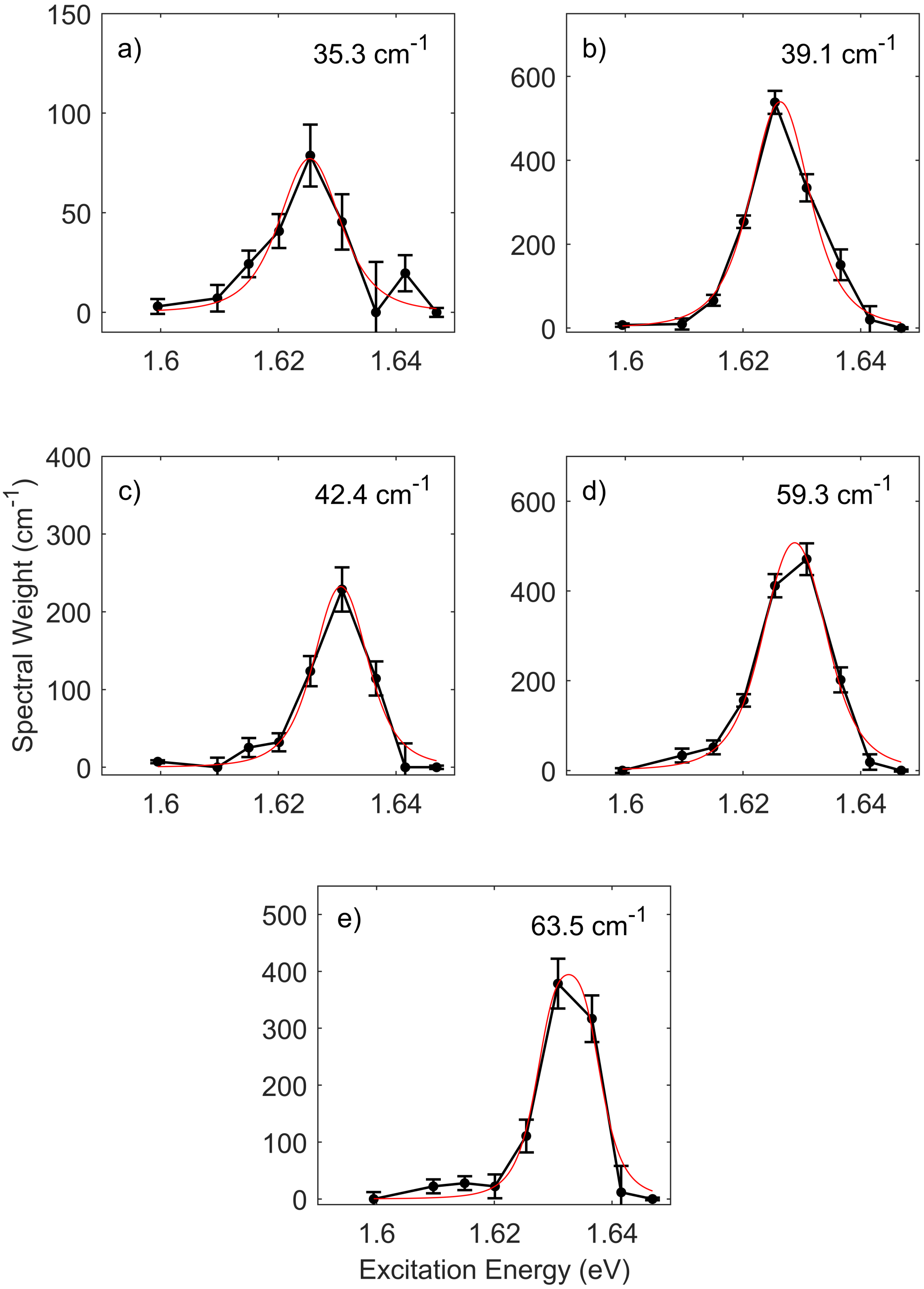

Figure 6.51: Resonance Raman profiles for the low frequency Raman peaks observed on HS1 when resonant with the $MoSe_2$ A exciton are presented. In each case the resonance profile has been fitted to a single phonon event model for a single electronic excitation with the fitted profile shown as a red line. Error bars shown were obtained from fitting the Raman spectra.

6.5 Discussion

The following sections present a discussion of the resonance Raman results presented in the previous section. There are two sections to this analysis the first considers the behaviour of the intralayer excitons in HS1 and HS2 providing a comparison of there two sample regions. The second section then focuses on the low frequency modes observed on HS1 comparing the resonance behaviour of these peaks to the more typical bulk TMDC Raman peaks and proposing the origin of these peaks in the Raman spectra.

6.5.1 Intralayer Excitons in TMDC Heterostructures

The resonance Raman data for both HS1 and HS2 has been analysed at each of the intralayer excitons and has revealed resonances with excitons, trions and additional anomalous states. In this section the resonance behaviour of HS1, HS2 are compared to the results for the constituent monolayers. To aid in this discussion the results of resonance Raman analysis for all four sample regions is summarised in Table 6.26. For each of the intralayer excitons it is possible to classify the different states in each case as either the neutral exciton (X), the trion (T) or an anomalous resonance (A).

For the $MoSe_2$ A exciton resonance Raman data was obtained for both HS1 and HS2 and indicates the presence of two excitonic states. However, for monolayer $MoSe_2$ it was not possible to measure the resonance Raman behaviour due to intense PL from the

		Sample Region			
		HS1	HS2	ML $MoSe_2$	ML WSe_2
$MoSe_2$ A	T	1.627±0.001	1.629±0.002	1.622±0.001 *	-
	X	1.648±0.005	1.650±0.003	1.649±0.001 *	-
WSe_2 A	T	1.706±0.001	1.706±0.005	-	-
	X	1.732±0.003	1.734±0.002	-	1.742 ± 0.002
	A	-	1.688±0.001	-	-
WSe_2 A*	A(2s)	-	-	-	1.866±0.001
WSe_2 A**	A(3s/4s)	-	-	-	1.904±0.002
$MoSe_2$ B	T	-	1.822±0.009	1.828±0.002	-
	X	1.845±0.002	1.846±0.016	1.862±0.001	-
	A	1.754±0.002	-	1.802±0.001	-
WSe_2 B	T	2.110±0.011	2.138±0.007	-	2.136±0.004
	X	2.164±0.003	2.163±0.002	-	2.162±0.004

Table 6.26: This table provides a summary of the different states observed for both heterostructures and monolayers. For each resonance the multiple excitonic states have been labelled as follows: neutral exciton (X), trion (T) and states with anomalous resonance behaviour (A). For monolayer $MoSe_2$ A exciton it was not possible to resolve the resonance behaviour and so the energies given for the exciton and trion are those determined from the PL spectrum and are labelled with an asterisk (*).

sample. To allow for a comparison with the heterostructures the energies shown in Table 6.26 for the exciton and trion in monolayer MoSe$_2$ were obtained from the PL spectrum. Comparing the energies of the MoSe$_2$ A exciton for all three sample regions we find they are all in excellent agreement to within the given errors. For the trions observed at the MoSe$_2$ A exciton the energies obtained for HS1 and HS2 are in agreement, but are found to be $\sim$ 6 meV above the energy of the trion in monolayer MoSe$_2$. A shift in the energy of the trion is not unexpected as the energy of this state is dependent on the carrier density [255, 92]. The formation of the heterostructure should result in charge transfer between the two layers due to their band alignment. As a result a the shift in the energy of the trion is likely a result of the change in carrier density in the heterostructures. Therefore, the MoSe$_2$ A exciton energy is in agreement for all sample regions and shows no appreciable change in energy. The energy of the trion in HS1 and HS2 is observed to shift to higher energies, and is attributed to charge transfer altering the carrier density.

Considering next the resonance Raman behaviour of the WSe$_2$ A excitons for the heterostructures two states were required to fit the data. These were attributed to the neutral exciton and trion and for HS1 and HS2 the energies of the X and T (see Table 6.26) are both in agreement to within the obtained errors. However, for monolayer WSe$_2$ the resonance Raman behaviour only required the presence of a single electronic state at 1.742 eV attributed to the neutral A exciton. This is $\sim$ 9 meV greater than the energies of the X in HS1 and HS2 and so there is a significant shift in the energy of the X in the heterostructures. The presence of the trion state in both HS1 and HS2 also suggests a significant change in the carrier density in agreement with the shift proposed for the trions at the MoSe$_2$ A exciton. The separations of the X and T in HS1 and HS2 are 26 and 28 meV respectively. Comparing these separations to the monolayer WSe$_2$ PL spectra indicates a possible assignment of the T in the heterostructures to the negatively charged intra-valley trion. However, it is difficult to be certain of the precise nature of this trion state, due to the dependence on charge carrier density and the presence of other excitonic states in WSe$_2$ such as biexcitons. Although the latter possibility is considered unlikely due to the low oscillator strength and excitation density of the biexciton states [132, 92, 93]. Comparing the obtained energies for the WSe$_2$ A exciton with the PL spectra there is also further evidence of shifts with the X in HS1 observed at 1.729±0.001 eV and HS2 at 1.739±0.001 eV. It is possible that the shift in energy of the exciton at the WSe$_2$ is a result in the difference in the dielectric environment between the heterostructure and monolayer [33], which can alter the exciton binding energies. However, we would also expect to see similar shifts for the MoSe$_2$ A excitons in the heterostructure. For similar TMDC heterobilayers several recent studies report photoluminescence spectra as a function of twist angle and observe changes on the energies of the exciton and trion states, which may be able to explain the variation in the energies of the WSe$_2$ A X [122]. Further studies of the intralayer excitons as a function of twist angle are required to confirm this mechanism.

In monolayer WSe_2 there are several additional excitonic states in Table 6.26 denoted as the A* and A**. These states have been attributed to resonances with excited states of the WSe_2 A exciton. For HS1 and HS2 there was no observed resonant enhancement at the expected energies of the WSe_2 A* or A** states. For monolayer WSe_2 the A exciton showed only resonant enhancement with the neutral exciton, whereas both HS1 and HS2 were resonant with both excitons and trions. The emergence of trions in the WSe_2 layer suggests a change in the carrier density resulting from charge transfer in the heterostructure. In gated PL and reflectance contrast measurements the appearance of the trion is associated with a decrease in the strength of the neutral exciton [255, 92, 261] Therefore, in HS1 and HS2 the lack of resonance with the WSe_2 A* and A** states is likely due to the suppression of the WSe_2 A exciton due to changes in charge carrier density.

In HS2 near resonance with the WSe_2 and $MoSe_2$ A excitons an additional Raman peak was observed at 245.8 cm^{-1}. Comparison of the Raman spectra in Section 6.3.1 revealed that it is not possible from the Raman spectra along to associated this peak with either the WSe_2 or $MoSe_2$ phonons. The resonance Raman data for this peak was analysed and was shown to be resonant with two excitonic states at 1.688 ± 0.001 and 1.703 ± 0.002 eV. Comparing these energies to those for HS2 in Table 6.26 suggests that the peak at 1.703 eV is in agreement with the energy of the trion at the WSe_2 A exciton. However, for the BS Raman peaks at the WSe_2 A exciton there is no evidence of a resonance at 1.688 eV for any other Raman peaks. Reports of the excitonic states in monolayer WSe_2 have demonstrated the presence of a dark exciton and charged biexcitons at similar energies, and could explain the state at 1.688 eV. On the other hand the energy of the 245.8 cm^{-1} peak is 30.5 meV, and so an outgoing resonance with the $MoSe_2$ A X would be expected at $\sim$ 1.681 eV. Whilst there energies are not in direct agreement they are close enough that a double resonance between the WSe_2 A trion and $MoSe_2$ A exciton is worth considering. The band alignment of the WSe_2 and $MoSe_2$ layers should result in charge transfer of electrons in the WSe_2 conduction band to the lower energy states in $MoSe_2$ and with holes transferring from the $MoSe_2$ valence band to the WSe_2 band. Studies of the charge transfer dynamics in TMDC heterostructures [103, 105] suggests that phonons play an important role in overcoming the momentum mismatch between the Brillouin zones of the different layers and allowing relaxation to lower energy states. This may support the interpretation that this anomalous low energy state is the result of scattering between the WSe_2 and $MoSe_2$ monolayer. However, there is no clear evidence suggesting which of the two proposed explanations is correct. Further measurements of other heterostructures combined with gated measurements may allow further clarification of the origin of this anomalous state.

In Table 6.26 the energies associated with the $MoSe_2$ B exciton are shown for all samples and reveal the presence of three different resonances associated with a neutral exciton, trion and anomalous state. For both heterostructures and the monolayer region a state has been attributed to the $MoSe_2$ B X, and in HS1 and HS2 the energy of this state is in found to be in excellent agreement with an energy of $\sim$ 1.846 eV. In comparison the state attributed to the neutral B exciton in monolayer $MoSe_2$ is observed at 1.862 eV and is $\sim$ 16 meV higher in energy. For HS2 and monolayer $MoSe_2$ a resonance was also observed with a lower energy state attributed to the B trion. The identification of the neutral exciton and trions at the B excitons in $MoSe_2$ is not trivial with only a few reported observations in literature. The results of reflectance contrast measurements by Wang et al. provide the clearest identification of neutral and charged exciton at the B excitons in $MoSe_2$ and WSe_2 layers [255]. These results indicate that the neutral B exciton is observed in the range of 1.84 to 1.87 eV with the negatively charged trion in the range of 1.815 to 1.845 eV and the positively charged trion in the range of 1.800 to 1.840 eV. Therefore our results for the energy of the excitons and trions at the $MoSe_2$ B resonance in each sample are consistent with the work of Wang et al. Whilst the energies obtained for HS2 and monolayer $MoSe_2$ suggest a difference in the exciton and trion separation the uncertainty in the energies for HS2 means it is difficult to be sure if this shift is significant. The lack of a lower energy trion in HS1 compared to HS2 can also be explained by difference in the carrier density of the heterostructures which has been shown to be dependent on the sample twist angle [100].

In addition to the excitons and trions observed when resonant with the $MoSe_2$ B exciton an anomalous resonance is observed in both HS1 and monolayer $MoSe_2$, but not in HS2. In both cases the anomalous resonance is only observed for three particular Raman peaks with shifts of $\sim$ 481, 530 and 582 cm^{-1}. The frequencies of these peaks are in agreement to within 1 cm^{-1} when comparing HS1 and monolayer $MoSe_2$ (see Table 6.4 in Section 6.3.1). The anomalous resonance behaviour in both cases is similar with the resonance profiles of the peaks narrower than their peak energies and demonstrate a increase in the resonance energy as a function of Raman shift. However, we do not observe the expected incoming or outgoing resonances required for a resonance with a single excitonic state. Instead the resonance profiles are attributed to a double resonance process involving the incoming resonance at the $MoSe_2$ B exciton and the outgoing resonance of a lower energy anomalous state. The lower energy state energies as given in Table 6.26 as 1.754 and 1.802 eV for HS1 and monolayer $MoSe_2$ respectively. For monolayer $MoSe_2$ we proposed that this resonance may involve scattering from the $MoSe_2$ B exciton to the 2s excited state of the $MoSe_2$ A exciton (see Chapter 4). However, the difference in energy of the anomalous state in HS1 and monolayer $MoSe_2$ shows a shift of 48 meV and so likely involves a different excitonic state in HS1. The involvement of identical Raman peaks suggests the underlying mechanism is similar, and must be the result of of multi-phonon processes. Although, the precise assignment of these peaks to a particular set of underlying phonons is not possible due to the degeneracy of several different combination modes allowing for multiple assignments to each Raman peak. The measurements presented in this thesis do not allow for the nature of these anomalous resonances to be addressed further. Therefore, we can conclude that the anomalous resonances observed in both HS1 and in monolayer $MoSe_2$ both result from similar scattering processes coupling to a lower energy state, and have not been previously reported in literature. However, further measurements are required to determine the precise nature of the excitonic states involved.

Finally the resonance Raman behaviour at the WSe_2 B exciton has been investigated for all sample regions. From Table 6.26 two states have been identified in both the heterostructures and monolayer WSe_2. The highest energy states in each case have been attributed to the neutral exciton the obtained energies are in agreement to within the obtained errors and indicate at state at $\sim$ 2.163 eV. The energy of this state is also in agreement with the energy of the neutral exciton reported by Wang et al. between 2.145 and 2.17 eV [255]. The second state was attributed to the trion and for HS2 and monolayer WSe_2 the energies of this state are in good agreement. Whereas, the energy of the trion state in HS1 is found to have an energy of 2.110 eV and is $\sim$ 27 meV below the energy of the trion in HS2 and monolayer WSe_2. The results of Wang et al. suggests the WSe_2 B trion has an energy between 2.1 and 2.145 eV, although it is not possible from the energy of the states to determine if the trion is positively or negatively charged. Therefore, it is possible to assign the lower energy state in HS1, HS2 and monolayer WSe_2 to the WSe_2 B trion. The shift in energy for HS1 is the result of differences in the charge carrier density and could result from charge transfer in the heterostructure. However, as demonstrated in Section 6.3.2 there are the Raman spectra are also signifiant different for all three sample regions. For both HS1 and HS2 the Raman peak at $\sim$ 249 cm^{-1} still appears resonant at the highest energies accessible by our setup and suggests the presence of additional higher energy excitonic states. These higher energy states may be associated with excited states of the B exciton or the C exciton in WSe_2 which have been reported using reflectance contrast and resonance Raman spectroscopy [132, 193, 35]. In particular there are also several new Raman peaks on HS1 at 290.7, 309.1 and 353.8 cm^{-1} and a Raman peak at 240.4 cm^{-1}, which may show anomalous resonance behaviour. These peaks are discussed in more detail in Section 6.5.1.1 and may indicate hybridisation of the WSe_2 B exciton with $MoSe_2$ states.

In conclusion the intralayer excitons in both HS1 and HS2 have been probed using resonance Raman spectroscopy and compared to the results from the constituent monolayers. Overall the energies of the intralayer excitons in HS1 and HS2 are in good agreement with the energies observed in the constituent monolayers. For the heterostructures the resonance Raman behaviour in several instances indicates a change in carrier density likely a result of charge transfer between the layers. This leads to the appearance of significant trion scattering at the WSe_2 A exciton and shifts in the energies of the trion states observed at the other intralayer excitons. For the $MoSe_2$ A and WSe_2 B excitons the observed energies of the neutral excitons are in good agreement with no appreciable shifts in energy. However, at the WSe_2 A and $MoSe_2$ B excitons the state attributed to the neutral exciton are shifted between 10 and 16 meV. The exact mechanism for the shift in the energy of these excitons is not clear. A change in dielectric would require changes in the binding energies for all excitons and so seems unlikely. Although this may be consistent with reported shifts in the energies of the intralayer excitons in other heterobilayers as a function of twist angle. At present there are only a limited number of reports probing the intralayer excitons in heterobilayers and none to our knowledge probing the B excitons or higher energy states. Consequently, it is not obvious if the changes in the energies of these excitons are to be expected or not and requires further measurements of other heterobilayers to ensure this result is significant. However, there are several indications of twist angle dependence affecting the resonance Raman behaviour of the heterostructures, such as the shift of the $MoSe_2$ B anomalous resonance energy on HS1 and its disappearance in HS2; appearance of a new Raman peak at 245.8 cm^{-1} only in HS2 coupling to states between the WSe_2 and $MoSe_2$ A excitons; and the contrasting resonance behaviour at the WSe_2 B exciton resonance. These observations potentially indicate the coupling between different excitonic states via large wavevector phonons and dark states, significant modification of electronic state energies as a function of twist angle and the possibility of hybridisation between layers in TMDC heterostructure which in this case can only be accessed via resonance Raman spectroscopy. There is a host of new and unexplored physics available in these TMDC heterostructure, but to fully understand the differences in the intralayer excitons behaviour requires further resonance Raman studies as both a function of twist angles and gate voltage.

6.5.1.1 Hybridisation of the WSe_2 B Exciton in HS1

On HS1 when resonant with the WSe_2 B exciton three new Raman peaks are observed and warrant further discussion. These new peaks at 290.7, 309.1 and 353.8 cm^{-1} are only seen on HS1 and are not observed at the A exciton resonance. When resonant with the WSe_2 B exciton there are significant differences between the heterostructure and monolayer Raman spectra. In particular on HS1 an intense Raman peak at 240.4 cm^{-1} is observed. Although there are peaks in both HS2 and monolayer WSe_2 at similar frequencies these peaks have relatively low intensities. However, on HS1 the peak at 240.4 cm^{-1} is the dominant peak in the Raman spectra. The resonance profile for this peak is also unusual when compared to the other Raman peaks observed on HS1 at the B exciton resonance. The resonance profiles for the other peaks on HS1 are the result of resonance with two different states at the WSe_2 B exciton. The 240.4 cm^{-1} peak resonance profile can be explained by two states at similar energies to the other Raman peaks. However, the amplitudes for the different scattering channels are significantly different and require the interstate scattering terms to be the dominant scattering channel in order to explain the narrower resonance profile centred at $\sim$ 2.148 eV. Due to the low intensity of the peaks at 290.7, 309.1 and 353.8 cm^{-1} it was not possible to extract useful resonance profile. Although, a qualitative comparison suggests they have a similar resonance behaviour to the 240.4 cm^{-1} Raman peak. The appearance of these new peaks and their atypical resonance behaviour suggests a similar underlying mechanism.

Consideration of the mode assignments for the Raman peaks at 240.4, 290.7, 309.1 and 353.8 cm^{-1} indicates that it is possible to determine multiphonon processes using the WSe_2 dispersion relation to explain all of these peaks. Of these only the 309.1 cm^{-1} peak has a possible assignment to the $A_2''(\Gamma)$ phonon. This Raman peak is not observed in monolayer WSe_2 due to the motion of the vibration being anti-symmetric upon reflection in the plane of the W atoms. However, this peak is allowed in multilayer WSe_2 and has been reported in the Raman spectra of WSe_2 bilayers [52]. Interestingly the Raman peak at 353.8 cm^{-1} can be assigned to the equivalent $A_2''(\Gamma)$ phonon in $MoSe_2$ [194, 144]. A further review of the Raman spectra reported for heterobilayers in literature reveals that the 309.1 cm^{-1} Raman is seen in several different heterobilayers containing a WSe_2 layer [107, 281, 282]. Similarly the $MoSe_2$ A_2'' peak has also been observed at $\sim$ 353 cm^{-1} in several heterobilayers containing a $MoSe_2$ layer[107, 283]. These Raman peaks were also observed along with the typical zone centre $MoSe_2$ and WSe_2 in all cases. Although, this is not unexpected as these measurements were performed at energies above 2.33 eV at room temperature and are likely resonant with the C excitons in both $MoSe_2$ and WSe_2 [132, 133]. In contrast our results observe both of these peaks when resonant with the WSe_2 B exciton with no coincident resonance observed in monolayer $MoSe_2$. Including $MoSe_2$ Raman peaks in our mode assignment for the HS1 Raman spectra reveals natural explanations for the 240.4, 290.7 and 353.8 cm^{-1} peaks to zone centre single phonon processes. The 240.4 cm^{-1} peak can be assigned to the $A_1'(\Gamma)$ phonon, which is the dominant peak in the $MoSe_2$ Raman spectra and is observed when resonant with the $MoSe_2$ A and B excitons in HS1, HS2 and monolayer $MoSe_2$. The Raman peak at 290.7 cm^{-1} has an assignment to the $E'(\Gamma)$ and is frequently reported in literature [194, 144]. As previously discussed the 353.8 cm^{-1} Raman peak also has an assignment to the $A_2''(\Gamma)$ phonon. The only Γ point phonon not assigned is the $E''(\Gamma)$ phonon. This peak is forbidden in backscattering geometry due to the in plane symmetry of the vibrational mode [48]. However, unlike the A_2'' phonon the transition from monolayer to multilayer does not change the symmetry of this mode and so it is still expected to be forbidden regardless of the number of layers in the sample. As a result if we assign the 353.8 cm^{-1} to the $A_2''(\Gamma)$ phonon in $MoSe_2$ it is possible to explain the remaining anomalous Raman peaks to $MoSe_2$ zone centre single phonon processes. Comparing the anomalous peaks at 240.4 and 290.7 cm^{-1} to those observed when resonant with the $MoSe_2$ intralayer excitons on HS1 we find the frequencies of these peaks to be in excellent agreement.

The breaking of the symmetry in the heterobilayer provides a natural explanation for the appearance of the WSe_2 $A_2''(\Gamma)$ point phonon in a heterobilayer. But does not explain why this peak is not observed at the WSe_2 A exciton. Similarly the $MoSe_2$ $A_2''(\Gamma)$ is only seen at the WSe_2 B exciton and is not observed at the $MoSe_2$ A or B excitons. In order to observe phonons associated with the $MoSe_2$ layer at the WSe_2 B exciton requires hybridisation of either the phonon modes or the electronic states. If the phonons themselves were hybridised we would expect to see scattering with the anomalous Raman peaks at multiple resonances. However, it is entirely believable that hybridisation of the electronic states could occur at a single resonance due to the alignment of the energies of the relevant states. As has previously discussed the energy of the lower energy state in HS1 is shifted by $\sim$ 20 meV compared to HS2 and monolayer WSe_2 suggests a change in the underlying electronic states. The lack of similar anomalous peaks in HS2 indicates a possible twist angle dependence on this hybridisation. This is not surprising and is supported by the DFT predictions of Gillen et al. who demonstrate that the twist angle of the structure can tune the energies of both the inter and intralayer excitons [112].

For the hybridisation of the electronic states it is useful to consider the possible states involved. An obvious candidate is the WSe_2 B exciton, although it is possible that the degeneracy of this anomalous resonance with the WSe_2 B exciton is coincidental this seems unlikely. As a result a likely state involve in the hybridisation is the WSe_2 B exciton. The other potential states that could be involved are the $MoSe_2$ intralayer excitons and the interlayer excitons present in the heterobilayer. Of these two possibilities the most likely is the interlayer exciton, due to the visibility of the A_2'' phonons. In order to see strong scattering from these Raman peaks requires a change in the out of plane symmetry. As such, an interlayer exciton is more likely to be asymmetric upon reflection in plane of the metal atoms. If this proposal is correct the anomalous Raman peaks observed when resonant with the $MoSe_2$ are the result of a hybridisation of the

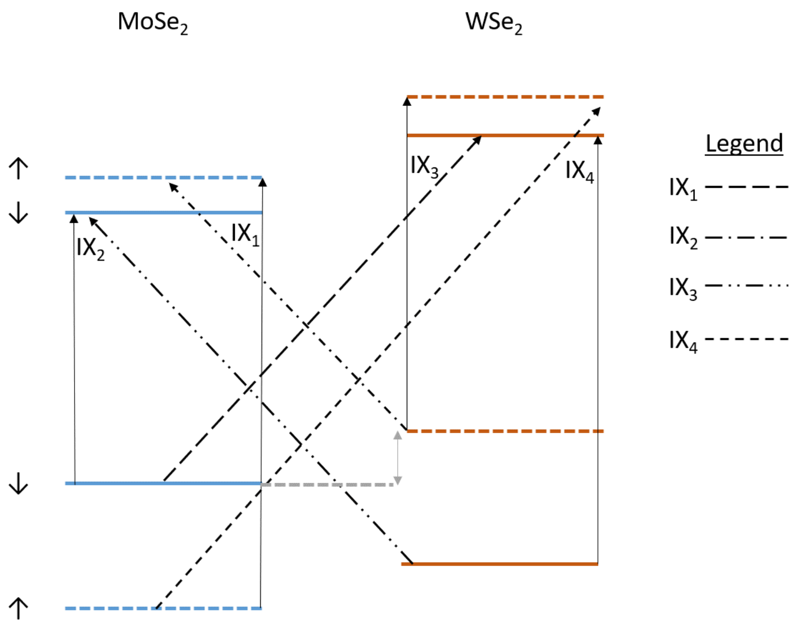

Figure 6.52: Diagram showing the four possible interlayer excitons which can form in a MoSe$_2$ and WSe$_2$ heterobilayer with a twist angle of 60°. The blue and orange lines distinguish between the two different materials, with dashed and solid lines indicating the spin states. The different interlayer excitons are distinguished by the different black dashed lines and the band offset between the valence bands of the two materials is indicated by the grey arrow.

WSe$_2$ B exciton. The anomalous Raman peaks are not observed at the other resonance as they are not hybridised with interlayer excitations.

Recently there have been similar reports of hybridisation in a MoSe$_2$/WS$_2$ heterobilayer [122]. In this instance the hybridisation was associated with the alignment of the conduction band states in the two layers. For our heterostructure a similar statement could be made regarding the valence band states of the MoSe$_2$ and WSe$_2$ layers which are predicted to be degenerate in DFT calculations [112]. Whilst the tunnelling between the two layers will depend on the energies of the single particle electronic states. When considering the hybridisation of the excitons the relevant energies will be the excitonic energies. If the hybridisation was dependent on the alignment of the single particle valence band states then we would expect to see hybridisation of both the MoSe$_2$ and WSe$_2$ B excitons. Our experimental results demonstrate the observation of the new Raman peaks at only the WSe$_2$ B exciton. This supports our interpretation that the relevant energies are those associated with the intralayer and interlayer excitons. Therefore, we would only expect to observe hybridisation with a single intralayer exciton.

	Exciton Energies (eV)		
	A(1s)	B(1s)	IX
WSe_2	1.742	2.166	-
E+X_b	1.911	2.335	-
$MoSe_2$	1.648	1.854	-
E+X_b	1.833	2.039	-
$WSe_2/MoSe_2$	-	-	1.328
E+IX_b	-	-	1.486

Table 6.27: The energies of the different optical transitions observed in HS1 are given. For each transition we provide the measured excitonic energy and the total energy of the state including the excitonic binding energy (E+X_b), which is determined using the excitonic binding energies predicted by Ruiz-Tijerinma and Fal'ko [129].

Predicted Energies (eV)	
IX1	1.328
IX2	1.768
IX3	2.084
IX4	2.306

Table 6.28: Predicted energies for the three higher energy interlayer excitons (IX) are presented along with the measured energy of the bright IX_1 exciton observed in HS1.

Using the energies of the intralayer and interlayer excitons, theoretical predictions of the excitonic binding energies [129] and conduction band and valence band spin splitting we can predict the energies of the different interlayer excitons. The energies of the optical transitions are given in Table 6.27. To correctly predict the energies of the different interlayer excitons we must also include the exciton binding energies in our calculations. The binding energies used are those calculated by Ruiz-Tjerina and Fal'ko and are 169, 185 and 158 meV for the WSe_2, $MoSe_2$ and Interlayer excitons respectively. As illustrated in Figure 6.52 there are four possible interlayer excitons at the K point. The predicted energies of the three higher energy interlayer excitons are given in Table 6.28. From this prediction we obtain a band offset between the two layers of 371 meV. The predicted energies of the interlayer excitons reveals that IX_3 is predicted to have an energy of 2.084 eV and is the most likely candidate for hybridisation with the WSe_2 B1s intralayer exciton.

As discussed, the hybridisation of the WSe_2 B exciton with an interlayer exciton is able to explain the observation of $MoSe_2$ phonons in HS1 at a WSe_2 resonance, and can account for the anomalous resonance behaviour of these peaks. The appearance of the Raman peaks at 309.1 and 353.8 cm $^{-1}$, which are only observed in bilayer or few layer WSe_2 and $MoSe_2$ has been observed previously in other homo and heterobilayers, and can be explained due to the change in symmetry of the excitonic state when hybridised. These peaks are not seen at the other intralayer excitons and suggests that these states have monolayer symmetry. We also identify the IX_3 interlayer exciton as a likely candidate for this hybridisation. Whilst, this model is compelling due to its ability to explain multiple features in our experiment data the hybridisation with an interlayer exciton is yet to be fully proven. An obvious experiment to test our proposed hybridisation model would require applying an electric field perpendicular to the heterobilayer. As has been shown for the interlayer excitons in TMDC heterostructures a double gate device can be used to tune the energy of the interlayer excitons. If our proposed model is correct the resonance Raman behaviour for the anomalous peaks should be significantly modulated by the application of a electric field normal to the sample plane. This would allow a tuning of the interlayer exciton energies and result in a detuning of the hybridised states.

6.5.2 Origin of Low Frequency Modes

Section 6.3.3 demonstrated the presence of LF Raman peaks seen exclusively on HS1. The LF modes are observed when resonant with both $MoSe_2$ and WSe_2 intralayer excitons and have a characteristic Raman spectra when exciting the different materials. Comparing the WSe_2 and $MoSe_2$ spectra the LF peaks appear similar in both cases but with their frequencies shifted depending on which material is being excited. This change in frequency of the LF peaks is likely due to the different masses of the transition metal atoms. Overall this suggests that the LF modes arise via the same mechanism and are associated with the different TMDC layers.

The resonance profiles for the LF Raman peaks were analysed and at each resonance were found to be associated with a single excitonic state. The energies from this analysis and the assignment of the underlying excitonic state to either the exciton or trion are summarised in Table 6.29. At both the $MoSe_2$ and WSe_2 A exciton the LF peaks are resonant with trion states. However, at the $MoSe_2$ B exciton it is not possible to attribute the LF peak resonance to either the exciton or trion. Attempts were also made to observe the LF peaks when resonant with the WSe_2 B exciton. However, these measurements were unable to resolve the LF peaks even using exposure times of ~ 1 hour. This is not surprising as the intensity of the LF modes is two orders of magnitude weaker than the bulk TMDC peaks, and the Raman intensity at the B exciton is also a order of magnitude lower than the A exciton. Similar, attempts to observe the LF peaks at 2.33 eV were also unsuccessful.

LF Raman peaks have been reported for both few layer and bulk TMDCs [284, 177, 44], and are attributed to layer breathing (LB) and shear modes (SM). The LB and SM modes have been studied as a function of twist angle for both twisted homobilayers and TMDC heterostructures [27, 107]. The results of Nayak et al. identified the LF peaks associated with the SM and LB modes in $MoSe_2/WSe_2$ heterobilayers and confirmed their frequencies to be between 15 to 30 cm^{-1} [107]. Therefore, it is unlikely that the LF peaks observed on HS1 are LB or SM modes due to their higher frequencies between 34 to 64 cm^{-1}. Furthermore, LB and SM modes are the result of collective motions of the TMDC layers and so we would expect the LF peaks associated with these modes to have identical frequencies when resonant with either layer. As a result, the observation of different LF peaks when resonant with the WSe_2 and $MoSe_2$ excitons provides further evidence that these are not LB or SM modes.

	Energy (eV)	X or T
WSe_2 A	1.707 ± 0.001	T
$MoSe_2$ A	1.627 ± 0.001	T
$MoSe_2$ B	1.845 ± 0.001	X/T

Table 6.29: Summary of the energies and assignments for the underlying excitonic states resonant with the LF Raman peaks on HS1.

A difference between the $MoSe_2$/WSe_2 heterobilayers investigated by Nayak et al. and our samples is the encapsulation between layers of hBN. The coupling of the hBN and TMDC layers may allow for additional LB and SM in our spectra. Recently, Ding et al. reported several LF peaks in an encapsulated monolayer of WS_2 at 28.8, 33.1 and 51.1 cm^{-1} and proposed that the 28.8 cm^{-1} peaks is a TMDC-hBN shear mode [179]. However, the DFT calculations used to support this assertion are unable to reproduce the frequency of the observed peak. The choice of WS_2 as the TMDC layer is also concerning as the 33.1 cm^{-1} peak has been reported for unencapsulated WS_2 monolayers [177], and the origin of this peak remains unclear. The 51.1 cm^{-1} has been reported in several studies and is associated with shear motion between the hBN layers [285]. This frequency is close to the LF peak observed at 52.9 cm^{-1} on HS1, however it is unlikely that this peak is a hBN shear mode as it is only seen when resonant with the WSe_2 excitons. Therefore, SM and LB modes do not seem capable of explaining the LF Raman peaks observed on HS1.

Our assertion that the LF peaks are not SM or LB modes requires a brief consideration of why these features are not observed in our spectra. A review of the literature reveals that the SM and LB modes have only been reported when exciting with energies resonant with the C exciton above 2.33 eV at room temperature [107, 177, 44]. In addition, neither the resonance Raman behaviour or the temperature dependence of the SM or LB has been reported. As a result differences in the experimental conditions may explain the absence of SM or LB modes, or our samples are not of comparable quality to those reported in literature. However, the observation of intense interlayer exciton PL for HS2 suggests a good interface between the TMDC layers. Subsequently, the most likely explanation for the absence of SM or LB modes in our spectra is due to a difference in either excitation energy, temperature or the throughput/signal to noise of our system. Notably, all reports of the SM and LB modes have used notch filters to allow measurements of Raman shifts <10 cm^{-1}. In comparison the triple spectrometer setup used in our experiments allows for measurements over a broad wavelength range, but is only able to reliably measure to within 20 cm^{-1} of the laser line. Therefore, the lack of SM and LB modes in our measurements is likely due to differences in the experimental setup between our work and those reported in literature.

The LF Raman peaks are only observed for HS1 and are not seen on HS2, and suggests that these peaks may be sensitive to the sample twist angle. In twisted homobilayers of MoS_2 moiré phonons have been observed and their twist angle dependence investigated [123]. In heterobilayers the alignment of the layers can produce a moiré interference pattern, which introduce an additional periodic potential across the sample [181]. The resulting moiré superlattice is dependent on the twist angle and is spatially larger than the monolayer TMDC lattice. The resulting moiré reciprocal lattice vector allows zone folding of large wavevector phonons onto the Brillouin zone centre. To ascertain if the LF peaks observed on HS1 are moiré phonons an analysis of the phonon dispersion

Table 6.30: The predicted frequencies for the acoustic phonons have been obtained using the wavevectors indicates in Figure 6.53. The predicted frequencies of the TA phonons are highlighted as these were used to determine the wavevectors shown in Figure 6.53. The experimental values for the low frequency spectra from Section 6.3.3 are also provided for reference.

Predicted Frequencies

	$MoSe_2$			WSe_2	
	k_1	k_2	k_3	k_1	k_2
LA	64.9	60.7	55.7	56.7	51.7
TA	41.5	39.7	35.8	37.2	33.7
ZA	20	18.8	15.8	17.9	14.6

Experimental Values

	1	2	3	4	5
WSe_2 A	34.6±0.1	38.8±1.1	52.9±0.1	57.8±0.5	-
$MoSe_2$ A	35.3±0.1	39.1±0.1	42.4±0.1	59.3±0.1	63.5±0.3
$MoSe_2$ B	35.4±0.3	38.9±0.4	42.1±0.2	59.0±0.2	63.8±0.9

relations reported by Kumar et al. [62] for monolayer $MoSe_2$ and WSe_2 was carried out. The phonon dispersion used in this analysis was calculated by Kumar et al. [62] and is shown in Figure 6.53.

Investigation of the phonon dispersion in Figure 6.53 reveals that the LF peaks must occur due to the zone folding of the acoustic phonon branches. However, are only three acoustic phonon branches predicted for monolayer TMDCs and so a single wavevector cannot explain the number of LF peaks observed on HS1. Instead we propose that the observed LF peaks are the result of zone folding via both the moiré and crystallographic superlattice wavevectors. For this analysis we have assumed that the moiré reciprocal lattice vector is aligned with the Γ to K wavevector in the monolayer Brillouin zone, which is a valid assumption for small twist angles [123]. The LF peaks observed on HS1 form two bands of peaks between 30 to 45 cm^{-1} and 50 to 65 cm^{-1}. From the phonon dispersion relation we assert that the higher frequency band is due to zone folded LA phonons, while the lower frequency band is due to zone folded TA phonons. The frequency of the two peaks at 35.4 and 39.1 cm^{-1} when resonant with $MoSe_2$ excitons were selected, and the wavevectors required to reproduce these frequencies were determined using the phonon dispersion relation. The wavevector for the 39.1 cm^{-1} peak is then interpreted as our moiré wavevector(k_m), and the difference between the two wavevectors is defined as our crystallographic wavevector (k_c). In Figure 6.53 the three wavevectors corresponding to k_m, k_m-k_c and k_m+k_c have been projected onto the phonon dispersion relations for both $MoSe_2$ and WSe_2. For each wavevector the predicted frequencies of the TA and LA phonons are compared to the experimental frequencies of the LF Raman peaks in Table 6.30.

Comparing first the experimental and predicted frequencies for the TA phonon in $MoSe_2$

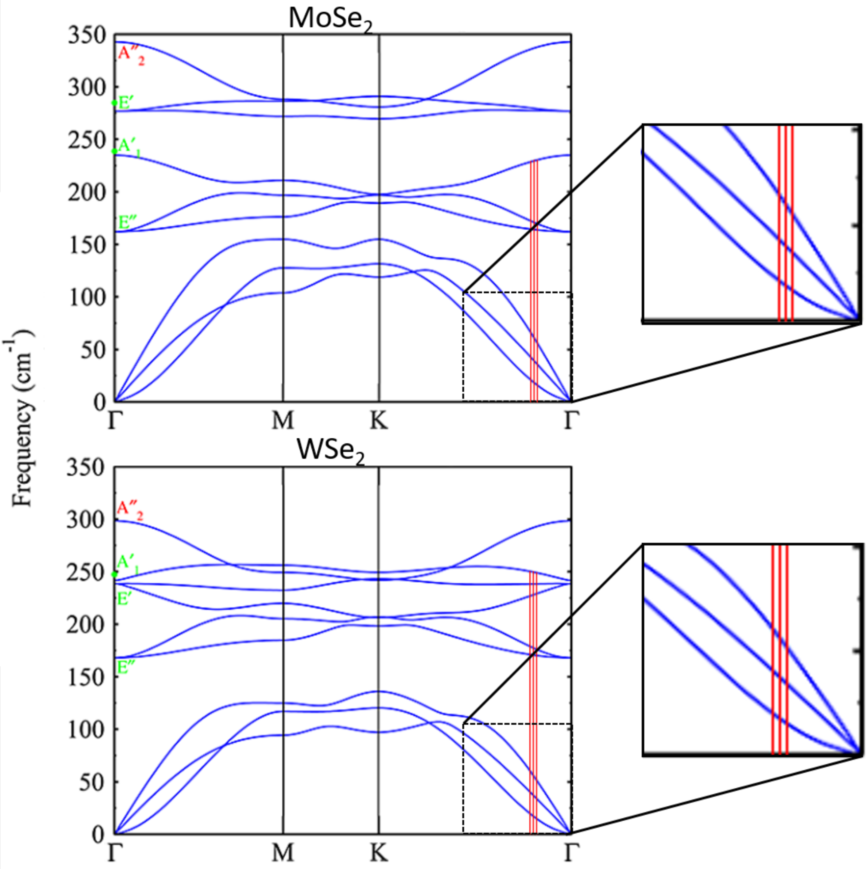

Figure 6.53: The phonon dispersion relations reported by Kumar et al. are presented here for both monolayer $MoSe_2$ and WSe_2. To explore the origin of the low frequency Raman peaks lines have been drawn at several wavevectors assuming that each of the peaks arising in the range of 30 to 50 cm^{-1} are associated with different wavevectors along the TA phonon branch between the Γ and K points of the Brillouin zone. This Figure has been adapted with permission from [62]. Copyright 2019 American Chemical Society.

the experimental and predicted frequencies of the TA(k_m+k_c) phonon are in remarkable agreement. Likewise in WSe_2 the predicted frequencies of the TA(k_M-k_c) and TA(k_m) phonons are in agreement to within the errors given. The higher frequency peaks predicted by the LA phonons and experimental frequencies of the LF Raman peaks are in close agreement. However, for the $MoSe_2$ and WSe_2 spectra we observe either the k_m-k_c or k_m+k_c peak but not both in our experiments. Although, it is possible that these peaks are present in our spectra but are too weak to be clearly resolved. In addition ,the predicted frequencies for the ZA phonons were also obtained but are not shown as they are all below 20 cm^{-1}. The lack of a third band of peaks associated with the ZA phonons in our experimental results is not surprising as the frequencies of these peaks would be at the limit of our experimental system. Furthermore, these predictions give no indication as to the relative strength of the ZA, TA or LA phonons and so it is possible that the ZA peaks could have a significantly lower Raman cross-section.

Further evidence supporting our proposed zone folding is the predicted frequency for the A_1' zone folded phonon. When resonant with $MoSe_2$ excitons in HS1 an additional Raman peak is observed at 235.8 cm^{-1}, and is 5 cm^{-1} below the A_1' peak at 240.8 cm^{-1}. From our analysis the predicted frequency of the A_1' (k_m) phonon has been extracted, and the frequency difference between the $A_1'(\Gamma\ )$ and $A_1'(k_m)$ phonons is determined to be 5.1 cm^{-1}. This is in excellent agreement with the separation of the peaks at 235.8 and 240.8 cm^{-1} and supports that this peak is the result of zone folding of the A_1' phonon in HS1. In this case we only observe a single peak with no obvious indication of crystallographic side bands. However, as seen in Figure 6.53 the phonon dispersion for the acoustic phonons at k_m is approximately linear, whereas the dispersion of the A_1' branch is non-linear and does not vary significantly near k_m. As a result the difference between the predicted frequencies for k_m and $k_m \pm k_c$ along the A_1' branch is less than 0.75 cm^{-1} and so it may not be possible to clearly separate these peaks in the Raman spectra.

Thus far the zone folding model presented here is able to reproduce the frequencies of the LF peaks using only two wavevectors. We propose that these two wavevectors results from the crystallographic and moiré superlattices. The zone folding of the phonons results in a low frequency spectrum consisting of moiré folded phonons and side bands resulting from the crystallographic wavevector. The presence of both crystallographic and moiré superlattices is expected in homobilayer structures due to the commensurate nature of the lattice vectors [123]. For our heterostructures the lattice constants of the $MoSe_2$ and WSe_2 differ by around 0.2% [286], and so can likely be considered commensurate allowing for crystallographic superlattices. The sizes of the two superlattices are dependent on the twist angle and are not always identical. As a result, the crystallographic and moiré superlattices can have wavevectors with different magnitudes as proposed in our model.

The relationship between the moiré reciprocal lattice vector and the sample twist angle is given by $\mid K^m \mid = 2b sin(\frac{\theta}{2})$ where θ is the twist angle, and b is the magnitude of the reciprocal lattice vector for the monolayer TMDC lattice and K_M is the moiré and $K_{\Gamma-K}$ is wavevector for the monolayer BZ along the direction Γ to K [123, 181]. In this case the sample twist angle can be constrained between 0 to 30°, due to the symmetry of the TMDC lattice. From our analysis using the phonon dispersion relation the ratio of $k_m/K_{\Gamma-K}$ has been determined for each wavevector and is provided in Table 6.31. This ratio can be predicted by $\frac{|K^m|}{|K_{\Gamma-K}|} = 4sin(\frac{\theta}{2})$. The predicted value of $\frac{|K_m|}{|K_{\Gamma-K}|}$ for HS1 is with a twist angle of 57 ° is found to be 0.105 ± 0.04 where the error was determined using the uncertainty of 1° inherent in the measurement of the twist angle. The values of $K_m/K_{\Gamma-K}$ obtained from the phonon dispersion analysis are shown in Table 6.31.

Table 6.31: Values determined for K_m, K_m-K_c, K_m+K_c and K_c were the given values are the ratio $K_m/K_{\Gamma-K}$.

K_m	K_m-K_c	K_m+K_c	K_c
0.192	0.175	0.204	0.017

Comparing the results in Table 6.31 to the predicted moiré wavevector we find a factor of two difference in the magnitudes of the wavevectors. This unexpected result suggests that the LF Raman peaks are either due to zone folded phonons at twice k_m or that the observed LF peaks are two phonon moiré modes. The only other report of moiré phonons in TMDCs materials to date is in twisted homobilayers of MoS_2 [123],which observed Raman peaks consistent with first order moiré phonons. In addition the lack of moiré phonons in HS2 is unexpected as in MoS_2 homobilayers the moiré phonons were observed for samples with twist angles from 10 to 50 °. Therefore, further investigations of other $MoSe_2/WSe_2$ heterobilayers are necessary to reproduce these results. This would require measurements with both twist angles near 57° and at a larger angles. This would allow us to establish if the observed peaks are due to twice the moiré wavevector or if these peaks are two phonon moiré peaks.

Our measurements have also provided information on the resonance behaviour of the LF modes, which are resonant with both the $MoSe_2$ and WSe_2 intra-layer excitons. At the $MoSe_2$ and WSe_2 A excitons a comparison of the LF peak resonance behaviour to the BS TMDC Raman peaks reveals that the LF peaks are only resonantly enhanced when resonant with the A trions (See Table 6.29). When resonant with the $MoSe_2$ B exciton there is no clear difference in resonance behaviour of the LF or bulk TMDC Raman peaks. However, the nature of the excitonic states at the B excitons is not well defined with only a few reports of B trions in literature on TMDCs [254, 88, 253] and with only one report of clearly separated neutral and charged B excitons [255]. Regardless the preferential coupling of the LF modes to trions is intriguing. The resonance behaviour of moiré phonons with the intralayer excitons has not been previously addressed and so it is not known if this coupling is peculiar to the $MoSe_2/WSe_2$ heterostructure. A possible reason for this may be the charge distribution in the monolayers when resonant with the trion enhancing the Van der Waals interaction between the constituent layers and so increasing the interlayer coupling. However, a more thorough analysis of the possible mechanisms theoretically would be necessary to further understand the nature of the preferential coupling to trions.

Overall the resonance Raman behaviour of the LF modes suggest that these peaks are the result of moiré phonons arising from zone folding. The different Raman peak frequencies when exciting at the $MoSe_2$ or WSe_2 intralayer excitons can be understood due to the difference in mass of the Mo and W atoms. The resonance Raman profiles for these peaks demonstrate that they are resonant with the intralayer excitons in $MoSe_2$ and WSe_2 with the resulting energies in agreement with those obtained from analysis of the bulk TMDC peaks. However, when resonant with the $MoSe_2$ A and WSe_2 A excitons the LF Raman peaks appear to be only strongly resonant with trions. The physical reason for this preferential coupling of the LF modes to the trion states is intriguing, but further experiments on different twist angle samples are required to elucidate the underlying physics. An obvious continuation of this work would be to investigate the nature of other heterostructures with a range of twist angles to confirm the origin of the LF Raman peak as moiré phonons.

6.6 Conclusions

This chapter has presented a thorough analysis of the resonance Raman behaviour of two heterobilayers with different twist angles. The Raman spectra of both heterostructures and monolayers have been compared and new peaks identified that are exclusive to the heterostructures. The most intriguing of these are the low frequency modes observed on HS1 between 30 to 65 cm^{-1} and the observation of additional higher frequency peaks exclusive to HS1 when resonant with the WSe_2 B exciton. At the WSe_2 B exciton the HS1 reveals new peak at 290.7, 309.1 and 353.8 cm^{-1} along with a peak at 240.4 cm^{-1} which is surprisingly intense. The resonance behaviour of the Raman peaks reveals that the typical WSe_2 TMDC peaks (at 248.7, 255.2, 260.4 cm^{-1}) have resonance profiles which are explained by two excitonic states at 2.110 and 2.164 eV. The resonance profile of the peak at 240.4 cm^{-1} also appears to be resonant at a different energy but from analysis is also found to be explained using the two identified excitonic states, but with much stronger interstate scattering terms. However, assignment of the peaks at 309.1 and 353.8 cm^{-1} reveals that these peaks are due to the $A''_2(\Gamma)$ phonons for WSe_2 and $MoSe_2$ respectively. The peak at 240.4 and 290.7 cm^{-1} can also be explained by the $A'_1(\Gamma)$ and $E'(\Gamma)$ phonons associated with the $MoSe_2$ layer respectively. The appearance of $MoSe_2$ phonons at the WSe_2 B exciton and anomalous resonance of the 240.4 cm^{-1} peak indicate a hybridisation of WSe_2 and $MoSe_2$ excitonic states. The $A''_2(\Gamma)$ point phonon are not Raman active in monolayer TMDCs due to the crystal symmetry and suggests that the excitonic state involved is the result of the hybridisation of the WSe_2 B intralayer exciton with a interlayer exciton.

For the low frequency modes observed on HS1 between 30 and 65 cm^{-1} analysis of the phonon dispersion indicates these peaks are the result of zone folded acoustic phonons. To account for the number of low frequency peaks seen requires zone folding with multiple wavevectors. This is attributed to zone folding with the moiré superlattice wavevector with additional side band resulting from the crystallographic superlattice vector. This model can also account for the additional Raman peak on HS1 when resonant with the $MoSe_2$ excitons at 235.8 cm^{-1} as a zone folded A'_1 phonon. The magnitude obtained for our moiré wavevector is found to be a factor of two larger than expected from theory and contrasts with results on MoS_2 homobilayers [123]. This suggests that either the zone folded phonons are the result of two phonon moiré Raman peaks or associated with zone folding at twice the moiré wavevector. However, to further clarify this will require additional measurements on other heterobilayer samples with larger twist angles. The resonance behaviour of the low frequency Raman peaks was also analysed and at the A excitons reveals that they are only strongly resonant with the A trions. Whereas, the typical bulk TMDC Raman peaks are all observed to have resonance profiles which require the involvement of both excitons and trions. The coupling of these zone folded moiré peaks to trions may indicate a different underlying mechanism for the exciton-phonon interactions and can be further investigated through use of gated samples.

Overall these results demonstrate the ability of resonance Raman spectroscopy to probe the properties of heterobilayer TMDC samples and provides a powerful probe for investigating moiré effects. If the proposed interpretation of our experimental results can be confirmed this will demonstrate the ability of Raman to provide valuable information on the electronic and vibrational properties of TMDC heterostructures. The development of resonance Raman as a material sensitive probe for exploring the fundamental physics of hybridisation and moiré effects, which could lead to new methods for evaluating the quality of sample interfaces in these structures.

Chapter 7

Conclusions

The aim of this thesis was to explore the different excitonic states in TMDC monolayers and heterobilayers using resonance Raman spectroscopy. The resonance Raman behaviour at the A and B excitons in WSe_2 and B exciton in $MoSe_2$ has been probed, and shown to involve scattering with multiple excitonic states. In TMDC heterobilayers the effect of twist angle on both phonons and excitons in these materials has been explored and attributed to the formation of a moiré superlattice resulting in zone folding of both optical and acoustic phonons. The investigation of the A and B excitons in heterobilayers has revealed the possible hybridisation of intra and inter-layer excitons in a $MoSe_2/WSe_2$ heterostructure.

Resonance Raman studies of both encapsulated monolayers of $MoSe_2$ and WSe_2 were presented in this thesis. For $MoSe_2$ and WSe_2 monolayers the resonance Raman spectra have revealed a plethora of both single phonon and multiphonon Raman peaks. Comparison of these peaks to previous assignments of their underlying phonons in literature reveals the potential erroneous assignment of several Raman peaks. A thorough combinatorial assignment of the Raman peaks was carried out using available phonon dispersion relations, and demonstrated multiple possible assignments for each of the high frequency multiphonon Raman peaks, which can involve up to third and fourth order phonon processes. This analysis highlights the difficulty and need for caution when considering the assignment of Raman peaks. In monolayer $MoSe_2$ the resonance Raman profiles demonstrate significant asymmetry, and is the result of scattering with multiple excitonic states at 1.828 and 1.862 eV, which are attributed to the B trion and neutral exciton respectively. The resonance Raman measurements also reveal several continuously dispersive Raman peaks, which indicate the presence of additional large wavevector dark states. In addition the Raman peaks at 481.5, 531.2 and 581.1 cm^{-1} demonstrated anomalous resonance Raman profiles, and are the result of a double resonance between the neutral B exciton and a lower energy state at 1.802 eV. A possible assignment for this state is to the $MoSe_2$ 2s excited state of the A exciton. The coupling of only these three Raman peaks to this excitonic state suggests that the phonons mediating this process requires particular symmetries, wavevectors or energies. Although, the precise scattering mechanism with this lower energy state is still unclear and requires further consideration.

Resonance Raman spectroscopy of an encapsulated WSe_2 monolayer has revealed three resonances between 1.7 and 2.25 eV, which are attributed to the 1s A and B excitons and to an excited 2s (A*) state of the A exciton at 1.866 eV. For the WSe_2 A exciton the resonance profiles were analysed and indicate this resonance involves a single excitonic state at 1.742 eV assigned to the neutral A exciton. For the WSe_2 A* state the resonance profiles for the Raman peaks near 250 cm^{-1} are all due to resonance with a single excitonic state at 1.866 eV. However, a new Raman peak at 494.6 cm^{-1} is also observed when resonant with the A* state and found to have an asymmetric resonance profile. Analysis of the resonance profile reveals this asymmetry can be explained by resonance with two excitonic states at 1.866 and 1.904 eV and indicates a double resonance process between the 2s and a higher energy state. This higher energy state has possible assignments to either a 3s/4s excited state or to a large wavevector dark state. When resonant with the WSe_2 B exciton the obtained resonance profiles demonstrate a significant asymmetry, due to the involvement of two excitonic states with energies between 2.133 to 2.144 eV and 2.159 to 2.171 eV and are attributed to the WSe_2 B trion and neutral exciton respectively. However, the Raman peaks at 230.5 and 234.5 cm^{-1} only couple to one of the excitonic states, which may suggests a difference in the exciton-phonon coupling for these peaks. Comparison of the Raman spectra at the WSe_2 A and B exciton also reveals that at the B exciton the spectra are dominated by multiphonon Raman peaks. This difference in the relative scattering strength of the multiphonon peaks is is likely due to the availability of large wavevector states at the Γ when resonant with the B exciton. Lastly, the observation of strong resonances with both the WSe_2 A and B excitons demonstrates that the atypical exciton-phonon coupling proposed by Del Corro et al. in WSe_2 is erroneous.

The resonance Raman profiles for both HS1 and HS2 have been analysed when resonant with both the $MoSe_2$ and WSe_2 intralayer excitons. Overall the energies obtained for resonance with the $MoSe_2$ and WSe_2 A and B neutral excitons are in agreement with the values obtained for the monolayers. However, at the WSe_2 A exciton in both HS1 and HS2 the resonance profiles are asymmetric and require a two state model involving both neutral excitons and trions. The appearance of trions in the heterostructures but not the monolayers suggests this maybe the result of charge transfer between the layers. In addition for the heterostructures there is no obvious resonance with the WSe_2 A* (2s) state. At the $MoSe_2$ B exciton in HS1 the Raman peaks at 481.5, 531.2 and 581.1 cm^{-1} have anomalous resonance profiles similar to the double resonance seen in monolayer $MoSe_2$. Analysis of these profiles reveals this is due to resonance with a state at 1.754 eV and the neutral B exciton. In comparison to monolayer $MoSe_2$ this significantly lower in energy than the state at 1.802 eV observed in monolayer $MoSe_2$, which was tentatively assigned to the 2s state of the $MoSe_2$ A exciton. The involvement of the same Raman peaks as observed for the monolayer suggest a similar scattering mechanism, and so could indicate the involvement of an excited 2s state of the $MoSe_2$ A trion.

For the WSe_2 B exciton the resonance Raman analysis of HS2 is in agreement with the results for monolayer WSe_2 involving two excitonic states at 2.137 and 2.163 eV attributed to the trion and neutral exciton. For HS1 the resonance profiles are more diverse with a Raman peak at 240.4 cm^{-1} appearing to show a different resonance behaviour to the typical WSe_2 Raman peaks. Despite this it is possible to explain the resonance behaviour of all Raman peaks on HS1 using two excitonic states at 2.110 and 2.164 eV. On the other hand, the Raman spectra obtained when resonant with the WSe_2 B exciton on HS1 also reveals several new peaks at 290.7, 309.1 and 353.8 cm^{-1}. A peak is observed at 240.4 cm^{-1} on HS1 and has a much higher intensity, becoming the dominant Raman peak in the spectra. The Raman peak at 309.1 cm^{-1} is assigned to the $A_2''(\Gamma)$ and has been reported in homobilayers and heterobilayers containing WSe_2 layers. The Raman peak at 353.8 cm^{-1} is also assigned to the $A_2''(\Gamma)$ $MoSe_2$ phonon. The participation of $MoSe_2$ phonons at this resonance leads to the assignment of the peaks at 240.4 and 290.7 cm^{-1} to the Raman active $MoSe_2$ $A_1'(\Gamma)$ and $E'(\Gamma)$ phonons. For monolayer TMDCs the $A_2''(\Gamma)$ Raman peak is inactive in monolayers due to the difference in crystal symmetry. The involvement of both $MoSe_2$ phonons at the WSe_2 B resonance and required change in symmetry to observe the $A_2''(\Gamma)$ phonons indicates the potential hybridisation of the WSe_2 B exciton with an interlayer excitonic state. However, to confirm and validate this theory will require further Raman measurements with gated heterobilayer samples.

The resonance Raman behaviour of two $MoSe_2/WSe_2$ heterobilayers HS1 and HS2 with twist angles of 57 ° and 6 ° has been investigated. Comparison of the Raman spectra obtained on both the heterostructures and monolayers has revealed the appearance of several new Raman peaks in the heterobilayers. For HS1 a set of low frequency Raman peaks were observed between 30 and 65 cm^{-1} when resonant with both $MoSe_2$ and WSe_2 intralayer excitons. On HS1 when resonant with the $MoSe_2$ intralayer excitons a peak at 235.8 cm^{-1} is also observed in the Raman spectra. Analysis of the resonance profiles for the low frequency peaks demonstrated resonance with the intralayer excitons, however these peaks were found to only couple strongly to trion states. Using phonon dispersion relations analysis of the low frequency Raman peaks reveals that these are zone folded acoustic phonons, whilst the peak at 235.8 cm^{-1} is a zone folded A_1' phonon. The zone folding occurs due to the resulting moiré and crystallographic superlattice in the heterobilayers. Surprisingly, the magnitude of the moiré wavevector obtained from our analysis is a factor of two larger than the theoretically predicted value. This suggests that these peaks are either single phonons associated with twice the moiré wavevector or two phonon moiré Raman peaks, but further investigation of other heterobilayers is required to clarify this mechanism.

In general the results of resonance Raman spectroscopy on TMDC encapsulated monolayers and heterobilayers have revealed significant information regarding exciton-phonon interactions in these materials. For encapsulated monolayers we have demonstrated scattering with excited Rydberg states and the potential coupling of B to A excitons via scattering with multiple phonons. The comparison of low temperature Raman spectra and reported results at room temperature has revealed the potential erroneous assignment of Raman peaks in literature and demonstrates the need for more thorough temperature dependent investigations. For heterostructures the Raman spectra have allowed the observation of moiré phonons, potential hybridisation of intra and interlayer excitons and revealed several differences in the energy of the excitonic states involved in the heterobilayers. From these results it is clear that further measurements of different twist angle heterobilayers and the use of gated samples will be required to confirm both the hybridisation of excitonic states and anomalous magnitude of the moiré wavevector. Nevertheless, these results demonstrate that resonance Raman spectroscopy at cryogenic temperatures can provide a wealth of information regarding the properties of 2D materials. The application of resonance Raman to investigate moiré effects and hybridisation of excitonic states has potential to contribute significantly to the understanding of Van der Waals structures and inform future applications.

7.1 Outlook and Perspectives

The aim of this thesis was to better understand the optical transitions in both TMDC monolayer and heterobilayers. Overall the results from our experiments clearly demonstrate the abundance of new physics which can be probed using resonance Raman spectroscopy. In the short term a natural extension of this work is to perform resonance Raman spectroscopy measurements on a gated TMDC heterobilayer as a function of gate voltage. These measurements would be able to confirm the proposed hybridisation of the WSe_2 B exciton with an interlayer exciton and, given recent publications [278, 277, 122, 129], is an area of significant interest at present in TMDC research. Likewise gated measurements would allow for the coupling of the low frequency Raman peaks to trion states to be probed allowing the underlying mechanism to be elucidated. These experiments would allow the unambiguous assignment of the neutral and charged excitonic states and enable more detailed investigations of interstate scattering processes. It would also be interesting to further investigate the moiré folded phonons by measuring additional samples with a variety of twist angles. So far there is only one other report of moiré phonons which were observed for twisted homobilayers [123]. Our observation of zone folded phonons at twice the expected moiré wavevector and additional peaks attributed to crystallographic sidebands may indicate new physics unique to heterobilayers.

A particular challenge demonstrated in this thesis is the assignment of the observed Raman peaks in our spectra to the underlying phonons. For multiphonon processes this is particularly challenging due to the number of different combinations of phonons which can produce peaks with almost degenerate frequencies. A possibility to aid in the assignment of these peaks would be a more complete theoretical analysis to evaluate the symmetries of two phonon and higher order processes allowing the selection rules for these peaks to be obtained and may reduce the number of possible assignments. Similarly DFT analysis of the dispersive Raman peaks observed in our experiments would also clarify their proposed assignments. Our results also suggest that temperature dependence Raman measurements could assist in understanding the Raman peak assignments and allow for combination modes involving both emission and absorption of phonons to be identified. Raman studies of the resonant spectra as a function of applied strain and use of polarisation resolved measurements may also allow for improved assignment of the Raman peaks. Studies of TMDC alloys, Janus monolayer or isotopically pure TMDCs [287, 288] could also further our understanding of the different TMDC Raman peaks and their assignments.

In the medium to long-term the most promising applications of TMDCs are in optoelectronic and valleytronic applications. As demonstrated in this thesis, resonance Raman can provide information on both the A and B excitonic states interstate scattering and large wavevector dark states which are not observed in other optical measurements.

In particular phonon mediated processes are involved in ultrafast charge transfer, formation of interlayer excitons and contribute to valley depolarisation. The coupling of phonons at the interfaces of 2D materials is also significant and in Graphene limits the mobility of electrical devices [289]. The understanding of the coupling of phonons at the interfaces of 2D materials to underlying electronic states could have significant impact on the practical applications. As a technique resonance Raman spectroscopy provides a powerful tool to further understand these processes.

Considering the field of 2D materials it is clear that there is still a wealth of physics to be understood. In particular the area of Van der Waals structures is still relatively new with the dramatic discovery of superconductivity in twisted bilayer Graphene [28] occurring within the last two years. The emerging role of moiré effects in these materials is likely to result in the discovery of other novel physical effects and provides an additional method for tuning of device properties. At present the limiting factor for the application of these materials in devices is the scalability of fabrication techniques. Mechanical exfoliation at present is ubiquitous with the samples utilised in research due to the high quality and broad array of available materials, whilst CVD, MBE or ALD grown TMDCs are not yet mature enough for these applications. Although, it seems likely that the challenges with scalable growth of TMDCs and other 2D materials will be overcome given time, as has been observed with Graphene through programs such as the European Graphene Flagship. The array of potential applications of TMDCs and Van der Waals heterostructures in optoelectronic and valleytronic devices presents an optimistic future for the field of 2D materials.

References

[1] J. Frenkel. On the Transformation of Light into Heat in Solids. *Zeits. f. Physik*, 8(1929):198, 1931.

[2] É.I. Rashba. The Prediction of Excitons. *Uspekhi Fizicheskih Nauk*, 144(10):347, 2011.

[3] Gregory H. Wannier. The Structure of Electronic Excitation Levels in Insulating Crystals. *Physical Review*, 52(x):191, 1937.

[4] Martin A. Green. Improved value for the silicon free exciton binding energy. *AIP Advances*, 3(11), 2013.

[5] S. Tarucha, H. Okamoto, Y. Iwasa, and N. Miura. Exciton binding energy in GaAs quantum wells deduced from magneto-optical absorption measurement. *Solid State Communications*, 52(9):815–819, dec 1984.

[6] K S Novoselov, A K Geim, S V Morozov, D Jiang, M I Katsnelson, I V Grigorieva, S V Dubonos, and A A Firsov. Two-dimensional gas of massless Dirac fermions in graphene. *Nature*, 438(7065):197–200, 2005.

[7] Yuanbo Zhang, Yan Wen Tan, Horst L. Stormer, and Philip Kim. Experimental observation of the quantum Hall effect and Berry's phase in graphene. *Nature*, 438(7065):201–204, 2005.

[8] Changgu Lee, Xiaoding Wei, Jeffrey W Kysar, and James Hone. Measurement of the Elastic Properties and Intrinsic Strength of Monolayer Graphene. *Science*, 321(July):385–388, 2008.

[9] Kin Fai Mak, Changgu Lee, James Hone, Jie Shan, and Tony F. Heinz. Atomically thin MoS_2: A new direct-gap semiconductor. *Physical Review Letters*, 105(13):2–5, 2010.

[10] Likai Li, Yijun Yu, Guo Jun Ye, Qingqin Ge, Xuedong Ou, Hua Wu, Donglai Feng, Xian Hui Chen, and Yuanbo Zhang. Black phosphorus field-effect transistors. *Nature Nanotechnology*, 9(5):372–377, 2014.

[11] Wei Qiang Han, Lijun Wu, Yimei Zhu, Kenji Watanabe, and Takashi Taniguchi. Structure of chemically derived mono- and few-atomic-layer boron nitride sheets. *Applied Physics Letters*, 93(22):1–4, 2008.

[12] Nicolas Mounet, Marco Gibertini, Philippe Schwaller, Davide Campi, Andrius Merkys, Antimo Marrazzo, Thibault Sohier, Ivano Eligio Castelli, Andrea Cepellotti, Giovanni Pizzi, and Nicola Marzari. Two-dimensional materials from high-throughput computational exfoliation of experimentally known compounds. *Nature Nanotechnology*, 13(3):246–252, 2018.

[13] Kailiang Zhang, Yulin Feng, Fang Wang, Zhengchun Yang, and John Wang. Two dimensional hexagonal boron nitride (2D-hBN): Synthesis, properties and applications, 2017.

[14] M. A. Méasson, Y. Gallais, M. Cazayous, B. Clair, P. Rodière, L. Cario, and A. Sacuto. Amplitude Higgs mode in the 2 H - NbSe$_2$ superconductor. *Physical Review B - Condensed Matter and Materials Physics*, 89(6):1–5, 2014.

[15] Mohammed Moaied, Jiyoul Lee, and Jisang Hong. A 2D ferromagnetic semiconductor in monolayer Cr-Trihalide and its Janus structures. *Physical Chemistry Chemical Physics*, 20(33):21755–21763, 2018.

[16] Chaojie Cui, Fei Xue, Wei-Jin Hu, and Lain-Jong Li. Two-dimensional materials with piezoelectric and ferroelectric functionalities. *npj 2D Materials and Applications*, 2(1):18, 2018.

[17] Shao Yu Chen, Thomas Goldstein, Dhandapani Venkataraman, Ashwin Ramasubramaniam, and Jun Yan. Activation of New Raman Modes by Inversion Symmetry Breaking in Type II Weyl Semimetal Candidate T-MoTe$_2$. *Nano Letters*, 16(9):5852–5860, 2016.

[18] Yonghao Yuan, Jie Pan, Xintong Wang, Yuqiang Fang, Canli Song, Lili Wang, Ke He, Xucun Ma, Haijun Zhang, Fuqiang Huang, Wei Li, and Qi-Kun Xue. Evidence of anisotropic Majorana bound states in 2M-WS$_2$. *Nature Physics*, 2019.

[19] Kin Fai Mak, Keliang He, Changgu Lee, Gwan Hyoung Lee, James Hone, Tony F Heinz, and Jie Shan. Tightly bound trions in monolayer MoS$_2$. *Nature materials*, 12(3):207–211, 2013.

[20] Matthew Z Bellus, Frank Ceballos, Hsin-ying Chiu, and Hui Zhao. Tightly Bound Trions in Transition Metal Dichalcogenide Heterostructures. *ACS Nano*, 9(6):6459–6464, 2015.

[21] Deep Jariwala, Artur R. Davoyan, Joeson Wong, and Harry A. Atwater. Van der Waals Materials for Atomically-Thin Photovoltaics: Promise and Outlook. *ACS Photonics*, 4(12):2962–2970, 2017.

[22] F K Perkins, a L Friedman, E Cobas, P M Campbell, G G Jernigan, and B T Jonker. Chemical vapor sensing with monolayer MoS_2. *Nano Letters*, 13(2):668–673, 2013.

[23] John R. Schaibley, Hongyi Yu, Genevieve Clark, Pasqual Rivera, Jason S. Ross, Kyle L. Seyler, Wang Yao, and Xiaodong Xu. Valleytronics in 2D materials. *Nature Reviews Materials*, 1(11), 2016.

[24] Huayang Guo, Changyong Lan, Zhifei Zhou, Peihua Sun, Dapeng Wei, and Chun Li. Transparent, flexible, and stretchable WS_2 based humidity sensors for electronic skin. *Nanoscale*, 9(19):6246–6253, 2017.

[25] Jae Hwan Jeong, Jong Hun Kim, Rakesh Joshi, Namwon Kim, and Gwan-Hyoung Lee. Mechanical properties of two-dimensional materials and their applications. *Journal of Physics D: Applied Physics*, 52(8):083001, 2018.

[26] Pasqual Rivera, John R Schaibley, Aaron M Jones, Jason S Ross, Sanfeng Wu, Grant Aivazian, Philip Klement, Kyle Seyler, Genevieve Clark, Nirmal J Ghimire, Jiaqiang Yan, D G Mandrus, Wang Yao, and Xiaodong Xu. Observation of long-lived interlayer excitons in monolayer $MoSe_2$-WSe_2 heterostructures. *Nature communications*, 6:6242, 2015.

[27] Alexander A. Puretzky, Liangbo Liang, Xufan Li, Kai Xiao, Bobby G. Sumpter, Vincent Meunier, and David B. Geohegan. Twisted $MoSe_2$ Bilayers with Variable Local Stacking and Interlayer Coupling Revealed by Low-Frequency Raman Spectroscopy. *ACS Nano*, 10(2):2736–2744, 2016.

[28] Yuan Cao, Valla Fatemi, Shiang Fang, Kenji Watanabe, Takashi Taniguchi, Efthimios Kaxiras, and Pablo Jarillo-Herrero. Unconventional superconductivity in magic-angle graphene superlattices. *Nature*, 556(7699):43–50, 2018.

[29] Hoi Chun Po, Liujun Zou, Ashvin Vishwanath, and T. Senthil. Origin of Mott Insulating Behavior and Superconductivity in Twisted Bilayer Graphene. *Physical Review X*, 8(3):31089, 2018.

[30] Norbert Nemec and Gianaurelio Cuniberti. Hofstadter butterflies of bilayer graphene. *Physical Review B - Condensed Matter and Materials Physics*, 75(20):1–4, 2007.

[31] David C Smith, Joseph H Spencer, Jeremy Sloan, Liam P Mcdonnell, Harrison Trewhitt, Reza J Kashtiban, and Eric Faulques. Resonance Raman Spectroscopy of Extreme Nanowires and Other 1D Systems 1 . Sample Preparation : Melt Filling of SWNTs with Mercury Telluride (HgTe) and Other. *J.Vis.Exp*, (110):1–14, 2016.

[32] W. O. Winer. Molybdenum disulfide as a lubricant: A review of the fundamental knowledge. *Wear*, 1967.

[33] Ilkka Kylänpää and Hannu Pekka Komsa. Binding energies of exciton complexes in transition metal dichalcogenide monolayers and effect of dielectric environment. *Physical Review B - Condensed Matter and Materials Physics*, 92(20):1–6, 2015.

[34] Jiong Yang, Tieyu Lü, Ye Win Myint, Jiajie Pei, Daniel Macdonald, Jin Cheng Zheng, and Yuerui Lu. Robust Excitons and Trions in Monolayer $MoTe_2$. *ACS Nano*, 9(6):6603–6609, 2015.

[35] Elena Del Corro, Humberto Terrones, Ana Elias, Cristiano Fantini, Simin Feng, Minh An Nguyen, Thomas E. Mallouk, Mauricio Terrones, and Marcos A. Pimenta. Excited Excitonic States in 1L, 2L, 3L, and Bulk WSe_2 Observed by Resonant Raman Spectroscopy. *ACS Nano*, 8(9):9629–9635, 2014.

[36] Bruno R. Carvalho, Leandro M. Malard, Juliana M. Alves, Cristiano Fantini, and Marcos A. Pimenta. Symmetry-dependent exciton-phonon coupling in 2D and bulk MoS_2 observed by resonance Raman scattering. *Physical Review Letters*, 114(13):1–5, 2015.

[37] Liam P McDonnell, Chung-Che Huang, Qingsong Cui, Daniel W. Hewak, and David C Smith. Probing Excitons, Trions and Dark Excitons in Monolayer WS_2 using Resonance Raman Spectroscopy. *Nano Letters*, 18(2):acs.nanolett.7b05184, feb 2018.

[38] M. Cardona and W.J. Firth. *Light scattering in solids*, volume 8. 1976.

[39] K S Novoselov, D Jiang, F Schedin, T J Booth, V V Khotkevich, S V Morozov, and a K Geim. Two-dimensional atomic crystals. *Proceedings of the National Academy of Sciences of the United States of America*, 102(30):10451–10453, 2005.

[40] a. Molina-Sánchez and L. Wirtz. Phonons in single-layer and few-layer MoS_2 and WS_2. *Physical Review B - Condensed Matter and Materials Physics*, 84(15):1–8, 2011.

[41] B. Radisavljevic, A. Radenovic, J. Brivio, V. Giacometti, and A. Kis. Single-layer MoS_2 transistors. *Nature nanotechnology*, 6(3):147–50, 2011.

[42] Andrey N. Enyashin, Lena Yadgarov, Lothar Houben, Igor Popov, Marc Weidenbach, Reshef Tenne, Maya Bar-Sadan, and Gotthard Seifert. New route for stabilization of 1T-WS_2 and MoS_2 phases. *Journal of Physical Chemistry C*, 115(50):24586–24591, 2011.

[43] Muharrem Acerce, Damien Voiry, and Manish Chhowalla. Metallic 1T phase MoS_2 nanosheets as supercapacitor electrode materials. *Nature Nanotechnology*, 10(4):313–318, 2015.

[44] Liangbo Liang, Jun Zhang, Bobby G. Sumpter, Qing Hai Tan, Ping Heng Tan, and Vincent Meunier. Low-Frequency Shear and Layer-Breathing Modes in Raman Scattering of Two-Dimensional Materials. *ACS Nano*, 11(12):11777–11802, 2017.

[45] Manish Chhowalla, Hyeon Suk Shin, Goki Eda, Lain-Jong Li, Kian Ping Loh, and Hua Zhang. The chemistry of two-dimensional layered transition metal dichalcogenide nanosheets. *Nature chemistry*, 5(4):263–75, 2013.

[46] Xiaohui Hu, Liangzhi Kou, and Litao Sun. Stacking orders induced direct band gap in bilayer $MoSe_2$ -WSe_2 lateral heterostructures. *Scientific Reports*, 6(July):1–9, 2016.

[47] Tao Jiang, Hengrui Liu, Di Huang, Shuai Zhang, Yingguo Li, Xingao Gong, Yuen Ron Shen, Wei Tao Liu, and Shiwei Wu. Valley and band structure engineering of folded MoS_2 bilayers. *Nature Nanotechnology*, 9(10):825–829, 2014.

[48] Xiao-Long Zhang and Wu-Ming Liu. Electron-Phonon Coupling and its implication for the superconducting topological insulators. *Scientific Reports*, 5:8964—-, mar 2015.

[49] Lorenz Maximilian Schneider, Jan Kuhnert, Simon Schmitt, Wolfram Heimbrodt, Ulrich Huttner, Lars Meckbach, Tineke Stroucken, Stephan W. Koch, Shichen Fu, Xiaotian Wang, Kyungnam Kang, Eui-Hyeok Yang, and Arash Rahimi-Iman. Spin-Layer- and Spin-Valley-Locking in CVD-Grown AA'- and AB-Stacked Tungsten-Disulfide Bilayers. pages 1–16, 2019.

[50] V. G. Tissen, M. R. Osorio, J. P. Brison, N. M. Nemes, M. García-Hernández, L. Cario, P. Rodière, S. Vieira, and H. Suderow. Pressure dependence of superconducting critical temperature and upper critical field of 2H-NbS_2. *Physical Review B - Condensed Matter and Materials Physics*, 87(13):1–6, 2013.

[51] Y. H. Huang, R. S. Chen, J. R. Zhang, and Y. S. Huang. Electronic transport in $NbSe_2$ two-dimensional nanostructures: Semiconducting characteristics and photoconductivity. *Nanoscale*, 7(45):18964–18970, 2015.

[52] Weijie Zhao, Zohreh Ghorannevis, and AK K Kumar. Lattice dynamics in mono- and few-layer sheets of WS_2 and WSe_2. *Nanoscale*, 5(20):9677–9683, 2013.

[53] Kai Xu, Zhenxing Wang, Feng Wang, Yun Huang, Fengmei Wang, Lei Yin, Chao Jiang, and Jun He. Ultrasensitive Phototransistors Based on Few-Layered HfS_2. *Advanced Materials*, 27(47):7881–7887, 2015.

[54] Bhakti Jariwala, Damien Voiry, Apoorv Jindal, Bhagyashree A. Chalke, Rudheer Bapat, Arumugam Thamizhavel, Manish Chhowalla, Mandar Deshmukh, and Arnab Bhattacharya. Synthesis and Characterization of ReS_2 and $ReSe_2$ Layered Chalcogenide Single Crystals. *Chemistry of Materials*, 28(10):3352–3359, 2016.

[55] Blanka Magyari-Köpe, Zhi-Xun Shen, Chaofan Zhang, Michal J. Mleczko, Yoshio Nishi, Hsueh-Hui Kuo, Hye Ryoung Lee, Ian R. Fisher, Robert G. Moore, and Eric Pop. $HfSe_2$ and $ZrSe_2$: Two-dimensional semiconductors with native high-κ oxides. *Science Advances*, 3(8):e1700481, 2017.

[56] Filip A. Rasmussen and Kristian S. Thygesen. Computational 2D Materials Database: Electronic Structure of Transition-Metal Dichalcogenides and Oxides. *Journal of Physical Chemistry C*, 119(23):13169–13183, 2015.

[57] Weijie Zhao, Zohreh Ghorannevis, Leiqiang Chu, Minglin Toh, Christian Kloc, Ping-Heng Tan, and Goki Eda. Evolution of electronic structure in atomically thin sheets of WS_2 and WSe_2. *ACS nano*, 7(1):791–7, 2013.

[58] Yi Zhang, Tay-Rong Chang, Bo Zhou, Yong-Tao Cui, Hao Yan, Zhongkai Liu, Felix Schmitt, James Lee, Rob Moore, Yulin Chen, Hsin Lin, Horng-Tay Jeng, Sung-Kwan Mo, Zahid Hussain, Arun Bansil, and Zhi-Xun Shen. Direct observation of the transition from indirect to direct bandgap in atomically thin epitaxial $MoSe_2$. *Nature nanotechnology*, 9(2):111–5, 2014.

[59] Tawinan Cheiwchanchamnangij and Walter R L Lambrecht. Quasiparticle band structure calculation of monolayer, bilayer, and bulk MoS_2. *Physical Review B - Condensed Matter and Materials Physics*, 85(20):1–4, 2012.

[60] Eugene S. Kadantsev and Pawel Hawrylak. Electronic structure of a single MoS_2 monolayer. *Solid State Communications*, 152(10):909–913, 2012.

[61] A Kumar and P K Ahluwalia. Electronic structure of transition metal dichalcogenides monolayers 1H-MX2 (M = Mo, W; X = S, Se, Te) from ab-initio theory: new direct band gap semiconductors. *The European Physical Journal B*, 85(6):18–22, 2012.

[62] S. Kumar and U. Schwingenschlögl. Thermoelectric response of bulk and monolayer $MoSe_2$ and WSe_2. *Chemistry of Materials*, 27(4):1278–1284, 2015.

[63] Wencan Jin, Po Chun Yeh, Nader Zaki, Datong Zhang, Jerzy T. Sadowski, Abdullah Al-Mahboob, Arend M. Van Der Zande, Daniel A. Chenet, Jerry I. Dadap, Irving P. Herman, Peter Sutter, James Hone, and Richard M. Osgood. Direct measurement of the thickness-dependent electronic band structure of MoS_2 using angle-resolved photoemission spectroscopy. *Physical Review Letters*, 111(10):1–5, 2013.

[64] K. Sugawara, T. Sato, Y. Tanaka, S. Souma, and T. Takahashi. Spin- and valley-coupled electronic states in monolayer WSe_2 on bilayer graphene. *Applied Physics Letters*, 107(7):1–5, 2015.

[65] Ashwin Ramasubramaniam, Doron Naveh, and Elias Towe. Tunable band gaps in bilayer transition-metal dichalcogenides. *Physical Review B - Condensed Matter and Materials Physics*, 84(20):1–10, 2011.

[66] Z. Y. Zhu, Y. C. Cheng, and U. Schwingenschlogl. Giant spin-orbit-induced spin splitting in two-dimensional transition-metal dichalcogenide semiconductors. *Physical Review B - Condensed Matter and Materials Physics*, 84(15):1–5, 2011.

[67] Gui Bin Liu, Wen Yu Shan, Yugui Yao, Wang Yao, and Di Xiao. Three-band tight-binding model for monolayers of group-VIB transition metal dichalcogenides. *Physical Review B - Condensed Matter and Materials Physics*, 88(8):1–10, 2013.

[68] Wang Yao, Di Xiao, and Qian Niu. Valley-dependent optoelectronics from inversion symmetry breaking. *Physical Review B - Condensed Matter and Materials Physics*, 77(23):1–7, 2008.

[69] Di Xiao, Gui Bin Liu, Wanxiang Feng, Xiaodong Xu, and Wang Yao. Coupled spin and valley physics in monolayers of MoS_2 and other group-VI dichalcogenides. *Physical Review Letters*, 108(19):1–5, 2012.

[70] Ting Cao, Gang Wang, Wenpeng Han, Huiqi Ye, Chuanrui Zhu, Junren Shi, Qian Niu, Pingheng Tan, Enge Wang, Baoli Liu, and Ji Feng. Valley-selective circular dichroism of monolayer molybdenum disulphide. *Nature communications*, 3(May):887, 2012.

[71] Xiaodong Xu. Spin and pseudospins in transition metal dichalcogenides. *Proceedings - 2014 Summer Topicals Meeting Series, SUM 2014*, 10(April):1–2, 2014.

[72] K F Mak, K L McGill, J Park, and P L McEuen. The valley Hall effect in MoS_2 transistors. *Science (New York, N.Y.)*, 344(6191):1489–92, 2014.

[73] Ashish Arora, Robert Schmidt, Robert Schneider, MacIej R. Molas, Ivan Breslavetz, Marek Potemski, and Rudolf Bratschitsch. Valley Zeeman splitting and valley polarization of neutral and charged excitons in monolayer $MoTe_2$ at high magnetic fields. *Nano Letters*, 16(6):3624–3629, 2016.

[74] Peter Y. Yu and Manuel Cardona. *Fundamentals of Semiconductors*. Graduate Texts in Physics. Springer Berlin Heidelberg, Berlin, Heidelberg, 2010.

[75] K. Kosmider and J. Fernandez-Rossier. Electronic properties of the MoS_2-WS_2 heterojunction. *Physical Review B - Condensed Matter and Materials Physics*, 87(7):2–5, 2013.

[76] Timothy C. Berkelbach, Mark S. Hybertsen, and David R. Reichman. Theory of neutral and charged excitons in monolayer transition metal dichalcogenides. *Physical Review B - Condensed Matter and Materials Physics*, 88(4):1–6, 2013.

[77] Z. H. Lin, T. Y. Wang, G. B. Stringfellow, and P. C. Taylor. Exciton binding energies in GaInAs/InP quantum wells determined by thermally modulated photoluminescence. *Applied Physics Letters*, 52(19):1590–1592, 1988.

[78] Hannu Pekka Komsa and Arkady V. Krasheninnikov. Effects of confinement and environment on the electronic structure and exciton binding energy of MoS_2 from first principles. *Physical Review B - Condensed Matter and Materials Physics*, 86(24):1–6, 2012.

[79] Diana Y. Qiu, Felipe H. Da Jornada, and Steven G. Louie. Optical spectrum of MoS_2: Many-body effects and diversity of exciton states. *Physical Review Letters*, 111(21):1–5, 2013.

[80] Alexey Chernikov, Timothy C. Berkelbach, Heather M. Hill, Albert Rigosi, Yilei Li, Ozgur Burak Aslan, David R. Reichman, Mark S. Hybertsen, and Tony F. Heinz. Exciton binding energy and nonhydrogenic Rydberg series in monolayer WS_2. *Physical Review Letters*, 113(7):1–5, 2014.

[81] A. T. Hanbicki, M. Currie, G. Kioseoglou, A. L. Friedman, and B. T. Jonker. Measurement of high exciton binding energy in the monolayer transition-metal dichalcogenides WS_2 and WSe_2. *Solid State Communications*, 203:16–20, 2015.

[82] Heather M. Hill, Albert F. Rigosi, Cyrielle Roquelet, Alexey Chernikov, Timothy C. Berkelbach, David R. Reichman, Mark S. Hybertsen, Louis E. Brus, and Tony F. Heinz. Observation of excitonic Rydberg states in monolayer MoS_2 and WS_2 by photoluminescence excitation spectroscopy. *Nano Letters*, 15(5):2992–2997, 2015.

[83] T. Sekine, T. Nakashizu, K. Toyoda, K. Uchinokura, and E. Matsuura. Raman scattering in layered compound 2H-WS_2. *Solid State Communications*, 35(4):371–373, 1980.

[84] C. Sourisseau, F. Cruege, M. Fouassier, and M. Alba. Second-order Raman effects, inelastic neutron scattering and lattice dynamics in 2H-WS_2. *Chemical Physics*, 150(2):281–293, 1991.

[85] A. Carvalho, R. M. Ribeiro, and A. H. Castro Neto. Band nesting and the optical response of two-dimensional semiconducting transition metal dichalcogenides. *Physical Review B - Condensed Matter and Materials Physics*, 88(11):1–6, 2013.

[86] Liang, W Y A R Beal, and J C Knights. Transmission spectra of some transition metal dichalcogenides. II. Group VIA: trigonal prismatic coordination. *Journal of Physics C: Solid State Physics*, 5, 1971.

[87] Gerd Plechinger, Philipp Nagler, Julia Kraus, Nicola Paradiso, Christoph Strunk, Christian Schuller, and Tobias Korn. Identification of excitons, trions and biexcitons in single-layer WS_2. *Physica Status Solidi - Rapid Research Letters*, 9(8):457–461, 2015.

[88] Matthias Drüppel, Thorsten Deilmann, Peter Krüger, and Michael Rohlfing. Diversity of trion states and substrate effects in the optical properties of an MoS_2 monolayer. *Nature Communications*, 8(1):1–7, 2017.

[89] R. T. Cox, V. Huard, K. Kheng, S. Lovisa, R. B. Miller, K. Saminadayar, A. Arnoult, J. Cibert, S. Tatarenko, and M. Potemski. Exciton trions in II-VI heterostructures. *Acta Physica Polonica . . .*, 94(2):99–109, 1998.

[90] Yumeng You, Xiao-xiao Zhang, Timothy C Berkelbach, Mark S Hybertsen, David R Reichman, and Tony F Heinz. Observation of biexcitons in monolayer WSe_2. 11(May):477–482, 2015.

[91] Hyun Seok Lee, Min Su Kim, Hyun Kim, and Young Hee Lee. Identifying multiexcitons in MoS_2 monolayers at room temperature. *Physical Review B*, 93(14):1–6, 2016.

[92] Matteo Barbone, Alejandro R.P. Montblanch, Dhiren M. Kara, Carmen Palacios-Berraquero, Alisson R. Cadore, Domenico De Fazio, Benjamin Pingault, Elaheh Mostaani, Han Li, Bin Chen, Kenji Watanabe, Takashi Taniguchi, Sefaattin Tongay, Gang Wang, Andrea C. Ferrari, and Mete Atatüre. Charge-tuneable biexciton complexes in monolayer WSe_2. *Nature Communications*, 9(1), 2018.

[93] Zhipeng Li, Tianmeng Wang, Zhengguang Lu, Chenhao Jin, Yanwen Chen, Yuze Meng, Zhen Lian, Takashi Taniguchi, Kenji Watanabe, Shengbai Zhang, Dmitry Smirnov, and Su Fei Shi. Revealing the biexciton and trion-exciton complexes in BN encapsulated WSe_2. *Nature Communications*, 9(1):1–7, 2018.

[94] T. P. Lyons, S. Dufferwiel, M. Brooks, F. Withers, T. Taniguchi, K. Watanabe, K. S. Novoselov, G. Burkard, and A. I. Tartakovskii. The valley Zeeman effect in inter- and intra-valley trions in monolayer WSe_2. 2018.

[95] D. Vaclavkova, J. Wyzula, K. Nogajewski, M. Bartos, A. O. Slobodeniuk, C. Faugeras, M. Potemski, and M. R. Molas. Singlet and triplet trions in WS_2 monolayer encapsulated in hexagonal boron nitride. *Nanotechnology*, 29(32), 2018.

[96] Andres Castellanos-Gomez, Michele Buscema, Rianda Molenaar, Vibhor Singh, Laurens Janssen, Herre S.J. Van Der Zant, and Gary A. Steele. Deterministic transfer of two-dimensional materials by all-dry viscoelastic stamping. *2D Materials*, 1(1), 2014.

[97] Sefaattin Tongay, Wen Fan, Jun Kang, Joonsuk Park, Unsal Koldemir, Joonki Suh, Deepa S Narang, Kai Liu, Jie Ji, Jingbo Li, Robert Sinclair, and Junqiao Wu. Tuning Interlayer Coupling in Large-Area Heterostructures with CVD- Grown MoS_2 and WS_2 Monolayers. 2, 2014.

[98] V. Ongun Özçelik, Javad G. Azadani, Ce Yang, Steven J. Koester, and Tony Low. Band alignment of two-dimensional semiconductors for designing heterostructures with momentum space matching. *Physical Review B*, 94(3), 2016.

[99] Frank Ceballos, Matthew Z. Bellus, Hsin-Ying Chiu, and Hui Zhao. Probing charge transfer excitons in a $MoSe_2$ WS_2 van der Waals heterostructure. *Nanoscale*, 7(41):17523–17528, 2015.

[100] Evgeny M. Alexeev, Alessandro Catanzaro, Oleksandr V. Skrypka, Pramoda K. Nayak, Seongjoon Ahn, Sangyeon Pak, Juwon Lee, Jung Inn Sohn, Kostya S. Novoselov, Hyeon Suk Shin, and Alexander I. Tartakovskii. Imaging of Interlayer Coupling in van der Waals Heterostructures Using a Bright-Field Optical Microscope. *Nano Letters*, 17(9):5342–5349, 2017.

[101] Dinh Hoa Luong, Hyun Seok Lee, Guru Prakash Neupane, Shrawan Roy, Ganesh Ghimire, Jin Hee Lee, Quoc An Vu, and Young Hee Lee. Tunneling Photocurrent Assisted by Interlayer Excitons in Staggered van der Waals Hetero-Bilayers. *Advanced Materials*, 29(33):1–8, 2017.

[102] Jiaqi He, Nardeep Kumar, Matthew Z Bellus, Hsin-Ying Chiu, Dawei He, Yongsheng Wang, and Hui Zhao. Electron transfer and coupling in graphene-tungsten disulfide van der Waals heterostructures. *Nature communications*, 5:5622, 2014.

[103] Xiaoping Hong, Jonghwan Kim, Su-Fei Shi, Yanfeng Yu Yanfeng Yu Yanfeng Yu Zhang, Chenhao Jin, Yinghui Sun, Sefaattin Tongay, Junqiao Wu, Yanfeng Yu Yanfeng Yu Yanfeng Yu Zhang, and Feng Wang. Ultrafast charge transfer in atomically thin MoS_2/WS_2 heterostructures. *Nature Nanotechnology*, 9(August):1–5, 2014.

[104] Bastian Miller, Alexander Steinhoff, Borja Pano, Julian Klein, Frank Jahnke, Alexander Holleitner, and Ursula Wurstbauer. Long-Lived Direct and Indirect Interlayer Excitons in van der Waals Heterostructures. *Nano Letters*, 17(9):5229–5237, 2017.

[105] Chenhao Jin, Eric Yue Ma, Ouri Karni, Emma C. Regan, Feng Wang, and Tony F. Heinz. Ultrafast dynamics in van der Waals heterostructures. *Nature Nanotechnology*, 13(11):994–1003, 2018.

[106] Oleg L. Berman and Roman Ya Kezerashvili. High-temperature superfluidity of the two-component Bose gas in a transition metal dichalcogenide bilayer. *Physical Review B*, 93(24):1–14, 2016.

[107] Pramoda K. Nayak, Yevhen Horbatenko, Seongjoon Ahn, Gwangwoo Kim, Jae Ung Lee, Kyung Yeol Ma, A. Rang Jang, Hyunseob Lim, Dogyeong Kim, Sunmin Ryu, Hyeonsik Cheong, Noejung Park, and Hyeon Suk Shin. Probing Evolution of Twist-Angle-Dependent Interlayer Excitons in $MoSe_2$ /WSe_2 van der Waals Heterostructures. *ACS Nano*, 11(4):4041–4050, 2017.

[108] John Schaibley. Control of interlayer valley excitons in atomically-thin $MoSe_2$ -WSe_2 heterostructures. *Ultrafast Phenomena and Nanophotonics XXI*, 10102(February 2017):101021E, 2017.

[109] Kyle L. Seyler, Pasqual Rivera, Hongyi Yu, Nathan P. Wilson, Essance L. Ray, David G. Mandrus, Jiaqiang Yan, Wang Yao, and Xiaodong Xu. Signatures of moiré-trapped valley excitons in $MoSe_2$ /WSe_2 heterobilayers. *Nature*, 567(7746):66–70, 2019.

[110] Jens Kunstmann, Fabian Mooshammer, Philipp Nagler, Andrey Chaves, Frederick Stein, Nicola Paradiso, Gerd Plechinger, Christoph Strunk, Christian Schüller, Gotthard Seifert, David R. Reichman, and Tobias Korn. Momentum-space indirect interlayer excitons in transition-metal dichalcogenide van der Waals heterostructures. *Nature Physics*, 14(8):801–805, 2018.

[111] Qijing Zheng, Wissam A. Saidi, Yu Xie, Zhenggang Lan, Oleg V. Prezhdo, Hrvoje Petek, and Jin Zhao. Phonon-Assisted Ultrafast Charge Transfer at van der Waals Heterostructure Interface. *Nano Letters*, 17(10):6435–6442, 2017.

[112] Roland Gillen and Janina Maultzsch. Interlayer excitons in $MoSe_2$/WSe_2 heterostructures from first principles. *Physical Review B*, 97(16):1–7, 2018.

[113] D. G. Mandrus, P. Rivera, J. Yan, K. L. Seyler, J. R. Schaibley, W. Yao, X. Xu, and H. Yu. Valley-polarized exciton dynamics in a 2D semiconductor heterostructure. *Science*, 351(6274):688–691, 2016.

[114] M. Baranowski, A. Surrente, L. Klopotowski, J. M. Urban, N. Zhang, D. K. Maude, K. Wiwatowski, S. Mackowski, Y. C. Kung, D. Dumcenco, A. Kis, and P. Plochocka. Probing the Interlayer Exciton Physics in a MoS_2/$MoSe_2$/MoS_2 van der Waals Heterostructure. *Nano Letters*, 17(10):6360–6365, 2017.

[115] John R Schaibley, Pasqual Rivera, Hongyi Yu, Kyle L Seyler, Jiaqiang Yan, David G Mandrus, Takashi Taniguchi, Kenji Watanabe, Wang Yao, and Xiaodong Xu. Directional interlayer spin-valley transfer in two-dimensional heterostructures. *Nature communications*, 7:13747, 2016.

[116] R. H. Bromley. Two-dimensional strain measurement by moiré. *Proceedings of the Physical Society. Section B*, 69(3):373–381, 1956.

[117] J Vangindertael, R Camacho, W Sempels, H Mizuno, P Dedecker, and K P F Janssen. Methods and Applications in Fluorescence - An introduction to optical super-resolution microscopy for the adventurous biologist. *Methods and Applications in Fluorescence*, 6(2):55, 2018.

[118] Seok-Joo Byun, Seok Yong Byun, Jangkyo Lee, Won Mok Kim, Han-Pil Kim, Min Yong Jeon, and Taek-Sung Lee. An efficient simulation and analysis method of moiré patterns in display systems. *Optics Express*, 22(3):3128, 2014.

[119] P. J. Zomer, M. H D Guimarães, J. C. Brant, N. Tombros, and B. J. Van Wees. Fast pick up technique for high quality heterostructures of bilayer graphene and hexagonal boron nitride. *Applied Physics Letters*, 105(1), 2014.

[120] I. Brihuega, P. Mallet, H. González-Herrero, G. Trambly De Laissardière, M. M. Ugeda, L. Magaud, J. M. Gómez-Rodríguez, F. Ynduráin, and J. Y. Veuillen. Unraveling the intrinsic and robust nature of van hove singularities in twisted bilayer graphene by scanning tunneling microscopy and theoretical analysis. *Physical Review Letters*, 109(19):1–5, 2012.

[121] Taisuke Ohta, Jeremy T. Robinson, Peter J. Feibelman, Aaron Bostwick, Eli Rotenberg, and Thomas E. Beechem. Evidence for interlayer coupling and moiré periodic potentials in twisted bilayer graphene. *Physical Review Letters*, 109(18):1–6, 2012.

[122] Evgeny M. Alexeev, David A. Ruiz-Tijerina, Mark Danovich, Matthew J. Hamer, Daniel J. Terry, Pramoda K. Nayak, Seongjoon Ahn, Sangyeon Pak, Juwon Lee, Jung Inn Sohn, Maciej R. Molas, Maciej Koperski, Kenji Watanabe, Takashi Taniguchi, Kostya S. Novoselov, Roman V. Gorbachev, Hyeon Suk Shin, Vladimir I. Fal'ko, and Alexander I. Tartakovskii. Resonantly hybridized excitons in moiré superlattices in van der Waals heterostructures. *Nature*, 567(7746):81–86, 2019.

[123] Miao Ling Lin, Qing Hai Tan, Jiang Bin Wu, Xiao Shuang Chen, Jin Huan Wang, Yu Hao Pan, Xin Zhang, Xin Cong, Jun Zhang, Wei Ji, Ping An Hu, Kai Hui Liu, and Ping Heng Tan. Moiré phonons in twisted bilayer MoS_2. *ACS Nano*, 12(8):8770–8780, 2018.

[124] Haiming Zhu, Jue Wang, Zizhou Gong, Young Duck Kim, James Hone, and X. Y. Zhu. Interfacial Charge Transfer Circumventing Momentum Mismatch at Two-Dimensional van der Waals Heterojunctions. *Nano Letters*, 17(6):3591–3598, 2017.

[125] Aubrey T. Hanbicki, Hsun Jen Chuang, Matthew R. Rosenberger, C. Stephen Hellberg, Saujan V. Sivaram, Kathleen M. McCreary, Igor I. Mazin, and Berend T. Jonker. Double Indirect Interlayer Exciton in a $MoSe_2/WSe_2$ van der Waals Heterostructure. *ACS Nano*, 12(5):4719–4726, 2018.

[126] Fengcheng Wu, Timothy Lovorn, and A. H. Macdonald. Theory of optical absorption by interlayer excitons in transition metal dichalcogenide heterobilayers. *Physical Review B*, 97(3):1–10, 2018.

[127] Wang Yao, Xiaodong Xu, Gui-Bin Liu, Jianju Tang, and Hongyi Yu. Moiré excitons: From programmable quantum emitter arrays to spin-orbitcoupled artificial lattices. *Science Advances*, 3(11):e1701696, 2017.

[128] Chenhao Jin, Emma C. Regan, Aiming Yan, M. Iqbal Bakti Utama, Danqing Wang, Sihan Zhao, Ying Qin, Sijie Yang, Zhiren Zheng, Shenyang Shi, Kenji Watanabe, Takashi Taniguchi, Sefaattin Tongay, Alex Zettl, and Feng Wang. Observation of moiré excitons in WSe_2 /WS_2 heterostructure superlattices. *Nature*, 567(7746):76–80, 2019.

[129] David A. Ruiz-Tijerina and Vladimir I. Fal'Ko. Interlayer hybridization and moiré superlattice minibands for electrons and excitons in heterobilayers of transition-metal dichalcogenides. *Physical Review B*, 99(12):30–32, 2019.

[130] Humberto R. Gutierrez, Nestor Perea-Lopez, Ana Laura Elias, Ayse Berkdemir, Bei Wang, Ruitao Lv, Florentino Lopez-Urias, Vincent H. Crespi, Humberto Terrones, and Mauricio Terrones. Extraordinary room-temperature photoluminescence in triangular WS_2 monolayers. *Nano Letters*, 13(8):3447–3454, 2013.

[131] Hyungjin Kim, Der Hsien Lien, Matin Amani, Joel W. Ager, and Ali Javey. Highly Stable Near-Unity Photoluminescence Yield in Monolayer MoS_2 by Fluoropolymer Encapsulation and Superacid Treatment. *ACS Nano*, 11(5):5179–5185, 2017.

[132] Ashish Arora, Maciej Koperski, Karol Nogajewski, Jacques Marcus, Clément Clement Faugeras, and Marek Potemski. Excitonic resonances in thin films of WSe_2: From monolayer to bulk material. *Nanoscale*, 7(23):10421–10429, 2015.

[133] Ashish Arora, Karol Nogajewski, MacIej Molas, MacIej Koperski, and Marek Potemski. Exciton band structure in layered $MoSe_2$: From a monolayer to the bulk limit. *Nanoscale*, 7(48):20769–20775, 2015.

[134] Maciej R. Molas, Karol Nogajewski, Artur O. Slobodeniuk, Johannes Binder, Miroslav Bartos, and Marek Potemski. Optical response of monolayer, few-layer and bulk tungsten disulfide. pages 13128–13141, 2017.

[135] R. Suzuki, M. Sakano, Y. J. Zhang, R. Akashi, D. Morikawa, A. Harasawa, K. Yaji, K. Kuroda, K. Miyamoto, T. Okuda, K. Ishizaka, R. Arita, and Y. Iwasa. Valley-dependent spin polarization in bulk MoS_2 with broken inversion symmetry. *Nature Nanotechnology*, 9(8):611–617, 2014.

[136] Jieun Lee, Kin Fai Mak, and Jie Shan. Electrical control of the valley Hall effect in bilayer MoS_2 transistors. *Nature Nanotechnology*, 11(5):421–425, 2016.

[137] Danovich Mark, Zólyomi Viktor, I Fal'ko Vladimir, and L Aleiner Igor. Auger recombination of dark excitons in WS_2 and WSe_2 monolayers. *2D Materials*, 3(3):35011, 2016.

[138] Erfu Liu, Jeremiah van Baren, Zhengguang Lu, Mashael M. Altaiary, Takashi Taniguchi, Kenji Watanabe, Dmitry Smirnov, and Chun Hung Lui. Gate Tunable Dark Trions in Monolayer WSe_2. *Physical Review Letters*, 123(2):027401, 2019.

[139] Xiao-Xiao Zhang, Ting Cao, Zhengguang Lu, Yu-Chuan Lin, Fan Zhang, Ying Wang, Zhiqiang Li, James C. Hone, Joshua a. Robinson, Dmitry Smirnov, Steven G. Louie, and Tony F. Heinz. Magnetic brightening and control of dark excitons in monolayer WSe_2. *Nature Nanotechnology*, (June):1–7, 2016.

[140] F. Volmer, S. Pissinger, M. Ersfeld, S. Kuhlen, C. Stampfer, and B. Beschoten. Intervalley dark trion states with spin lifetimes of 150 ns in WSe_2. *Physical Review B*, 95(23):1–12, 2017.

[141] Bruno R. Carvalho, Yuanxi Wang, Sandro Mignuzzi, Debdulal Roy, Mauricio Terrones, Cristiano Fantini, Vincent H. Crespi, Leandro M. Malard, and Marcos a. Pimenta. Intervalley scattering by acoustic phonons in two-dimensional MoS_2 revealed by double-resonance Raman spectroscopy. *Nature Communications*, 8:14670, 2017.

[142] H P Myers. *Introductory Solid State Physics*, volume 1. Taylor and Francis, 1990.

[143] Xin Zhang, Xiao-Fen Qiao, Wei Shi, Jiang-Bin Wu, De-Sheng Jiang, and Ping-Heng Tan. Phonon and Raman scattering of two-dimensional transition metal dichalcogenides from monolayer, multilayer to bulk material. *Chem. Soc. Rev.*, 44(9):2757–2785, 2015.

[144] Ismail Bilgin, Aldo S. Raeliarijaona, Michael C. Lucking, Sebastian Cooper Hodge, Aditya D. Mohite, Andres De Luna Bugallo, Humberto Terrones, and Swastik Kar. Resonant Raman and Exciton Coupling in High-Quality Single Crystals of Atomically Thin Molybdenum Diselenide Grown by Vapor-Phase Chalcogenization. *ACS Nano*, 12(1):740–750, 2018.

[145] Andrea C Ferrari. Raman spectroscopy of graphene and graphite: Disorder, electron-phonon coupling, doping and nonadiabatic effects. *Solid State Communications*, 143(1-2):47–57, jul 2007.

[146] Andrea C Ferrari and Denis M Basko. Raman spectroscopy as a versatile tool for studying the properties of graphene. *Nature nanotechnology*, 8(4):235–246, apr 2013.

[147] Junku Liu, Qunqing Li, Yuan Zou, Qingkai Qian, Yuanhao Jin, Guanhong Li, Kaili Jiang, and Shoushan Fan. The Dependence of Graphene Raman D band on Carrier Density. 2013.

[148] Ayse Berkdemir, Humberto R. Gutiérrez, Andrés R. Botello-Méndez, Néstor Perea-López, Ana Laura Elías, Chen-Ing Chia, Bei Wang, Vincent H. Crespi, Florentino López-Urías, Jean-Christophe Charlier, Humberto Terrones, and Mauricio Terrones. Identification of individual and few layers of WS_2 using Raman Spectroscopy. *Scientific Reports*, 3:1–8, 2013.

[149] R. Saito, Y. Tatsumi, S. Huang, X. Ling, and M. S. Dresselhaus. Raman spectroscopy of transition metal dichalcogenides. *Journal of Physics Condensed Matter*, 28(35), 2016.

[150] Publisher Taylor and R Loudon. *Advances in Physics The Raman effect in crystals.* Number November. 2011.

[151] J.M. Chen and C.S. Wang. Second order Raman spectrum of MoS_2. *Solid State Communications*, 14(9):857–860, may 1974.

[152] Changgu Lee, Hugen Yan, Louis E. Brus, Tony F. Heinz, James Hone, and Sunmin Ryu. Anomalous lattice vibrations of single- and few-layer MoS_2. *ACS Nano*, 4(5):2695–2700, 2010.

[153] H. Terrones, E. Del Corro, S. Feng, J. M. Poumirol, D. Rhodes, D. Smirnov, N. R. Pradhan, Z. Lin, M. A.T. Nguyen, A. L. Elías, T. E. Mallouk, L. Balicas, M. A. Pimenta, and M. Terrones. New First Order Raman-active Modes in Few Layered Transition Metal Dichalcogenides. *Scientific Reports*, 4:1–9, 2014.

[154] Matthias Staiger, Roland Gillen, Nils Scheuschner, Oliver Ochedowski, Felix Kampmann, Marika Schleberger, Christian Thomsen, and Janina Maultzsch. Splitting of monolayer out-of-plane A_1' Raman mode in few-layer WS_2. *Physical Review B - Condensed Matter and Materials Physics*, 91(19):1–8, 2015.

[155] Kangwon Kim, Jae Ung Lee, Dahyun Nam, and Hyeonsik Cheong. Davydov Splitting and Excitonic Resonance Effects in Raman Spectra of Few-Layer $MoSe_2$. *ACS Nano*, 10(8):8113–8120, 2016.

[156] Sanghun Kim, Kangwon Kim, Jae Ung Lee, and Hyeonsik Cheong. Excitonic resonance effects and Davydov splitting in circularly polarized Raman spectra of few-layer WSe_2. *2D Materials*, 4(4), 2017.

[157] Yanlong Wang, Chunxiao Cong, Caiyu Qiu, and Ting Yu. Raman spectroscopy study of lattice vibration and crystallographic orientation of monolayer MoS_2 under uniaxial strain. *Small*, 9(17):2857–2861, 2013.

[158] Qianhui Zhang, Zhenyue Chang, Guanzhong Xu, Ziyu Wang, Yupeng Zhang, Zai-Quan Xu, Shujian Chen, Qiaoliang Bao, Jefferson Zhe Liu, Yui-Wing Mai, Wenhui Duan, Michael S. Fuhrer, and Changxi Zheng. Strain Relaxation of Monolayer WS_2 on Plastic Substrate. *Advanced Functional Materials*, 26(47):8707–8714, 2016.

[159] Rusen Yan, Jeffrey R. Simpson, Simone Bertolazzi, Jacopo Brivio, Michael Watson, Xufei Wu, Andras Kis, Tengfei Luo, Angela R. Hight Walker, and Huili Grace Xing. Thermal conductivity of monolayer molybdenum disulfide obtained from temperature-dependent Raman spectroscopy. *ACS Nano*, 8(1):986–993, 2014.

[160] Namphung Peimyoo, Jingzhi Shang, Weihuang Yang, Yanlong Wang, Chunxiao Cong, and Ting Yu. Thermal conductivity determination of suspended mono- and bilayer WS_2 by Raman spectroscopy. *Nano Research*, 8(4):1210–1221, 2015.

[161] Yanfeng Chen, Dumitru O. Dumcenco, Yiming Zhu, Xin Zhang, Nannan Mao, Qingliang Feng, Mei Zhang, Jin Zhang, Ping Heng Tan, Ying Sheng Huang, and Liming Xie. Composition-dependent Raman modes of $Mo1\text{-}xWxS_2$ monolayer alloys. *Nanoscale*, 6(5):2833–2839, 2014.

[162] Qingkai Qian, Zhaofu Zhang, and Kevin J. Chen. In Situ Resonant Raman Spectroscopy to Monitor the Surface Functionalization of MoS_2 and WSe_2 for High-k Integration: A First-Principles Study. *Langmuir*, 34(8):2882–2889, 2018.

[163] Shao Yu Chen, Changxi Zheng, Michael S. Fuhrer, and Jun Yan. Helicity-Resolved Raman Scattering of MoS_2, $MoSe_2$, WS_2, and WSe_2 Atomic Layers. *Nano Letters*, 15(4):2526–2532, 2015.

[164] Jae-Ung Lee, Hyeonsik Cheong, Jung Hwa Kim, Songhee Han, Minjung Kim, and Zonghoon Lee. Determination of the thickness and orientation of few-layer tungsten ditelluride using polarized Raman spectroscopy. *2D Materials*, 3(3):034004, 2016.

[165] Lifa Zhang and Qian Niu. Chiral Phonons at High-Symmetry Points in Monolayer Hexagonal Lattices. *Physical Review Letters*, 115(11):1–5, 2015.

[166] Ming-Yang Li, Chih-Wen Yang, Jun Yi, Robert A. Kaindl, Hanyu Zhu, Yuan Wang, Xiang Zhang, Jun Xiao, Lain-Jong Li, and Lifa Zhang. Observation of chiral phonons. *Science*, 359(6375):579–582, 2018.

[167] Chen Hao, Zhang Wei, Niu Qian, and Zhang Lifa. Chiral phonons in two-dimensional materials. *2D Materials*, 6(1):12002, 2019.

[168] Sandro Mignuzzi, Andrew J. Pollard, Nicola Bonini, Barry Brennan, Ian S. Gilmore, Marcos a. Pimenta, David Richards, and Debdulal Roy. Effect of disorder on Raman scattering of single-layer MoS_2. *Physical Review B - Condensed Matter and Materials Physics*, 91(19):1–7, 2015.

[169] Amber McCreary, Ayse Berkdemir, Junjie Wang, Minh An Nguyen, Ana Laura Elías, Néstor Perea-López, Kazunori Fujisawa, Bernd Kabius, Victor Carozo, David A. Cullen, Thomas E. Mallouk, J. Zhu, and Mauricio Terrones. Distinct photoluminescence and Raman spectroscopy signatures for identifying highly crystalline WS_2 monolayers produced by different growth methods. *Journal of Materials Research*, 31(7):931–944, 2016.

[170] Jiake Li, Weitao Su, Fei Chen, Li Fu, Su Ding, Kaixin Song, Xiwei Huang, and Lijie Zhang. Atypical Defect-Mediated Photoluminescence and Resonance Raman Spectroscopy of Monolayer WS_2. *Journal of Physical Chemistry C*, 123(6):3900–3907, 2019.

[171] Anand P S Gaur, Satyaprakash Sahoo, J. F. Scott, and Ram S. Katiyar. Electron - Phonon interaction and double-resonance Raman studies in monolayer WS_2. *Journal of Physical Chemistry C*, 119(9):5146–5151, 2015.

[172] Ursula Wurstbauer, Bastian Miller, Qing-hai Tan, Yu-jia Sun, Xue-lu Liu, Yanyuan Zhao, Qihua Xiong, and Ping-heng Tan. Observation of forbidden

phonons , Fano resonance and dark excitons by resonance Raman scattering in few-layer WS_2. *2D Materials*, 4:031007, 2017.

[173] Joanna Kutrowska-Girzycka, Joanna Jadczak, and Leszek Bryja. The study of dispersive b'-mode in monolayer MoS_2 in temperature dependent resonant Raman scattering experiments. *Solid State Communications*, 275(February):25–28, 2018.

[174] Jae Ung Lee, Kangwon Kim, Songhee Han, Gyeong Hee Ryu, Zonghoon Lee, and Hyeonsik Cheong. Raman Signatures of Polytypism in Molybdenum Disulfide. *ACS Nano*, 10(2):1948–1953, 2016.

[175] Jeremiah Van Baren, Gaihua Ye, Jia An Yan, Zhipeng Ye, Pouyan Rezaie, Peng Yu, Zheng Liu, Rui He, and Chun Hung Lui. Stacking-dependent interlayer phonons in 3R and 2H MoS_2. *2D Materials*, 6(2), 2019.

[176] Guillaume Froehlicher, Etienne Lorchat, Olivia Zill, Michelangelo Romeo, and Stéphane Berciaud. Rigid-layer Raman-active modes in N-layer transition metal dichalcogenides: interlayer force constants and hyperspectral Raman imaging. *Journal of Raman Spectroscopy*, 49(1):91–99, 2018.

[177] Maria O'Brien, Niall McEvoy, Damien Hanlon, Toby Hallam, Jonathan N Coleman, and Georg S Duesberg. Mapping of Low-Frequency Raman Modes in CVD-Grown Transition Metal Dichalcogenides: Layer Number, Stacking Orientation and Resonant Effects. *Scientific reports*, 6(August 2015):19476, 2016.

[178] Jinho Yang, Jae-Ung Lee, and Hyeonsik Cheong. Excitation energy dependence of Raman spectra of few-layer WS_2. *FlatChem*, pages 1–7, 2017.

[179] Li Ding, Muhammad Shoufie Ukhtary, Mikhail Chubarov, Tanushree H. Choudhury, Fu Zhang, Rui Yang, Ao Zhang, Jonathan A. Fan, Mauricio Terrones, Joan M. Redwing, Teng Yang, Mingda Li, Riichiro Saito, and Shengxi Huang. Understanding Interlayer Coupling in TMD-hBN Heterostructure by Raman Spectroscopy. *IEEE Transactions on Electron Devices*, 65(10):4059–4067, 2018.

[180] Pierce Maguire, Clive Downing, Jakub Jadwiszczak, Maria O'Brien, Darragh Keane, John B. McManus, Georg S. Duesberg, Valeria Nicolosi, Niall McEvoy, and Hongzhou Zhang. Suppression of the shear Raman mode in defective bilayer MoS_2. *Journal of Applied Physics*, 125(6), 2019.

[181] Victor Carozo, Clara M. Almeida, Erlon H.M. Ferreira, Luiz Gustavo Cançado, Carlos Alberto Achete, and Ado Jorio. Raman signature of graphene superlattices. *Nano Letters*, 11(11):4527–4534, 2011.

[182] Jaya Kumar Panda, Anushree Roy, Mauro Gemmi, Elena Husanu, Ang Li, Daniele Ercolani, and Lucia Sorba. Electronic band structure of wurtzite GaP nanowires via temperature dependent resonance Raman spectroscopy. *Applied Physics Letters*, 103(2), 2013.

[183] Joseph H. Spencer, David C. Smith, Liam P. McDonnell, Jeremy Sloan, and Reza J. Kashtiban. Coherence lifetime broadened optical transitions in a 2 atom diameter HgTe nanowire: a temperature dependent resonance Raman study. *RSC Adv.*, 6(98):95387–95395, 2016.

[184] O. N. Torrens, M. Zheng, and J. M. Kikkawa. Energy of K-momentum dark excitons in carbon nanotubes by optical spectroscopy. *Physical Review Letters*, 101(15):3–6, 2008.

[185] A A. Mitioglu, P. Plochocka, G. Deligeorgis, S. Anghel, L. Kulyuk, and D. K. Maude. Second-order resonant Raman scattering in single-layer tungsten disulfide WS2. *Physical Review B - Condensed Matter and Materials Physics*, 89(24):1–5, 2014.

[186] Huaihong Guo, Teng Yang, Mahito Yamamoto, Lin Zhou, Ryo Ishikawa, Keiji Ueno, Kazuhito Tsukagoshi, Zhidong Zhang, Mildred S. Dresselhaus, and Riichiro Saito. Double resonance Raman modes in monolayer and few-layer $MoTe_2$. *Physical Review B*, 91(20):205415, 2015.

[187] Tsachi Livneh, Juan S. Reparaz, and Alejandro R. Goni. Low-temperature resonant Raman asymmetry in 2H-MoS_2 under high pressure. *Journal of Physics Condensed Matter*, 29(43), 2017.

[188] Xin Lu, M. I.B. Utama, Xingzhi Wang, Weigao Xu, Weijie Zhao, Man Hon Samuel Owen, and Qihua Xiong. Gate-Tunable Resonant Raman Spectroscopy of Bilayer MoS_2. *Small*, 13(35):2–7, 2017.

[189] Lee Jae-Ung, Kim Kangwon, and Cheong Hyeonsik. Resonant Raman and photoluminescence spectra of suspended molybdenum disulfide. *2D Materials*, 2(4):44003, 2015.

[190] Luojun Du, Mengzhou Liao, Jian Tang, Qian Zhang, Hua Yu, Rong Yang, Kenji Watanabe, Takashi Taniguchi, Dongxia Shi, Qingming Zhang, and Guangyu Zhang. Strongly enhanced exciton-phonon coupling in two-dimensional WS_2. *Physical Review B*, 97(23):235145, 2018.

[191] Nils Scheuschner, Oliver Ochedowski, Marika Schleberger, and Janina Maultzsch. Resonant Raman profiles and μ-photoluminescence of atomically thin layers of molybdenum disulfide. *Physica Status Solidi (B) Basic Research*, 249(12):2644–2647, 2012.

[192] Jae-Ung Lee, Jaesung Park, Y.-W. Young-Woo Son, and Hyeonsik Cheong. Anomalous excitonic resonance Raman effects in few-layered MoS 2. *Nanoscale*, 7(7):3229–3236, 2015.

[193] E. del Corro, A. Botello-Méndez, Y. Gillet, A. L. Elias, H. Terrones, S. Feng, C. Fantini, Daniel Rhodes, N. Pradhan, L. Balicas, X. Gonze, J.-C. Charlier, M. Terrones, and M. A. Pimenta. Atypical ExcitonPhonon Interactions in WS_2 and WSe_2 Monolayers Revealed by Resonance Raman Spectroscopy. *Nano Letters*, 16(4):2363–2368, 2016.

[194] P. Soubelet, A. E. Bruchhausen, A. Fainstein, K. Nogajewski, and C. Faugeras. Resonance effects in the Raman scattering of monolayer and few-layer $MoSe_2$. *Physical Review B - Condensed Matter and Materials Physics*, 93(15):1–9, 2016.

[195] Nils Scheuschner, Roland Gillen, Matthias Staiger, and Janina Maultzsch. Interlayer resonant Raman modes in few-layer MoS_2. *Physical Review B*, 91(23):235409, 2015.

[196] Richard M Martin. Breakdown of Selection Rules in Resonance Raman Scattering. *Physical Review Letters*, (2):1–3, 1970.

[197] Maciej R Molas, Karol Nogajewski, Marek Potemski, and Adam Babiński. Raman scattering excitation spectroscopy of monolayer WS_2. *Scientific Reports*, 7:5036, jul 2017.

[198] Chenhao Jin, Jonghwan Kim, Joonki Suh, Zhiwen Shi, Bin Chen, Xi Fan, Matthew Kam, Kenji Watanabe, Takashi Taniguchi, Sefaattin Tongay, Alex Zettl, Junqiao Wu, and Feng Wang. Interlayer electron-phonon coupling in WSe_2/hBN heterostructures. *Nature Physics*, 13(2):127–131, 2017.

[199] Colin M. Chow, Hongyi Yu, Aaron M. Jones, Jiaqiang Yan, David G. Mandrus, Takashi Taniguchi, Kenji Watanabe, Wang Yao, and Xiaodong Xu. Unusual Exciton-Phonon Interactions at van der Waals Engineered Interfaces. *Nano Letters*, 17(2):1194–1199, 2017.

[200] Sumi Bhuyan, Vishwas Jindal, Dipankar Jana, and Sandip Ghosh. Signatures of self-trapping of trions in monolayer MoS_2. *Journal of Physics D: Applied Physics*, 51(43), 2018.

[201] J. Jadczak, L. Bryja, J. Kutrowska-Girzycka, P. Kapuściński, M. Bieniek, Y. S. Huang, and P. Hawrylak. Room temperature multi-phonon upconversion photoluminescence in monolayer semiconductor WS_2. *Nature Communications*, 10(1), 2019.

[202] S. Shree, M. Semina, C. Robert, B. Han, T. Amand, A. Balocchi, M. Manca, E. Courtade, X. Marie, T. Taniguchi, K. Watanabe, M. M. Glazov, and B. Urbaszek. Observation of exciton-phonon coupling in $MoSe_2$ monolayers. *Physical Review B*, 98(3):1–11, 2018.

[203] Vijila Chellappan, Ai Lin Christina Pang, Soumya Sarkar, Zi En Ooi, and Kuan Eng Johnson Goh. Effect of Phonons on Valley Depolarization in Monolayer WSe_2. *Electronic Materials Letters*, 14(6):766–773, 2018.

[204] Aaron M Jones, Hongyi Yu, Nirmal J Ghimire, Sanfeng Wu, Grant Aivazian, Jason S Ross, Bo Zhao, Jiaqiang Yan, David G Mandrus, Di Xiao, Wang Yao, and Xiaodong Xu. Optical generation of excitonic valley coherence in monolayer WSe_2. *Nature nanotechnology*, 8(9):634–638, 2013.

[205] Jason S Ross, Sanfeng Wu, Hongyi Yu, Nirmal J Ghimire, Aaron M Jones, Grant Aivazian, Jiaqiang Yan, David G Mandrus, Di Xiao, Wang Yao, and Xiaodong Xu. Electrical control of neutral and charged excitons in a monolayer semiconductor. *Nature communications*, 4:1474, 2013.

[206] Jason S Ross, Philip Klement, Aaron M Jones, Nirmal J Ghimire, Jiaqiang Yan, MandrusD. G., Takashi Taniguchi, Kenji Watanabe, Kenji Kitamura, Wang Yao, David H Cobden, and Xiaodong Xu. Electrically tunable excitonic light-emitting diodes based on monolayer WSe_2 p-n junctions. *Nat Nano*, 9(4):268–272, 2014.

[207] Chunxiao Cong, Jingzhi Shang, Xing Wu, Bingchen Cao, Namphung Peimyoo, Caiyu Qiu, Litao Sun, and Ting Yu. Synthesis and Optical Properties of Large-Area Single-Crystalline 2D Semiconductor WS_2 Monolayer from Chemical Vapor Deposition. *Advanced Optical Materials*, 2(2):131–136, 2014.

[208] Jung Joon Pyeon, Soo Hyun Kim, Doo Seok Jeong, Seung-Hyub Baek, Chong-Yun Kang, Jin-Sang Kim, and Seong Keun Kim. Wafer-scale growth of MoS_2 thin films by atomic layer deposition. *Nanoscale*, 8(20):10792–10798, 2016.

[209] Ming Wei Chen, Dmitry Ovchinnikov, Sorin Lazar, Michele Pizzochero, Michael Brian Whitwick, Alessandro Surrente, Michał Baranowski, Oriol Lopez Sanchez, Philippe Gillet, Paulina Plochocka, Oleg V. Yazyev, and Andras Kis. Highly Oriented Atomically Thin Ambipolar $MoSe_2$ Grown by Molecular Beam Epitaxy. *ACS Nano*, 11(6):6355–6361, 2017.

[210] Zhengyang Cai, Bilu Liu, Xiaolong Zou, and Hui Ming Cheng. Chemical Vapor Deposition Growth and Applications of Two-Dimensional Materials and Their Heterostructures, 2018.

[211] Yuan Huang, Eli Sutter, Norman N. Shi, Jiabao Zheng, Tianzhong Yang, Dirk Englund, Hong Jun Gao, and Peter Sutter. Reliable Exfoliation of Large-Area High-Quality Flakes of Graphene and Other Two-Dimensional Materials. *ACS Nano*, 9(11):10612–10620, 2015.

[212] Xixia Zhang, Fei Lou, Chunlong Li, Xiang Zhang, Ning Jia, Tongtong Yu, Jingliang He, Baitao Zhang, Haibing Xia, Shanpeng Wang, and Xutang Tao. Flux

method growth of bulk MoS_2 single crystals and their application as a saturable absorber. *CrystEngComm*, 17(21):4026–4032, 2015.

[213] Qing Hua Wang, Kourosh Kalantar-Zadeh, Andras Kis, Jonathan N Coleman, and Michael S Strano. Electronics and optoelectronics of two-dimensional transition metal dichalcogenides. *Nature Nanotechnology*, 7(11):699–712, 2012.

[214] K. Funahashi, J. Pu, M.-Y. Li, L.-J. Li, Y. Iwasa, and T. Takenobu. Large-area WSe_2 electric double layer transistors on a plastic substrate. *Japanese Journal of Applied Physics*, 54(6):1–5, 2015.

[215] Yan Lu, Xiao Li Li, Xin Zhang, Jiang Bin Wu, and Ping Heng Tan. Optical contrast determination of the thickness of SiO_2 film on Si substrate partially covered by two-dimensional crystal flakes. *Science Bulletin*, 60(8):806–811, 2015.

[216] Song-lin Li, Hisao Miyazaki, Haisheng Song, Hiromi Kuramochi, and Shu Nakaharai. Quantitative Raman Spectrum and Reliable Thickness Identification for Atomic Layers on Insulating Substrates. (8):7381–7388, 2012.

[217] Michele Buscema, Gary a. Steele, Herre S J van der Zant, and Andres Castellanos-Gomez. The effect of the substrate on the Raman and photoluminescence emission of single-layer MoS_2. *Nano Research*, 7(4):561–571, 2014.

[218] Kathleen M. McCreary, Aubrey T Hanbicki, Simranjeet Singh, Roland K Kawakami, Glenn G Jernigan, Masa Ishigami, Amy Ng, Todd H Brintlinger, Rhonda M Stroud, and Berend T Jonker. The Effect of Preparation Conditions on Raman and Photoluminescence of Monolayer WS_2. *Scientific Reports*, 6(1):35154, 2016.

[219] K. Gołasa, M. R. Molas, K. Nogajewski, M. Grzeszczyk, M. Zinkiewicz, M. Potemski, and A. Babinski. The effect of substrate on vibrational properties of single-layer MoS_2. *Acta Physica Polonica A*, 130(5):1172–1175, 2016.

[220] Gábor Zsolt Magda, János Pet, Gergely Dobrik, Chanyong Hwang, László P. Biró, and Levente Tapasztó. Exfoliation of large-area transition metal chalcogenide single layers. *Scientific Reports*, 5:14714, 2015.

[221] A. K M Newaz, D. Prasai, J. I. Ziegler, D. Caudel, S. Robinson, R. F. Haglund, and K. I. Bolotin. Electrical control of optical properties of monolayer MoS_2. *Solid State Communications*, 155:49–52, 2013.

[222] R. S. Sundaram, M. Engel, A. Lombardo, R. Krupke, A. C. Ferrari, Ph. Avouris, and M. Steiner. Electroluminescence in Single Layer MoS_2. *Nano Letters*, 13(4):1416–1421, 2013.

[223] Min Su Kim, Seok Joon Yun, Young Hee Yongjun Young Hee Yongjun Lee, Changwon Seo, Gang Hee Han, Ki Kang Kim, Young Hee Yongjun Young Hee Yongjun

Lee, and Jeongyong Kim. Biexciton Emission from Edges and Grain Boundaries of Triangular WS_2 Monolayers. *ACS Nano*, 10(2):2399–2405, 2016.

[224] Yongjun Lee, Seok Joon Yun, Youngbum Kim, Min Su Kim, Gang Hee Han, A K Sood, and Jeongyong Kim. Near-field spectral mapping of individual exciton complexes of monolayer WS_2 correlated with local defects and charge population. *Nanoscale*, 9(6):2272–2278, 2017.

[225] Fabian Cadiz, Cedric Robert, Gang Wang, Wilson Kong, Xi Fan, Mark Blei, Delphine Lagarde, Maxime Gay, Marco Manca, Takashi Taniguchi, Kenji Watanabe, Thierry Amand, Xavier Marie, Pierre Renucci, Sefaattin Tongay, and Bernhard Urbaszek. Ultra-low power threshold for laser induced changes in optical properties of 2D Molybdenum dichalcogenides. 2016.

[226] V. Orsi Gordo, M. A.G. Balanta, Y. Galvão Gobato, F. S. Covre, H. V.A. Galeti, F. Iikawa, O. D.D. Couto, F. Qu, M. Henini, D. W. Hewak, and C. C. Huang. Revealing the nature of lowerature photoluminescence peaks by laser treatment in van der Waals epitaxially grown WS_2 monolayers. *Nanoscale*, 10(10):4807–4815, 2018.

[227] Haotian Wang, Hongtao Yuan, Seung Sae Hong, Yanbin Li, and Yi Cui. Physical and chemical tuning of two-dimensional transition metal dichalcogenides. *Chemical Society Reviews*, 44(9):2664–2680, 2015.

[228] Anna N. Hoffman, Michael G. Stanford, Cheng Zhang, Ilia N. Ivanov, Akinola D. Oyedele, Maria Gabriela Sales, Stephen J. McDonnell, Michael R. Koehler, David G. Mandrus, Liangbo Liang, Bobby G. Sumpter, Kai Xiao, and Philip D. Rack. Atmospheric and Long-term Aging Effects on the Electrical Properties of Variable Thickness WSe 2 Transistors. *ACS Applied Materials and Interfaces*, 10(42):36540–36548, 2018.

[229] Peng Zhao, Angelica Azcatl, Pavel Bolshakov, Jiyoung Moon, Christopher L. Hinkle, Paul K. Hurley, Robert M. Wallace, and Chadwin D. Young. Effects of annealing on top-gated MoS_2 transistors with HfO_2 dielectric. *Journal of Vacuum Science and Technology B, Nanotechnology and Microelectronics: Materials, Processing, Measurement, and Phenomena*, 35(1):01A118, 2017.

[230] Woosuk Choi, Muhammad Arslan Shehzad, Sanghoon Park, and Yongho Seo. Influence of removing PMMA residues on surface of CVD graphene using a contact-mode atomic force microscope. *RSC Advances*, 7(12):6943–6949, 2017.

[231] G. Cassabois, P. Valvin, and B. Gil. Hexagonal boron nitride is an indirect bandgap semiconductor. *Nature Photonics*, 10(4):262–266, 2016.

[232] Seongjoon Ahn, Gwangwoo Kim, Pramoda K. Nayak, Seong In Yoon, Hyunseob Lim, Hyun Joon Shin, and Hyeon Suk Shin. Prevention of Transition Metal

Dichalcogenide Photodegradation by Encapsulation with h-BN Layers. *ACS Nano*, 10(9):8973–8979, 2016.

[233] Gwan Hyoung Lee, Xu Cui, Young Duck Kim, Ghidewon Arefe, Xian Zhang, Chul Ho Lee, Fan Ye, Kenji Watanabe, Takashi Taniguchi, Philip Kim, and James Hone. Highly Stable, Dual-Gated MoS_2 Transistors Encapsulated by Hexagonal Boron Nitride with Gate-Controllable Contact, Resistance, and Threshold Voltage. *ACS Nano*, 9(7):7019–7026, 2015.

[234] A Ajayi Obafunso, V Ardelean Jenny, D Shepard Gabriella, Wang Jue, Antony Abhinandan, Taniguchi Takeshi, Watanabe Kenji, F Heinz Tony, Strauf Stefan, X Y Zhu, and C Hone James. Approaching the intrinsic photoluminescence linewidth in transition metal dichalcogenide monolayers. *2D Materials*, 4(3):31011, 2017.

[235] F. Cadiz, E. Courtade, C. Robert, G. Wang, Y. Shen, H. Cai, T. Taniguchi, K. Watanabe, H. Carrere, D. Lagarde, M. Manca, T. Amand, P. Renucci, S. Tongay, X. Marie, and B. Urbaszek. Excitonic linewidth approaching the homogeneous limit in MoS_2-based van der Waals heterostructures. *Physical Review X*, 7(2):1–12, 2017.

[236] Jerome T. Mlack, Paul Masih Das, Gopinath Danda, Yung Chien Chou, Carl H. Naylor, Zhong Lin, Néstor Perea López, Tianyi Zhang, Mauricio Terrones, A. T.Charlie Johnson, and Marija Drndic. Transfer of monolayer TMD WS_2 and Raman study of substrate effects. *Scientific Reports*, 7(September 2016):1–8, 2017.

[237] Joon Young Kwak, Jeonghyun Hwang, Brian Calderon, Hussain Alsalman, Nini Munoz, Brian Schutter, and Michael G. Spencer. Electrical characteristics of multilayer MoS2 FETs with MoS 2/graphene heterojunction contacts. *Nano Letters*, 14(8):4511–4516, 2014.

[238] Carmen Palacios-Berraquero, Dhiren M. Kara, Alejandro R.P. Montblanch, Matteo Barbone, Pawel Latawiec, Duhee Yoon, Anna K. Ott, Marko Loncar, Andrea C. Ferrari, and Mete Atatüre. Large-scale quantum-emitter arrays in atomically thin semiconductors. *Nature Communications*, 8(May):1–6, 2017.

[239] Haitao Chen, Vincent Corboliou, Alexander S Solntsev, Duk-Yong Choi, Maria A Vincenti, Domenico de Ceglia, Costantino de Angelis, Yuerui Lu, and Dragomir N Neshev. Enhanced second-harmonic generation from two-dimensional $MoSe_2$ on a silicon waveguide. *Light: Science and Applications*, 6(10):e17060–e17060, 2017.

[240] T. Sundius. Computer fitting of Voigt profiles to Raman lines. *Journal of Raman Spectroscopy*, 1(5):471–488, nov 1973.

[241] F. C. Tai, S. C. Lee, J. Chen, C. Wei, and S. H. Chang. Multipeak fitting analysis of Raman spectra on DLCH film. *Journal of Raman Spectroscopy*, 40(8):1055–1059, aug 2009.

[242] Dahyun Nam, Jae Ung Lee, and Hyeonsik Cheong. Excitation energy dependent Raman spectrum of $MoSe_2$. *Scientific Reports*, 5:17113, 2015.

[243] Colin M. Chow, Hongyi Yu, Aaron M. Jones, John R. Schaibley, Michael Koehler, David G. Mandrus, R. Merlin, Wang Yao, and Xiaodong Xu. Phonon-assisted oscillatory exciton dynamics in monolayer MoSe2. *npj 2D Materials and Applications*, 1(1), 2017.

[244] Gabriella D. Shepard, Jenny V. Ardelean, Obafunso A. Ajayi, Daniel Rhodes, Xiaoyang Zhu, James C. Hone, and Stefan Strauf. Trion-Species-Resolved Quantum Beats in $MoSe_2$. *ACS Nano*, 11(11):11550–11558, 2017.

[245] E. Courtade, B. Han, S. Nakhaie, C. Robert, X. Marie, P. Renucci, T. Taniguchi, K. Watanabe, L. Geelhaar, J. M.J. Lopes, and B. Urbaszek. Spectrally narrow exciton luminescence from monolayer MoS_2 and $MoSe_2$ exfoliated onto epitaxially grown hexagonal BN. *Applied Physics Letters*, 113(3), 2018.

[246] T. Korn, S. Heydrich, M. Hirmer, J. Schmutzler, and C. Schller. Low-temperature photocarrier dynamics in monolayer MoS_2. *Applied Physics Letters*, 99(10):2014–2017, 2011.

[247] S. Horzum, H. Sahin, S. Cahangirov, P. Cudazzo, A. Rubio, T. Serin, and F. M. Peeters. Phonon softening and direct to indirect band gap crossover in strained single-layer $MoSe_2$. *Physical Review B - Condensed Matter and Materials Physics*, 87(12):1–5, 2013.

[248] Bo Peng, Hao Zhang, Hezhu Shao, Yuanfeng Xu, Xiangchao Zhang, and Heyuan Zhu. Towards intrinsic phonon transport in single-layer MoS_2. *Annalen der Physik*, 511(6):504–511, 2016.

[249] Lindsay Bassman, Aravind Krishnamoorthy, Hiroyuki Kumazoe, Masaaki Misawa, Fuyuki Shimojo, Rajiv K. Kalia, Aiichiro Nakano, and Priya Vashishta. Electronic Origin of Optically-Induced Sub-Picosecond Lattice Dynamics in $MoSe_2$ Monolayer. *Nano Letters*, 18(8):4653–4658, 2018.

[250] William M. Parkin, Adrian Balan, Liangbo Liang, Paul Masih Das, Michael Lamparski, Carl H. Naylor, Julio A. Rodríguez-Manzo, A. T Charlie Johnson, Vincent Meunier, and Marija Drndić. Raman Shifts in Electron-Irradiated Monolayer MoS2. *ACS Nano*, 10(4):4134–4142, 2016.

[251] P. Renucci, M. M. Glazov, B. Han, S. Shree, M. Manca, K. Watanabe, X. Marie, T. Taniguchi, C. Robert, L. E. Golub, E. Courtade, B. Urbaszek, and T. Amand. Exciton States in Monolayer $MoSe_2$ and $MoTe_2$ Probed by Upconversion Spectroscopy. *Physical Review X*, 8(3):1–17, 2018.

[252] G. Wang, I. C. Gerber, L. Bouet, D. Lagarde, A. Balocchi, M. Vidal, T. Amand, X. Marie, and B. Urbaszek. Exciton states in monolayer $MoSe_2$: Impact on interband transitions. *2D Materials*, 2(4), 2015.

[253] Reelika Kaupmees, Hannu Pekka Komsa, and Jüri Krustok. Photoluminescence Study of B-Trions in MoS_2 Monolayers with High Density of Defects. *Physica Status Solidi (B) Basic Research*, 1800384:3–7, 2018.

[254] Maciej R. Molas, Katarzyna Gołasa, Łukasz Bala, Karol Nogajewski, Miroslav Bartos, Marek Potemski, and Adam Babiński. Tuning carrier concentration in a superacid treated MoS_2 monolayer. (December 2018):1–7, 2018.

[255] Zefang Wang, Liang Zhao, Kin Fai Mak, and Jie Shan. Probing the Spin-Polarized Electronic Band Structure in Monolayer Transition Metal Dichalcogenides by Optical Spectroscopy. *Nano Letters*, 17(2):740–746, 2017.

[256] Jorge Quereda, Bart J van Wees, Talieh S Ghiasi, Feitze A van Zwol, and Caspar H van der Wal. Observation of bright and dark exciton transitions in monolayer $MoSe_2$ by photocurrent spectroscopy. *2D Materials*, 5(1):015004, 2017.

[257] Liang Guo, Meng Wu, Ting Cao, Daniele M. Monahan, Yi Hsien Lee, Steven G. Louie, and Graham R. Fleming. Exchange-driven intravalley mixing of excitons in monolayer transition metal dichalcogenides. *Nature Physics*, 15(3):228–232, 2019.

[258] E. Courtade, M. Semina, M. Manca, M. M. Glazov, C. Robert, F. Cadiz, G. Wang, T. Taniguchi, K. Watanabe, M. Pierre, W. Escoffier, E. L. Ivchenko, P. Renucci, X. Marie, T. Amand, and B. Urbaszek. Charged excitons in monolayer WSe_2: Experiment and theory. *Physical Review B*, 96(8):1–12, 2017.

[259] Zefang Wang, Yi Hsin Chiu, Kevin Honz, Kin Fai Mak, and Jie Shan. Electrical Tuning of Interlayer Exciton Gases in WSe_2 Bilayers. *Nano Letters*, 18(1):137–143, 2018.

[260] C. Robert, T. Amand, F. Cadiz, D. Lagarde, E. Courtade, M. Manca, T. Taniguchi, K. Watanabe, B. Urbaszek, and X. Marie. Fine structure and lifetime of dark excitons in transition metal dichalcogenide monolayers. *Physical Review B*, 96(15):1–8, 2017.

[261] Ziliang Ye, Lutz Waldecker, Eric Yue Ma, Daniel Rhodes, Abhinandan Antony, Bumho Kim, Xiao Xiao Zhang, Minda Deng, Yuxuan Jiang, Zhengguang Lu, Dmitry Smirnov, Kenji Watanabe, Takashi Taniguchi, James Hone, and Tony F. Heinz. Efficient generation of neutral and charged biexcitons in encapsulated WSe_2 monolayers. *Nature Communications*, 9(1):6–11, 2018.

[262] Maciej R Molas, Karol Nogajewski, Marek Potemski, and Adam Babiński. Raman scattering excitation spectroscopy of monolayer WS(2). *Scientific Reports*, 7:5036, jul 2017.

[263] Xin Luo, Yanyuan Zhao, Jun Zhang, Minglin Toh, Christian Kloc, Qihua Xiong, and Su Ying Quek. Effects of lower symmetry and dimensionality on Raman spectra in two-dimensional WSe_2. *Physical Review B - Condensed Matter and Materials Physics*, 88(19):1–7, 2013.

[264] Mei Yang, Xuerui Cheng, Yuanyuan Li, Yufen Ren, Miao Liu, and Zeming Qi. Anharmonicity of monolayer MoS_2 , $MoSe_2$, and WSe_2 : A Raman study under high pressure and elevated temperature. *Applied Physics Letters*, 110(9), 2017.

[265] Namphung Peimyoo, Jingzhi Shang, Weihuang Yang, Yanlong Wang, Chunxiao Cong, and Ting Yu. Thermal conductivity determination of suspended mono- and bilayer WS_2 by Raman spectroscopy. *Nano Research*, 8(4):1210–1221, 2015.

[266] Sujay B Desai, Gyungseon Seol, Jeong Seuk Kang, Hui Fang, Corsin Battaglia, Rehan Kapadia, Joel W Ager, Jing Guo, and Ali Javey. Strain-induced indirect to direct bandgap transition in multilayer WSe_2. *Nano letters*, 14(8):4592–4597, 2014.

[267] M. S. Saito, R., Grüneis, A., Samsonidze, G. G., Brar, V. W., Dresselhaus, G., Dresselhaus, R Saito, A Grüneis, Gr Grüneis, Ge G Samsonidze, V W Brar, G Dresselhaus, M S Dresselhaus, A Jorio, L G Cançado, Can Cançado, C Fantini, M A Pimenta, and A G Souza Filho. Double resonance Raman spectroscopy of single-wall carbon nanotubes. *New Journal of Physics*, 51(1):157, 2003.

[268] G. Wang, X. Marie, I. Gerber, T. Amand, D. Lagarde, L. Bouet, M. Vidal, A. Balocchi, and B. Urbaszek. Giant Enhancement of the Optical Second-Harmonic Emission of WSe_2 Monolayers by Laser Excitation at Exciton Resonances. *Physical Review Letters*, 114(9):1–6, 2015.

[269] Shao-Yu Chen, Thomas Goldstein, Jiayue Tong, Takashi Taniguchi, Kenji Watanabe, and Jun Yan. Superior Valley Polarization and Coherence of 2s Excitons in Monolayer WSe_2. *Physical Review Letters*, 120(4):046402, 2018.

[270] Shao Yu Chen, Zhengguang Lu, Thomas Goldstein, Jiayue Tong, Andrey Chaves, Jens Kunstmann, L. S.R. Cavalcante, Tomasz Woźniak, Gotthard Seifert, D. R. Reichman, Takashi Taniguchi, Kenji Watanabe, Dmitry Smirnov, and Jun Yan. Luminescent Emission of Excited Rydberg Excitons from Monolayer WSe_2. *Nano Letters*, 19(4):2464–2471, 2019.

[271] J. Jadczak, J. Kutrowska-Girzycka, T. Smoleński, P. Kossacki, Y. S. Huang, and L. Bryja. Exciton binding energy and hydrogenic Rydberg series in layered ReS_2. *Scientific Reports*, 9(1):1–9, 2019.

[272] A. V. Stier, N. P. Wilson, K. A. Velizhanin, J. Kono, X. Xu, and S. A. Crooker. Magnetooptics of Exciton Rydberg States in a Monolayer Semiconductor. *Physical Review Letters*, 120(5), 2018.

[273] Duy Le, Alexei Barinov, Edwin Preciado, Miguel Isarraraz, Iori Tanabe, Takashi Komesu, Conrad Troha, Ludwig Bartels, Talat S. Rahman, and Peter A. Dowben. Spin-orbit coupling in the band structure of monolayer WSe_2. *Journal of Physics Condensed Matter*, 27(18):1–6, 2015.

[274] Pasqual Rivera, Alexander J. Marsden, Nicholas D.M. Hine, Paul V. Nguyen, Gabriel C. Constantinescu, Neil R. Wilson, Viktor Kandyba, David H. Cobden, Kyle Seyler, Alexei Barinov, Zachary P.L. Laker, and Xiaodong Xu. Determination of band offsets, hybridization, and exciton binding in 2D semiconductor heterostructures. *Science Advances*, 3(2):e1601832, 2017.

[275] Frank Ceballos, Matthew Z. Bellus, Hsin-Ying Chiu, and Hui Zhao. Ultrafast Charge Separation and Indirect Exciton Formation in a MoS_2 $MoSe_2$ van der Waals Heterostructure. *ACS Nano*, 8(12):12717–12724, 2014.

[276] Alberto Ciarrocchi, Dmitrii Unuchek, Ahmet Avsar, Kenji Watanabe, Takashi Taniguchi, and Andras Kis. Polarization switching and electrical control of interlayer excitons in two-dimensional van der Waals heterostructures. *Nature Photonics*, 13(2):131–136, 2019.

[277] Chenhao Jin, Emma C. Regan, Aiming Yan, M. Iqbal Bakti Utama, Danqing Wang, Ying Qin, Sijie Yang, Zhiren Zheng, Kenji Watanabe, Takashi Taniguchi, Sefaattin Tongay, Alex Zettl, and Feng Wang. Observation of Moiré Excitons in WSe_2/WS_2 Heterostructure Superlattices. *Nature*, pages 2–7, 2018.

[278] Nan Zhang, Alessandro Surrente, Michal Baranowski, Duncan K. Maude, Patricia Gant, Andres Castellanos-Gomez, and Paulina Plochocka. Moiré Intralayer Excitons in a $MoSe_2/MoS_2$ Heterostructure. *Nano Letters*, 18(12):7651–7657, 2018.

[279] Iann C. Gerber, Emmanuel Courtade, Shivangi Shree, Cedric Robert, Takashi Taniguchi, Kenji Watanabe, Andrea Balocchi, Pierre Renucci, Delphine Lagarde, Xavier Marie, and Bernhard Urbaszek. Interlayer excitons in bilayer MoS_2 with strong oscillator strength up to room temperature. *Physical Review B*, 99(3):1–8, 2019.

[280] Hiram J. Conley, Bin Wang, Jed I. Ziegler, Richard F. Haglund, Sokrates T. Pantelides, and Kirill I. Bolotin. Bandgap engineering of strained monolayer and bilayer MoS_2. *Nano Letters*, 13(8):3626–3630, 2013.

[281] Ming Hui Chiu, Ming Yang Li, Wengjing Zhang, Wei Ting Hsu, Wen Hao Chang, Mauricio Terrones, Humberto Terrones, and Lain Jong Li. Spectroscopic signatures for interlayer coupling in MoS_2-WSe_2 van der waals stacking. *ACS Nano*, 8(9):9649–9656, 2014.

[282] Kai Wang, Bing Huang, Mengkun Tian, Frank Ceballos, Ming Wei Lin, Masoud Mahjouri-Samani, Abdelaziz Boulesbaa, Alexander A. Puretzky, Christopher M.

Rouleau, Mina Yoon, Hui Zhao, Kai Xiao, Gerd Duscher, and David B. Geohegan. Interlayer Coupling in Twisted WSe_2/WS_2 Bilayer Heterostructures Revealed by Optical Spectroscopy. *ACS Nano*, 10(7):6612–6622, 2016.

[283] Shinichiro Mouri, Wenjing Zhang, Daichi Kozawa, Yuhei Miyauchi, Goki Eda, and Kazunari Matsuda. Thermal dissociation of inter-layer excitons in MoS_2/MoSe $_2$ hetero-bilayers. *Nanoscale*, 9(20):6674–6679, 2017.

[284] Jianting Ji, Shan Dong, Anmin Zhang, and Qingming Zhang. Low-frequency interlayer vibration modes in two-dimensional layered materials. *Physica E: Low-Dimensional Systems and Nanostructures*, 80:130–141, 2016.

[285] A. Loiseau I. Stenger, L. Schué, M. Boukhicha, B. Berini, B. Plaçais and J. Barjon. Low frequency Raman spectroscopy of few-atomic-layer thick hBN crystals. 0(5):302, 1385.

[286] A. C. Dias, Fanyao Qu, David L. Azevedo, and Jiyong Fu. Band structure of monolayer transition-metal dichalcogenides and topological properties of their nanoribbons: Next-nearest-neighbor hopping. *Physical Review B*, 98(7), 2018.

[287] Ang Yu Lu, Hanyu Zhu, Jun Xiao, Chih Piao Chuu, Yimo Han, Ming Hui Chiu, Chia Chin Cheng, Chih Wen Yang, Kung Hwa Wei, Yiming Yang, Yuan Wang, Dimosthenis Sokaras, Dennis Nordlund, Peidong Yang, David A. Muller, Mei Yin Chou, Xiang Zhang, and Lain Jong Li. Janus monolayers of transition metal dichalcogenides. *Nature Nanotechnology*, 12(8):744–749, 2017.

[288] Amey Apte, Vidya Kochat, Pankaj Rajak, Aravind Krishnamoorthy, Praveena Manimunda, Jordan A. Hachtel, Juan Carlos Idrobo, Syed Asif Syed Amanulla, Priya Vashishta, Aiichiro Nakano, Rajiv K. Kalia, Chandra Sekhar Tiwary, and Pulickel M. Ajayan. Structural Phase Transformation in Strained Monolayer $MoWSe_2$ Alloy. *ACS Nano*, 12(4):3468–3476, 2018.

[289] N Sule and I Knezevic. Phonon-limited electron mobility in graphene calculated using tight-binding Bloch waves. *Journal of Applied Physics*, 112(5), 2012.